Dynamic Characteristics and Evaluation of Ground Response for Sands with Non-Plastic Fines

A thesis presented in fulfilment of the requirements for the
Degree of Doctor of Philosophy
in the
Department of Civil and Natural Resources Engineering

M. Jawad Arefi

University of Canterbury,
Christchurch, New Zealand
April 2014

To my parents

Acknowledgements

I am indebted to many individuals and organizations for their assistance in my studies and particularly in this thesis research.

Prof. Misko Cubrinovski, my thesis and academic supervisor, developed the basic ideas behind this research and provided constructive comments and guidance without which this work would not have been possible. His enthusiasm for the present work and his kind interest in my educational development are deeply appreciated.

Dr. Brendon Bradley, my associate supervisor, supervised many of the modelling and analysis studies drawn upon in this work and consistently provided encouragement and constructive criticism. His insightful comments on many aspects of this thesis resulted in immeasurable improvements.

Dr. Md Mizanur Rahman assisted to set up and to calibrate the equipment required in this research. His help in the preparation of laboratory testing program is gratefully acknowledged.

I am indebted to Dr Liam Wotherspoon for providing valuable in-situ field data collected after the Canterbury earthquake sequence in Christchurch.

Among my friends, I would like to thank Dr. Sean Rees, Merrick Taylor, Saumyasuchi Das, Kelly Robinson and Masoud Moghaddasi for their distinctive support and numerous invaluable discussions and suggestions.

I am thankful to the University of Canterbury, which has been my second home for five critical years. Also I'd like to thank the Civil & Natural Resources Engineering Department for their help and support throughout. I would particularly like to thank

many individuals who made me feel at home and give me encouragement in time of need. Most notable are Louise Barton, Elizabeth Ackermann and Alan Jolliffe. I also wish to acknowledge John Kooloos and Siale Faitotonu for their technical support in the geomechanics laboratory.

I am grateful to the University of Canterbury and the New Zealand Geotechnical Society for UC Doctoral and NZGS scholarships provided over the course of this work. Financial support was also provided by the ECan and EQC and their support for this work is very much appreciated. The very important set of strong-motion records was made possible by the GeoNet project sponsored by EQC. The existence of the CanNet component of the network came about because of the vision and persistence of Dr. John Berrill in promoting the concept.

As always, the love and support of my wife, Naeema, for her sacrifice and devoted effort at homemaking, and for providing immeasurable moral support and tender loving care so valuable in the trials of writing a thesis.

Abstract

Deformational properties of soil, in terms of modulus and damping, exert a great influence on seismic response of soil sites. However, these properties for sands containing some portion of fines particles have not been systematically addressed. In addition, simultaneous modelling of the modulus and damping behaviour of soils during cyclic loading is desirable. This study presents an experimental and computational investigation into the deformational properties of sands containing fines content in the context of site response analysis. The experimental investigation is carried on sandy soils sourced from Christchurch, New Zealand using a dynamic triaxial apparatus while the computational aspect is based on the framework of total-stress one-dimensional (1D) cyclic behaviour of soil.

The experimental investigation focused on a systematic study on the deformational behaviour of sand with different amounts of fines content (particle diameter ≤ 75μm) under drained conditions. The silty sands were prepared by mixing clean sand with three different percentages of fines content. A series of bender element tests at small-strain range and stress-controlled dynamic triaxial tests at medium to high-strain ranges were conducted on samples of clean sand and silty sand. This allowed measurements of linear and nonlinear deformational properties of the same specimen for a wide strain range. The testing program was designed to quantify the effects of void ratio and fines content on the low-strain stiffness of the silty sand as well as on the nonlinear stress-strain relationship and corresponding shear modulus and damping properties as a function of cyclic shear strains.

Shear wave velocity, V_s, and maximum shear modulus, G_{max}, of silty sand was shown to be significantly smaller than the respective values for clean sands measured

at the same void ratio, e, or same relative density, D_r. However, the test results showed that the difference in the level of nonlinearity between clean sand and silty sands was small. For loose samples prepared at an identical relative density, the behaviour of clean sand was slightly less nonlinear as compared to sandy soils with higher fines content. This difference in the nonlinear behaviour of clean sand and sandy soils was negligible for dense soils. Furthermore, no systematic influence of fines content on the material damping curve was observed for sands with fines content FC = 0 to 30%.

In order to normalize the effects of fines on moduli of sands, equivalent granular void ratio, e^*, was employed. This was done through quantifying the participation of fines content in the force transfer chain of the sand matrix. As such, a unified framework for modelling of the variability of shear wave velocity, V_s, (or shear modulus, G_{max}) with void ratio was achieved for clean sands and sands with fines, irrespective of their fines content.

Furthermore, modelling of the cyclic stress-strain behaviour based on this experimental program was investigated. The modelling effort focused on developing a simple constitutive model which simultaneously models the soil modulus and damping relationships with shear strains observed in laboratory tests. The backbone curve of the cyclic model was adopted based on a modified version of Kondner and Zelasko (MKZ) hyperbolic function, with a curvature coefficient, a. In order to simulate the hysteretic cycles, the conventional Masing rules (Pyke 1979) were revised. The parameter n, in the Masing's criteria was assumed to be a function of material damping, h, measured in the laboratory. As such the modulus and damping produced by the numerical model could match the stress-strain behaviour observed in the laboratory over the course of this study. It was shown that the Masing parameter

n, is strain-dependent and generally takes values of $n \leq 2$. The model was then verified through element test simulations under different cyclic loadings. It was shown that the model could accurately simulate the modulus and the damping simultaneously.

The model was then incorporated within the OpenSees computational platform and was used to scrutinize the effects of damping on one-dimensional seismic site response analysis. For this purpose, several strong motion stations which recorded the Canterbury earthquake sequence were selected. The soil profiles were modelled as semi-infinite horizontally layered deposits overlying a uniform half-space subjected to vertically propagating shear waves. The advantages and limitations of the nonlinear model in terms of simulating soil nonlinearity and associated material damping were further scrutinized.

It was shown that generally, the conventional Masing criteria unconservatively may underestimate some response parameters such as spectral accelerations. This was shown to be due to larger hysteretic damping modelled by using conventional Masing criteria. In addition, maximum shear strains within the soil profiles were also computed smaller in comparison to the values calculated by the proposed model. Further analyses were performed to study the simulation of backbone curve beyond the strain ranges addressed in the experimental phase of this study. A key issue that was identified was that relying only on the modulus reduction curves to simulate the stress-strain behaviour of soil may not capture the actual soil strength at larger strains. Hence, strength properties of the soil layer should also be incorporated to accurately simulate the backbone curve.

Table of contents

List of figures

List of tables

Symbols and abbreviations

Symbols

a	=	Curvature coefficient in the hyperbolic model
A_n	=	Cross sectional area
b	=	Fines influence factor
$[C]$	=	Viscous damping matrix
C_E	=	Viscous damping coefficient
d	=	Diameter of small spheres
d_{31}	=	Piezoelectric charge constant
d_{50}	=	Diameter of sand of which 50% of particles are smaller than
D_r	=	Relative density
D_{10}	=	Diameter of which 10% of soil particles are smaller than
e	=	Void ratio
e_g	=	Intergranular void ratio
e_{max}	=	Maximum void ratio
e_{min}	=	Minimum void ratio
e^*	=	Equivalent granular void ratio
E_{eq}	=	Equivalent Young's modulus
E_{max}	=	Maximum Young's modulus
f		Frequency
f_c	=	Fines content (decimal)
f_{cth}	=	Threshold fines content
f_{ch}	=	Characteristic frequency
f_{max}	=	Maximum frequency propagated in each soil layer
f_r	=	Resonance frequency
f_s	=	Sleeve resistance

F_{bb}	=	Backbone function
FC	=	Fines content (percentage)
FR	=	Friction ration in CPT tests
g	=	Gravity acceleration
G	=	Shear modulus
G_{max}	=	Maximum shear modulus
G_s	=	Specific gravity
G_{sec}	=	Secant shear modulus
G_t	=	Tangent shear modulus
h	=	Material damping ratio
h_i	=	Thickness of layer i
h_{max}	=	Maximum material damping ratio
h_{min}	=	Minimum material damping ratio
$\{u\}$	=	Unit vector
I_c	=	Soil behaviour type index
k	=	Spring stiffness
k_h	=	Coefficient of permeability
$[K]$	=	Stiffness matrix
l	=	Travel length
L_{tt}	=	Wave path length
ΔL	=	Double amplitude axial displacement
m		Porosity
m_w		Mass of water
$[M]$	=	Mass matrix
M_L	=	Richter earthquake magnitude
M_w	=	Moment earthquake magnitude
M_s	=	Mass of solid particles in each specimen

n	=	Masing coefficient
OCR	=	Overconsolidation ratio
p'	=	Effective mean normal stress
p'_{ss}	=	Effective mean stress at steady state
P_C, P_E	=	Single amplitude compression and extension axial loads
PGA	=	Peak ground acceleration
PGA_v	=	Vertical peak ground acceleration
PI	=	Plasticity index
q	=	Deviatoric stress
q_c	=	Penetration resistance
Q_t, Q_{tn}	=	Normalized penetration resistance
R^2	=	Coefficient of determination
R_{rup}	=	Distance to the rupture point
S_a	=	Spectral acceleration
t	=	Signal propagation time
Δt	=	Time delay in bender element
$\ddot{u}_g$	=	Acceleration at the base of the soil column
$\{u\}$	=	Vector of nodal relative displacements
$\{\dot{u}\}$	=	Vector of nodal relative acceleration
$\{\ddot{u}\}$	=	Vector of nodal relative acceleration
V_s, V_{sE}	=	Shear wave velocity
V_s^m, V_s^p	=	Measured and predicted shear wave velocities
V_t, V_f, V_i	=	Volume of lost water during test; final and initial volumes
V_v, V_s	=	Volume of voids and solids
w	=	Water content
W	=	Area of elastic energy
ΔW	=	Area of hysteretic loop

α	=	Tortuosity factor
γ	=	Shear strain
γ_a	=	Cyclic shear strain amplitude
γ_r	=	Reference strain
ε_a	=	Axial strain
$(\varepsilon_a)_{SA}$	=	Single-amplitude axial strain
ε_r	=	Radial strain
θ	=	Rotation angle
λ	=	Wavelength
ν	=	Poisson ratio
ξ	=	Rayleigh damping
ρ, ρ_E	=	Soil density
ρ_f	=	Mass density of fluid
ρ_g	=	Mass density of solid grains
ρ_{sat}	=	Saturated soil density
σ'_0	=	Effective confining stress
σ_1, σ_3	=	Principal stresses
σ_d	=	Single amplitude cyclic deviatoric stress
σ'_m	=	Mean effective confining stress
σ'_v	=	Vertical effective stress
τ	=	Shear stress
τ_a	=	Cyclic shear stress amplitude
τ_{max}	=	Maximum shear stress
ϕ	=	Curvature coefficient of unloading-reloading cycles
χ	=	Disparity ratio
ω	=	Circular frequency

Abbreviations

1D	=	One dimensional
BE	=	Bender elements
CBD	=	Central business district
CERA	=	Canterbury earthquake recovery authority
CPS	=	Canterbury Plains Seismicity Zone
CPT	=	Cone penetration test
DP	=	Differential pressure
F	=	Ferrymead
FB	=	Fitzgerald bridge
LVDT	=	Linear variable differential transformer
MASW	=	Multi-channel analysis of surface waves
MDOF	=	Multi degree of freedom
NZS	=	New Zealand Standard
OpenSees	=	Open System for earthquake engineering simulation
SA-SR	=	Sub-angular, sub-rounded
SPT	=	Standard penetration test
S/N	=	Signal-to-noise ratio
TS-RC	=	Torsional shear – resonant column
TX	=	Triaxial

1 Introduction

1.1 Background

The evaluation of the risk posed by earthquakes to engineered structures at a site of interest (seismic hazard analysis) may be separated into the components of earthquake source (some geological fault at depth D, and distance R from the site), travel path of the ground motion, and the local site effects and interaction with the engineered structures. The conceptual model comprising these components is shown schematically in Figure 1-1. Although source and path effects are also important, there are many uncertainties associated with source mechanism and geological parameters along the transmission path. Hence, simpler approaches comprising only local site effects are generally adopted for ground motion analyses. Moreover, seismic site effects can be regarded as a systematic feature of the observed ground motion at the sites of interest.

Case histories, from earthquakes such as 1985 Mexico City (Cassaro and Romero, 1986, Seed et al., 1987), 1989 Loma Prieta earthquake (Seed et al. 1990; Borcherdt and Glassmoyer 1992), 1995 Kobe (Bardet et al. 1995), and 2011 Christchurch (Cubrinovski et al., 2011) demonstrated the clear correlation between ground motion amplification and local soil conditions. Consequently engineers are concerned with an accurate evaluation of the local site response for the seismic design of structures (e.g. NZS 1170.5 2004, ASCE 7, Eurocode 8). As such, in this thesis specific attention is given to the study of the soil characteristics and local site response on strong ground motions.

The assessment of seismic site response is difficult, in part because soils tend to exhibit highly nonlinear stress-strain behaviour during strong earthquakes. To understand such a complex response and mitigate its consequences, one must have both a fundamental understanding of dynamic soil behaviour as well as mathematical models capable of predicting soil response under earthquake excitation.

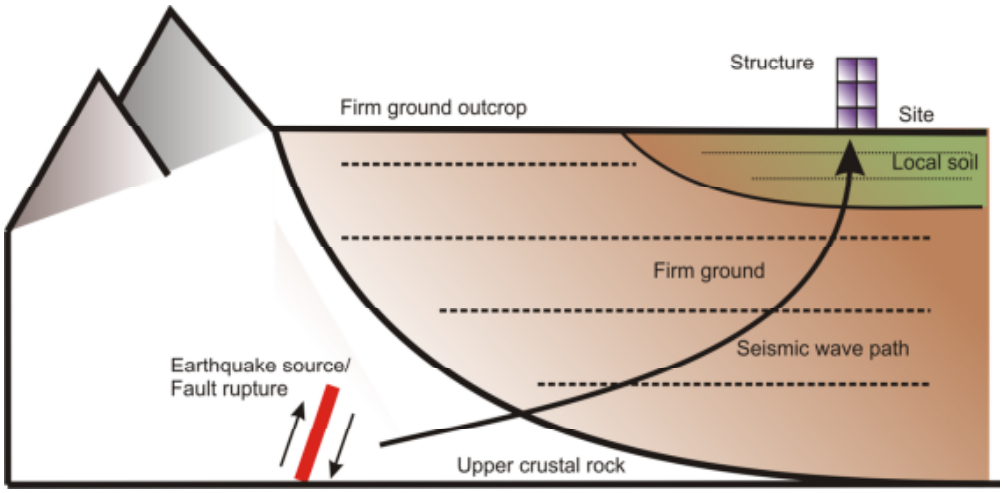

Figure 1-1 Schematic figure of propagation of seismic waves from earthquake source through the upper crustal rock, firm ground, and local soil deposit (after ISO, 2005)

The factors which influence the dynamic soil behaviour under cyclic loading generally fall into two groups: 1) parameters relating to soil loading and state parameters, and 2) factors pertaining to the intrinsic material properties. The effects of these factors on the dynamic properties of local soils has been the subject of numerous studies to better understand site response during earthquakes (e.g. Kokusho et al., 1982, Seed and Idriss, 1970, Sun et al., 1988, Vucetic, 1990, Hardin and Drnevich, 1972b, Tatsuoka and Shibuya, 1991). However, a review of available literature reveals that experimental data on the effects of fines (particles diameter less than 0.075mm) on the dynamic behaviour of sands are scarce. It has been shown that fines content can affect the cyclic behaviour and the liquefaction resistance of soils in a

great extent (e.g. Thevanayagam and Mohan 2000; Cubrinovski and Rees 2008; Rahman et al. 2008).

The sandy soils underlying the city of Christchurch, located in the South Island of New Zealand, have variable amounts of fines. On the other hand, the 2010-11 Canterbury earthquake sequence showed that the seismic hazard in the city is quite high; hence the amplification due to local soil sites can be disastrous to the built-environment. Moreover, little laboratory testing has been performed on general stress-strain behaviour of the fines-containing sandy soils of Christchurch. Therefore, there is a need for a systematic experimental testing to better understand the dynamic behaviour of these soils.

Different methods of mathematical soil modelling are used to simulate seismic site response. In the absence of pore water pressure generation, total stress nonlinear modelling of soil is capable of simulating the nonlinear stress-strain path during the cyclic loading. In this class of modelling, the cyclic stress-strain relationships are generally characterized by a backbone curve and a series of rules that describe unloading-reloading behaviour. However, because most nonlinear total stress numerical codes use Masing rule (Pyke 1979), they cannot adequately simulate the nonlinear dynamic soil characteristics. For instance, the poor fits to experimental damping curves often result in overestimation of damping in many mathematical models. As a consequence seismic response parameters may unconservatively be under-predicted. Modifying Masing criteria to account adequately for experimental dynamic soil properties can help in predicting the soil response under earthquake excitation.

1.2 Objectives and scope of work

There are three main objectives in this thesis: 1) to scrutinize the effects of fines on the deformational properties of fines-containing sand and establish modulus reduction and material damping curves for such soils, 2) to develop a relatively simple constitutive model capable of fitting any desired set of laboratory G-γ (shear modulus vs. strain) and h-γ (damping vs. strain) curves over the entire range of relevant strains, and 3) to examine the effects of nonlinearity on site response of selected Christchurch strong motion station sites using the developed stress-strain model.

The first objective aims to identify the low- and high-strain deformational properties of soils under cyclic loading and to understand how addition of fines to sand can affect these properties. In this context, the effects of fines content on the low-strain shear modulus, the modulus reduction and the material damping curves has been be scrutinized. One of the key problems in the assessment of the influence of fines on sand behaviour is establishing a common basis for comparison of clean sands and sands with fines. Hence, a measure for an identical density state has been considered to quantify the effect of fines content on the modulus and the damping behaviour of sands.

The employed testing program in this study involves testing sandy soils sourced from Christchurch, New Zealand and measuring the low-strain shear modulus, modulus reduction, and material damping curves of these sandy specimens in the laboratory utilizing a bender element device and dynamic triaxial apparatus. The bender element device has been used to measure the low-strain modulus of soils with a high accuracy. The triaxial apparatus, on the other hand, has been used to establish G-γ and h-γ curves (modulus reduction and the material damping ratio curves) for a

wide range of strains. This study deals only with non-plastic fines with fines content below a threshold fines content of ~30% using sandy soils sourced from sites in Christchurch. Four mixtures of sandy specimens were created with adding fines content of FC = 0, 10, 20 and 30% and a wide range of specimen densities (e = 0.483 – 0.826; D_r = 40 – 95%) were targeted. All specimens were tested under a confining pressure of p' = 100kPa. The method of testing essentially follows the Japanese Geotechnical Society Standard (2000) procedure for determination of deformation properties of geomaterials using a cyclic triaxial test. 27 cyclic tests were performed under drained conditions on isotropically consolidated specimens of clean and silty sand. All these experimental tests were performed in the geomechanics laboratory at the University of Canterbury.

The second objective aims to provide a simple and practical model that can simulate simultaneously the experimental modulus reduction and material damping curves for sandy soils. The modulus reduction curves are often modelled adequately in nonlinear constitutive models using hyperbolic (e.g. Matasovic and Vucetic, 1993) or Ramberg-Osgood (1943) formulations. Conventional Masing (1926) criteria are generally employed to model the cyclic hysteresis of soils. The difference between the damping ratio measured in the laboratory and the predicted damping using Masing criteria has demonstrated the limitations of these rules (e.g. Ishihara 1996). Moreover, the damping that results from the use of Masing criteria is believed to unconservatively underestimate some of the seismic response parameters (e.g. Stewart et al., 2008). Hence, it is aimed to circumvent the damping problem inherent in using Masing rules. The scope of this objective is limited to total-stress and one-dimensional analyses, although the developed concept can be applicable to two-dimensional analyses.

The majority of current codes related to total-stress site response analysis employ Masing criteria. Therefore, implementation of the improved version of the Masing criteria in a finite element software package (e.g. OpenSees) is desirable. Furthermore, there is a need to compare the response in terms of modelled material damping. Towards this end, the nonlinear dynamic curves of Christchurch soil measured in the laboratory combined with the developed constitutive model are to be employed in nonlinear ground response analyses. As such, the abilities of the conventional Masing criteria and the proposed formulation can be assessed against simulation of damping. The effect of nonlinearity and in particular damping on the site response analyses on a case study from the 2010 Darfield earthquake has been investigated. One of the strong motion stations which recorded the Canterbury earthquake sequence is selected for this purpose.

1.3 Thesis organization

Following this introduction, Chapter 2 describes the literature review in relation to the measurement of the dynamic soil properties using a bender element device and dynamic triaxial testing. Influences of different factors on the dynamic soil properties are then presented. The effects of fines on the behaviour of sandy soils are discussed. Finally previous developments for different site response analysis approaches are summarized.

Chapter 3 provides information regarding the soils analysed in this work and the employed methodology for sample preparation and laboratory testing. A general description of the dynamic laboratory test equipment used to evaluate the nonlinear soil properties, along with a brief review of the theory upon which the laboratory testing is founded are also summarized in Chapter 3.

Chapter 4 presents the results of the maximum shear modulus (G_{max}), the modulus reduction (G-γ) and material damping (h-γ) of the Fitzgerald Bridge (FB) sand. The first half of the chapter considers bender element test results on the FB soil samples to investigate the influence of void ratio and fines content on the shear wave velocity and maximum shear modulus. The second half provides the triaxial test results in terms of nonlinear stress-strain relationships and modulus reduction and material damping curves for FB sand.

Chapter 5 considers the equivalent granular void ratio, e^*, to interpret the effects of fines on the modulus and damping properties.

Chapter 6 develops a simple shear stress-shear strain model which can accurately simulate stress-strain behaviour of sand as represented by conventional modulus reduction and material damping curves. A brief review of previous attempts to reach this objective is also presented. Verification of the proposed model employing several types of cyclic loads is presented.

Chapter 7 presents the results of using the derived soil parameters/models and strong motion inputs in seismic response analyses employing the Masing criteria and the proposed formulation in Chapter 6. In addition, this chapter compares the capabilities of the nonlinear site response analyses with respect to observed ground motion during the 4 September 2010 Darfield, Canterbury earthquake.

Chapter 8 draws together conclusions from this study. It highlights the main contributions the study has made to the knowledge of the dynamic soil properties, stress-strain behaviour and its mathematical modelling. Finally, in the context of acknowledging the limitations of the project, further research has been suggested.

Appendix A discusses the local site conditions found in Christchurch. The stratigraphy of several strong motion stations which are selected for site response purposes are described. The dynamic soil properties required for modelling the soil profiles underneath the selected strong motion stations are also presented.

Appendix B provides the C++ interface and implementation code of the stress-strain model discussed in Chapter 6. The developed code is implemented into the finite element software OpenSees.

Appendix C presents a simple 1-D model of a hypothetical soil profile analysed by the finite element program OpenSees incorporating the developed uniaxial material model.

Finally, Appendix D presents the stress-strain cyclic loops measured during the laboratory testing of sandy specimens.

2 Literature review

2.1 Introduction

The seismic energy released in the event of a fault rupture propagates as stress waves (pressure or *P*-type, and shear or *S*-type waves) radially away from the earthquake source through crustal rock to the earth's surface (Figure 2-1). Waves that reach the earth's surface can cause damage to engineered structures and lifelines, and may initiate catastrophic ground failure (landslides, rock fall, and avalanche) and tsunami. The nature of the ground motion that interacts with structures at the ground surface is modified by the materials through which it passes from the source to the site. The soil and rock deposits can be considered to act as signal processing filters, in that the energy of these waves may be amplified at certain frequencies while attenuated at others, affecting the dynamic response of engineered structures at the ground surface. This is referred to as an impedance effect, and is caused by the reduction in density, stiffness and consequently velocity of the incoming wave energy (e.g. Kramer 1996). Therefore, the earthquake event (how the rupture occurs in time and space), the path of the waves as they travel through the earth, and the local soil conditions are key factors for analysing the ground motion and its influences on the built environment. Thus, a seismic hazard analysis generally involves three components:

1) A seismicity model which defines the earthquake occurrence probability in regions close to the area of interest;

2) An attenuation model which approximates the energy loss and wave modification as the seismic waves travel to the basement rock under the area; and

3) A site response model that predicts the changes to the earthquake waves as they propagate up through the soil layers underlying the site.

The work presented in this thesis focuses on the site response component of the seismic hazard analysis. It involves experimental characterization of the modulus reduction (G-γ) and damping (h-γ) properties of Christchurch fine silty sands, the development of an updated hysteretic soil constitutive model to accurately simulate soil behaviour, followed by its implementation in a numerical code (OpenSees) to evaluate the local site response at sites of interest in Christchurch, New Zealand following the 2010-2011 Canterbury earthquake sequence.

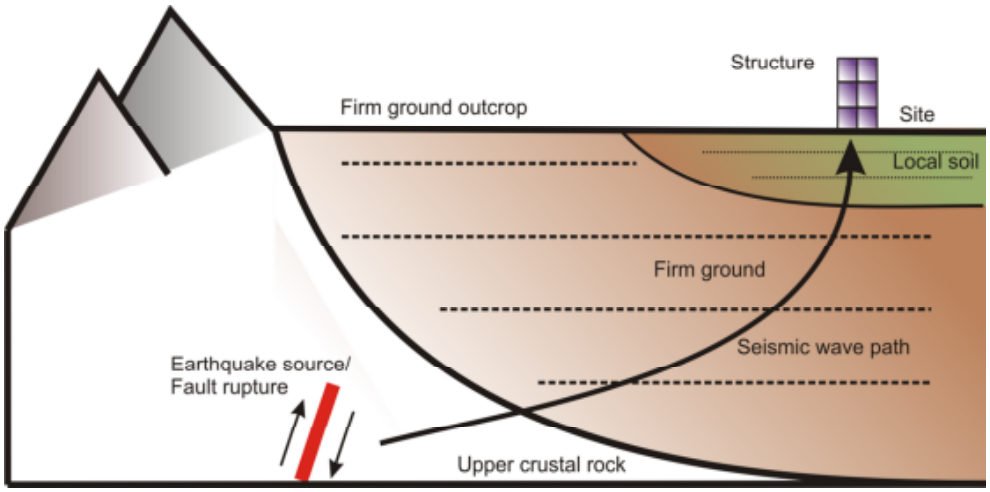

Figure 2-1 Schematic illustration of seismic wave propagation through the upper crustal rock, firm ground, and local surficial soil layers (after ISO, 2005)

The seismic response of a soil deposit is dictated primarily by the stiffness, damping, thickness and density of the soil deposit in addition to the characteristics of the representative bedrock motion. The stiffness and damping characteristics are the most important local soil parameters required for dynamic response analyses of earth structures. Furthermore, these parameters can be influenced by different factors (Tatsuoka and Shibuya, 1991a, Darendeli, 2001, Kramer, 1996, Ishihara, 1996,

Iwasaki and Tatsuoka, 1977, Seed and Idriss, 1970, Stokoe et al., 1999, Sun et al., 1988). Section 2.2 of this chapter first provides a brief review of the measurement procedures for determining the modulus and damping properties of soil and then presents the major studies that have investigated the influence of loading conditions and material type on the behaviour of modulus and damping soil properties.

Previous studies have not systematically examined the influence of fines content on the general trend of G-γ and h-γ properties of sand. Whereas, it has been shown that fines content can affect the cyclic behaviour of soils in a great extent (e.g. Cubrinovski and Rees, 2008, Thevanayagam and Mohan, 2000, Rahman et al., 2008). One of the objectives of this work is to study the effects of fines content on the modulus and damping properties of sand. Section 2.3 presents background information on the effects of fines on the behaviour of sandy soils observed during recent laboratory studies. This includes reviews of relevant literature so as to better understand how fines affect the internal structure of sand and clarify their effect on the steady state of deformation as well as the cyclic resistance of sand.

Finally Section 2.4 discusses the mathematical modelling of modulus reduction and material damping properties of soil in the context of seismic site response analyses. This review addresses many theoretical and analytical aspects of constitutive modelling of soil and therefore attention is only limited to studies that are more closely related to the present work.

2.2 Modulus reduction (G-γ) and material damping (h-γ) soil properties

Accurate measurement of the modulus reduction and damping properties of soil is crucial in dynamic response analyses, as well as in the design and performance evaluation of earth structures and foundations. A few techniques are currently practiced to experimentally evaluate the dynamic soil behaviour in the laboratory as well as in the field under in-situ conditions (e.g. Stokoe and Santamarina, 2000, Kramer, 1996). These techniques include testing in low- to intermediate- and high-strain ranges and under variable confining pressures and drainage conditions. The bender element (BE) device was employed in this study to measure the shear wave velocity, V_s, and low-strain stiffness of soil specimen. The first part of this section reviews the use of BE in the laboratory to accurately measure V_s. However, soil exhibits nonlinear behaviour within the shear strain range of 0.001% to 1%, which corresponds to the range of primary interest for earthquake engineers. The measurement of the nonlinear dynamic properties (shear modulus, G, and material damping, h) within this range is further explained in Section 2.2.2.

Several factors can affect the modulus and material damping properties of soils including strain amplitude, mean effective confining pressure, soil type, plasticity of soils, and loading frequency, amongst others. The relative importance of each parameter and the trends from previous studies are discussed in the second part of this section. The effects of fines content on shear modulus and damping curves are discussed in more detail in chapters four and five.

2.2.1 The measurement of stiffness at small strains using BE

The maximum shear modulus G_{max}, represents one of the critical geotechnical parameters when evaluating the response of soil deposits and earth structures under cyclic loading conditions and is measured at small-strain levels. Various types of dynamic laboratory techniques have been developed to measure the so-called maximum or small-strain shear modulus, G_{max} (e.g. Stokoe and Santamarina, 2000). They may be divided into two approaches:

1) Vibration methods such as torsional shear and resonant column (TS-RC) tests (e.g. Stokoe and Santamarina, 2000, Kramer, 1996, Japanese Geotechnical Society, 2000),

2) Wave propagation methods such as the ultra-sonic method and the bender element test (e.g. Shirley, 1978, Pennington, 1999).

The bender element (*BE*) method was originally developed by Shirley and Anderson (1975) to obtain maximum shear modulus G_{max}. The use of the bender element to measure the shear wave velocity, V_s, and the small-strain shear modulus, G_{max}, is popular due to its simplicity, reliability and optimal soil-transducer coupling (Lee and Santamarina, 2005, Leong et al., 2005).

The bender element is an electromechanical transducer capable of converting mechanical energy (S-waves) into electrical energy and vice versa. It comprises two thin layers of piezoelectric ceramic platelets, typically made of a perovskite mineral such as lead zirconate titanate or barium titanate, with a central shim of brass, stainless steel, or other ferrous nickel alloy to provide additional rigidity (Shirley 1978). When a potential difference (voltage) is applied to the bender element, the induced polarization across the platelets will cause the element to bend. In this way,

the bender element may act as a very small shear wave (*S*-wave) signal generator (Figure 2-2). Conversely, when an element is forced to bend as a result of S-wave arrival, a high-frequency voltage is generated and the bender element may also act as an *S*-wave signal receiver or sensor (Shirley, 1978, Viggiani and Atkinson, 1995, Blewett et al., 1999). The disturbance associated with the vibratory movement of the particles is very small (shear strain levels in the order of $<10^{-4}$%) which avoids permanent deformation of the soil. Therefore, it is assumed that the material is deformed within the elastic range, but with a level of particle vibration sufficiently large enough after travelling through the material (with associated radiation damping) to deflect the receiving bender element and induce a voltage that may be measured by an oscilloscope.

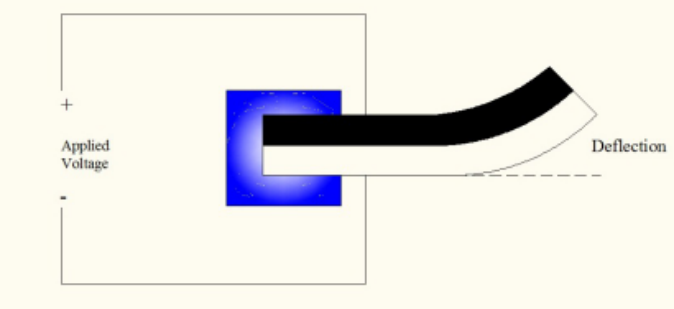

Figure 2-2 Exaggerated schematic view of bender element

The type of high-frequency wavelet excitation can include single frequency sinusoidal wave or frequency sweep, random noise, or a step function (Stokoe and Santamarina, 2000). There are two types of bender elements: series and parallel. For the same applied voltage, the parallel-type connection provides twice the displacement than the series-type connection; therefore it is suggested to use a parallel transmitter bender element and a series-type for receiver (Leong et al., 2005).

Unfortunately, the correct interpretation of bender element test results may be difficult. The common issues encountered are explained in the following section.

2.2.1.1 BE test interpretation

In order to evaluate the low-strain shear modulus from the measured shear wave velocity using the bender elements, equation (2-1) can be employed; this equation is derived based on the theory of wave propagation in an elastic media (e.g. Kramer 1996). By analysis of the transmitted and received movements of the sensors, it is possible to derive the time of signal propagation, t, required to travel a distance, l. The shear wave velocity and the maximum shear modulus can then be computed as:

$$G_{\max} = \rho * V_s^2 = \rho\left(\frac{l}{t}\right)^2 \tag{2-1}$$

Equation (2-1) requires three parameters, soil density, ρ, shear wave travel length, l, and wave travel time, t. The accuracy with which G_{max} is measured depends on the accuracy in measuring sample density, the path length between the bender elements and the travel time. There are a number of uncertainties associated with each parameter, hence care should be taken in the process of measuring them. These uncertainties are elaborated in the following sub-sections.

2.2.1.2 Soil density, ρ:

Saturated soils have a multiphase nature which means the use of saturated soil density, ρ_{sat}, in equation (2-1) implicitly assumes that the pore water and solid particles that comprise the soil skeleton move together as a single phase. This assumption can be valid if the frequency of vibration is low as in the resonant column tests. In this case the solid particles and the water can move together because of the

high viscosity of the pore fluid and therefore the inertia of the fluid can be simply added to the inertia of the soil (low inertial effect). However, fluid-solid coupling can cause difficulty with the interpretation of the actual dynamic behaviour of water-saturated porous media in the case of high-frequency vibrations induced in the bender element test.

Biot (1941) was the first researcher to develop a fundamental analysis of an elastic wave propagating through a fluid saturated elastic isotropic porous medium using macroscopic continuum mechanics. This theory relates the physical properties of a saturated porous solid, specifically the density, elastic properties of soil skeleton, and compressibility of pore fluid and solid grains and considers three types of coupling; mechanical, inertial, and viscous. The mechanical coupling only exists in the presence of longitudinal waves (*P* waves) and may therefore be ignored for the evaluation of shear wave propagation during bender element tests (Gajo et al., 1997). It has been shown (e.g. Gajo et al., 1997) that inertial coupling is important only when the viscosity effect is relatively small compared to the inertial effect and relative motion is permitted between soil and fluid, in which case a shear wave propagates at a higher velocity corresponding to a density smaller than ρ_{sat}. This is normally the case when the frequency of the travelling wave is higher than the characteristic frequency f_{ch} (Gajo et al., 1997, Youn et al., 2008, Camacho-Tauta et al., 2012).

$$f_{ch} = \frac{mg}{2\pi k_h} \tag{2-2}$$

where m is porosity, g is gravity acceleration [m/s^2], and k_h is coefficient of permeability [m/s]. This effect is of particular interest in sands where high soil permeability corresponds to higher hydrodynamic interactions between the soil and

the water, and consequently a higher frequency dependent shear wave velocity. Wavelengths in the BE tests are assumed to greatly exceed typical pore dimensions and a porous medium can therefore be idealized as two continuous and superimposed phases (Qiu and Fox, 2008).

Based on theoretical and experimental test results, Gajo et al. (1997) reported that incorrectly assuming the degree of viscous and inertial coupling can lead to an error of about 15% in the shear modulus calculation whereas experimental errors in G_{max} may be as low as 1-2%. Camacho-Tauta et al. (2012) showed that for particulate materials the shear wave velocity at high frequency may be up to 6% greater than the shear wave velocity at low frequency and consequently the error of calculation of maximum shear modulus may be up to 12%. Qiu and Fox (2008) reported that the error associated with ignoring the dispersive nature of the shear wave velocity can be as high as 30%.

Berryman (1980) quantitatively compared measurements of elastic-wave speeds in a water-saturated porous structure of sintered glass beads to the prediction of Biot's theory and concluded that Biot's theory provides an accurate description of elastic wave propagation in fluid-saturated media. Later, Youn et al. (2008) conducted a series of torsional shear, resonant column (*RC-TS*) and bender element tests on silica sand at varying confining stresses. Figure 2-3 presents a comparison of measured shear wave velocities with theoretical response according to Biot (1941). It is shown that the shear wave velocity measured during high frequency bender element tests is higher than when obtained by RC-TS tests, and agrees well with the theoretical Biot values. When the velocity of a plane harmonic wave is a function of its frequency, then the propagating medium is called dispersive. However the shear modulus which

depends on the shear wave velocity, is a constant value and hence its evaluation using shear wave velocity can be rather sensitive.

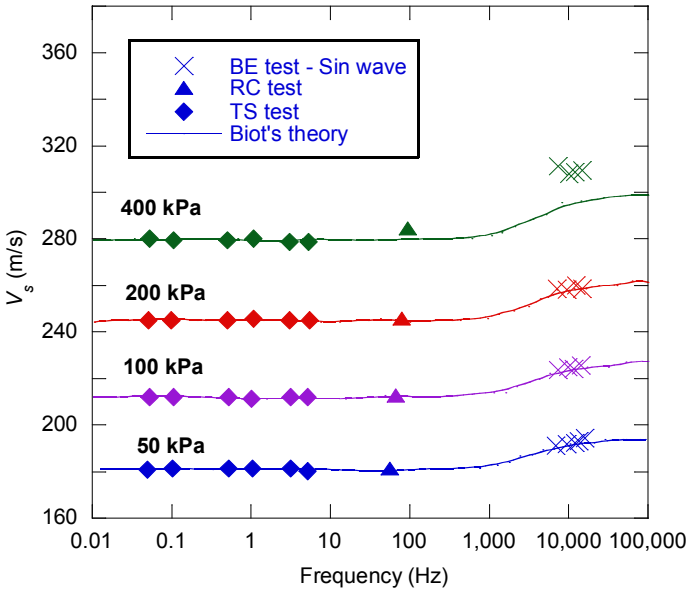

Figure 2-3 Agreement between the experimental and theoretical V_s as functions of frequency (silica sand, $e_i = 0.75$) (after Youn et al., 2008)

The use of equation (2-1) for multiphase soils requires an assumption for material density. In order to circumvent the possible error in calculating the modulus of saturated soils, an apparent mass density was suggested by Youn et al. (2008) to be used in the calculation of G_{max} obtained by bender element test results:

$$\rho_{\text{mod}} = (1-m)\rho_g + m\left(1-\frac{1}{\alpha}\right)\rho_f \tag{2-3}$$

where ρ_g is mass density of grains, m is the porosity, α is a tortuosity factor and ρ_f is mass density of fluid.

Qiu and Fox (2008) also provided some dimensionless charts which suggest that ρ_{mod} is a more appropriate value than ρ_{sat} to characterize small strain shear wave velocity in saturated sands. These charts allow routine determination of the ratio

between modified and saturated densities. Qiu and Fox (2008) showed that the modified density can be equal to saturated density for low hydraulic conductivity soils (e.g. clays) and can be less than saturated density for high hydraulic conductivity soils (e.g. sands and gravels). Based on Biot's theory it can be shown that the ratio of the effective density to saturated density can generally range from 0.75 to 1.0. The tortuosity factor, α, is the most influential parameter affecting the modified density; however its value is difficult to determine. Table 2-1 shows a list of tortuosity factors α found in the literature. It is clear that employing a high value for α in equation (2-3) results in the common assumption of bulk density equation. Figure 2-4 presents the variation of α with the change in porosity, m, for different proposed functions listed in Table 2-1.

Table 2-1 Tortuosity for different material types

Material type	α factor	Reference
Dry soil/ tubes	1	(Youn et al., 2008)
Spherical particles	$(1+m)/2m$	(Berryman 1981)
Particulate materials	2 - 3	(Stoll 1979)
Round grains	$m^{-1/2}$	(Gajo et al. 1997)
Saturated soil (low frequency)	infinity	(Youn et al., 2008)

m: Porosity

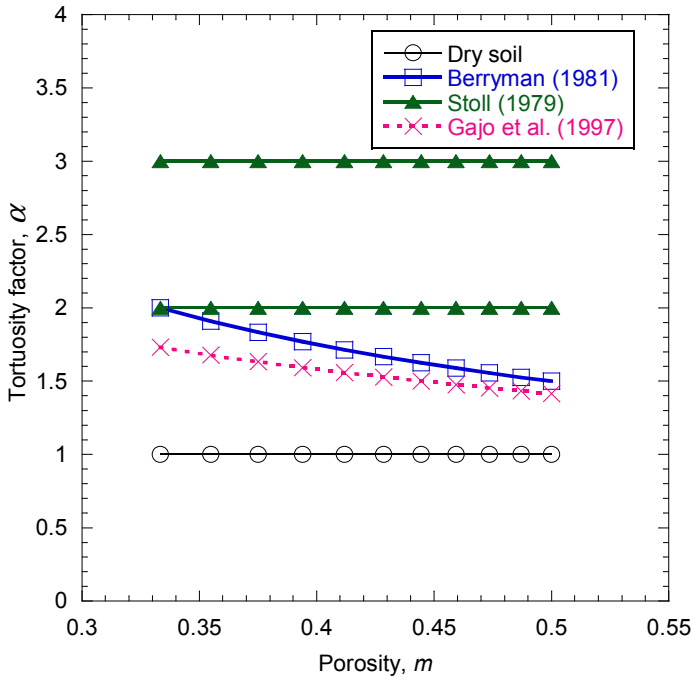

Figure 2-4 Tortuosity factor α, versus porosity *m* using different equations

2.2.1.3 Travel length, l:

Many studies have been conducted to identify the correct method to determine the length of the travel path between the sending and receiving bender elements. A clear consensus exists from these works that, the tip-to-tip distance between bender elements should be adopted as the shear wave travel length rather than the full height of the specimen (or some intermediary value) at the test stage when the *BE* test is carried out (Leong et al., 2005; Seiken Inc 2008, Lee and Santamarina, 2005, Viggiani and Atkinson, 1995, Gajo et al., 1997).

2.2.1.4 Travel time, t:

There are a number of uncertainties which makes the interpretation of wave travel time difficult. Bender elements radiate a combination of two *P*-waves and an *S*-wave in one polarized direction. These *P*-waves may appear as interference in the

received *S*-wave signal, producing what is referred as the "near field effects". This can alter the shape of the receiver signal and cause uncertainty in correctly picking the first arrival time of the shear wave (Figure 2-5); however this effect is more pronounced in tests on dry specimens. In addition, electrical crosstalk between source and receiver may also distort the received signals and consequentially, the determination of *t*. This effect manifests as an output signal having an early component which is quasi-simultaneous with the input signal. Electrical crosstalk can exert a great influence on the *BE* results of conductive soils such as wet clays and can be curtailed by grounding the cell and shielding the parallel platelet. (Lee and Santamarina, 2005, Viggiani and Atkinson, 1995, Jovicic et al., 1996).

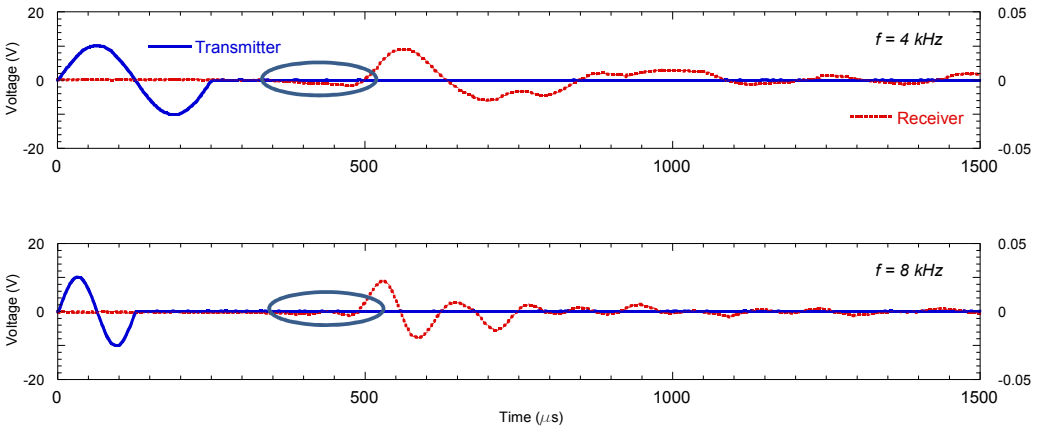

Figure 2-5 Influence of transmitter frequency on the near field effect

In spite of uncertainty caused by the near field effect the travel time can be reliably determined using first arrival, if appropriate measures are taken. It has been shown that the bender element responses can be enhanced greatly by applying the following testing procedures (e.g. Lee and Santamarina, 2005, Leong et al., 2005):

1) The frequency of the input sine pulse approaches the resonant frequency of the bender element-soil system and consequently the maximum output in the receiver produced (Figure 2-6),

2) The wave path length to the wavelength ratio (L_{tt}/λ) is at least 3.3 so the far-field component is clearly the dominant component and the shape of the receiver pulse is not obscured,

3) Good contact conditions exist between the sand particles and the receiver bender element,

4) The magnitude of applied voltage is high enough for the travelling wave to be detected by the receiver (Leong et al., 2005, Kumar and Madhusudhan, 2010) and,

5) Sinusoidal waves are used in order to produce similar input and output signals (Blewett et al., 1999, Lee and Santamarina, 2005).

Figure 2-6 illustrates measured input and output signals for a given bender element installation. It is shown that as the frequency of the sinusoidal transmitter approaches the resonant frequency of the bender element - soil system, the response is enhanced. It is apparent in this figure that although a step function includes all the frequencies, the received signal is distorted as shown in the top of the figure.

In addition to the listed testing procedures, different interpretation methods have been proposed to estimate the travel time more accurately. This includes first arrival, peak-to-peak, cross-correlation, and cross-power of input and output signals (e.g. Leong et al. 2005). However, based on an experimental study, Kumar and Madhusudhan (2010) showed that maximum error using different methods can be limited to within 6% if above testing precautions are followed.

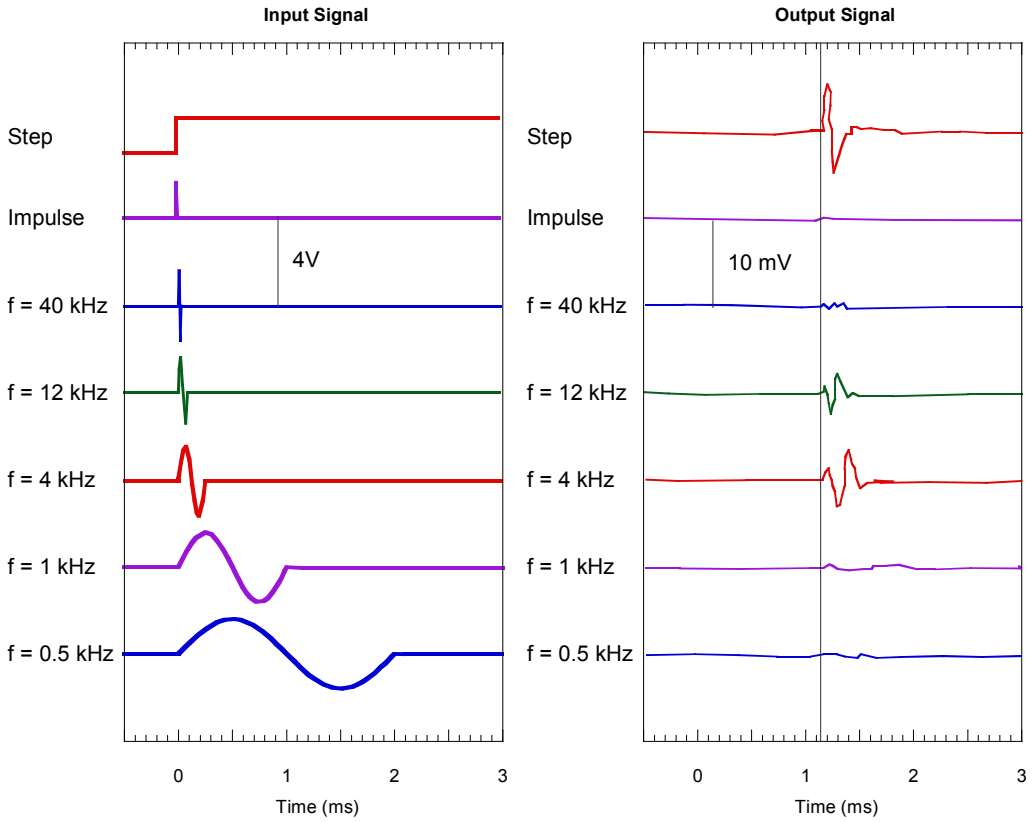

Figure 2-6 Different Input and output signals, Resonant frequency f_r = 3.6 kHz, L_{tt}/λ = 4.0 (after Lee and Santamarina, 2005)

2.2.2 Measurement of nonlinear modulus reduction and material damping properties of soil

The nonlinear dynamic soil behaviour is commonly characterized by strain-dependent shear modulus and material damping. Soils have nonlinear stress-strain relationships in which the tangential stiffness progressively decreases with strain. To capture this dependency, the (secant) shear modulus is typically plotted against strain, and values of shear modulus used for analysis of engineering problems are selected based on the level of mobilized strain. The shear modulus is usually expressed as either the tangent of the shear stress - shear strain relationship (τ-γ) in monotonic loading (Figure 2-7) or the secant modulus determined by the extreme points on a

hysteresis loop in cyclic loading as sketched in Figure 2-8. The relation between the secant shear modulus and the shear strain amplitude is often represented by a shear modulus degradation curve plotted in semi-log space against shear strain, γ, as shown in Figure 2-9a. For comparison of different test results, the plot is typically normalised by the small strain shear modulus (i.e. G/G_{max} vs γ, refer Figure 2-9b). The latter conveniently allows for the strain dependant shear modulus of the same or similar soils to be determined by combining with the measured G_{max} of the soil of interest. From the stiffness degradation curve, the mobilised shear stress τ may also be determined.

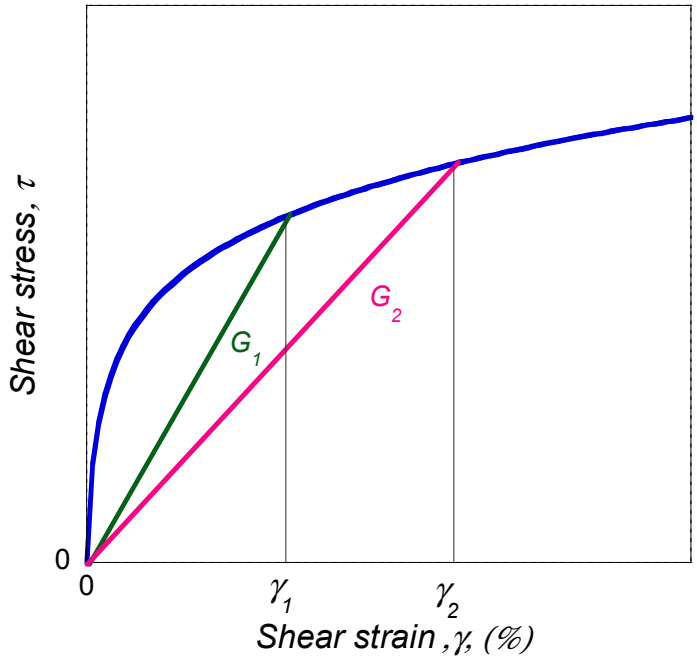

Figure 2-7 Monotonic stress-strain curve of soils and variation of secant shear modulus with shear strain

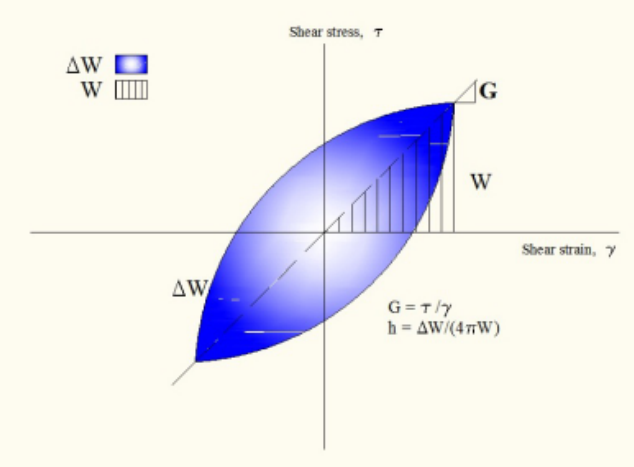

Figure 2-8 Estimation of secant shear modulus and material damping ratio during cyclic loading; the coordinates of the tips of the loop are defined by cyclic strain amplitude and the cyclic stress amplitude

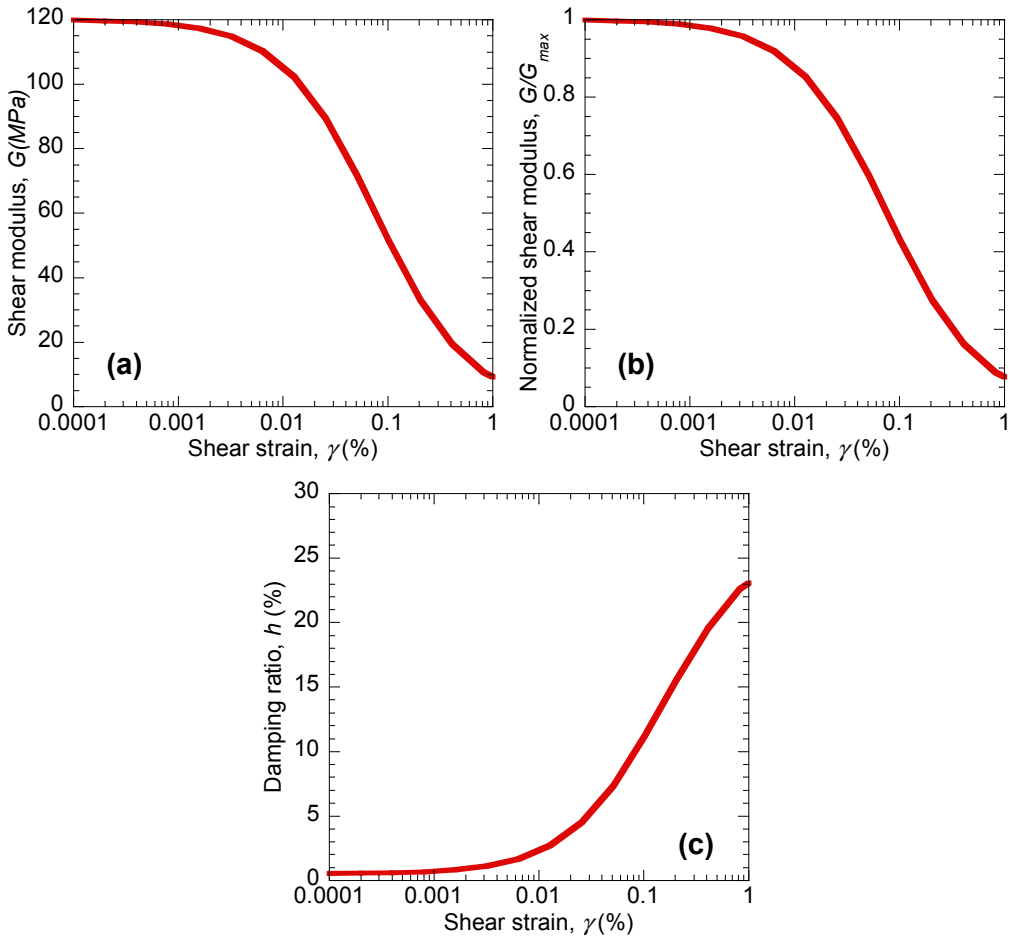

Figure 2-9 (a) Shear modulus degradation curve, (b) normalized modulus reduction curve and, (c) nonlinear material damping ratio curve

The loss of stiffness with strain on shearing causes a corresponding increase in energy dissipation as friction is mobilised. Under cyclic loading, this dissipation of energy is measured as system damping, *h*. The main source of energy dissipation is strain-dependent friction between soil particles (termed 'material damping'); in addition to a rate-dependent viscosity effect (termed 'viscous damping'). The internal damping of soil can be conveniently idealized by the equivalent viscous damping ratio, *h,* as shown in Figure 2-8. The material damping can be most easily recognised as being proportional to the area ΔW, enclosed within the hysteresis loop when a material is deformed as shown in Figure 2-8. It is readily apparent that this property will depend on the amplitude of the strain which determines the hysteresis loop (e.g. Matasovic and Vucetic, 1993). Figure 2-9c illustrates the relationship between the measured material damping ratio and the strain amplitude for a sandy soil employing a cyclic triaxial apparatus. Values of *h* can also be determined from resonant frequency tests or free vibration tests. However, values obtained in these manners seem to be somewhat higher than values measured from hysteretic stress-strain relationships (e.g. Silver and Seed, 1969). The detail calculations of shear modulus reduction and material damping curves employing a cyclic triaxial apparatus are presented in Chapter 3.

Dynamic behaviour of soils (in terms of G_{max}, G and, h) can be influenced by a number of factors which generally fall into two groups: 1) parameters relating to soil loading state condition, and 2) factors pertaining to the intrinsic material properties.The most important factors affecting the modulus and damping properties are the plasticity index (*PI*), confining pressure, and void ratio. The first of these, *PI* identifies the soil type behaviour (clay-like and sand-like) and mineralogy of the clays present, while the latter two define the soil state. Nonlinear dynamic soil properties

are also influenced by other factors (related to the method of measurement, soil state, stress history) but to a lesser degree. The major factors, affecting the modulus reduction and damping properties, are discussed in the following subsections.

2.2.3 Effects of soil type

The effect of soil type on the nonlinear G-γ and h-γ properties of soil has been documented by various researchers (Kokusho et al., 1982, Darendeli, 2001, Kramer, 1996, Vucetic and Dobry, 1991). The characteristics of 'soil type' include the intrinsic properties of the material itself, such as mineralogy (of which plasticity index, *PI,* is a proxy indicator in the case of clays), grain shape, and soil gradation. It is found by these studies that a gradual transition exists between normalized shear modulus and damping properties of non-plastic coarse-grained soil (normally sand and gravel) and plastic fine-grained soil (normally clay).

The 'soil type', as identified by *PI*, can exert a higher influence on the shape of normalized modulus reduction and damping curves than the other soil-type factors (Sun et al., 1988, Dobry and Vucetic, 1987, Kim and Novak, 1981). Normalized shear modulus curve of soils with a higher plasticity index, *PI*, moves to the right, showing degradation with a slower rate than for non-plastic soils. Furthermore, damping ratios of high plastic soils are lower than those of low plastic soils (Figure 2-10). In other words, increasing plasticity index, *PI,* results in a stiffer response with the corresponding damping reduced.

Vucetic and Dobry (1991) speculated that a relatively high surface area per unit weight of particle in high plasticity soil may introduce a greater number of particle contacts. Consequently, the larger electrical and chemical bonds can dominate the behaviour of the soil skeleton under load, which have the ability to take relatively

large shear strains before nonlinear behaviour appears in the soil. This will result in a more linear behaviour for clays with higher plasticity. Consequently, the difference in the nonlinear dynamic behaviour between plastic soils (e.g. clays) is even much wider than what is observed for non-plastic soils (e.g. Dobry and Vucetic, 1987).

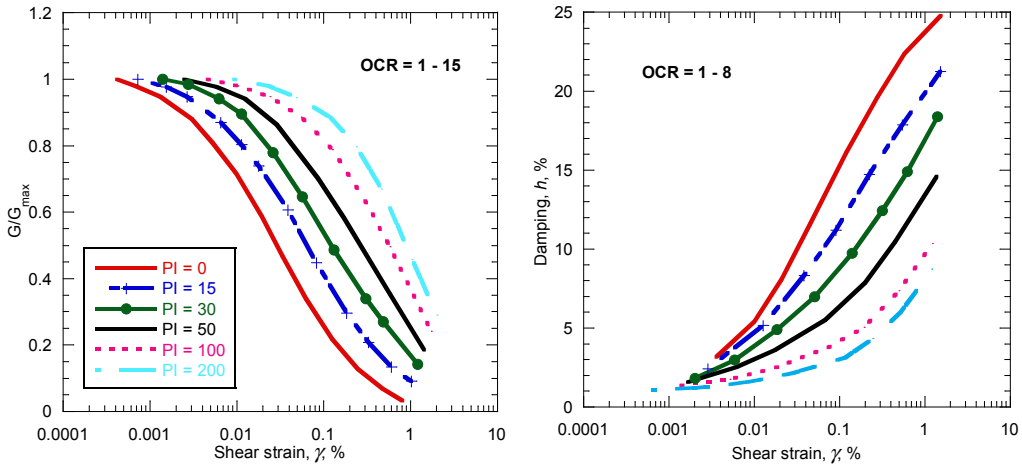

Figure 2-10 Relations between G/G_{max} versus γ and h versus γ curves and soil plasticity for normally and over-consolidated soils (after Vucetic and Dobry, 1991)

The effect of particle size of non-plastic coarse-grained soil on the G-γ and h-γ properties of soils has also been the subject of experimental studies. For instance, Seed et al. (1984) showed that the modulus reduction curves for gravelly soils are more nonlinear than those for sands whereas material damping ratios are very similar. However, previous studies have not systematically addressed the influence of non-plastic fines content (particle diameter < 75 μm) on the G-γ and h-γ properties of sand.

2.2.4 Effects of confining pressure

Dynamic testing on a range of soil types have been presented by Seed and Idriss (1970), Hardin and Drnvich (1972ba) , Hardin and Drnvich (1972ab), Kokusho (1980), Lo Presti et al. (1997), and Stokoe et al. (1999) amongst others to study the impacts of effective confining pressure on the G-γ and h-γ properties of soil. Previous investigations have shown that shear modulus values, normalized shear modulus and the material damping ratio of sand are greatly affected by the confining pressure (Seed and Idriss, 1970, Darendeli, 2001, Iwasaki et al., 1978). Figure 2-11 illustrates the general trend of such effects on the variation of G-γ and h-γ properties of silty sand. Figure 2-11a shows the effects of confining stress on the secant shear modulus of a silty sand obtained during testing using a resonant column device (Darendeli, 2001). Figure 2-11b,c illustrates a summary of the test results of the ROSRINE project in which numerous intact soil samples were recovered and tested by combined resonant column and torsional shear (RCTS) equipment (Stokoe et al., 1999, Darendeli, 2001). Darendeli (2001) found out that void ratio has negligible effects on the normalized modulus and damping curves, so the curves presented in Figure 2-11 are for constant void ratios.

The results of testing on sands show that increased confining pressure causes a stiffer response, and a corresponding reduction in material damping with strain. In other words, as confining pressure increases the reduction in secant modulus is more gradual and likewise the amount of damping reduces. As a consequence, the greatest soil nonlinearity is likely to occur at shallow depths, where the confining pressure is lowest.

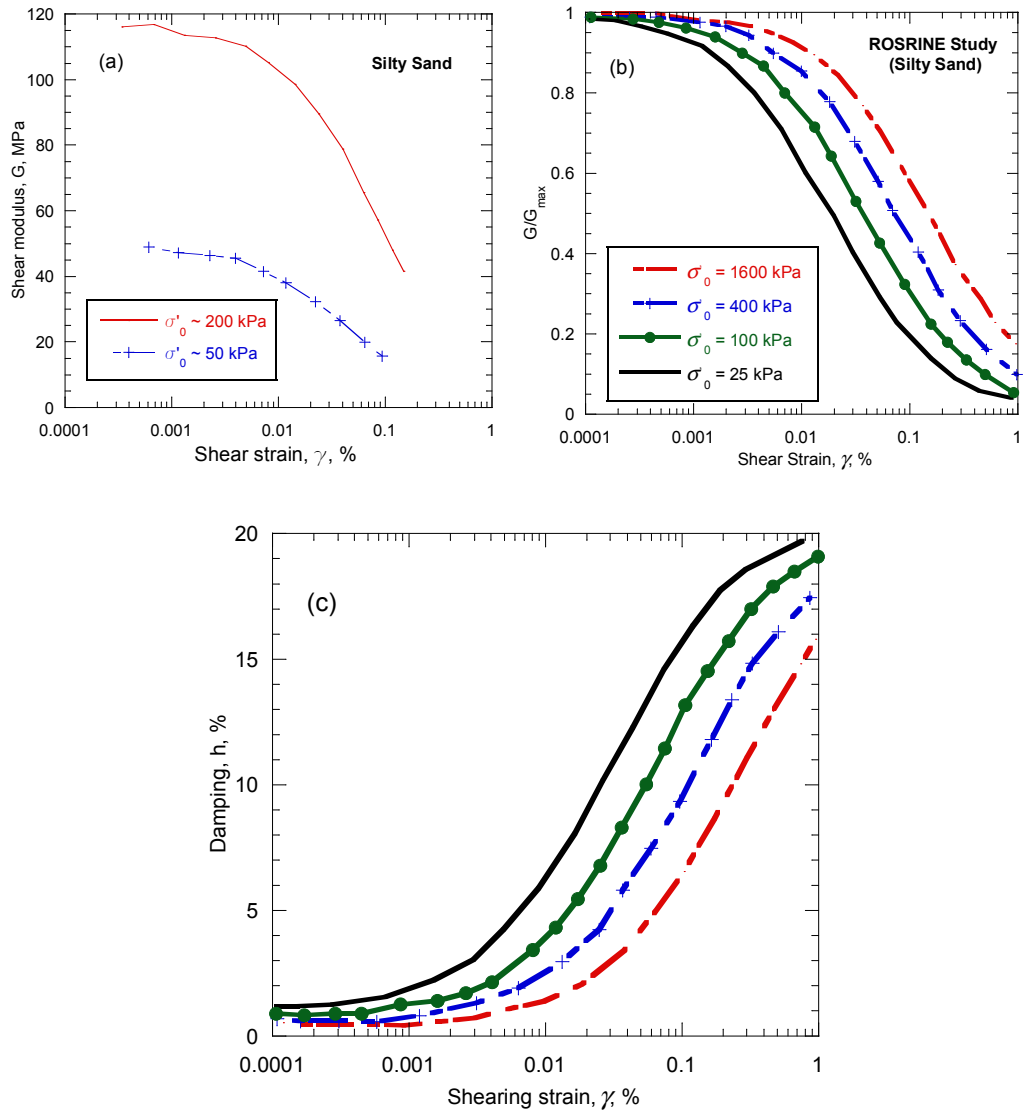

Figure 2-11 The effect of confining pressure on (a) shear modulus, (b) normalized shear modulus and, (c) damping ratio (after Darendeli, 2001).

The effect of confining pressure on the dynamic properties of clay is more complicated, and the behaviour is rather dominated by the plasticity of the material as noted in section 2.2.3. For instance, Sun et al. (1988) showed that the influence of confining pressure is negligible for clays with plasticity indices exceeding 25 and for shear strains below 1%. This is because the plasticity index exerts a higher influence on the scatter of modulus and damping curves than that of the confining pressure.

2.2.5 Effects of density

Based on extensive laboratory test data, elastic shear modulus, G_{max}, is suggested (Hardin, 1978, Kramer, 1996) to be expressed as the following empirical equation:

$$G_{\max} = A.F(e).\sigma'^{n}_{0} \tag{2-4}$$

where A is a dimensionless coefficient, $F(e)$ a function of void ratio, σ'_0 the mean principal stress, and n an empirical constant. Different equations are found in the literature for the void ratio function and are listed in Table 2-2. Parameters A and n are normally computed based on regression analyses and fitting-curve procedures. The importance of the void ratio along with the confining pressure in determining the maximum shear modulus of granular soils is clearly manifested in the above equation.

Table 2-2 Void ratio functions in the maximum shear modulus empirical equation

F(e)	Soil type	Reference
$\frac{(2.973-e)^2}{1+e}$	Cohesive soil and angular grain sands	(Hardin and Drnevich, 1972a)
$\frac{1}{0.3+0.7e^2}$	Sand and clay	(Hardin, 1978)
$\frac{(2.17-e)^2}{1+e}$	Round grain sands	(Seed et al., 1984)
e^{-a}	Sand and clay	(Jamiolkowski et al., 1991)

On the other hand, comprehensive studies of the parameters affecting the normalized shear moduli and damping curves of soils suggest that the void ratio may

marginally affect these curves (Seed and Idriss, 1970, Darendeli, 2001, Kramer, 1996, Kuribayashi et al., 1974, Silver and Seed, 1969). For instance, based on a large database, Darendeli (2001) concluded that the void ratio has somewhat secondary effects on controlling the nonlinear behaviour of soils compared to the mean effective confining pressure and soil type. However, Guha et al. (1993) tested several undisturbed Old Bay clay samples sourced from Oakland, California and concluded that the damping ratio at an arbitrary shear strain level, may decrease slightly with the increasing void ratio.

2.2.6 Effect of sample disturbance

For seismic site response analysis, evaluation of the in-situ dynamic soil properties is paramount. However, conventionally the specimens sampled from the representative site are tested in the laboratory in an attempt to measure the deformation properties of the soil. Intact specimens can be disturbed because of limitation of the in-situ sampling techniques or damaging the soil structure, cementation and fabric during laboratory test set-up. Therefore, effects of sample disturbance on the modulus reduction and damping ratio curves have been the subject of several studies. For example, Darendeli (2001) compared the nonlinear behaviour of undisturbed and remolded sand specimens using RCTS apparatus. He concluded that the normalized modulus curves of the undisturbed and remolded samples were almost identical. This similarity was also observed for damping ratios below 0.01%. Above this threshold the damping ratio of the reconstituted samples were measured higher than the intact specimens. Zeghal et al. (1995) back-calculated the variation of shear modulus and damping ratio with shear strain using stress-strain histories computed from down-hole accelerations at Lotung, Taiwan and then compared the

results with the experimental tests and concluded that there was a good correlation between normalized modulus reduction curves. However, there was discrepancy between the damping ratio curves. Although, the normalized modulus curves of reconstituted soil can be conveniently used for scaling the in-situ modulus but laboratory-measured damping ratios should be used with great caution.

2.2.7 Empirical curves and effects of other parameters

As emphasized previously, the shear modulus and damping properties of soils are critical in seismic response evaluation at both small- and large-strain response levels. As a result, several empirical relationships for the variation of the G-γ and h-γ properties of different soils during cyclic loading have been proposed (Sun et al., 1988, Vucetic and Dobry, 1991). These curves have been extensively used for estimating seismic site response in relatively shallow deposits (<30m).

For cohesionless soils, the variation of dynamic curves with change in soil properties is small and therefore it is assumed that the modulus degradation and damping curves fall within a narrow range for most cohesionless soils. Based on experimental studies, Seed et al. (1984) provided approximate upper and lower bound relationships for the normalized shear modulus and the damping ratio for sands with respect to shear strain (Figure 2-12a and 1-12); a representative average relationship for all of the test data was also proposed. It was considered that these bounds were likely to provide values of the normalized modulus and the damping ratio with sufficient accuracy for many practical purposes for sandy soil sites. In Figure 2-12a, solid lines represent these upper and lower bounds and the dashed line shows the average relationship. Similar modulus reduction curves were also suggested by Iwasaki et al. (1978) for clean Toyoura sand under different confining pressures

(Figure 2-12b). Moreover, Darendeli (2001) recently developed an empirical framework in which a simple model can generate normalized modulus reduction and material damping curves considering the influences of important factors which exert a great influence on the shape of G-γ and h-γ properties of soil. This framework is explained in more detail in Appendix A.

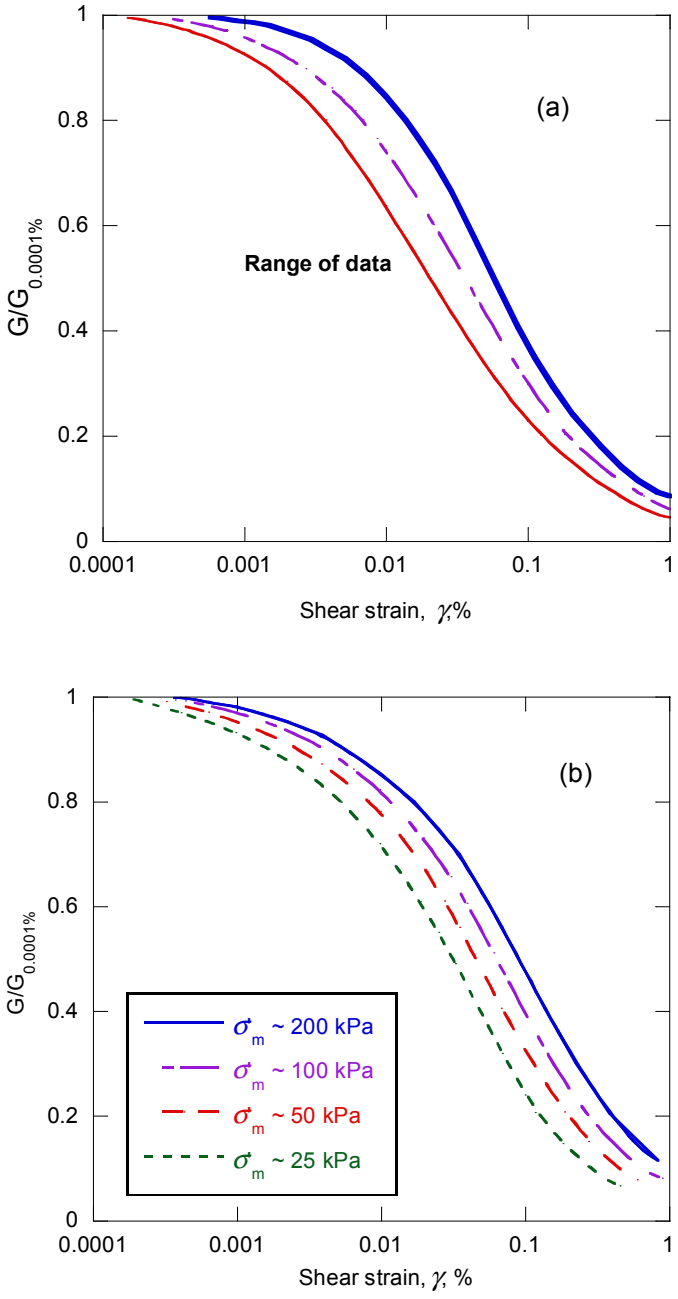

Figure 2-12 Variation of shear modulus with shear strain for sands recommended by (a) Seed et al. (1984), (b) Iwasaki et al. (1978)

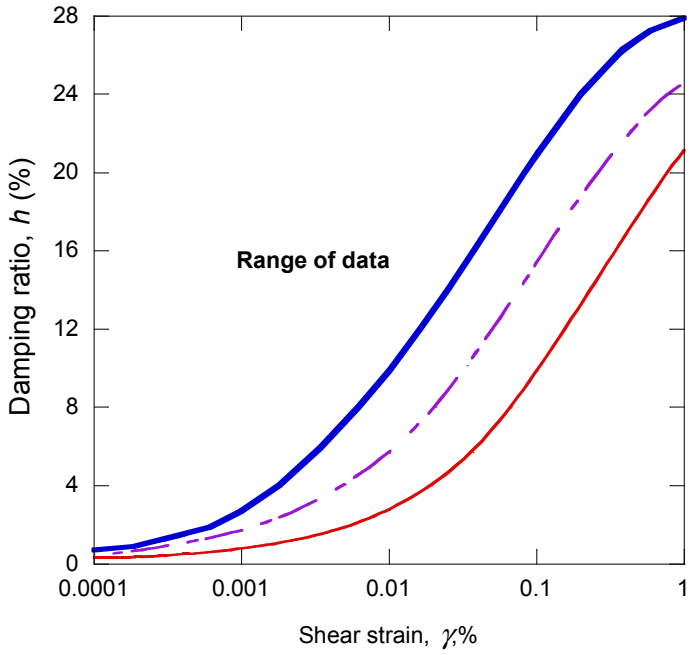

Figure 2-13 Variation of material damping ratio curves for sands from different studies, solid lines represent the boundaries (After Seed et al., 1984)

General trends reported in the literature and observations made by Hardin (1972a) and Darendeli (2001) show that in addition to the primary factors which were described previously, secondary parameters which have less important influences on the modulus reduction and the material damping ratio curves should also be considered. Table 2-3 lists such parameters along with the primary factors influencing the G-γ and h-γ properties of soil. For instance, number of loading cycles, frequency of vibration and, degree of saturation are amongst test conditions which have negligible effects on the shape of G-γ and h-γ properties of soil. However, it should be added that previous studies have not systematically examined the effects of fines on the dynamic soil behaviour. These effects will be scrutinized in Chapter 4 and 5 but first background information regarding the effects of fines on the soil skeleton structure and the behaviour of sandy soil in the presence of fines content is provided in the following sections.

Table 2-3 Relative importance of effects of some of state and loading conditions on modulus and damping ratio curve (after Darendeli, 2001, Hardin and Drnevich, 1972b)

Parameter	Impact on normalized modulus reduction curve	Impact on material damping ratio
Strain amplitude	***	***
Effective confining pressure	***	***
Soil type and plasticity	***	***
Void ratio	*	*
Number of loading cycles	*	***
Frequency	*	**
Degree of saturation	*	*

*** very important, ** important, * less important

2.3 Effects of non-plastic fines on sand behaviour

2.3.1 Background

The mechanical behaviour, such as stress-strain response, shear strength, resistance to liquefaction, modulus, and shear wave velocity of granular soils containing coarse and fine grains is dependent on mineralogy, shape, size, particle arrangement, intergrain contact density, bonding and, interactions at the microscopic

level. The soil matrix comprises different types and sizes of particles which participate in the internal interparticle contact force chain in various degrees and therefore can affect the level of resistance under an arbitrary loading condition.

Traditionally, void ratio, e, or relative density, D_r, which are good indices of solid mass density, have been chosen as the key state variables that directly affect the strength, stiffness and dilatancy of soils. This has worked sufficiently for clean sands as they correlate well with the internal force chain within the soil mass (e.g. Cubrinovski and Rees, 2008). However, observations from recent earthquake case histories (e.g. the 1995 Kobe earthquake, 1999 Kocaeli earthquake and 1999 Chi-Chi earthquake) and laboratory studies indicate that natural sandy soils which contain a significant amount of fines (passing sieve No. 200, particles diameter less than 0.075mm) behave differently from clean sands; therefore the global void ratio (or relative density) may be a poor index of contact density for such soils (Thevanayagam et al., 2002, Cubrinovski and Rees, 2008, Rahman et al., 2008, Rees, 2009, Ni et al., 2004). The review of these observations in this section focuses on how fines content influences the internal structure and the undrained stress-strain behaviour of sand followed by a study of current literature on how fines can affect the dynamic sand properties. It is to be noted that the study of the effects of the fines nature with regard to their plasticity is beyond the scope of this study and hence only studies on non-plastic fines are reviewed.

2.3.2 Effects of fines on soil skeleton structure

If two different-sized spherical particles are mixed, the packing can be affected by the proportion of the small and large size spheres as well as by the relative size of the particles. For instance, Figure 2-14a,b schematically illustrates how the volumes

of solids and voids vary with the increase in the percentage of small-size particles. At point L, adding smaller size particles into the densest possible packing of the larger spheres results to filling the voids and consequently reduction of the volume of voids as well as the minimum void ratio, e_{min}. Beyond point *T*, adding small particles reverses the trend where the volume of voids increases with the increase of percentage of small-size fraction. In the replacement-of-solids phase, larger particles are pushed apart and gradually smaller sized spheres are dominant until the entire volume of solids is comprised of small spheres (point S).

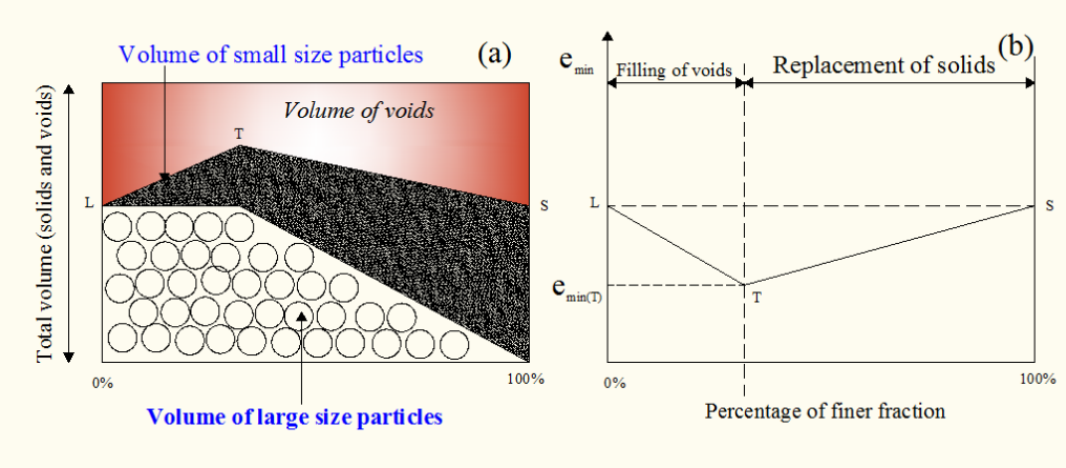

Figure 2-14 Effects of fines on binary packing of spherical particles: (a) variation in the volume of voids and solids and (b) variation in e_{min} (after Cubrinovski and Ishihara, 2002)

Relative size of the large and small spheres is the other important factor affecting the binary packing of spheres. Based on theory and some experimental data, Lade et al. (1998) showed that the small particles can be located in the voids between the large particles only if the diameter of the small spheres, *d*, is at least 6.5 times smaller than that of the large spheres.

Void ratio characteristics of gap-graded mixtures of silty sands are influenced by several other factors in addition to those introduced for the idealized binary packing

of spherical particles. This includes grain composition, grain shape and, interacting surface forces (e.g. Cubrinovski and Ishihara, 2002). For instance, Lade et al. (1998) investigated the loosest and densest soil structure using Cambria sand with varying Nevada fines content comprising a gap-graded mixture (Figure 2-15). It is apparent that the variation of minimum void ratio in Figure 2-15 is closely similar to that of the binary packing in Figure 2-14b. As indicated in Figure 2-15, there is a transition in the microstructure from a sand-controlled-matrix to a fines-controlled-matrix as the fines content increases from 20% to 40% approximately.

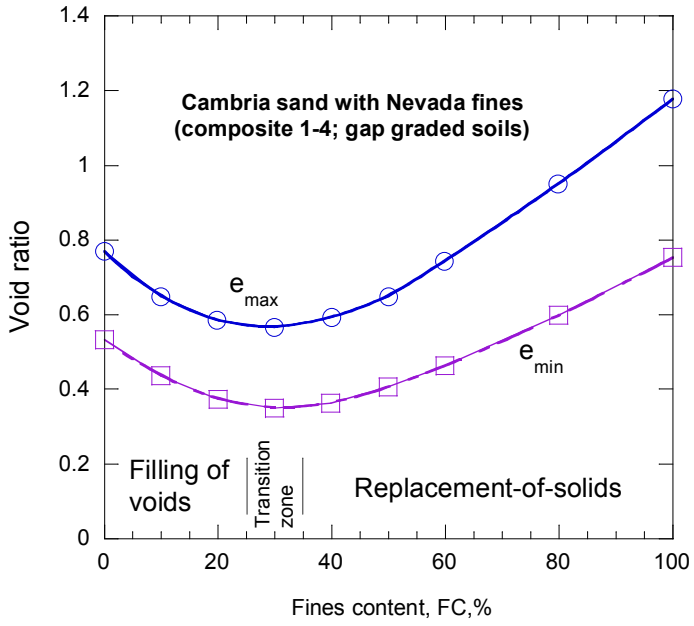

Figure 2-15 Variations of maximum and minimum void ratios for combinations of Cambria sand with Nevada fines (After Lade et al., 1998)

Unlike mixtures of sand and fines produced in the laboratory, natural soils have various gradation and basically infinite number of grain compositions. Therefore, their loosest and densest states produced by a certain set of laboratory test procedures might exhibit different trends from that shown in Figure 2-15. Apparently, both e_{max}

and e_{min} of natural soils tend to increase as fines content increases (Cubrinovski and Ishihara, 2002), as observed in data of over 300 soils from natural soil deposits in Japan (Figure 2-16a,b).

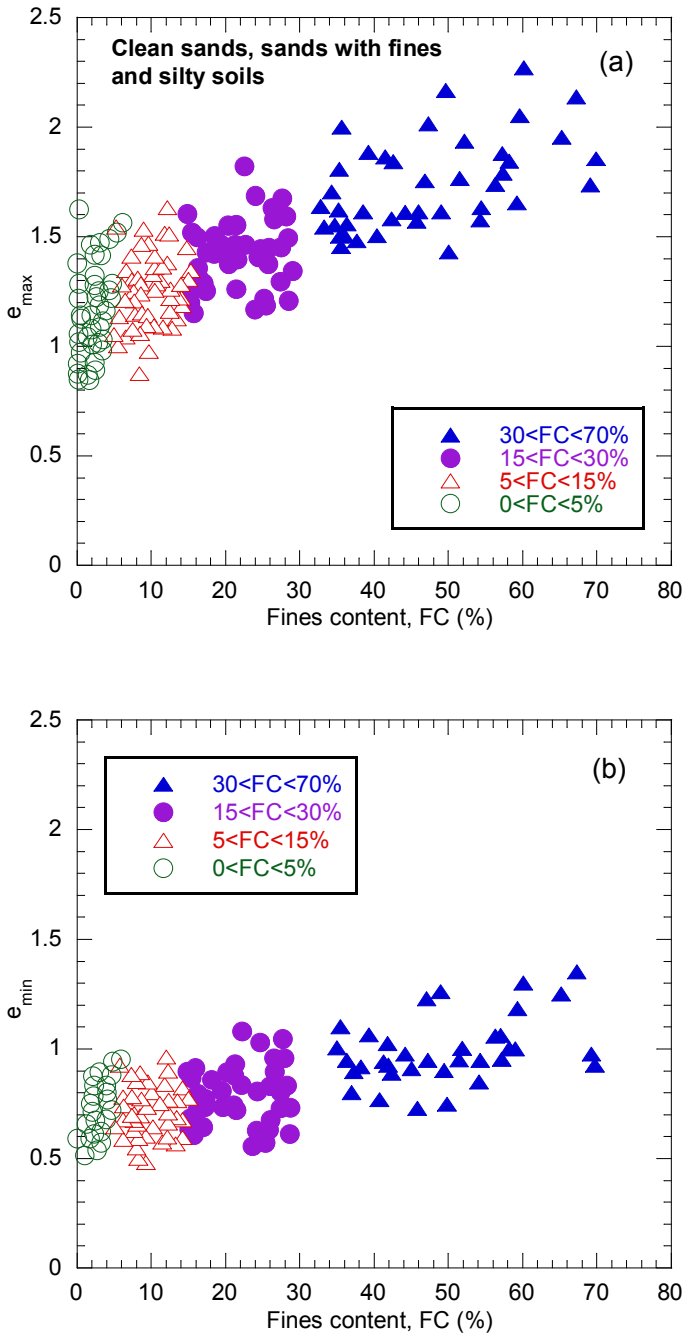

Figure 2-16 Effects of fines on maximum and minimum void ratio of sandy soils: (a) e_{max} vs. FC and (b) e_{min} vs. FC (after Cubrinovski and Ishihara, 2002)

In the case of gap-graded silty sand mixtures, because of the existence of large-enough pores between coarser grains, there is reason to believe that if the fines content quantity is smaller than a threshold value f_{cth}, some of the finer grains would tend to adjust their positions during deformation, sliding into the pores without significantly affecting the adjacent particles. As such fine particles may not actively participate in transferring the normal forces or sustain significant shear forces as shown in Figure 2-17a, and thus the space they occupy can be added to the void space (Thevanayagam et al., 2002), as schematically represented in Figure 2-18. In this way, the stress-strain behaviour is considered to be controlled by the sand matrix. This assumption led to introduction of an index known as the intergranular void ratio, e_g.

$$e_g = \frac{e + f_c}{1 - f_c} \tag{2-5}$$

where e is void ratio and f_c is fines content. Although conventional definition of fines content is based on mass proportion as shown in equation (2-6), it can be shown that this value can be very similar to volumetric proportion because of similar specific gravity of fines and coarse particles:

$$f_c = \frac{mass\ of\ fines}{total\ mass\ of\ solids} \tag{2-6}$$

$$\simeq \frac{volume\ of\ fines}{total\ volume\ of\ solids}$$

However, it can be argued that some portions of fines may contribute positively to the strength and stiffness of the soil especially with an increase in fines content (Figure 2-17b). Thus intergranular void ratio, defined in equation (2-5) may not be

adequate by itself to characterize the mechanical response of granular mixes as it ignores the way in which fines contribute to the mechanical properties of a mixed soil (Thevanayagam et al., 2002, Ni et al., 2004). Therefore, it has been suggested that the intergranular void ratio should be used for only soils with low fines content (Thevanayagam et al., 2002).

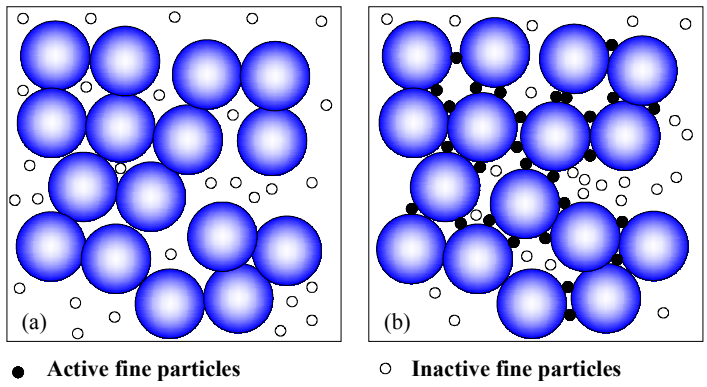

Figure 2-17 (a) Idealized schematic illustration showing the intergranular void ratio concept, (b) Schematic illustration showing the sand-dominated soil structure illustrating the equivalent granular void ratio concept.

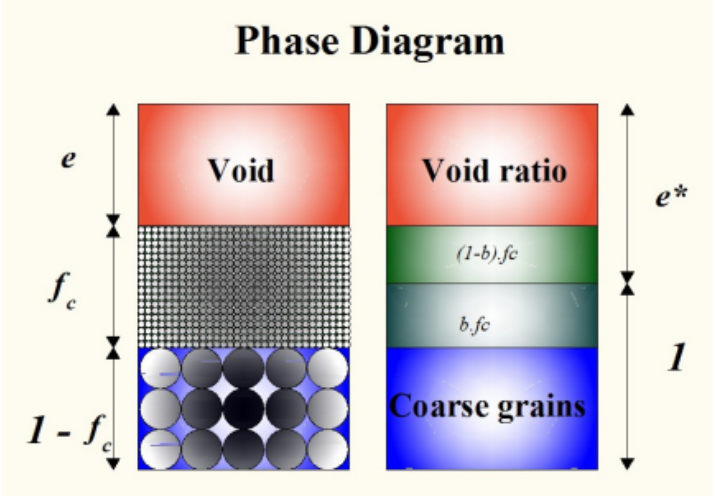

Figure 2-18 Phase diagram of fines containing sand structure

As a consequence, an alternative state variable referred to as the equivalent granular void ratio, e^*, was introduced (Thevanayagam et al., 2002, Thevanayagam,

2007). This variable is regarded as another useful inter-grain contact definition of initial state which normalizes the effects of fines on the behaviour of sand for gap-graded soils. This value allows a fraction of fine-sized particles to actively participate in the soil force-chain, rather than simply neglecting their effect (Thevanayagam and Liang, 2001). The equivalent granular void ratio, e^*, of sand up to threshold fines content, f_{cth}, is calculated using the following expression:

$$e^* = \frac{e + (1-b)f_c}{1-(1-b)f_c} \tag{2-7}$$

where b represents the fraction of fines that actively participate in the load transfer of the solid skeleton and varies from a value of zero (no effect; $e^* = e_g$) to one (as effective as sand particles; $e^* = e$). Fines content above the threshold limit, f_{cth}, change the soil structure into a fines dominating matrix therefore equation (2-7) is no longer valid. The values of threshold fines content, f_{cth}, depend on the grain-size composition and particle characteristics of the soil. Note that in some way equation (1-7) is similar to the equation (1-5); that is the void and solid spaces in equation (1-7) are updated using the concept of the b-value. The estimation of the b-value or the fraction of active fines in the transfer of shear between grains is the subject of other studies which are summarized in the following paragraphs.

2.3.2.1 The fines influence factor, b

Normally, predicting the value of b is controversial. Most of the b-values reported in various publications are determined by case-specific back-analysis; that is the constant b-value is selected irrespective of fines content so that a single correlation between equivalent granular void ratio and the measured behaviour can be achieved regardless of fines content (Rahman et al., 2008, Cubrinovski and Rees,

2008). However, this scheme may result in negative or multiple *b*-values and also requires extensive laboratory tests covering a range of fines content (Rahman et al., 2008, Ni et al., 2004, Rees, 2009).

However, Rahman et al. (2008) proposed a simple semi-empirical equation for predicting the value of *b* based on fines content and particle size. It has been surmised that fines content, f_c, and particle size disparity ratio, $\chi = D_{10}/d_{50}$ (where D is the diameter of the coarser grains and *d* is the diameter of the fines, and subscript 10 and 50 denote 10% lower fractal and median value, respectively) are the two key parameters affecting the *b* value:

$$b = \left[1 - \exp\left(-\mu \frac{(f_c / f_{cth})}{k}\right)\right]\left(r \frac{f_c}{f_{cth}}\right)^r \tag{2-8}$$

where $r = \chi^{-1} = d/D$, $k = (1 - r^{0.25})$, and μ is a fitting constant. Later, using results from several independent studies, Rees (2009) showed that *b* is also affected by the angularity of the sand particles and can also change throughout the loading procedure.

2.3.3 Effects of fines on undrained behaviour of sand

It was shown in the previous section that the degree of contribution by different sizes and types of soil particles within the soil matrix in the transfer of interparticle contact stresses may affect the deformational behaviour and the resistance it can offer under different loading conditions (Thevanayagam et al., 2002). It was discussed that silty sand and natural soils are composed of a mix of soils containing sands and fines content and therefore the mechanisms leading to large deformations in such soils are much more complex than in more uniform sands.

Many experimental studies have been undertaken to investigate the relative effects of fines on the dynamic characteristics, collapse potential, steady-state strength, and cyclic response of different mixes of silty sand (e.g. Thevanayagam and Mohan, 2000, Rees, 2009, e.g. Rahman, 2009, Yamamuro and Lade, 1997). The experimental studies thus far followed a comparative approach. The behaviour of silty sand prepared at different fines contents has been compared with the behaviour of clean sand e.g. using void ratio, relative density, intergranular void ratio, etc. Application of these concepts to describe the anticipated undrained behaviour of silty sand has resulted to some misleading interpretations (Thevanayagam and Mohan, 2000, e.g. Cubrinovski et al., 2010). Therefore, one of the key problems in the evaluation of the influence of fines on sand behaviour is establishing a common basis for comparison of clean sands and sands with fines. The following subsections provide a brief review of such experimental studies which use the void ratio and the equivalent granular void ratio as the basis for comparison of mechanical behaviour of silty sands.

2.3.3.1 General undrained response

Thevanayagam and Mohan (2000) showed that contraction tendency behaviour increases with an increase in fines content up to a threshold value (f_{cth}). Figure 2-19 presents how just a 10% increase in fines content may exert a great influence on the stress-strain curve and stress paths for sands at nearly the same global void ratio. Likewise, Yamamuro and Lade (1997) showed that the same observation is held true if relative density, D_r, is used as the basis for comparison (Figure 2-20). Although, due to difficulties in determining the maximum and minimum void ratios of fines-containing sands, effects of fines based on D_r may exhibit less consistent trends. This

general trend of more contractive behaviour with the increase of fines content may however be reversed and so the strength may increase with a further increase in fines content if the fines proportion is beyond a certain transition range (Thevanayagam, 2007). In contrast, if the intergranular void ratio e_g, is employed as the state variable for sands with low fines content in order to compare the contraction behaviour, nearly similar results will be obtained.

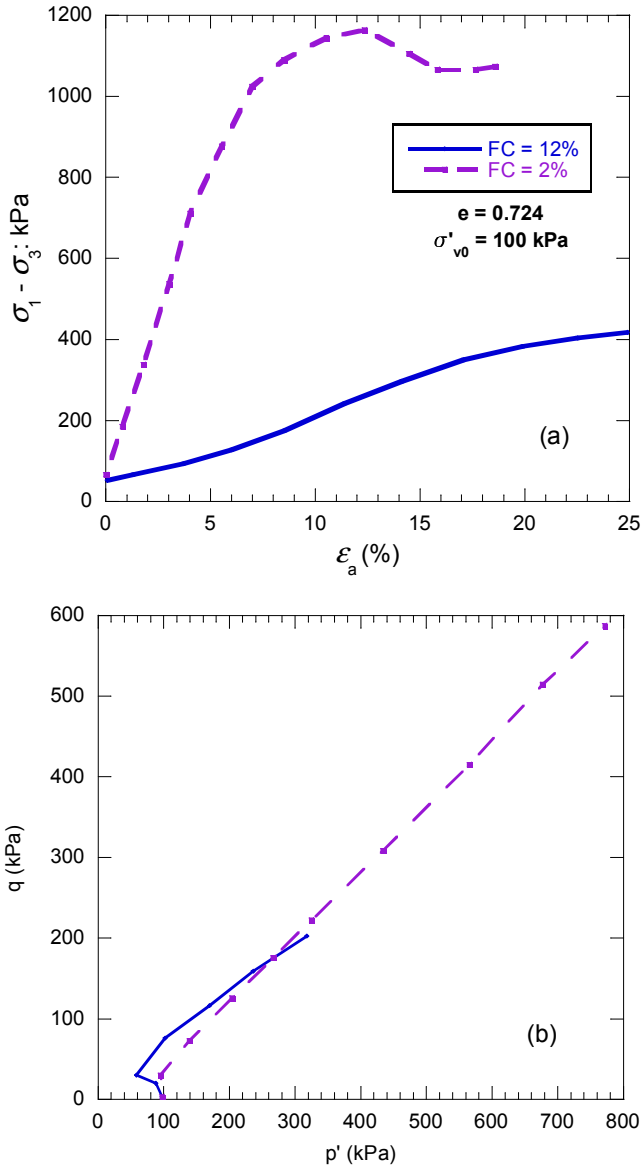

Figure 2-19 Comparisons at the same initial confining stress and nearly same void ratio: (a) stress-strain, (b) effective stress path (after Thevanayagam and Mohan, 2000)

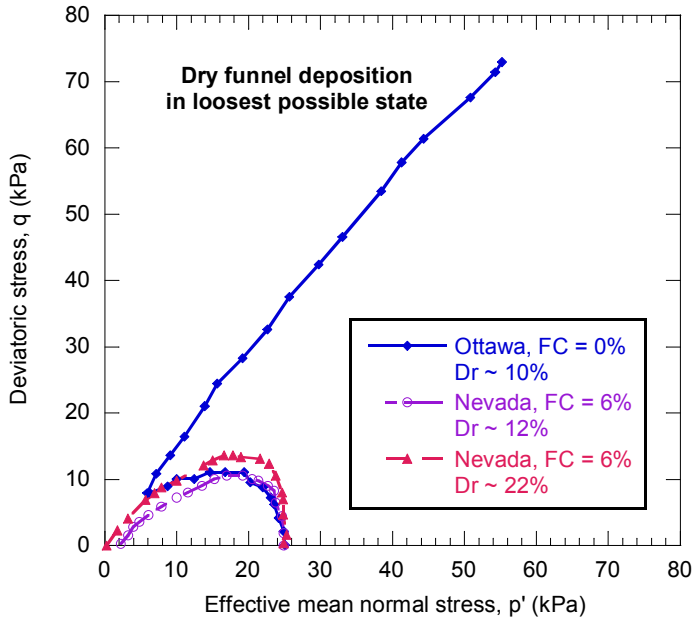

Figure 2-20 Undrained effective stress paths of triaxial tests on Ottawa and Nevada sand (after Yamamuro and Lade, 1997)

2.3.3.2 Steady-state response

The steady state or critical state of deformation is defined as the state at which a sandy soil deforms under constant shear stress, constant effective stress and constant volume. Cubrinovski and Ishihara (2000) and Thevanayagam et al. (2002) showed that the steady state line is dependent on fines content. The 2002 study mixed Foundry sand with different amounts of nonplastic crushed silica fines with varying proportions. The specimens were tested triaxially under strain-controlled monotonic undrained conditions and consequently steady state data were produced for sands with a range of fines content. Figure 2-21a shows that up to a certain fines content (f_{cth}) and at the same void ratio, the steady state strength decreases with an increase in fines content. This can be attributed to reduced interlocking frictional resistance between angular particles due to the presence of fines. However, Figure 2-21b show that when same data are plotted against e^* in lieu of e, assuming a $b = 0.25$, the behaviour of all

silty sand specimens is similar to that of the host sand. This is because the non-active fines are considered as voids based on equation (2-7). Similar trends were also found by Rahman et al. (2008) and Rees (2009) employing equation (2-8) to predict the *b*-value for five datasets extracted from the published literature.

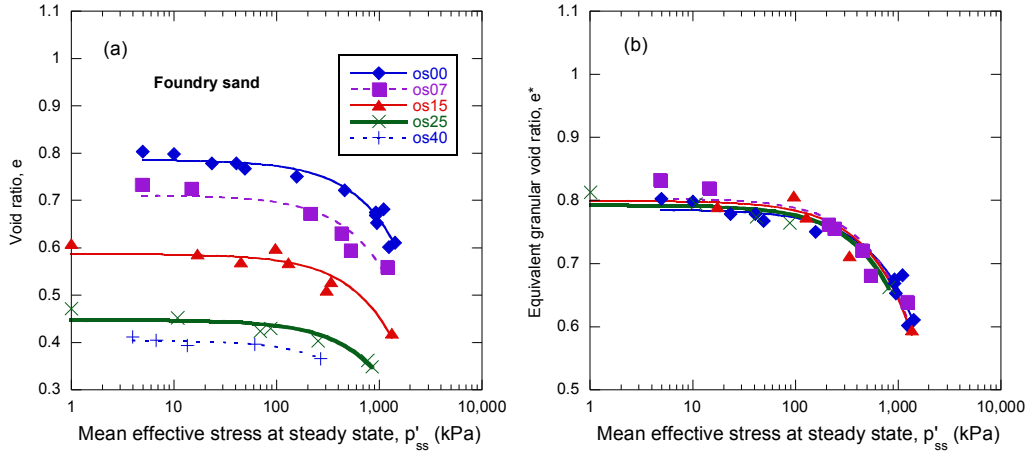

Figure 2-21 Steady state data (a) void ratio versus mean effective stress at steady state, (b) equivalent granular void ratio versus mean effective stress at steady state (after Thevanayagam et al., 2002)

2.3.3.3 Cyclic response

Similar investigations have been carried out to study whether cyclic resistance can be correlated to e^* in a manner that is approximately independent of fines content. For instance, Rahman et al. (2008) used four datasets from literature to scrutinize the performance of employing equation (2-8). Figure 2-22a, illustrates cyclic triaxial tests on Brenda 20/200 sand with nonplastic fines conducted by Vaid (1994). It is noted that at a given void ratio the liquefaction resistance decreases with increase in the fines content. This can be attributed to lower permeability and slower decrease of water pressures as well as larger compressibility of fines containing sand. However, if these data points are re-plotted based on e^* (Figure 2-22b), an essentially single correlation between e^* and cyclic resistance is obtained. Similar behaviour have been

reported for liquefaction resistance curves of Christchurch sands (Cubrinovski et al., 2010, Cubrinovski and Rees, 2008). These correlations allow the estimation of the liquefaction resistance of soils for any fines content below the threshold value.

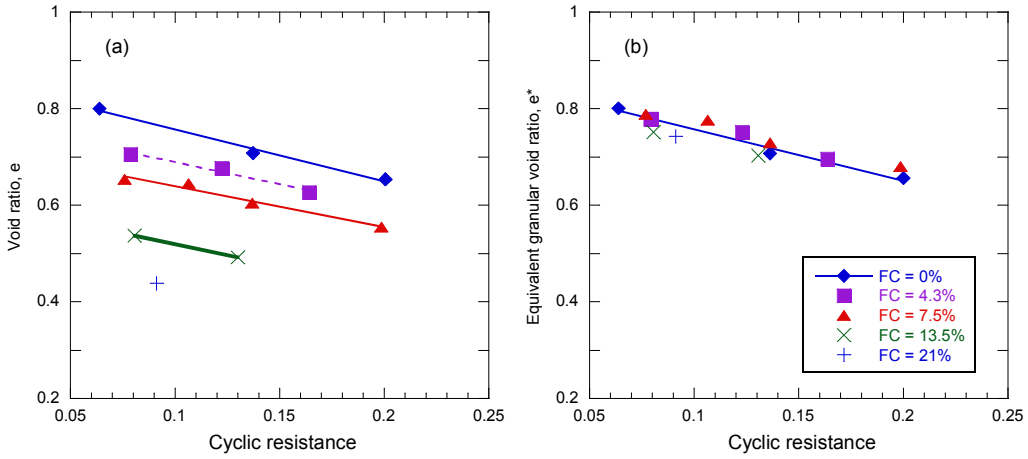

Figure 2-22 Cyclic resistance of 20/200 Brenda sand with silty fines: (a) source data after Vaid (1994); (b) interpreted based on e^* (after Rahman et al., 2008)

2.3.4 Effects of fines on G-γ and h-γ properties

It was explained in the previous sections that considerable attention has been given to the characterization of G-γ and h-γ properties of soil including effects of different factors on the shape of modulus reduction and damping curves. However effects of fines on those curves have not been systematically addressed. On the other hand, effect of fines on liquefaction resistance and steady state behaviour is reaching to a consensus. Therefore, there is a need to understand the dynamic behaviour of sands in the presence of fine particles. This section summarizes the studies found in the literature regarding the effects of non-plastic fines on small-strain modulus in addition to large-strain modulus and material damping curves.

2.3.4.1 Effects of fines on small-strain G_{max}

Like other mechanical behaviour of fines-containing sand, maximum shear modulus, G_{max}, is also expected to decrease with an increase in fines content when compared at similar void ratios. This trend is confirmed by several experimental studies (Wichtmann and Triantafyllidis, 2010, Iwasaki and Tatsuoka, 1977). For instance, Iwasaki and Tatsuoka (1977) tested various materials with a wide variety of grain size distributions including clean sands and well-graded natural sands to evaluate shear moduli of different soils. It was concluded that clean sands follow approximately similar trends introduced in equation (2-4) with slightly different fitting parameters whereas shear moduli of fines containing natural sands, in general, are less than those expressed by equation (2-4). Furthermore, as shown in Figure 2-23 a larger scatter is observed among the data of natural sands compared with the case of clean sands. Wichtmann and Triantafyllidis (2010) proposed new fitting parameters for equation (2-4) to account for the influence of fines content on the maximum shear modulus.

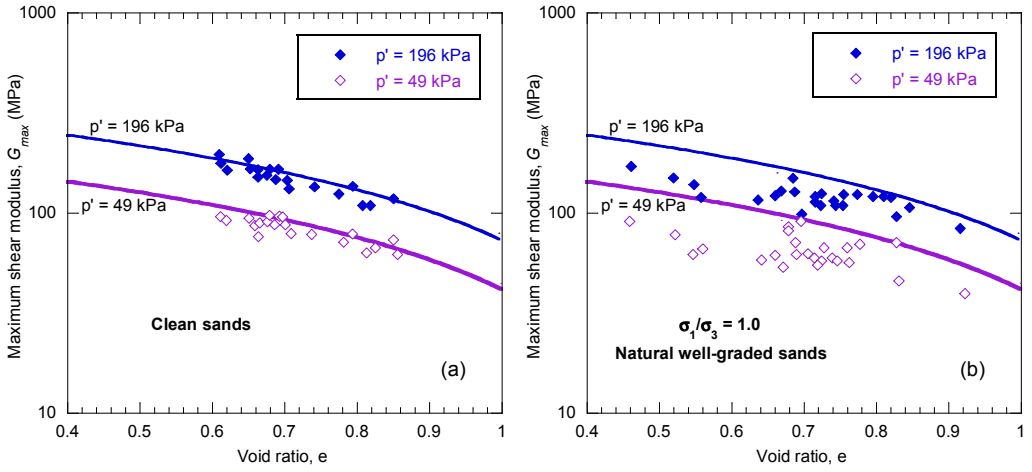

Figure 2-23 Maximum shear modulus G_{max}, versus void ratio e, for (a) clean sands, (b) natural sands (after Iwasaki and Tatsuoka, 1977)

Another approach to evaluate the maximum shear modulus consists of employing equivalent granular void ratio e^* (Thevanayagam and Liang, 2001, Rahman et al., 2011), as a contact index in lieu of the global void ratio in equation (2-4). The global void ratio, e, was shown not to be a satisfactory index to represent the nature of contact density of active particles.

2.3.4.2 Effects of fines on nonlinear G-γ *properties*

Troncoso and Verdugo (1985) conducted a series of cyclic triaxial tests on sands with different silt contents in order to determine the dynamic behaviour of tailing sands used in the construction of dams (Figure 2-24). It is apparent in Figure 2-24 that like the liquefaction resistance and the steady state strength of soil, the shear modulus decreases significantly with the increase of fines at nearly constant void ratio and effective confining pressure. The minimum recorded shear strain in this study was $\gamma = 0.01\%$; hence, it is not possible to evaluate the maximum shear modulus and the normalized modulus reduction curve cannot be calculated based on this data.

As part of various research projects, dynamic characteristics of intact soil samples were investigated by Darendeli (2001) to investigate the influence of important factors on the nonlinear G-γ and h-γ properties of soil. However, due to non-systematic variation of fines content in the recovered intact samples in the presence of other parameters, no conclusive remarks could be obtained in terms of effects of fines on dynamic properties of sand.

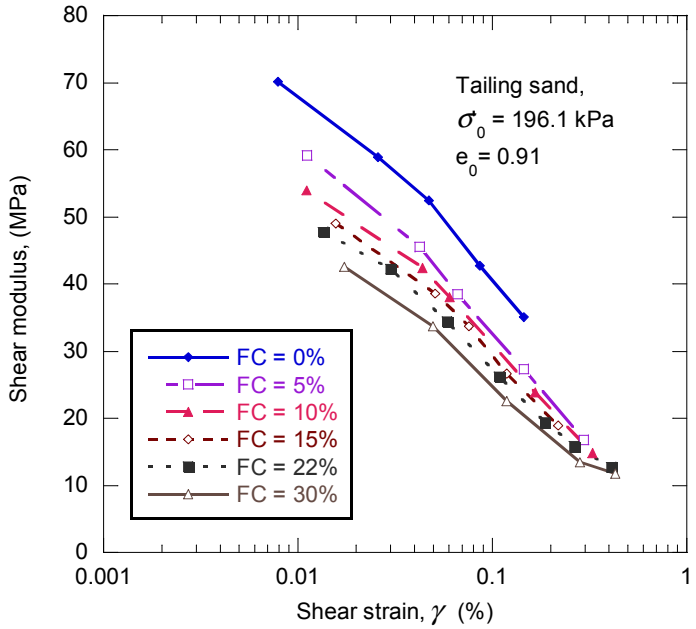

Figure 2-24 Shear modulus versus shear strain of a copper mine located in central Chile (after Troncoso and Verdugo, 1985)

2.4 One-dimensional Site response analysis

Local soil conditions can influence the characteristics of earthquake ground shaking which consequently will affect the way in which an overlying structure will behave. Site response analysis quantifies the effects of dynamic soil properties through calculation of surface acceleration time series, design acceleration response spectra or spectral amplification factors. The influence of local soil conditions on the earthquake ground motions has been recognized for many years. The 1985 Mexico City (Cassaro and Romero, 1986), the 1989 Loma Prieta, and 2011 Christchurch earthquakes (Cubrinovski et al., 2011, Bradley, 2012b) are some of the most prominent case histories which showed that local site conditions can play an important role on the soil behaviour subjected to ground shakings. Therefore, geotechnical engineers constantly propose different techniques for site response analysis purposes.

The development of quantitative methods for predicting the influence of local ground conditions on ground motion often requires basic simplifications and assumptions. In geotechnical terms, it is commonly assumed that the soil stiffness increases with depth due to the older age of deeper material and the confining effect of increasing overburden pressures. This often causes stress waves coming from depth to be refracted in a propagation direction that is almost vertical (Figure 2-1). Furthermore, structures are always designed with a factor of safety to support their weight as a result of gravity and thus the vertical component of the ground motion can generally be considered to have much less impact on earthquake resistance design than the horizontal component. As a result, with vertically propagating shear waves and a higher susceptibility of structures to horizontal motions, the sites in many seismic response analysis problems are approximated as horizontally layered soil deposits subject to horizontal shaking of vertically propagating shear waves (SH waves). This section describes the most commonly used methods for one dimensional ground response analysis which assumes the above simplifications.

2.4.1 Linear and equivalent linear approach

It is well known that soil behaviour is nonlinear at small strains but linear viscoelastic methods can provide useful results. In a typical linear site response analysis, horizontal soil layer stress-strain behaviour is approximated as a Kelvin-Voigt solid with a linear elastic shear modulus and viscous damping. The solution of the wave propagation equation can then be performed in either frequency or time domain. Commonly, finite rigidity is allowed in the underlying elastic medium, permitting energy to be radiated back into the underlying medium. Therefore, the problem of concern is a simple system of horizontal soil layers bounded above by the

free surface and below by a semi-infinite elastic medium representing the bedrock. For instance, Kramer (1996) has presented the transfer functions relating displacement, velocity and acceleration of layer *i* to that of layer *j* for layered damped soil on elastic rock.

For strong ground motion vibrations (medium and large earthquakes), the linear elastic solution is no longer valid since soil behaviour is inelastic, non-linear. Equivalent linear analysis performed in the frequency domain, has been introduced to approximate the nonlinear and cyclic behaviour of soil (e.g. Schnabel et al., 1972). The frequency domain solution of wave propagation provides the exact solution when the soil response is linear. The equivalent linear method is based on the assumption that a linear model will give a satisfactory approximation of maximum nonlinear deformation behaviour provided that the nonlinear G-γ and h-γ properties are chosen from the modulus reduction and the damping curves in accord with the average (effective) strain that occurs in the model during excitation. However, a constant linear shear modulus and damping at a representative level of strain is used throughout the duration of an earthquake, regardless of whether the strains are large or small at a particular time.

As explained in section 2.2.2, the hysteretic stress-strain behaviour of soils can be represented by an equivalent modulus curve, G, corresponding to the secant modulus through the end points of the hysteresis loop and an equivalent damping ratio curve, h, corresponding to the material damping. It was shown that the internal hysteretic damping of soil can be conveniently represented by an equivalent viscous damping ratio, h, and it can be most easily employed in equivalent linear method which use dashpots to accommodate the material damping.

An iterative procedure is used to find the shear moduli and damping ratios corresponding to the computed shear strain. First, for a given ground motion time series and an initial estimate of modulus and damping values, an effective shear strain (equal to about 50-70 % of peak strain calculated at the midpoint of each layer during the elastic analysis) is computed for a given soil layer. Modulus reduction and damping ratio curves are then used in the subsequent iteration for this effective strain amplitude to determine revised values of soil properties. If the calculated strains differ by too much from the trial values, adjustments are made and the process is repeated as many times as needed to obtain satisfactory agreement. The final resulting soil properties are thus referred to as strain compatible properties. While this process appears to converge for most practical problems, it is not clear how the effective strain that defines the value of the modulus and damping is to be chosen for a transient motion rather than a harmonic steady state condition.

The frequency-domain equivalent-linear approach is a widely used method to estimate site response effects because of its simplicity, flexibility and low computational requirements and implementation. However, it does not capture the full range of cyclic behaviour of soil such as residual straining, the variation in tangent stiffness during the response to ground motion excitation and excess pore pressure generation. Moreover, it has been shown that for soft soil sites or sites subjected to high seismic intensities, the use of the equivalent linear method may produce results that may not match with available observations (e.g. Hashash et al., 2010). In these cases, non-linear time-domain analysis is used to capture the important aspects of soil behaviour including the actual variation of shear modulus and damping ratio during shaking.

2.4.2 Nonlinear time domain approach

For solving problems involving true non-linear response of a soil deposit, numerical integration in the time domain is the method of choice. In order to capture the soil hysteretic response and nonlinearity due to medium and large ground motions, the system parameters of the non-linear constitutive model are updated at small time intervals. The 1D wave propagation equation in this case can be written as:

$$[M]\{\ddot{u}\}+[C]\{\dot{u}\}+[K]\{u\}=-[M]\{I\}\ddot{u}_g \tag{2-9}$$

where [M] = mass matrix; [C] = viscous damping matrix; [K] = stiffness matrix; $\{\ddot{u}\}$ = vector of nodal relative acceleration; $\{\dot{u}\}$ = vector of nodal relative velocities; and $\{u\}$ = vector of nodal relative displacements. $\ddot{u}_g$ is the acceleration at the base of the soil column and $\{I\}$ is the unit vector. The [M], [C] and [K] matrices are assembled using the incremental properties of the soil layers. This equation is solved numerically at each time step.

2.4.2.1 Soil material models

One of the basic requirements for the soil response to be computed by equation (2-9) is a non-linear constitutive model that describes the cyclic behaviour of soil – in simple terms, a set of rules is needed that will tell each soil element how to find its way around the stress-strain space. Most of the currently available nonlinear 1-D ground response analysis computer programs characterize the stress-strain relationship of the soil by cyclic stress-strain models. In the simplest form, a backbone function along with some unloading-reloading criteria is used to represent the hysteretic loading and unloading of soil. Laboratory test data such as modulus

degradation curves shown in Section 2.2.7 are used to calibrate the backbone curve and to choose the model properties.

The Kondner and Zelasko (Matasovic and Vucetic, 1993, Kondner and Zelasko, 1963) model is often used to describe the soil backbone stress-strain behaviour. Matasovic and Vucetic (1993) however, increased the number of its parameters for more accurate seismic response analyses. The improved model with the addition of two curve-fitting constants was compared with the experimental results and it was revealed that the stress-strain curve can be described with sufficient accuracy. The new function, called the MKZ model, assumes the following form:

$$\tau = \frac{G_{\max}\gamma}{1+\beta\left(\frac{\gamma}{\gamma_r}\right)^{\alpha}} \tag{2-10}$$

where τ = shear stress; γ = shear strain; γ_r = reference strain and α and β are the added constants. In the above equation, the curve-fitting constants α and β adjust the position of the curve along the ordinate and control the curvature. This model was further extended by Park and Hashash (2004) to incorporate the confining pressure dependency of the soil behaviour.

The Masing criteria (Masing 1926) and extended Masing criteria (Pyke 1979) often define the unloading-reloading criteria and behaviour under general cyclic loading conditions as shown in Figure 2-25. However, it has been shown that damping ratio can be excessively overestimated if the Masing rules are employed at large strains. One of the objectives of this thesis is to circumvent the discrepancy of damping between the experimental behaviour and that simulated by mathematical

models. More details of different aspects of modelling the hysteretic damping of soil are presented in Chapter 6.

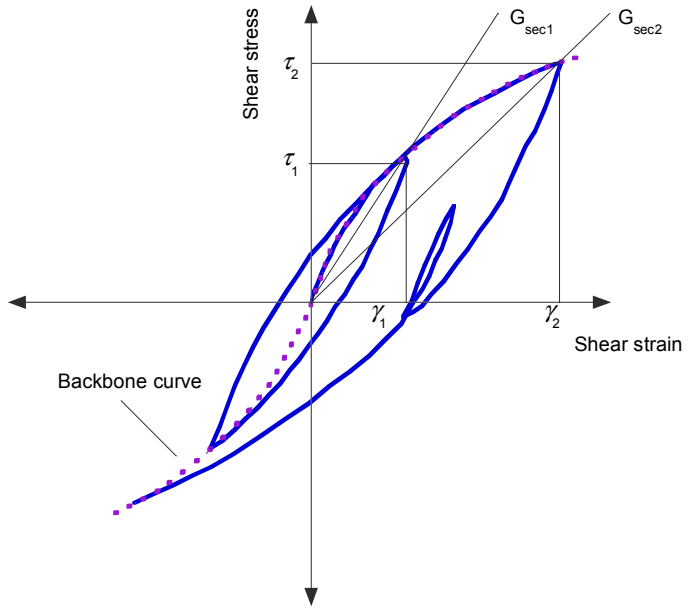

Figure 2-25 Hyperbolic nonlinear soil model with extended Masing rule to define loading and unloading behaviour.

Simple nonlinear constitutive relations described previously do not consider the generation of excessive pore water pressure and accumulation of shear strain during liquefaction. They also cannot capture the degradation of stiffness due to an increase in the number of cycles and dilation due to increased cyclic shear stiffness and strength. Advanced constitutive models based on the framework of plasticity normally can take into account the fully-coupled solid-fluid phases and can simulate soil behaviour more accurately (e.g. Cubrinovski, 1993, Prevost, 1989). Normally these models are defined by a set of key components i.e. a yield surface, kinematic hardening laws, and flow rules. Both simple and advanced constitutive material models are then employed in the framework of solution routines for mathematical representations of soil deposits.

2.4.2.2 Mathematical representation of soil column

The method of analysis employed in time-stepping procedures typically involves modelling the unbounded medium as a series of individual horizontal layers with varying properties. The layers can then be discretized using either a multi-degree-of-freedom (MDOF) lumped parameter or finite element with distributed mass as shown in Figure 2-26. In the case of the lumped mass system, each individual layer is represented by a corresponding mass which are interconnected by non-linear hysteretic springs and viscous damper elements for the modelling of stiffness and additional viscous damping of the soil deposit during horizontal displacement. The mass of the soil layers is lumped at the top and bottom of the layers to form the mass matrix. The stiffness matrix is updated at each time increment to incorporate non-linearity of the soil. The spring stiffness k_i of layer i can be obtained by considering the shear deformation of this soil layer. With a soil column of unit section area, a height of h_i and G as the shear modulus, the nonlinear spring stiffness is equal to:

$$k_i = \frac{G_i}{h_i} \tag{2-11}$$

Boundary conditions are required to be used at the base of the necessarily finite node to simulate the infinite extent of the soil domain in the vertical downward direction. The base of the soil column can be simply modelled as an infinitely stiff space. However, when the infinite domain is modelled by a finite model, there is danger that waves reflected from the free-surface will be reflected back off the artificial bottom boundary and cause errors in the response calculations. Hence, to take account of the finite rigidity of the underlying medium, a dashpot element suggested by Joyner and Chen (1975) can be used to incorporate the energy transmission of the visco-elastic half-space:

$$C_E = \rho_E V_{sE} \tag{2-12}$$

where C_E is the viscous damping coefficient, ρ_E is the density and V_{sE} is the shear wave velocity of the elastic bedrock. The viscous damping coefficient of the elastic bedrock is assumed to be proportional to the product of the mass density and shear wave velocity of the underlying rock. The control motion must be specified at the bottom of the system of either lumped masses or finite elements.

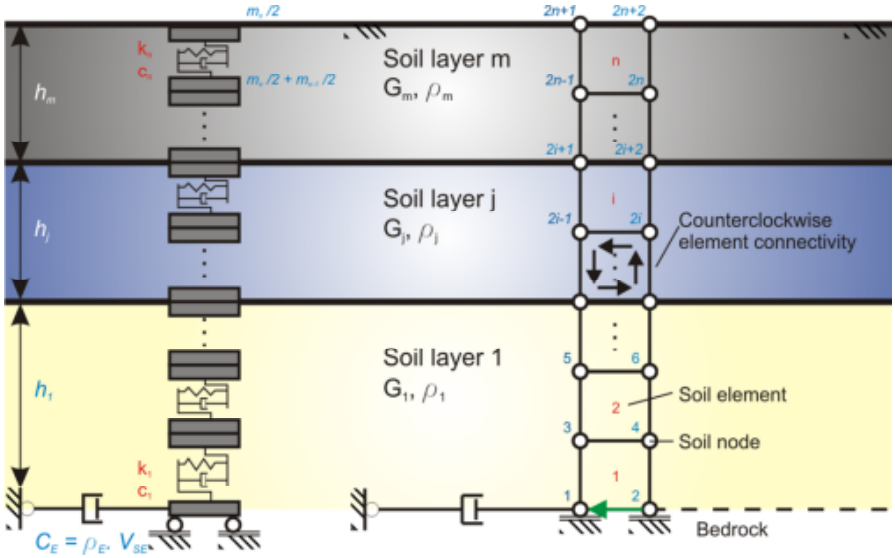

Figure 2-26 Schematic representation of the soil stratigraphy model, multi-degree-of-freedom lumped mass (left) and finite element (right) (modified after Stewart et al., 2008).

An important aspect of all discrete models is the convergence and stability of the solution in relation to refinement of the discretization scheme. That is, to find the minimum number of sublayers to subdivide the macro-layers of the soil deposit. Sub-layering criteria depend on several factors including the number of macro-layers, the rate of variation of mechanical impedance with depth, and the frequency content of the seismic excitation. According to Ohsaki (1982) the number of subdivisions, N_{sub}, is chosen such that (Lo Presti et al., 2006):

- The vibration periods computed by the algorithm are less than 5% error.
- The response of the system to a given excitation is less than 5% error.

In addition to the above, the layer thicknesses should be chosen so that the maximum frequency, f_{max}, that can be propagated through all layers within the soil column, is at least equal to 25 Hz (Stewart et al. 2008).

$$f_{\max} = \frac{(V_s)_i}{4h_i} \tag{2-13}$$

2.4.2.3 Damping formulations

Various forms of internal viscosity, friction and small scale thermal effects in soils results in material damping. Two basic approaches have commonly been employed for representing damping ratios in the stress-strain behaviour during cyclic loading, for application in site response analysis. The first approach, in which the soil is modelled by a series of springs and frictional elements of Iwan type (Iwan, 1967, Joyner and Chen, 1975), uses a set of unloading-reloading rules (e.g. Masing criteria) to establish the shape of the cyclic hysteresis curve. This rheological model has no viscous damping, and as a result the stress depends on the strain and strain history but not on the strain rate. The energy dissipation per cycle, therefore, does not depend upon the frequency. Therefore, use of the damping matrix, **[C],** in the equation of motion may become unnecessary.

In the second approach, however, the damping matrix, **[C],** may be added as a mathematical convenience, or to represent damping at very small strains where response of many hysteretic soil models is primarily linear elastic, underestimating damping values obtained from laboratory measurements (Vucetic et al., 1998, Park and Hashash, 2004). For practical purposes, early formulations used a simplified form

of the damping matrix which is proportional to the stiffness of the soil layers using the first natural model of vibration (Hashash and Park, 2001). The damping matrix in this case is expressed as:

$$[C] = \frac{2h}{\omega}[K] \tag{2-14}$$

where ω is circular frequency of the first natural model of the soil column and h is the equivalent damping ratio for each layer at small strains. The value of the equivalent damping ratio, h, can be obtained from the damping ratio curves at small strain. For instance, a constant small strain viscous damping is used in most non-linear models with a recommended upper bound value of 1.5-4% for most soils (Hashash and Park, 2001). The analyses show that with increasing soil column thickness the use of time domain analysis with the first natural mode results in an increasing underestimation of surface motion. As a result the **[C]** matrix can be extended to be a combination of the mass matrix and the stiffness matrix (Rayleigh damping model):

$$\begin{aligned} [C] &= a_0[M] + a_1[K] \\ \begin{bmatrix} h_i \\ h_j \end{bmatrix} &= \frac{1}{4\pi}\begin{bmatrix} \frac{1}{f_i} & f_i \\ \frac{1}{f_j} & f_j \end{bmatrix}\begin{bmatrix} a_0 \\ a_1 \end{bmatrix} \\ f_n &= (2n-1)\frac{\overline{V}_s}{4H} \end{aligned} \tag{2-15}$$

It is common practice to select the low frequency fixing point that corresponds to the first mode of the soil column, and the high-frequency fixing point to be equal to the predominant frequency of the input motion. Stewart et al. (2008) also recommended a value equal to five times the natural frequency for the latter case. Since the damping ratio has been known to be frequency independent, equal values of modal damping ratios are specified for the two modes.

Nevertheless, the frequency-dependency of damping calculated using Rayleigh formulation is inconsistent with most of the available experimental data. This data shows that material damping in soils is mostly frequency independent at very small strain levels over the frequency range of interest in engineering applications (i.e. 0.001 to 10 Hz). Moreover, high damping is artificially introduced outside the limited frequency range which filters out high frequency ground motion. However, **[C]** can be assumed to be independent of strain level and therefore, the effect of hysteretic damping induced by non-linear soil behaviour can be separated from (but added to) viscous damping. Furthermore, Park and Hashash (2004) introduced the extended Rayleigh damping formulation which uses four modes instead of two in order to reduce the over-damping of Rayleigh solution at high frequencies but this does not give a damping matrix which is banded.

2.4.3 Site response analyses in Christchurch

In the first detailed seismic hazard assessment for the city of Christchurch, Elder et al. (1991) modelled the deep, relatively soft sediment underlying the city. Elder et al. (1991) used the original Katayama (1982) attenuation model without modification to construct the bedrock spectra and employed the shape as input to their deep alluvium propagation model (Figure 2-27). The extreme bedrock response is also demonstrated in Figure 2-27. This is the spectrum resulting from maximum magnitude earthquakes defined by an upper bound magnitude-distance curve. Further, based on the site response analyses, they concluded that a very large part of the eastern city is potentially subject to liquefaction while amplification effects are pronounced in the areas to the north of the central city and in scattered south-western areas. Later, using the Elder et al. (1991) seismicity model in a pilot study of ground

shaking hazard, Berrill et al. (1993) computed the transfer functions at six different sites in the Christchurch area.

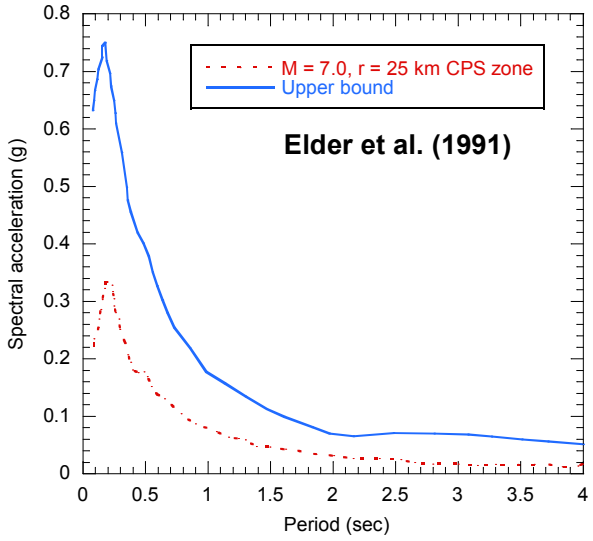

Figure 2-27 Response spectra at bedrock for Christchurch, (after Elder et al. 1991)

Following the 2010 Darfield and 2011 Christchurch earthquakes (Canterbury earthquake sequence), site response analysis in Christchurch attracted further attention. For instance, Smyrou et al. (2011) considered a generic soil profile to study the effects of pore water pressure generation and liquefaction. The bedrock motion recorded in the LPCC station was employed as the input motion in the effective stress analyses using FLAC (Itasca Consulting group, 2005). They showed that as shear waves propagate from the base of volcanic rock, the soil de-amplifies the low-period components of motion and amplifies those of high period. Moreover, the top 25m surficial soil layers play a dominant role in defining the ground motion characteristics at ground surface. The occurrence of liquefaction in the modelled site was clearly visible. Garini et al. (2013) showed that the high spectral values of the recorded motion during the 2011 Christchurch earthquake could not be explained by 1D total

stress analysis. However, effective stress analysis incorporating the excess pore water pressure could enhance the results comparing with the obtained surface ground motions.

The significance of the nonlinear soil response during the Canterbury earthquake sequence was also illustrated by Bradley (2012b) and Bradley (2012c). The recorded motion during the 2011 Christchurch earthquake on the engineering bedrock (LPCC) was compared with another recorded motion (LPOC) located on a thin surficial soil layer. It was illustrated that observed horizontal ground motion at the soil site had significantly lower short period ground motion amplitudes compared with the rock site; while notably larger spectral amplitudes at longer periods were recorded. The importance of local site effects was further emphasized showing that in spite of differences in source and path effects for the 2010 Darfield and the 2011 Christchurch earthquakes, the response spectral shapes of multiple strong motion locations were very similar.

2.4.4 Code-based site response analysis

The simplest approach for assessing local site response effects is the use of site class factors which categorize various surficial soil profiles into different classes and assign a single shape factor by which seismic response spectra for a given site subsoil class deviate from a rock spectrum. Earlier codes made use of natural period as a means to classify site conditions (e.g. UBC 1976). More recent codes such as the 1997 UBC and 1997 NEHRP provisions in the USA use the average shear-wave velocity over the upper 30m of a site as the sole index for site classification. Rodriguez-Marek et al. (2001) proposed a site classification system in order to capture the primary factors affecting seismic site response while minimizing the

amount of data required for site characterization. The proposed site classification system is based on two primary and two secondary parameters. The primary parameters are type of deposit in terms of stiffness (i.e. the average shear wave velocity) and depth to bedrock. The secondary classification parameters are depositional age and soil type.

The current New Zealand seismic design actions standard (NZS 1170.5, 2004) for building-type structures determines five site classes (A-E) and provides design response spectral shapes as shown for the 500-year return period in Christchurch in Figure 2-28. The elastic site spectra for New Zealand have been derived from results of a probabilistic seismic hazard model (NZS 1170.5, 2004). The spectral shape factors for each of the site subsoil classes are normalized by the codified peak ground acceleration for rock. The basic parameter for site classification in this Standard is the low-amplitude site period, recommended to be taken as four times the estimated travel-time of shear waves from the surface to rock when it has not been measured directly. The definitions of the site classes are generally descriptive rather than requiring knowledge of site properties, because these are not generally available in New Zealand. While such site classes are simple and easy to apply in practice, by necessity they provide a limited characterization of the effect of local soil response on surface ground motions.

All the strong motion stations considered in this study are categorized to be in the site class D (GeoNet, 2012). Figure 2-29 compares geometrical mean of the pseudo-acceleration response spectra recorded during the 4 September 2010 Darfield and the 22 February 2011 Christchurch earthquakes at selected strong motion stations as well as the design spectrum for site class D. It is apparent in this figure that although all the strong motion stations belong to the same soil site classification and the distances

between the sites are not large; their response is very different from each other. Moreover, the design spectra may differ significantly with the individual recorded spectral accelerations.

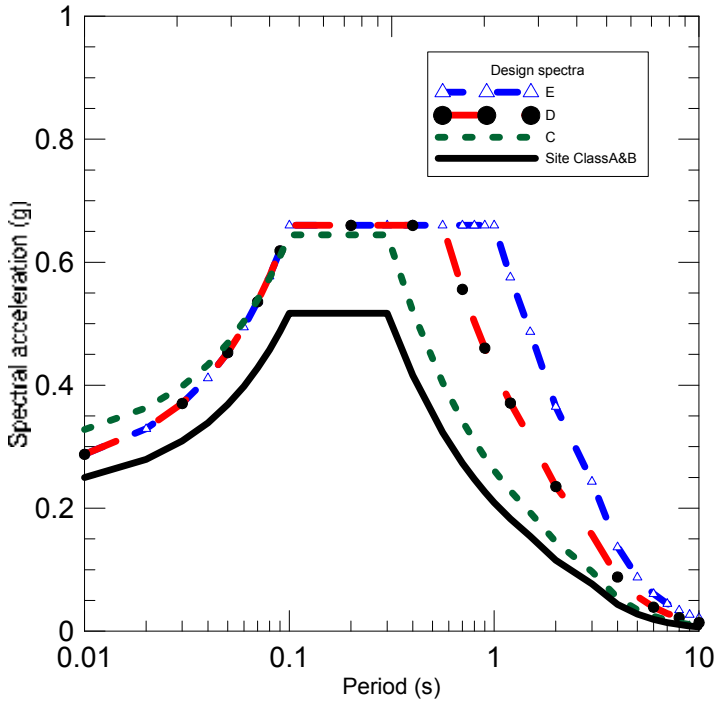

Figure 2-28 Effect of site class on seismic design spectra according to NZS 1170.5 (2004) for Christchurch (Z = 0.22) at 500 year return

In regions of complex depositional history, such as in Christchurch, the site effects can vary significantly over distances as short as hundreds of meters or less. This figure clearly demonstrates the importance of site-specific local soil effects on ground motions and that simple code-type site classification may not accurately capture such effects. Toshinawa et al. (1997) and Bradley (2012b) have also shown that the ground-motion characteristics in Christchurch may change over a scale of 1 km or less due to the high variability in the top 30m subsurface layers. The key benefits of site-specific response analysis are then the ability to assess the likely

response of the actual soil profile below the site, with a higher level of accuracy than the site class factor approach.

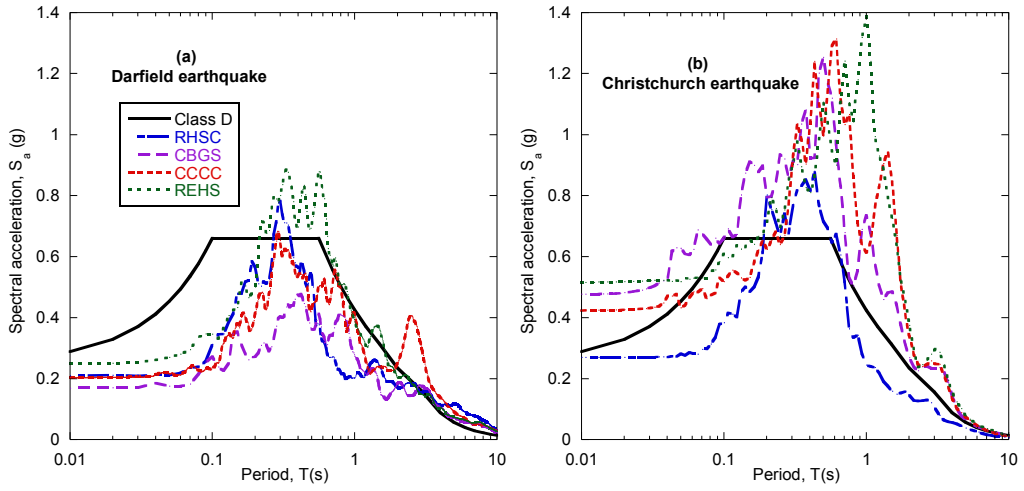

Figure 2-29 Comparison of geometric mean of the acceleration response spectra (a) 4 September 2010 Darfield and (b) 22 February 2011 Christchurch earthquakes at selected strong motion stations and the design spectrum for site class D (NZS 1170.5 2004).

2.5 Summary

This chapter presented the measurements of the G-γ and h-γ soil properties using BE device at linear range and the calculation of the modulus and the damping in the nonlinear stage of soil behaviour. The influences of loading conditions and material type on the G-γ and h-γ characteristics, in particular modulus and damping, were further discussed based on recent studies. From results of numerous experimental studies, it was shown that fines content can exert a great influence on the structure of a sandy soil matrix as well as on the mechanical characteristics of the mixture. The possible effects of fines on the G-γ and h-γ properties of soil were further explored. Finally, the general trends in the mathematical modelling of the dynamic soil properties in the context of one-dimensional ground response analysis were discussed.

3 Apparatus, test materials and procedures

3.1 Introduction

One of the objectives of this study is to investigate the effect of fines content on dynamic soil properties. Bender element (BE) and triaxial (TX) techniques are widely used test methods for measuring the dynamic properties of soils. In this study both the bender element device and the cyclic triaxial apparatus were employed to test several mixes of sand with varying fines content over a wide range of shear strains. All tests were performed under drained conditions and constant confining pressure. Soils sourced from Christchurch, New Zealand were specifically selected as an accompaniment to previous studies performed at the University of Canterbury on undrained sand response (Rees, 2009). This chapter describes the equipment and devices employed for quality testing. The procedures used for sample preparation, the bender element and drained triaxial tests are also explained. Lastly, the properties of the tested soils as well as the measurement techniques employed for interpreting the data are presented.

3.2 Apparatus description and test procedures

The testing device used in this study was a Seiken Inc. cyclic triaxial apparatus, model DTC-367, complemented with bender elements installed by the same company. Both bender elements and the triaxial apparatus are used worldwide in the study of dynamic soil properties at low and high strain levels, respectively, using the observed response of a cylindrical soil specimen subjected to stress waves or axial forces. Details of the triaxial apparatus and bender elements and calculations used for data interpretation are described in the following sections.

3.2.1 Triaxial testing system

The triaxial apparatus used in this study typically utilizes a soil specimen in conditions shown in Figure 3-1. A cross-sectional view of the same specimen in the triaxial cell of the device is presented in Figure 3-2. This device accommodates a solid specimen of cylindrical shape with a typical height of $h \approx 100mm$, and diameter of $d \approx 50mm$. The specimen was enclosed laterally using a rubber membrane and vertically by a top cap and bottom pedestal. Drainage from the sample was provided by porous discs built into the cap, the pedestal, and drainage lines. The cell was partially filled with de-aired water. Cell and pore pressures were independently controlled by an air compressor which is designed to handle pressures up to 1000 ± 1.5 kPa. The DTC-367 triaxial apparatus and all peripheral equipment were located in a controlled temperature environment (~19°C). All transducers and controllers were interfaced with a desktop computer via Kyowa sensor interface PCD-300 series. The apparatus hardware is shown in Figure 3-3.

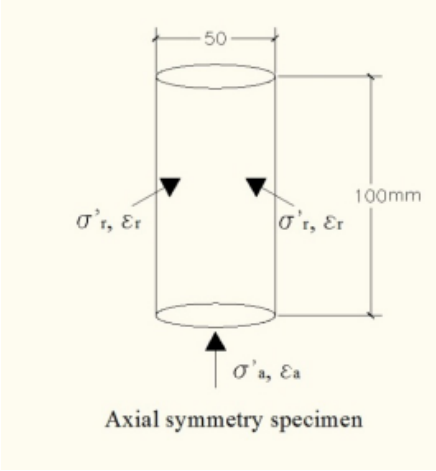

Figure 3-1 Idealization of soil specimen in a triaxial apparatus

A vertical load was applied using a servo controller (EO-260) and the pneumatic actuator, capable of testing a soil specimen in dynamic mode for loading frequencies

up to 10 Hz. The bottom platen was fixed during dynamic testing and compression-extension cycles were applied at the top of the specimen. A submersible load cell located inside the cell, and directly at the top of the specimen cap, recorded the axial force in order to avoid inevitable frictional forces. The maximum capacity of the load cell was 2 kN. However, to increase the accuracy of the measured axial load, a lower capacity of 500 N was chosen during dynamic testing. The load cell was calibrated before commencement of the testing scheme.

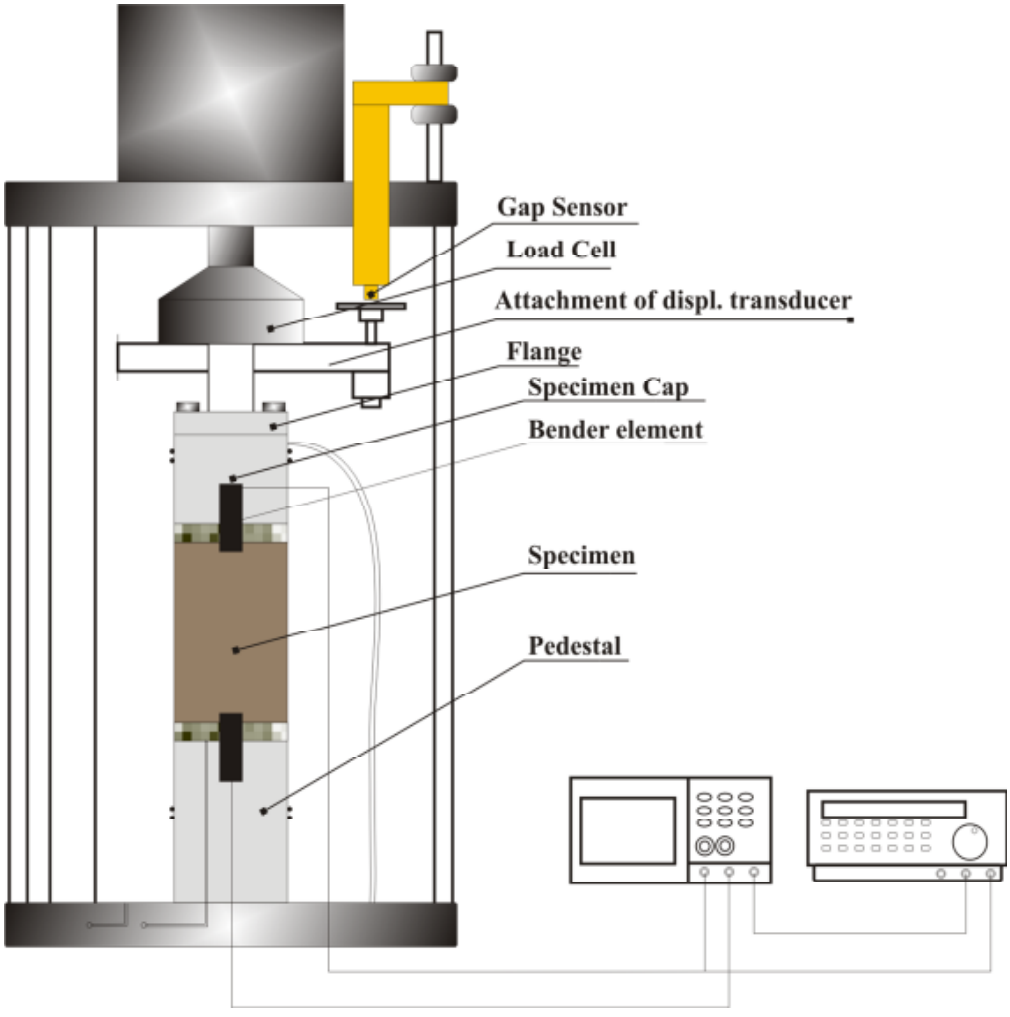

Figure 3-2 Schematic layout of the soil specimen in a triaxial cell

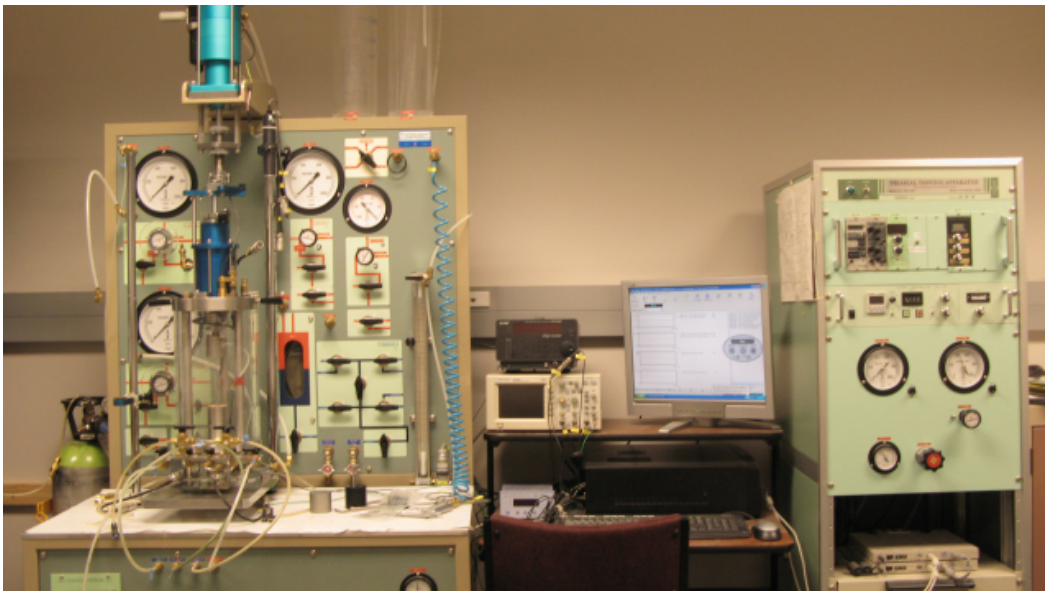

Figure 3-3 Triaxial apparatus setup in the temperature-controlled research room

The axial displacement was measured by an internal gap sensor and an external LVDT (linear variable differential transformer). The accuracy of which can be up to 0.1 μm and 0.05 mm respectively. The internal gap sensor was used to monitor deformation at a low strain range whereas the external LVDT was used at larger strain stages. The volume change of the sample was recorded in terms of '*ml*' and measured by a differential pressure transducer (DP-15) that measures the change in the pressure due to the change in the water head inside a burette connected to both top and bottom drainage lines.

3.2.2 Test procedures

In this study, triaxial test specimens were prepared at different densities employing a modified moist tamping method (e.g. Ishihara, 1996, Rahman, 2009). Each specimen consisted of ten compacted layers. Drained dynamic triaxial tests were performed on the remoulded specimens of sandy soils in order to define stress-strain relationships and to study the effect of fines content on the dynamic characteristics of

sand. Fines were defined as particles smaller than 75 μm. Details of sample preparation and testing procedures are described in the following subsections.

3.2.2.1 Specimen mould setup

First, thin layers of silicon grease were placed around the sides of the pedestal to prevent cell water from leaking into the specimen between the membrane and pedestal. The membrane was then placed around the outside of the pedestal. It extended 30 mm below the edge of the pedestal surface and was secured in place with two rubber O-rings (Figure 3-4a). The metallic split mould was then installed on the platen as shown in Figure 3-4b. The mould was secured in place with a pair of metal clamps. A vacuum was applied to the internal mould space to ensure a good fit of the membrane on the mould during material deposition. Two O-rings were set at the top of the split mould. The membrane was folded down over the mould top and held in place with a single O-ring. Thus, the mould and membranes were set and prepared for the reconstitution procedure.

3.2.2.2 Soil preparation

The remoulded samples required some initial preparation before the soil was poured into the specimen mould setup. The dried soil was soaked in a plastic container with a predetermined amount of de-aired water to reach a moisture content of 9% and then it was mixed with a glass rod to get a uniform material to be deposited into the prepared mould. The moist materials were left in the air-tight contained for over an hour before sample preparation.

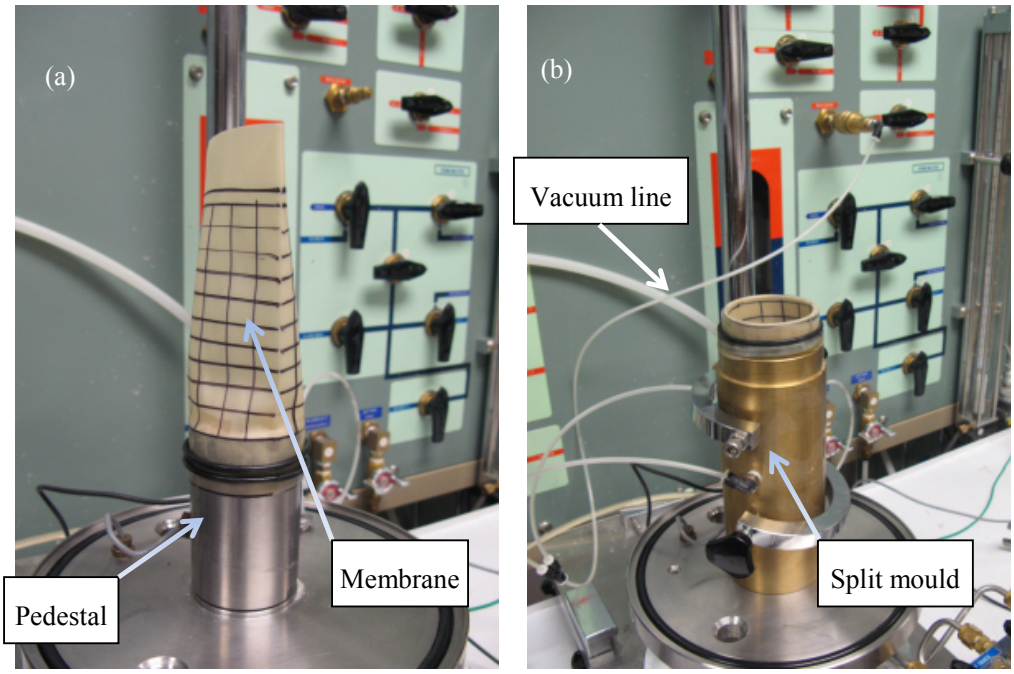

Figure 3-4 Setting of the mould and membrane

3.2.2.3 Soil deposition

The moist material prepared for deposition was carefully poured into the mould in small quantities using a small spoon. It was then compacted with a plastic rod with a foot diameter of 25mm. To ensure a uniform sample density, a modified moist tamping method was adopted as discussed in Rahman (2009). Figure 3-5a shows the tamping rod attached to a horizontal plastic strip to control the working depth ensuring a uniform sample density. However, no measurement was taken to verify that the target uniformity has reached.

In order to prepare a uniform specimen across the height, the sample was formed in ten separate layers. Each layer had a predetermined equal amount of soil which was weighed before deposition. The layer mass was calculated from the specimen's target void ratio and the specific gravity of the tested soil. Each layer was levelled to the target thickness by the modified tamping rod as shown in Figure 3-5b. The tamping

method provides a smooth surface at the interface of adjacent layers. Hence in order to eliminate the potential discontinuity, by means of small screwdriver, the surface of each layer was lightly grooved in cross-hatch pattern. Visual observation suggested the specimens to be reasonably uniform across the height. After preparing the top layer, the superfluous material was removed, the upper surface was levelled (Figure 3-5c), and the cap was placed over the level surface of the top layer. Thin layers of silicon grease were placed around the sides of the top cap. Then the membrane was rolled over the top cap and secured in place by two O-rings sitting on the mould. At this stage, the top and bottom platens were connected to the drainage lines and a small amount of vacuum (~30 kPa) was applied to the sample as shown in Figure 3-4d. This provided confinement to the sample and allowed the removal of the split mould. Great care was exercised throughout each specimen preparation, setting, and consolidation in order to avoid inducing any pre-shearing stress to the sample.

A wide range of specimen densities were achieved using the described modified moist tamping depositional method. Clean sand specimens had relative densities ranging from D_r = 0 – 80%, whilst silty sand specimens had relative densities from D_r = 40 – 80%.

3.2.2.4 Assembling of the triaxial cell

After sealing the sample laterally by the membrane and vertically by the top and bottom platens, the vertical loading ram was connected to the top cap without introducing any additional stresses to the sample as illustrated in Figure 3-6. The cell chamber was placed in position and the assembled triaxial cell was centred in the loading frame, in readiness for filling with de-aired water. The specimen is shown in Figure 3-6, before and after the triaxial cell was assembled and filled with water.

After filling the cell with water, the cell pressure was gradually raised to 30 kPa while the vacuum was simultaneously reduced to zero, maintaining the constant isotropic effective stress on the sample at 30 kPa.

3.2.2.5 CO_2 percolation and water saturation

In order to improve the degree of saturation and hence reduce the errors in measuring sample volume changes and pore pressure variations caused by the presence of gas in the triaxial system, de-aired water was used to flush all pore pressure lines. A Nold DeAerator (model 2100, Geokon Inc.) which runs at high speed under vacuum to agitate the water was used for all water de-aeration during the laboratory testing program. A running time of approximately ten minutes was applied. All de-aerated water for the triaxial cell was transferred using a plastic airtight container. The water was used to fill the de-aired water tank and the confining pressure tank. A vacuum was also applied to the tanks in order to improve the de-aeration. To ensure a high degree of saturation of the samples, saturation of the specimen was carried out by three stages: carbon dioxide percolation, de-aired water percolation, and application of back pressure.

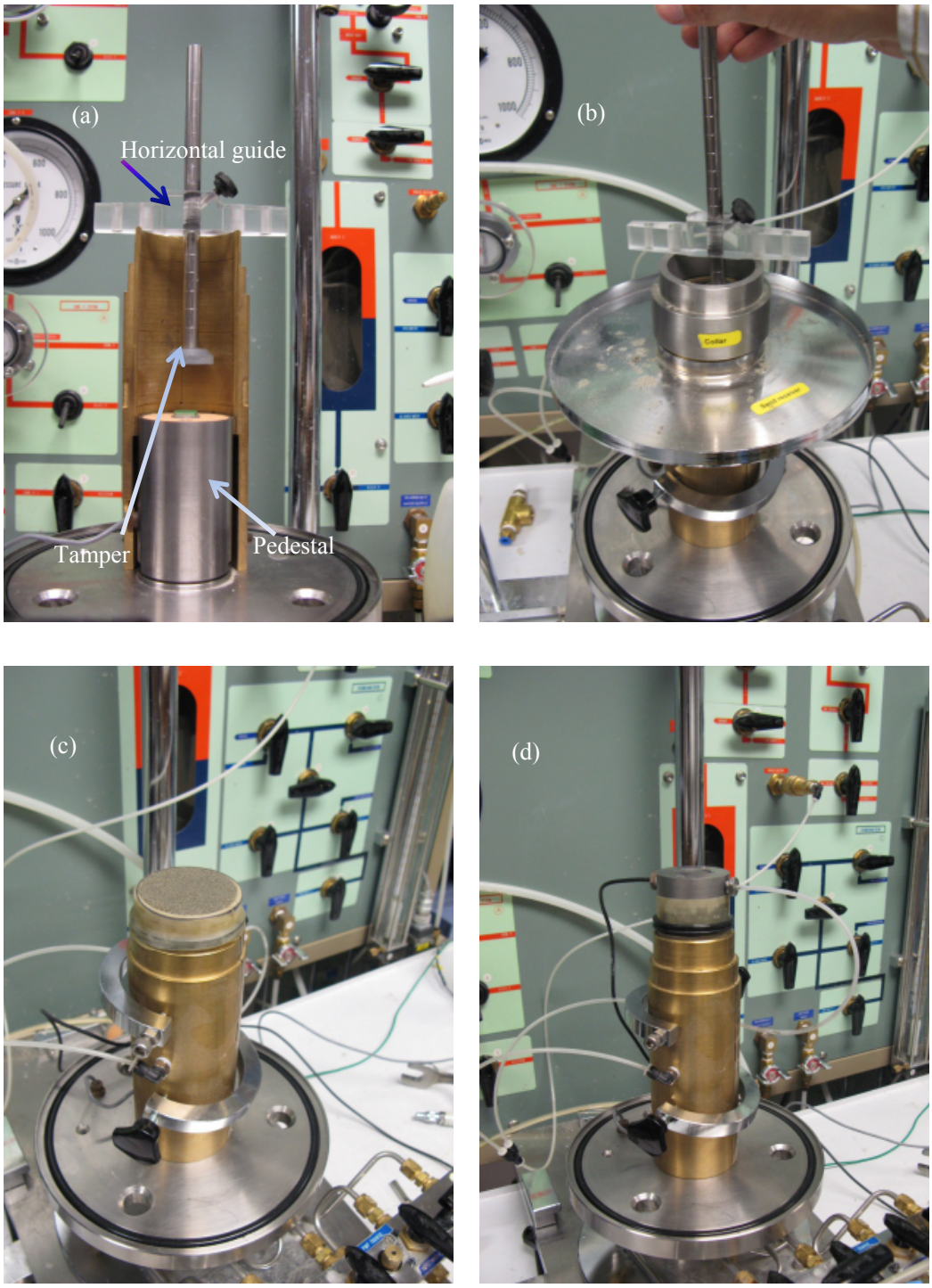

Figure 3-5 (a) Cross section of sample preparation mould, (b) Reconstituting the sample, (c) Top soil layer flush with the top of the mould, (d) Sealing the sample

Figure 3-6 Assembling the triaxial cell (left), filling the triaxial cell with water (right)

Carbon dioxide gas was percolated through the pedestal for approximately 30 minutes for the low fines content soils and for up to two hours for the samples of sand with higher fines content. The objective of CO_2 percolation was to replace the air within the specimen voids with CO_2 as the latter easily dissolves in water under pressure. Next, de-aired water was slowly introduced into the sample from the de-aired water tank through the bottom platen. After a sufficient amount of water percolation (more than four times the sample volume), a back pressure of 100 kPa was applied incrementally, while keeping the effective confining pressure constant at 30 kPa. The sample was then left to saturate overnight. Following the above procedure, a conventional Skempton's pore pressure parameter, *B*-value, greater than 0.95, was achieved implying full saturation.

3.2.2.6 Consolidation

In all the drained tests, the specimens were isotropically consolidated to the prescribed mean effective stress of p' = 100 kPa. Cell pressure was increased incrementally to 200 kPa while back pressure was kept constant at 100 kPa. Specimens were left to consolidate under the final confining stress for varying amounts of time. Consolidation was deemed complete when a volume change of less than 5 mm^3 was observed over a period of 30 minutes. The typical pressures applied during the saturation and consolidation phases are displayed schematically in Figure 3-7. The solid line and the dashed line represent the cell and back pressure, respectively. After consolidation, the sample was ready for the bender element and triaxial test.

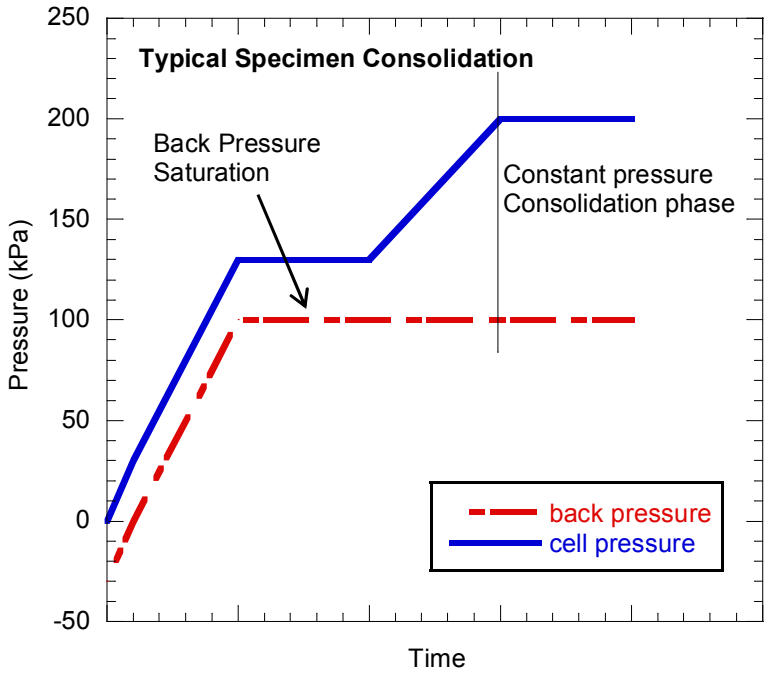

Figure 3-7 Typical cell and back pressures during specimen saturation and consolidation (time not to scale)

3.2.3 Bender element device

A pair of piezoelectric bender elements, made of ceramic bimorph was incorporated in the DTC-367 triaxial apparatus to measure the shear wave velocity and the maximum shear modulus of the soil at very low strains. A piezoceramic bimorph can bend or deflect in response to the application of an electrical charge. Likewise, the application of a mechanical deformation to the end of a bimorph will result in the development of an electrical charge. This feature enables the same type of elements to be used for both transmission and reception of shear waves. The term transmitter and receiver are used to indicate the role in which the element is operated.

Whether the piezoceramic expands or contracts depends on the direction of the crystal polarisation. If each piezoceramic is polarised in opposite directions, then the material deflects in response to opposite charges being applied to its surfaces. This is known as a series-type bender. If each side is polarised in the same direction (parallel-type), then a deflection is only produced if the same sign charge is applied to each side of the element (Lee and Santamarina, 2005). The transmitter element is electrically connected in parallel in order to induce a larger deflection (and hence transmitted signal strength) whereas the receiver element is connected in series and induces a larger voltage for recording.

The transmitter (17 × 10 × 0.5 mm) and receiver (13 × 10 × 0.45 mm) bender elements were coated with waterproofing material (epoxy resin) to avoid crosstalk effects. Both elements were positioned in the same plane to maximize amplitude. At the top of the sample, the S-wave source was built into the cap and the S-wave receiver was placed at the bottom of the sample in the pedestal. Although, the total length of the parallel and series bender elements are slightly different, the protrusion

length into the soil sample was about 3 mm for both transmitter and receiver bender elements. The cantilever length protruded into the soil is a key factor in the intensity of the generated wave (e.g. Leong et al. 2005). The piezoelectric charge constant, d_{31}, for both elements is 210×10^{-12} *m/V*. A schematic diagram of the transmitter bender element is shown in Figure 3-8.

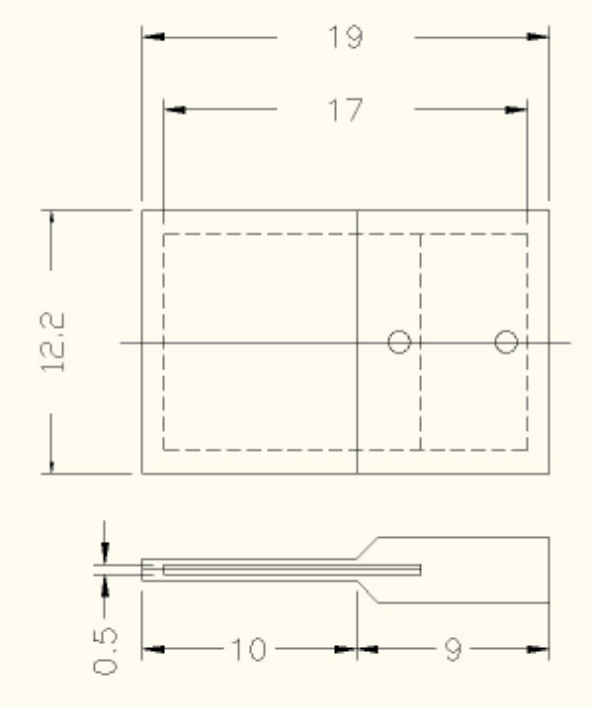

Figure 3-8 Schematic diagram of the transmitter bender elements (dimensions are in mm)

The rated voltage of the bender elements was 20 V. The other components of the test setup, consist of a multifunction synthesizer (NF corporation wave factory, model WF1943B) and digital oscilloscope (Agilent Technologies, model DSO 3062A, sampling rate 1G Sa/s) as illustrated in Figure 3-9. No power amplifier was used for input and output signals; instead, the oscilloscope was earthed to reduce the noise level as per the manufacturer's suggestion (Seiken Inc., 2009). The input signal to the soil sample was generated by the synthesizer and the response of the sample was acquired using the receiver.

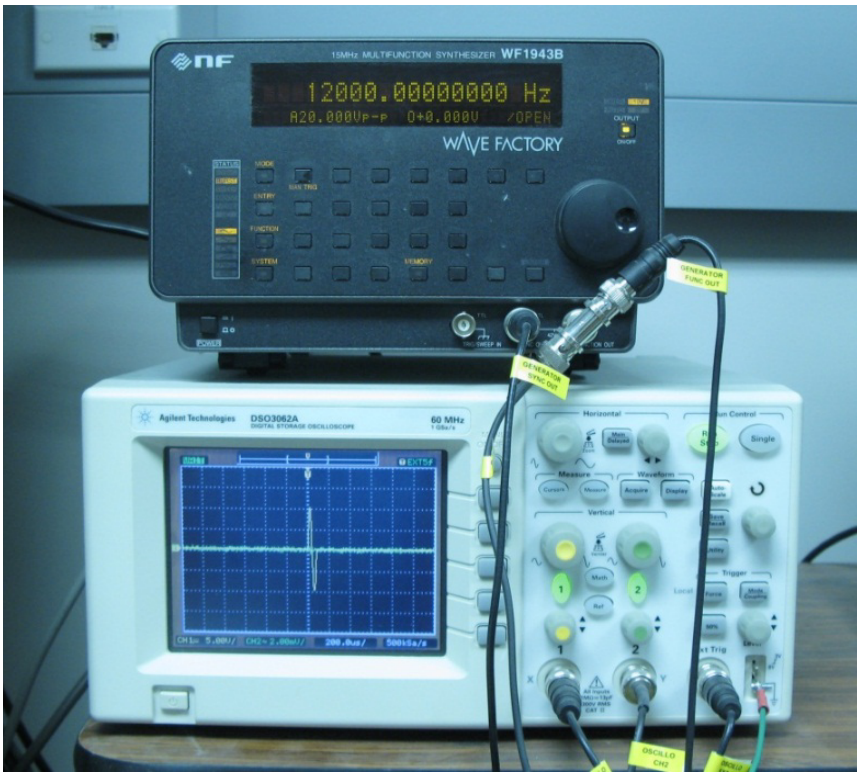

Figure 3-9 Multifunction generator and digital oscilloscope

The synthesizer's applied voltage and the received signal were recorded by the digital oscilloscope. The data was transferred to a computer for further signal processing (Figure 3-10). To examine the possibility of alternative travel paths for the generated signal, bender elements were utilized in an empty (specimen-free) triaxial cell filled with water. The recorded signals are presented in Figure 3-11, indicating that there is a small effect of voltage change which is in the level of noise and no energy is propagated through the apparatus frame or water. This implies that in presence of a specimen, most of the energy recorded by the receiver bender element is a result of wave propagation through the soil.

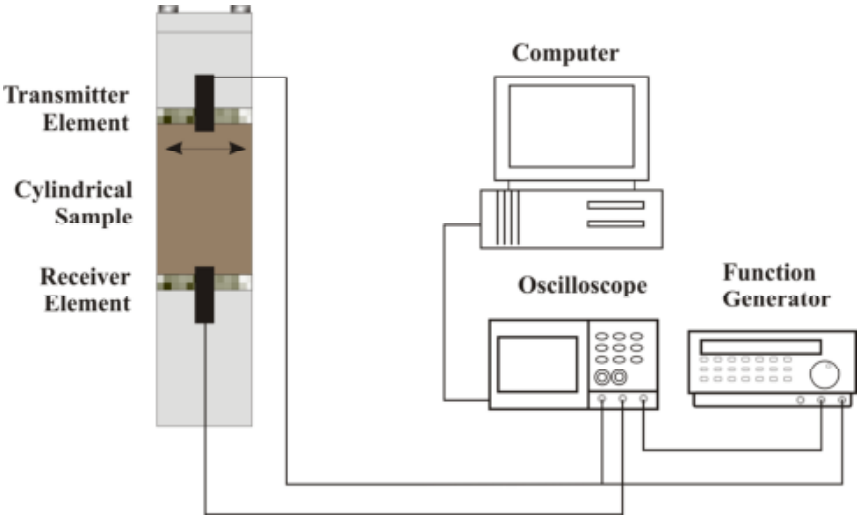

Figure 3-10 Schematic representation of the shear-wave velocity measurement (not to scale)

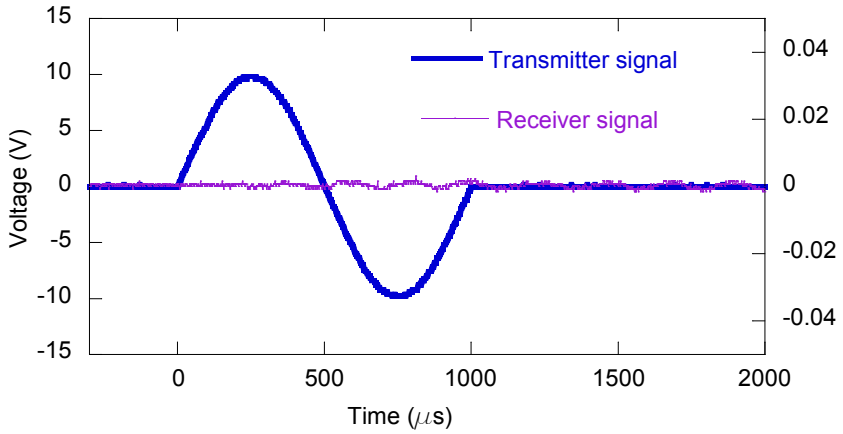

Figure 3-11 Response of the receiver bender element placed in the triaxial cell, filled with water without a soil specimen

3.2.4 Bender element test

After consolidation, the bender element test was conducted in order to measure the time difference between the transmitted pulse and the arrival of the received signal to determine the shear wave velocity of each specimen. The pulses with a single sine wave gave the best signals if the resonant frequency was triggered. Figure 3-12 shows the main frequency range used in this study (~ *4-12 kHz*). The frequency range was swept in order to identify the resonant frequency. Note that the magnitude of the

received signal is many orders of magnitude smaller than the transmitted signal. The the sample height to wavelength ratio, L_{tt}/λ, is a measure of the degree of attenuation due to geometric damping and was also calculated at the time of each test and used to check that the choice of transmitter frequency did not compromise the received signal through possible near field effects. To further improve the quality of the recorded signal, both the input and received signals were averaged using a stacking process with the digital oscilloscope. In this operation, 32 successive sets of wave traces were digitally added and averaged into the memory in real time. This resulted in clearer signals due to an increase in the signal-to-noise (*S/N*) ratio caused by mechanical vibrations or human disturbance in the laboratory.

The electronic equipment, mechanical connections and travel time in the epoxy resin coating make up the total time lag of the apparatus. The manufacturer suggests a total time lag $\Delta t = 21.2\ \mu s$, which is measured when the piezoelectric transducers for generating and detecting elastic waves are in direct contact with each other. All signals were then recorded on a desktop computer for further data processing. The interpretation procedures used to establish the first arrival of the shear wave pulses invariably contain a certain element of subjectivity but the consistency of the interpretation can be greatly improved following the recommended steps in this section and section 2.2.1.

The tip-to-tip distance between the transmitter and receiver elements was calculated at the end of the consolidation process using sample height, protrusion length of the elements and, the height reduction due to consolidation. At frequencies which showed minimal near-field effects on the received signals, the first arrival of

the *S*-wave was identified and the average of these travel times were adopted to calculate the shear wave velocity using the following equation:

$$V_s = \frac{L_{tt}}{t} \tag{3-1}$$

where V_s is shear wave velocity of the specimen, L_{tt} is the tip-to-tip distance at the end of consolidation and t is the average travel time for selected frequencies.

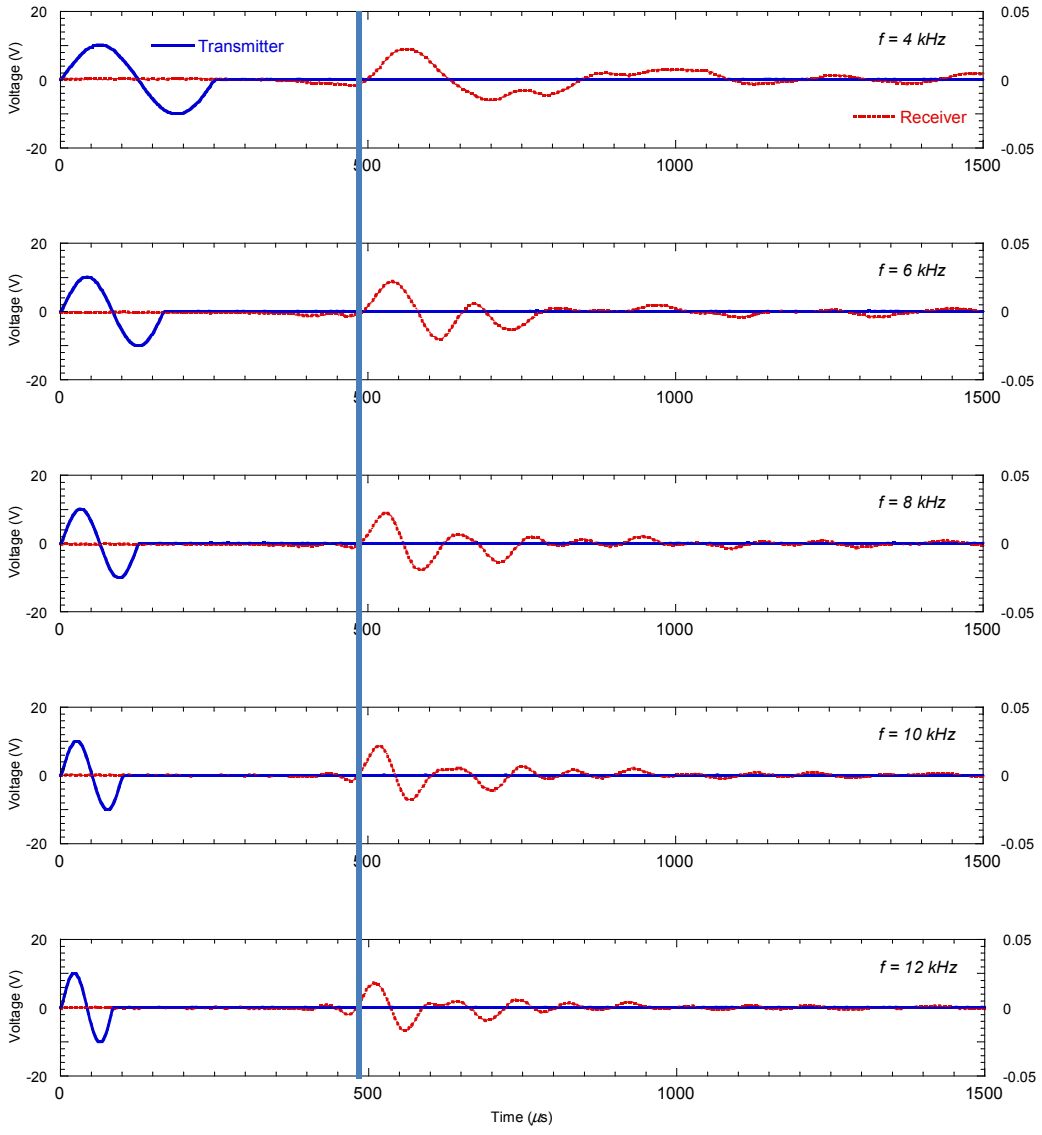

Figure 3-12 Input and output signals for specimen FB-27-10

3.2.5 Drained cyclic loading

After a specimen was consolidated to a desired confining stress and tested using the bender elements, cyclic loading was applied while the confining stress was kept constant during the whole cyclic stage. Kokusho (1980) reported that drained cyclic triaxial tests give almost an analogous strain-dependent variation of the normalized modulus and damping curves to those of undrained tests and, because drained tests are easier to conduct, all samples were sheared under drained conditions by applying cyclic axial loads. The effective confining pressure for all samples remained constant at $\sigma' = 100\ kPa$. The level of deviatoric stress was gradually increased and the samples were sheared until they failed. The sinusoidal excitation had constant force amplitude. In the TX test, the modulus and damping ratio are determined directly by monitoring the applied force and the displacement at the top of the specimen and converting them to stress and strain hysteretic loops.

First, eleven sinusoidal cycles of loading were imposed on the specimen in such a way that a single amplitude axial strain, $(\varepsilon_a)_{SA}$, was less than 0.001%. Then a similar cyclic load was applied to the specimen so that the new axial strain was about double the size of the strain that was used in the previous stage. This process was repeated as long as it was possible to double the amplitude of cyclic loads. Figure 3-13 shows typical sinusoidal cyclic loading imposed on each specimen at the early stages of shearing. It should be noted that no obvious instability was observed during the cyclic extensions which is to be expected in view of the relatively small strain involved in the tests. The Standards of Japanese Geotechnical Society for Laboratory Shear Test (Japanese Geotechnical Society, 2000) recommends using sinusoidal loads at a frequency within a range of 0.05 and 1.0 Hz. Since the experimental data (Hardin and

Drnevich 1972) indicate very little or no effect of frequency on the modulus and damping in sands for the frequency range of interest between about 0.1 and 25 Hz, in this experimental study, all tests were performed at a constant frequency, *f = 0.1 Hz*. Note that in these constant-frequency tests, the strain-rate increases proportionally to the increase in the strain level but these effects are beyond the scope of this work.

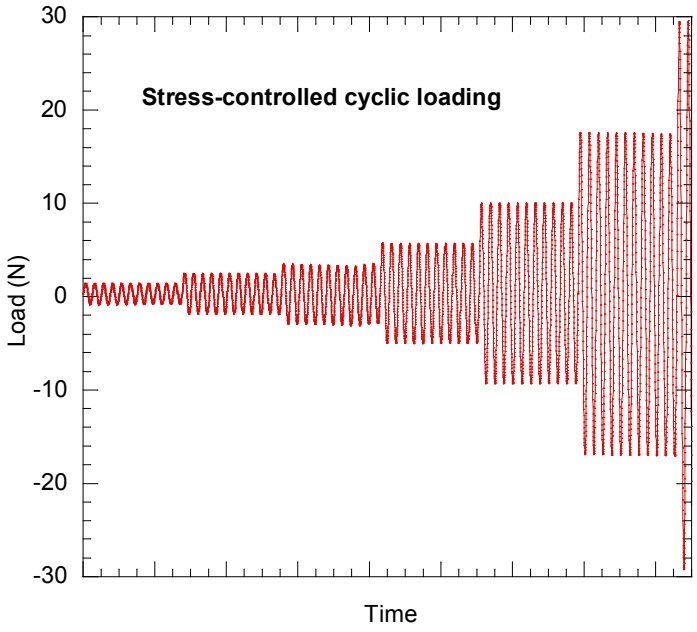

Figure 3-13 Typical record of cyclic triaxial loads performed under stress-controlled fashion with sinusoidal wave

3.3 Triaxial test measurements

The axial force was recorded by the submersible load cell within the triaxial cell. A single amplitude cyclic deviator stress, σ_d (kN/m^2) was measured as:

$$\sigma_d = \frac{P_C + P_E}{2A_n} \times 10\,(\text{kN/m}^2) \tag{3-2}$$

where P_C and P_E are single amplitude axial load (in N) on the compression and extension side in each cyclic loading stage, respectively and, A_n is cross-sectional area

of the specimen at the start of the cyclic loading stage (cm^2) (Japanese Geotechnical Society, 2000).

Single amplitude axial strains were calculated based on the recorded axial displacements:

$$(\varepsilon_a)_{SA} = \frac{\Delta L}{2H_n} \times 100(\%) \tag{3-3}$$

where ΔL is double amplitude axial displacement of the specimen in *cm*, and H_n is the specimen height in *cm* at the start of each cyclic loading stage. The axial strain in equation (3-3) is calculated in percentage.

Equivalent Young's modulus, E_{eq} (MN/m^2) for the 10th cycle of each loading stage in the triaxial test is determined from calculating the slope of the line that connects the end points of the 10th hysteresis loop as shown in Figure 3-14. Hence by calculating the axial strain and stress of the 10^{th} cycle of each loading stage employing equations (3-2) and (3-3):

$$E_{eq} = \frac{\sigma_d}{(\varepsilon_a)_{SA}} \times \frac{1}{10} \tag{3-4}$$

Note that 10 in the denominator is to provide consistent units. To represent the degradation of modulus with shear strain level each E_{eq} is calculated at different strain levels. The hysteretic damping ratio, *h (%)*, of the 10th cycle of each loading stage is also determined from calculating the ratio of the area within the hysteresis loop and the maximum potential energy stored in each cycle of motion, hence based on the parameters defined in section 2.2.2 and using the Standards of the Japanese Geotechnical Society (2000):

$$h = \frac{1}{2\pi} \cdot \frac{\Delta W}{W} \times 100(\%) \tag{3-5}$$

in which ΔW is the damped energy in a single loading cycle, which is defined as the area of the hysteresis loop on the deviator load, P, versus axial displacement, ΔH, curve ($N.cm$), and W is the equivalent elastic energy input in a single cyclic loading, which is defined as:

$$W = \frac{(P_C + P_E)\Delta L}{4}(N.cm) \tag{3-6}$$

Because all loadings were conducted under drained conditions, volume changes were calculated in order to estimate the void ratio after shearing the specimen.

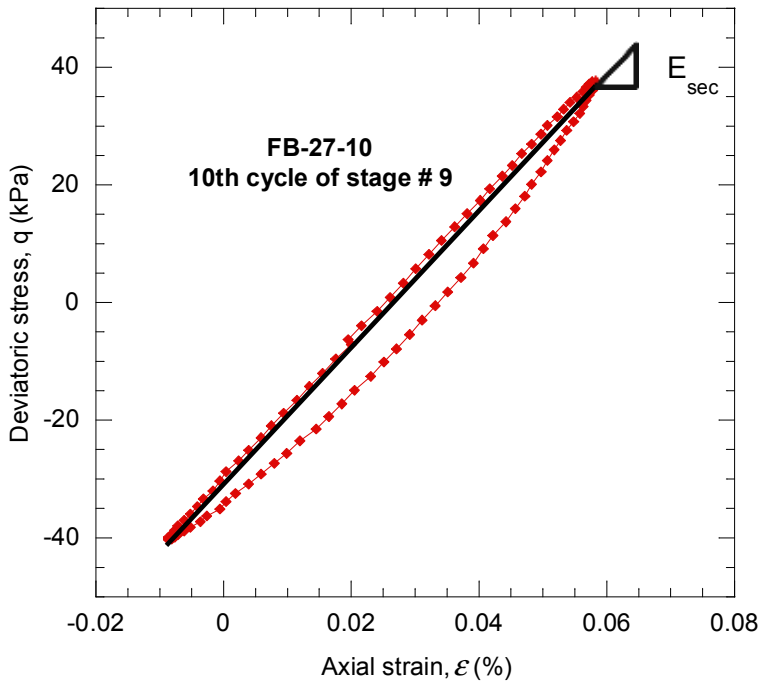

Figure 3-14 Calculation of the Young's modulus for FB-27-10 specimen, 10th cycle of stage number 9

The correct void ratio, e, measurement is crucial in this study as the void ratio is one of the parameters that define the state of soil density. The procedure proposed by Verdugo (1992) was adopted after the loading had been completed in order to determine the void ratio. This method simply involves weighing the materials after the test, rather than calculating the volume by measuring the height and the perimeter dimensions before consolidation. This method is relevant to saturated samples because the void ratio is directly related to the amount of water in the sample.

Following the completion of the testing, the drainage valves were closed and the back pressure released to zero. This was done to make sure no water seeped into or escaped out of the soil sample, and thus retained the same volume throughout the testing. The water level in the burette was lowered as much as possible and was recorded as V_i. The cell was detached from the loading ram, and then small cyclic loads were imposed manually on the vertical rod attached to the top cap as shown in Figure 3-15a. This triggers liquefaction in the specimen and facilitates draining the water upon opening the drainage valves connected to the burette. The drainage valves were opened to release the excess pore water pressure and, when closed, the vertical rod was again manually cyclically-loaded. This procedure was repeated until the burette was full and the level of the water in the burette, V_f, was recorded.

Lastly, the cell pressure was released, the cell water was removed from the triaxial cell, and the cell was dismounted. This enabled the outside of the specimen membrane to be fully dried using paper towels, which soaked up any excess cell water sitting on the specimen membrane. The specimen was then removed and placed in a steel bowl (Figure 3-15b). The top and bottom part of the sample were trimmed using a spatula in case any excess water from around the membrane and O-rings seeped into the specimen. The soil was then placed in a small steel bowl as shown in Figure

3-15c, weighed and, placed in an oven at 102°C to dry for at least 24 hours. This allowed the accurate assessment of the sample water content. The next step was to carefully dismantle the valves whilst the rest of the sample was sitting in the steel bowl. This involved using a water bottle to rinse all the tested soil into the bowl (Figure 3-15d). The primary concern was to ensure that all the tested soil was retained, and not to leave significant amounts sticking to the membrane, top-cap, pedestal, porous stone, etc. The tested soil within the bigger steel bowl was also placed in the oven. Following this, both bowls were weighed, allowing the mass of the dry tested soil to be determined, and the void ratio to be calculated, based on the mass of dry tested soil (m_d), water content, and water (m_w) in the specimen. All reported specimen void ratios for this research were derived using this method.

The void ratio, e, was calculated based on the moisture content and the mass of the soil sample according to the following equations:

$$w = \frac{m_w}{M_s} \qquad (3\text{-}7)$$

$$e = \frac{(V_t + V_f - V_i + w.m_d)}{m_d} \times G_s$$

where V_t is the volume of water lost during the drained test and w is the water content, m_w is the mass of water and M_s the mass of solids.

Figure 3-15 (a) Liquefaction induced by manually loading the specimen, (b) removing the specimen from triaxial cell, (c) trimmed specimen for moisture content calculations, and (d) soil being rinsed into the steel bowl using a water bottle

3.4 Material tested

The experimental study focused on a locally available natural sand material, chosen as representative soil of Christchurch, New Zealand (Rees, 2009). Sand-fines mixtures were formed by mixing sand material (>75μm) with controlled amounts of fines (<75μm). Sandy soils were obtained during field investigations by Rees (2009) from sites in Christchurch, New Zealand. The location of the two sites is shown in Figure 3-16. The sand material was obtained from Fitzgerald Bridge sand (FB) and the fines from Ferrymead (F). Sands used for testing were either clean Fitzgerald sand or clean Fitzgerald sand with 10-30% Ferrymead fines content.

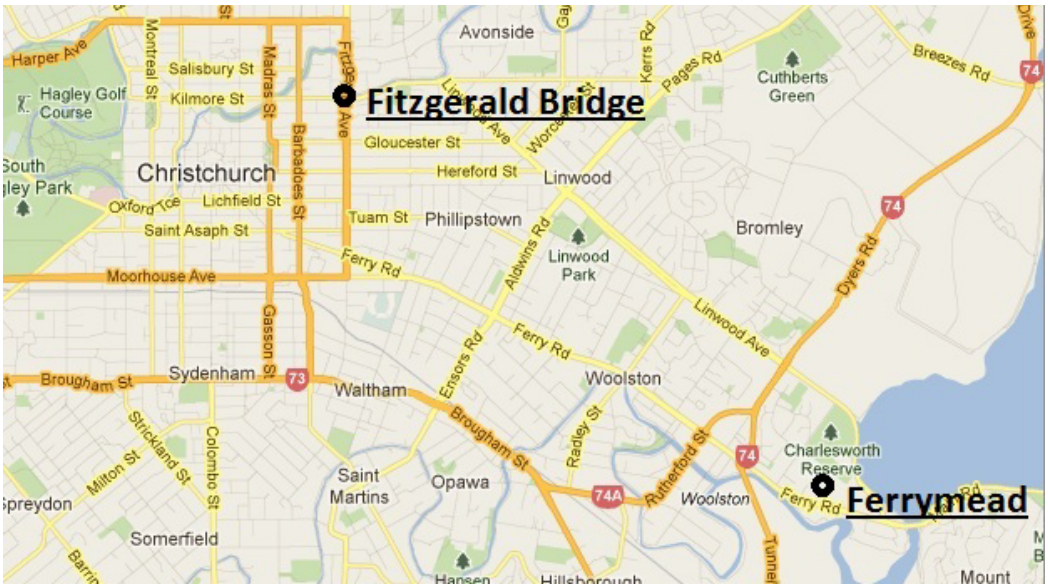

Figure 3-16 Site investigation locations in Christchurch, New Zealand, for the sourced sandy soils (after Rees, 2009, adopted from maps.google.co.nz)

After each test the soil was oven-dried at 102°C and gently ground using a mortar and rubber pestle to return the material to a homogenous state. The grounding was carried out very carefully to avoid any significant loss of fines due to the limited soil

recovered from the Christchurch site investigations (Figure 3-16). Each soil sample was then sieved to ensure the sand and silt proportion for next tests is systematically followed. A detailed description of the sandy and fine soils is given below.

3.4.1 Soil properties

The clean Fitzgerald sand was obtained by dry sieving Fitzgerald Bridge soil (FB). Ferrymead fine (F) was obtained by sieving and collecting the particles smaller than 0.075*mm* of Ferrymead soil. Plasticity tests using Atterberg limits (New Zealand Standard, 1986) were performed on the fines. All tested fines were found to be non-plastic as the plastic limit could not be identified during testing. The fines were silty and separated before they could be rolled into the target diameter required to compute the plastic limit. The clean sand particles, examined with a magnifying glass, were classified as sub-angular to sub-rounded (SA – SR) (Rees, 2009).

Varying fines content were added to the clean sand throughout testing in order to assess the effects of fines on the dynamic properties of sand. Four mixtures named FB-0 (FC = 0%), FB-10 (FC = 10%), FB-20 (FC = 20%) and FB-30 (FC = 30%) were created by mixing different amounts of the FB clean sand and F fines together. The physical properties and the particle size distribution curves of these two soil types are shown in Table 3-1 and Figure 3-17, respectively. These properties were determined based on the New Zealand Standard (New Zealand Standard, 1986), with the British Standard (British standard institution, 1990) used as a guideline for determining the maximum and minimum void ratios e_{max} and e_{min}.

Table 3-1 Properties of tested sandy soils

Soil	FC (%)	ρ_s (t/m^3)	D_{50} (mm)	D_{10} (mm)	e_{max}	e_{min}
FB-0	0	2.65	0.168	0.089	0.935	0.628
FB-10	10	-	-	-	0.908	0.579
FB-20	20	-	-	-	0.882	0.528
FB-30	30	-	-	-	0.855	0.427
F fines	100	2.65	0.016	-	-	-

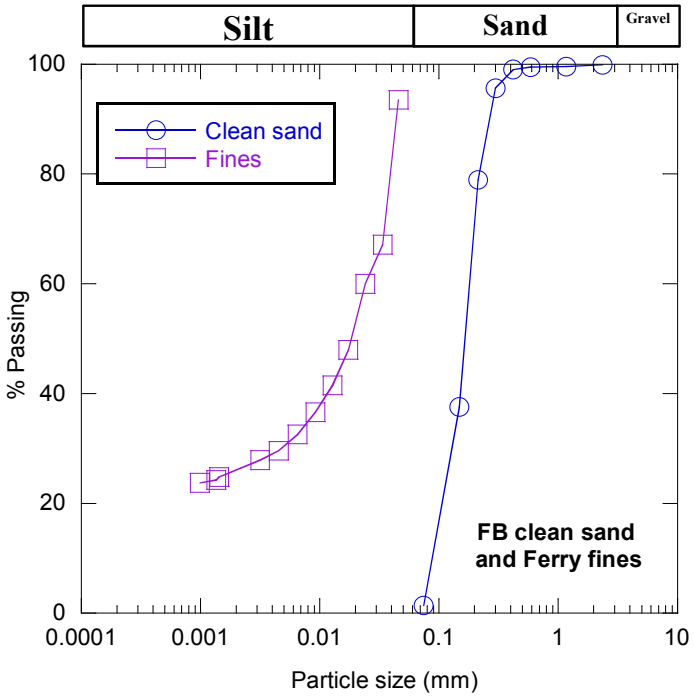

Figure 3-17 Particle size distribution of the Fitzgerald Bridge clean sand and Ferry fines component (after Rees, 2009)

The maximum void ratios, e_{max}, were measured following the British Standard by first covering the opening of a graduated cylinder (full of soil) with a piece of plastic, then turning it upside down very slowly, and measuring the volume. The minimum void ratios e_{min} were measured using a variation of the British Standard procedure as suggested by Rees (2009). The primary variation was that the soils were compacted under dry conditions on a shaking table, rather than saturated under water in order to retain as much fines as possible.

3.4.2 Test information

In Table 3-2, specific labelling and identification of the drained tests performed in this study is listed together with the information about the initial states of the samples. The reported void ratios and relative densities are computed based on the method proposed by Verdugo (1992) and after consolidation has finished.

Table 3-2 Summary of drained triaxial tests on Fitzgerald sand

Test No.	Fines content (%)	*e*	D_r *(%)*
FB-1	0	0.826	35.5
FB-2	10	0.777	39.8
FB-3	20	0.737	41
FB-4	30	0.662	45.1
FB-5	0	0.768	54.4
FB-6	10	0.745	49.5
FB-7	20	0.681	56.7
FB-8	0	0.799	44.2

FB-9	10	0.766	43.1
FB-10	20	0.726	44.1
FB-12	0	0.732	66.1
FB-13	10	0.687	67.2
FB-15	20	0.649	65.8
FB-16	30	0.573	65.8
FB-17	0	0.710	73.3
FB-18	10	0.595	95.1
FB-19	20	0.585	83.9
FB-20	0	0.689	80
FB-21	10	0.643	80.4
FB-22	20	0.589	82.8
FB-23	30	0.483	87
FB-25	0	0.674	85.2
FB-26	10	0.658	76
FB-27	10	0.720	57.1

3.5 Summary

This chapter outlined the employed testing procedures using a dynamic triaxial testing apparatus and associated bender element devices for the measurement of dynamic soil properties at low to high strain levels. The properties of the material tested for this purpose were also provided. This chapter also explained the adopted procedures for the preparation of the test specimens, the testing schemes, test measurements and key characteristics of the apparatus/devices. Finally, the general properties of each specimen prepared for testing were summarized in Table 3-2.

4 Effects of fines on shear modulus and damping of sands

4.1 Introduction

The Fitzgerald Bridge (FB) clean sand with Ferrymead (F) fines, as described in Chapter 3, were tested under drained cyclic loading conditions using a dynamic triaxial (TX) apparatus and bender element device (BE). Same soil materials have been tested by Rees (2009) under undrained conditions. The 2009 study comprised undrained monotonic and cyclic triaxial tests, and the effects of fines content on the steady state and cyclic resistance of the tested materials were scrutinized in detail.

The specimens in this study were tested at different void ratios (relative densities) and shear strain levels under drained conditions. At each void ratio (relative density) and shear strain level, the deformation properties were measured using TX and BE methods. The fines were systematically added to FB clean sand up to a maximum of FC = 30%. This range of fines content ensures that the mechanical properties of such soil is dominated by the sand-matrix and the evaluation of effects of fines can be made with reference to the clean FB sand behaviour. Figure 4-1 shows the variation of void ratios and fines contents of the tested samples of FB sand. Although, density changes during triaxial tests for dense specimens were negligible; for loose samples, the void ratio and relative density could vary up to 0.03 and 10% respectively.

It is well known that mechanical properties of sands are significantly influenced by the density of sand (e.g. Hardin, 1978, Ishihara, 1996). Therefore, it is desirable to compare the behaviour of the clean and fines-containing sands at identical density states. However, the identification of this identical density state is deemed difficult as

different density measures (e.g. void ratio, e, relative density, D_r, intergranular void ratio, e_g, equivalent granular void ratio, e^*, and state parameter, ψ) used in the evaluation of effects of fines on sand behaviour, may lead to different trends in behaviour (e.g. Cubrinovski et al., 2010). Therefore, establishing a proper basis for comparison of the behaviour of clean sand and sand with fines content can be problematic.

In this chapter, two widely used density state parameters i.e. void ratio, e, and relative density, D_r, were first chosen to evaluate and compare the deformation properties of sand for four levels of fines content and similar density states. Further, equivalent granular void ratio, e^*, is employed in Chapter 5 to evaluate the effects of fines. In this study, the void ratio and the relative density are defined as:

Void ratio-*e*:

$$e = \frac{V_v}{V_s} \tag{4-1}$$

where V_v and V_s are the volume of void space and the volume of solid particles, respectively.

Relative density, D_r:

$$D_r = \frac{e_{\max} - e}{e_{\max} - e_{\min}} \times 100(\%) \tag{4-2}$$

where e is measured at initial state after the consolidation and e_{max} and e_{min} are the maximum and minimum void ratios of the assumed soil, respectively. The e_{max} and e_{min} values for each set of FB sand with different fines content were listed in Table 3-

1. Note that when using e and D_r, no distinction is made between the proportion of sand and fine particles in terms occupied volume.

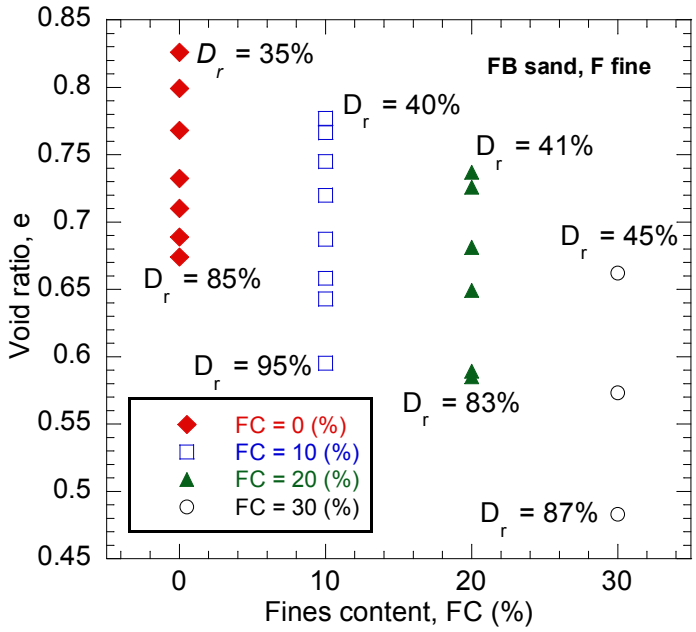

Figure 4-1 Void ratio and fines content of the tested samples

It has been previously documented that a threshold strain exists below which deformation properties are independent of the shear strain amplitude for soils subjected to cyclic loading (e.g. Hardin and Drnevich, 1972b). If soils are cycled at strains greater than the threshold strain, deformation properties of soils exhibit nonlinear behaviour. The threshold strain is commonly assumed to be about 0.001% for sandy soils (e.g. Hardin, 1978). Strains below the threshold strain are termed low-amplitude strains, and the mechanical properties measured at these strain levels are called small-strain moduli and damping ratios. Bender elements can generate stress waves inducing very small strains ($\gamma < 0.0001\%$) which makes them suitable to perform the small-strain tests for the measurement of the small-strain shear modulus (e.g. Brignoli et al., 1996, Leong et al., 2005). On the other hand, triaxial tests can

accurately measure the stress-strain behaviour under cyclic loading and using the stress-strain curves, one can then define the high-strain modulus and damping curves. In this chapter, the results of both small-strain and moderate- to large-strain measurements are presented for FB soils. The effects of fines on the modulus and damping properties are discussed using void ratio and relative density as initial state parameters. The chapter will conclude with comparisons of modulus reduction and damping curves measured for the FB sand in this study with the others found in the literature.

4.2 Shear wave velocity and maximum shear modulus of FB soils

The bender element device offers the opportunity to investigate stiffness properties of granular materials at very small strains. The small-strain stiffness properties of soils are critical for geotechnical earthquake engineering problems because they define the starting point of degradation curves. Therefore, prior to dynamic triaxial testing, each specimen was subjected to a sinusoidal shear wave excitation with varying frequencies by means of bender elements at the top and bottom of the sample. The frequencies were varied so that a resonance frequency could be determined. The test specimens were prepared using the procedures described in Chapter 3, producing samples with a wide range of fines content and densities as shown in Figure 4-1. The effects of density and fines content on the shear wave velocity measured by bender elements are first discussed in the following subsections. Finally, the small-strain or maximum shear modulus, G_{max}, is estimated using the shear wave velocity and soil density.

4.2.1 Effects of density

It is well known that shear wave velocity of sands is controlled by the grain-to-grain contacts, which in turn depend on the relative density, effective stress state, arrangement of particles and cementation, among others (e.g. Hardin, 1978). The effects of density were therefore investigated for the FB sandy soils. Table 4-1 presents the density range considered for the FB test specimens. The minimum and maximum achieved densities, along with the mid-range, are used to discuss the effects of density on the shear wave velocity of the four FB soils with different fines contents. The details of how shear wave velocity was computed using the measured wave travel time and the distance between the transmitter and receiver platelets are explained in Chapter 3.

Table 4-1 Density ranges of the tested FB soil specimens

Soil	Void ratio range	Relative density range
FB-0	e = 0.674 – 0.826	D_r = 85.2 – 35.5 %
FB-10	e = 0.595 – 0.777	D_r = 95.1 - 39.8 %
FB-20	e = 0.585 – 0.737	D_r = 83.9 – 41 %
FB-30	e = 0.483 – 0.662	D_r = 87 – 45.1 %

The shear wave velocity, V_s, versus void ratio relationships of the four FB sandy soils are presented in Figure 4-2. The observed trends show a typical reduction of the shear wave velocity with either an increase of the void ratio or a corresponding decrease of density. All specimens are tested under an effective confining pressure of 100 kPa. Power relationships ($V_s = A \, . \, e^{-x}$) are assumed to exist for the correlations

(Jamiolkowski 1991). The high value of correlation coefficients ($R^2 > 0.91$) illustrates the good fit between V_s and void ratio assuming a power relationship. Linear relationships (V_s = a + b. e) have also been suggested by others (e.g. Thevanayagam and Liang, 2001) which results in slightly improved trends and correlation coefficients, but since using power function allows to represent the maximum shear modulus, G_{max}, in the same functional form as V_s, this form is adopted herein.

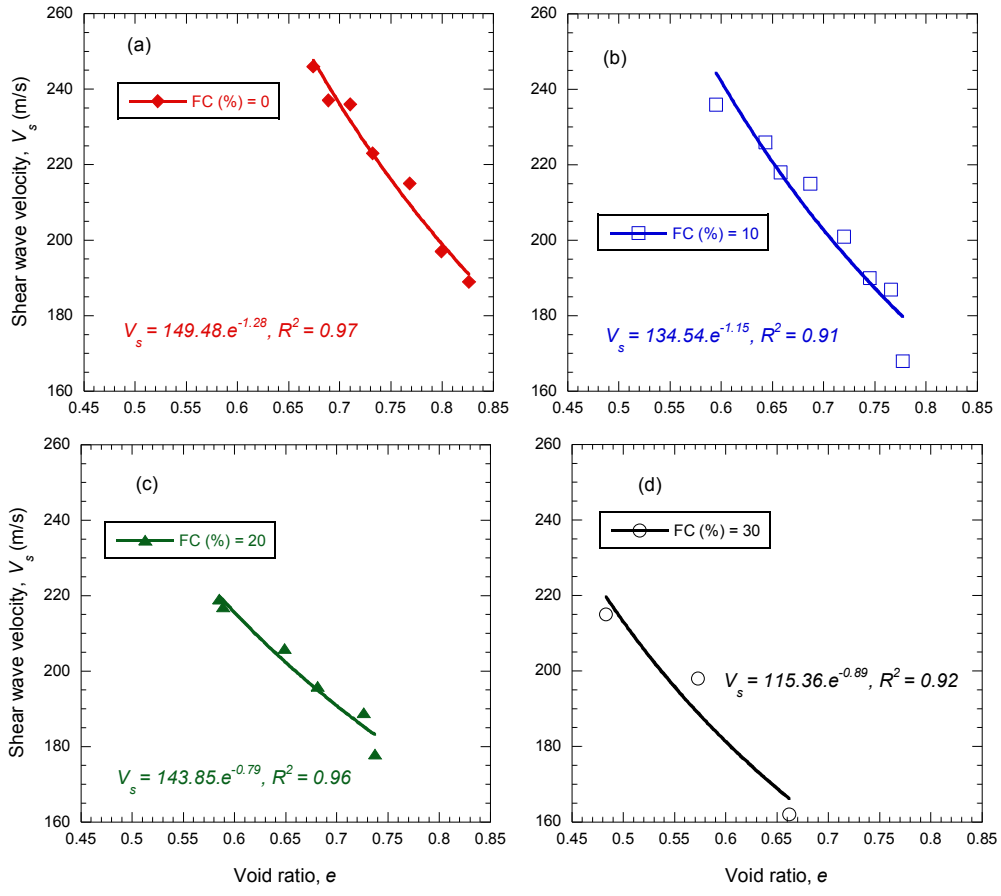

Figure 4-2 V_s vs void ratio curves for FB-0, FB-10, FB-20, and FB-30 specimens tested using bender elements under effective confining pressure of 100 kPa

Shear wave velocities versus relative densities observed in the tests of the four FB soils are also presented in Figure 4-3. Again these curves clearly show that

increased soil density results in a higher shear wave velocity, and a linear equation can accurately describe the V_s-D_r relationship. The linear equations fit to the data points and the corresponding linear coefficients are presented in each plot.

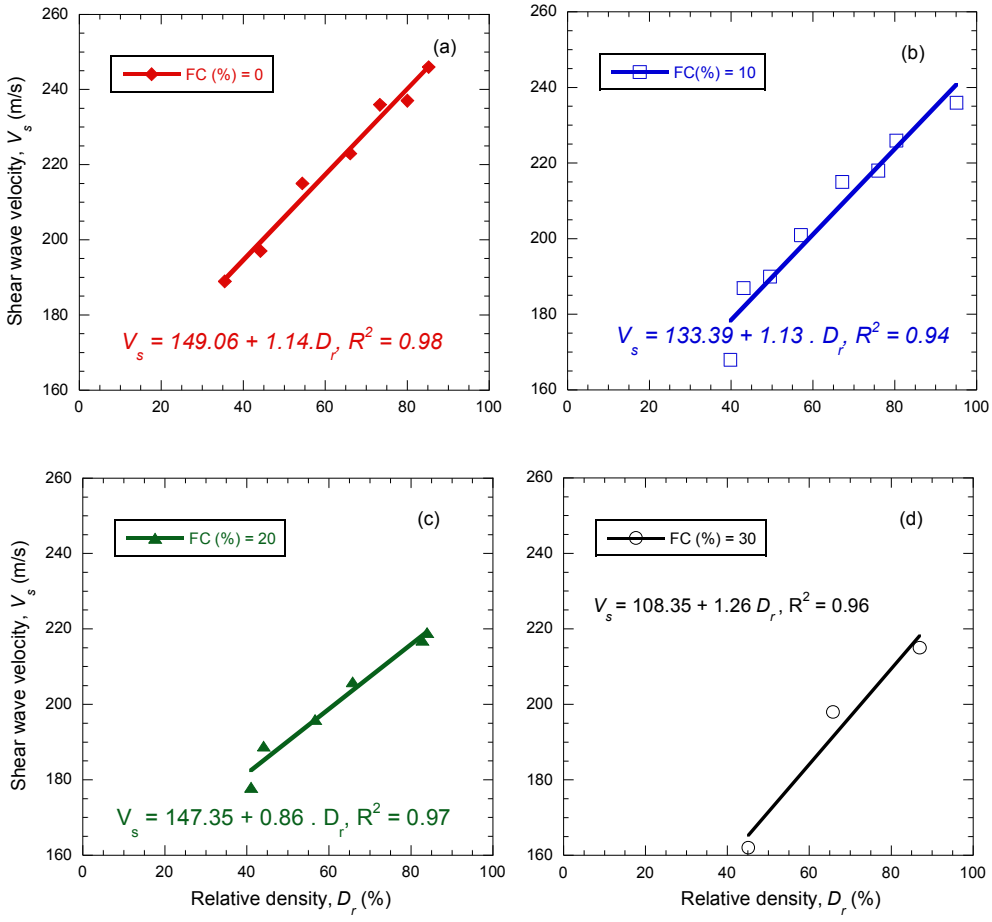

Figure 4-3 Shear wave velocity versus relative density curves for four FB-0, FB-10, FB-20, and FB-30 specimens tested using bender elements

4.2.2 Effects of fines content on the shear wave velocity of FB soils

The influence of fines content on the mechanical behaviour of sandy soils is less understood than the effects of changing density. To investigate such effects, the V_s-e and V_s-D_r curves are comparatively plotted for sands with different fines content. Figure 4-4 compares the V_s-e curves of the FB clean sands and three FB mixtures with different fines content (FB10, FB20, and FB30). It is clear that at identical void ratio

values, the shear wave velocity decreases as the fines content of the sands are increased. For instance, the measured V_s is about 215m/s for the dense FB-30 soil at $e = 0.483$ whereas V_s has about the same value for FB clean sand at a void ratio of $e = 0.768$. Another illustration of this trend is that, for example, at $e = 0.65$ the shear wave velocity is 220, 200, and, 170m/s for FB-10, FB-20 and, FB-30 clearly showing decrease in V_s with an increasing fines content. This trend can be explained with reference to the binary packing illustration presented in section 2.3. By definition, at a given void ratio, clean sands and fines-containing sands have identical ratios of volumes of voids and solids. However, a proportion of finer particles which is trapped between the coarse particles may not participate in the transfer of shear load and therefore act as void space. Smaller solid volume contributing to the force transfer, results in lower shear wave velocity of the specimen.

A similar trend is illustrated in Figure 4-5 where relationships between the relative density and V_s are shown for FB-0, FB-10, FB-20 and, FB-30. The accuracy of this plot is affected by the uncertainty in the values of e_{max} and the e_{min} for fines containing sands which introduces an additional error in the values of D_r. However, the general trend again indicates that shear wave velocities for silty soil is smaller than the respective value for clean sand at the same D_r. For example, at $D_r = 60\%$, the measured V_s is about 215m/s for the FB-0 soil whereas V_s is 185m/s for FB-30.

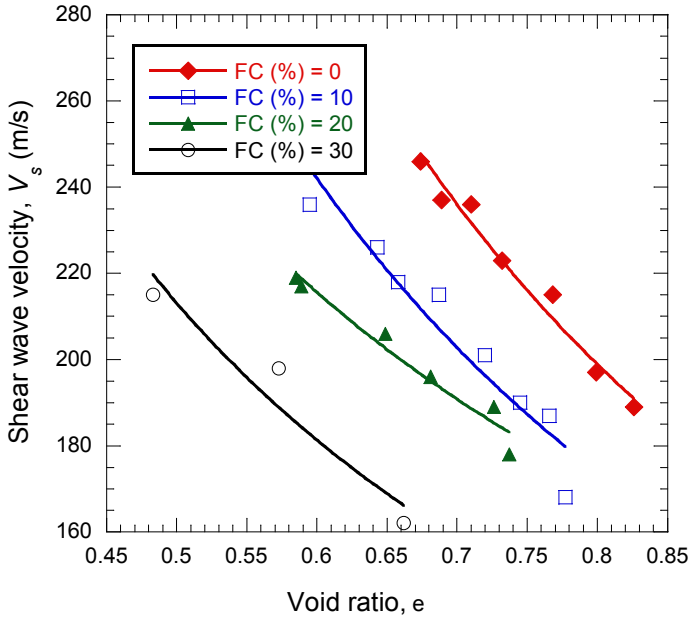

Figure 4-4 V_s versus void ratio curves of four percentages of fines content

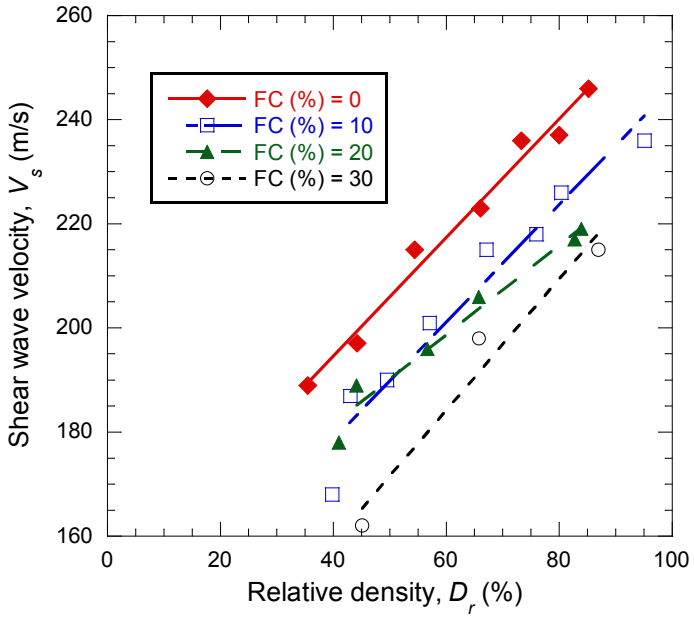

Figure 4-5 Relationship between the shear wave velocity and relative density of FB soils with different fines content

4.2.3 Evaluation of the maximum shear modulus

The shear modulus at small strains is referred to as the small-strain or maximum shear modulus, G_{max}, which is related to the shear wave velocity V_s by the equation: $G_{max} = \rho.V_s^2$; where ρ is the density of the soil sample. Figure 4-6 presents the $G_{max} - e$ data points assuming the total density of each soil specimen. The dashed lines in this figure represent the power function fits using regression through the data points. It was explained in Chapter 2 that a modified density can be employed in this equation in lieu of total soil density in order to estimate G_{max}. In this study, the tortuosity, α–factor, was calculated using Berryman's (1981) equation which results in similar values to Gajo (1997) formulation. The shear wave velocities illustrated in the previous sections were then converted to shear moduli using the calculated modified densities. The solid lines in Figure 4-6 represent the G_{max}-e relationships using the modified densities of soil. The reduction of the modified G_{max} compared to the original G_{max} was within the range of 4 – 14%.

Further, Figure 4-6 presents the maximum shear moduli, G_{max}, versus void ratio curves of the four FB sandy soils best fitted to different power equations as suggested by Jamiolkowski et al. (1991) and Thevanayagam and Liang (2001). Similarly high R^2 values to the V_s - e correlations are found for the G_{max} - e relationships.

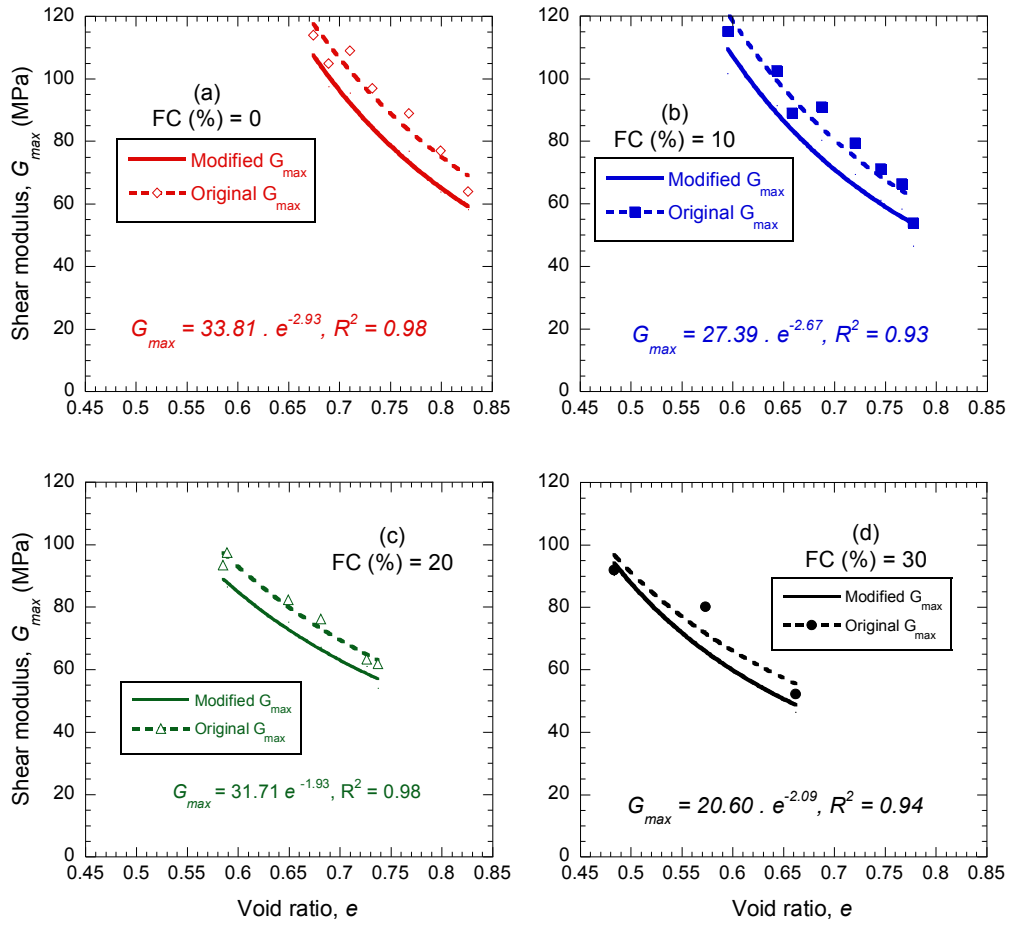

Figure 4-6 G_{max} vs void ratio curves for FB-0, FB-10, FB-20, and FB-30 specimens

4.2.4 Effects of fines on the FB shear moduli

It has been discussed and shown in section 4.2.2 that changing the fines content of sand affects the shear wave velocity of the sand. Likewise, when comparing maximum shear modulus at a similar initial density state, the FB soils with higher fines contents displayed lower G_{max} values. Figure 4-7a presents the maximum shear moduli of the four sets of FB soils using the void ratio as the measures of the density state. Again, the silty sand specimens show lower G_{max} values when compared with clean sands at the same global void ratio e, meaning that a proportion of silt in the sand matrix may not actively participate in the inter-granular friction forces.

Consequently, this introduces a difficulty in applying the Jamiolkowski et al. (1991) equation as a predictive tool for G_{max} of fines containing sands in the laboratory. However, some researchers (e.g. Iwasaki and Tatsuoka, 1977, Wichtmann and Triantafyllidis, 2010) have quantified this effect by multiplying the G_{max} value of clean sand by a reduction factor which is calculated based on a back analysis process in which individual G_{max} values for each fines content need to be measured in advance.

$$G_{\max} = B.f(e) \tag{4-3}$$

where B is the scaling factor for G_{max} of clean sand to approximate G_{max} for sand with fines and $f(e)$ is the functional form for the void ratio. It is clear that this reduction factor decreases with the increase in the content of fine particles. Furthermore, G_{max} tends to generally increase proportionally with the density increase (e.g. Baldi et al., 1988, Robertson and Campanella, 1983), this behaviour is highlighted in Figure 4-7b.

In Figure 4-8a,b the G_{max}-values for a similar void ratio $e = 0.66$ and similar relative densities are plotted versus fines content, respectively. Figure 4-8c shows the variation of the normalized maximum shear modulus with respect to fines content. It is evident that G_{max} values of sand with a fines content of 10% can amount up to 80% of the values of clean sand, measured for the same void ratio as shown in Figure 4-8a. However, the general prediction with relative density seems less accurate as e_{max} and e_{min} values for fines containing sand are uncertain (Figure 4.7b and Figure 4-8c). Moreover, there is some uncertainty around the calculated modulus at low relative densities and when these results are normalized with respect to G_{max} (e.g. Figure 4-8c) some specimens may not follow the general trend. Overall, these figures clearly indicate that it is misleading to estimate soil mechanical properties including V_s and

G_{max}, based on density measures such as e or D_r, without taking into account the effects of grain size distribution, especially fines content.

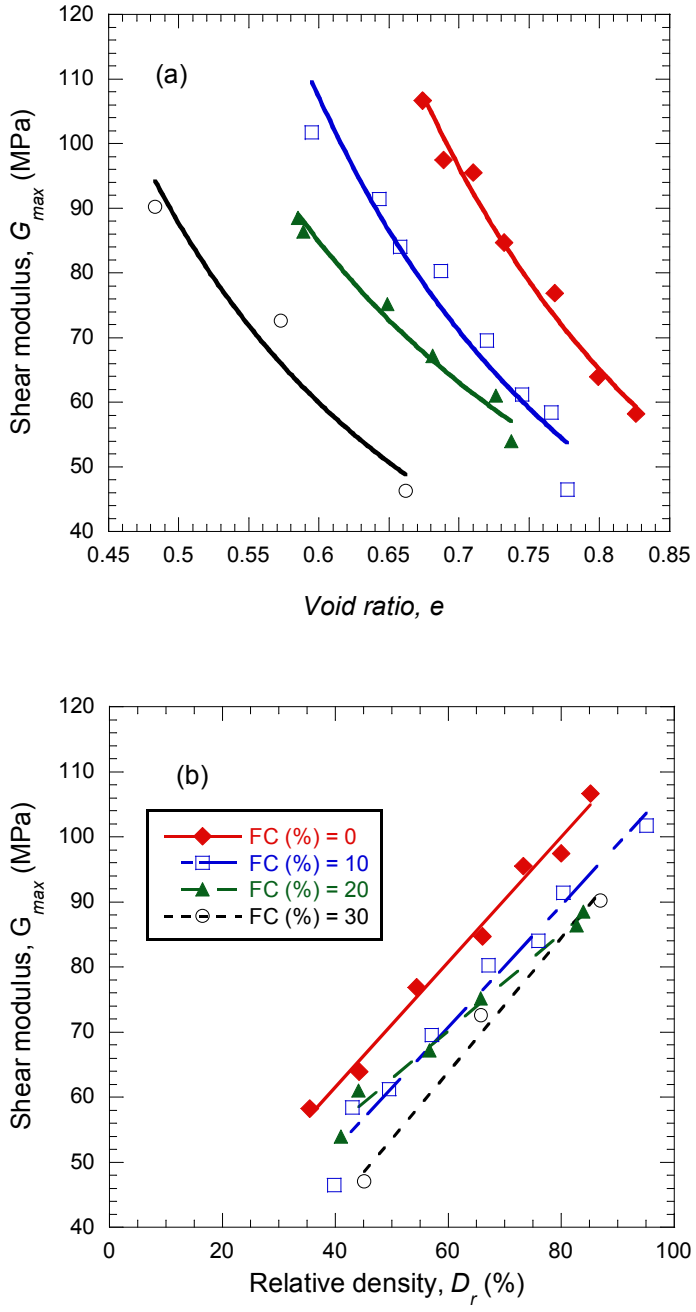

Figure 4-7 Maximum shear moduli versus (a) void ratio, (b) Relative density, relationships for FB soils with different fines content

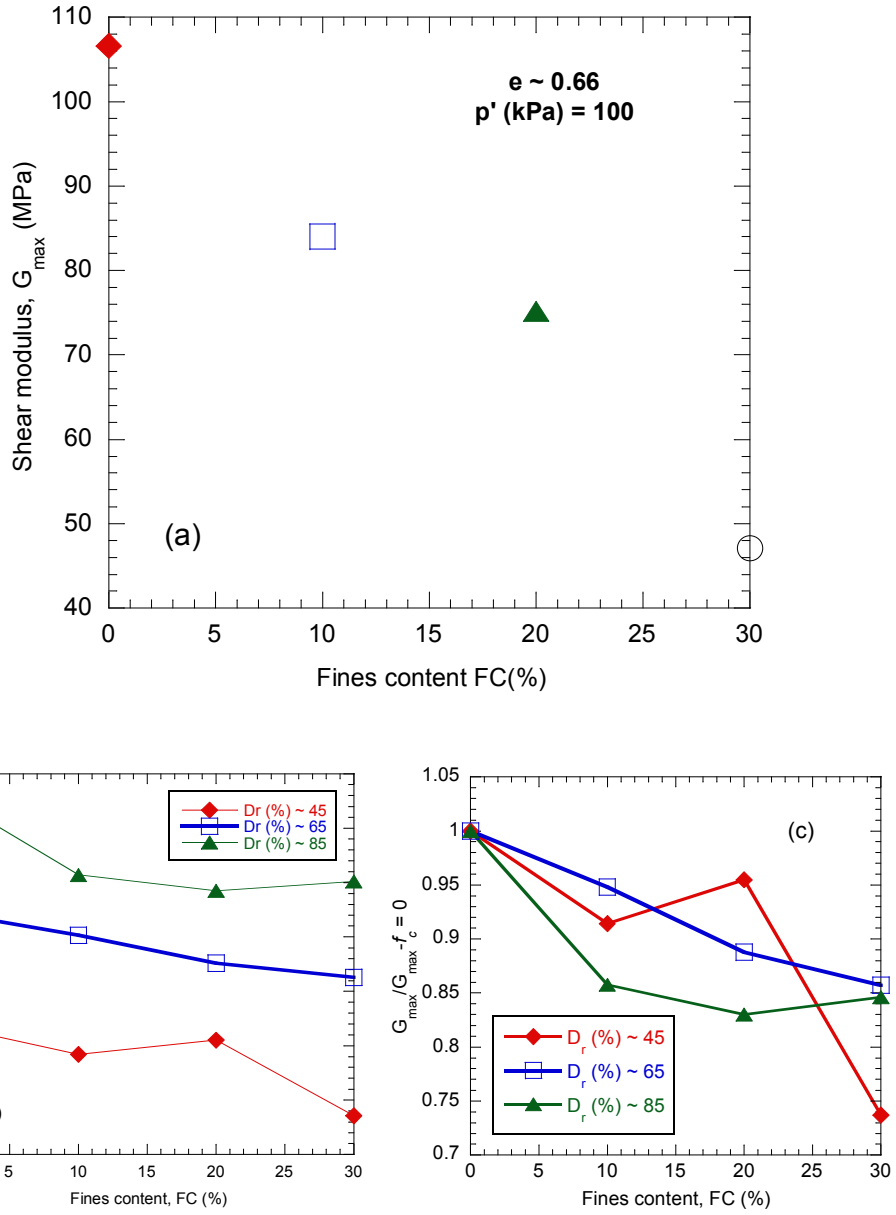

Figure 4-8 General decrease of G_{max} with increasing fines content, (a) for similar void ratio $e = 0.66$, (b) for similar relative densities and, (c) Variation of normalized maximum shear modulus, $\frac{G_{\max}}{G_{\max}@\ FC(\%) = 0}$, vs fines content

4.3 Nonlinear deformational properties of FB soil

After conducting the shear wave velocity tests on each specimen, cyclic triaxial tests were performed on the FB sandy soils to investigate the effects of fines on the drained nonlinear modulus and damping properties of sand-fines mixtures. The test specimens were loaded in a stress-controlled manner at a frequency of 0.1 Hz. An equal amplitude deviator stress (q) in both compression and extension was applied, centring the symmetric loading around $q = 0$ kPa. Young's modulus reduction and damping curves were calculated based on the procedures explained in Chapter 3. Density effects and the effects of fines content on the modulus reduction and damping curves of FB sand mixtures are discussed in the following sections.

4.3.1 Stress-strain response curves

Stress-controlled tests were performed in this investigation of FB sand. This section describes the drained cyclic triaxial test results in terms of stress-strain hysteresis loops. The sample is first subjected isotropically to an effective confining stress of 100 kPa, and then a cyclic axial stress which is induced by the vertical ram at the top of the sample is introduced. Because the sample is drained, there is no change in pore water pressure.

Stress-strain responses of the two FB sandy soils with FC = 0% and FC = 30% are presented in Figure 4-9 and Figure 4-10, respectively. It is observed that using internal load cell along with the gap sensor results in reasonably smooth hysteresis loops. It is shown that while the applied cyclic stresses are kept constant, there is a different maximum and minimum value of axial strains achieved in each cycle. With the completion of each cycle, a resulting accumulated axial strain or residual strain is created. After several cycles, there is a decreasing effect of subsequent cycling on the

residual strain. Hence in case the residual strain is accumulated, the relative density may change with the progressive increase in the cyclic amplitudes.

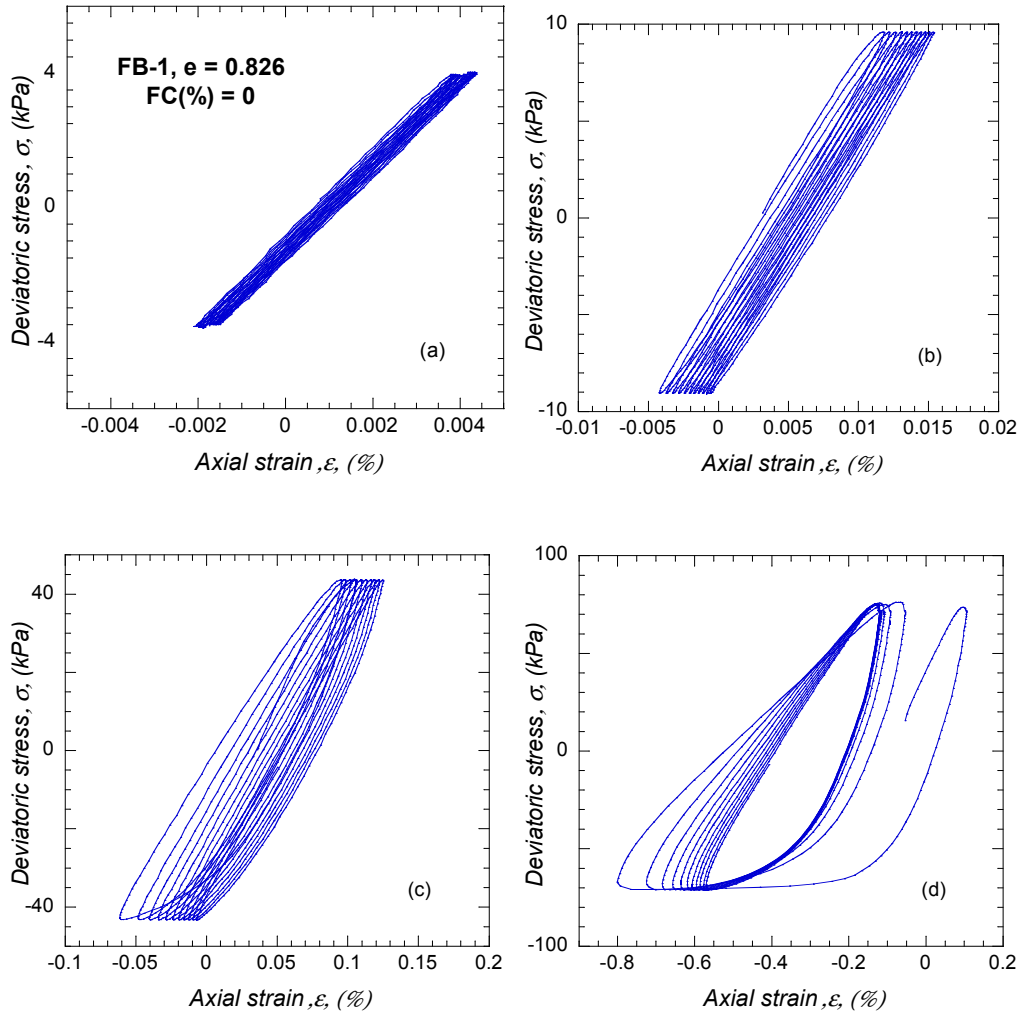

Figure 4-9 Stress-strain curves of FB-1 specimen with FC(%) = 0

The observed responses show that with increasing strains the area of the stress-strain loops increases whereas the slope of each loop tend to decrease. As was explained in Chapter 3, the 10th cycle at each loading stage was used to derive the modulus and damping values. The equivalent Young's modulus was determined from the slope of the line that connects the peak points of the 10th hysteresis loop. Kokusho (1980) showed negligible effect of number of cycles on the modulus of clean Toyoura

sand. The hysteretic damping ratio is also assessed from calculating the ratio of the area within the hysteresis loop and the maximum potential energy stored in each cycle. In this study, soil properties have all been determined for the 10th stress-strain cycles.

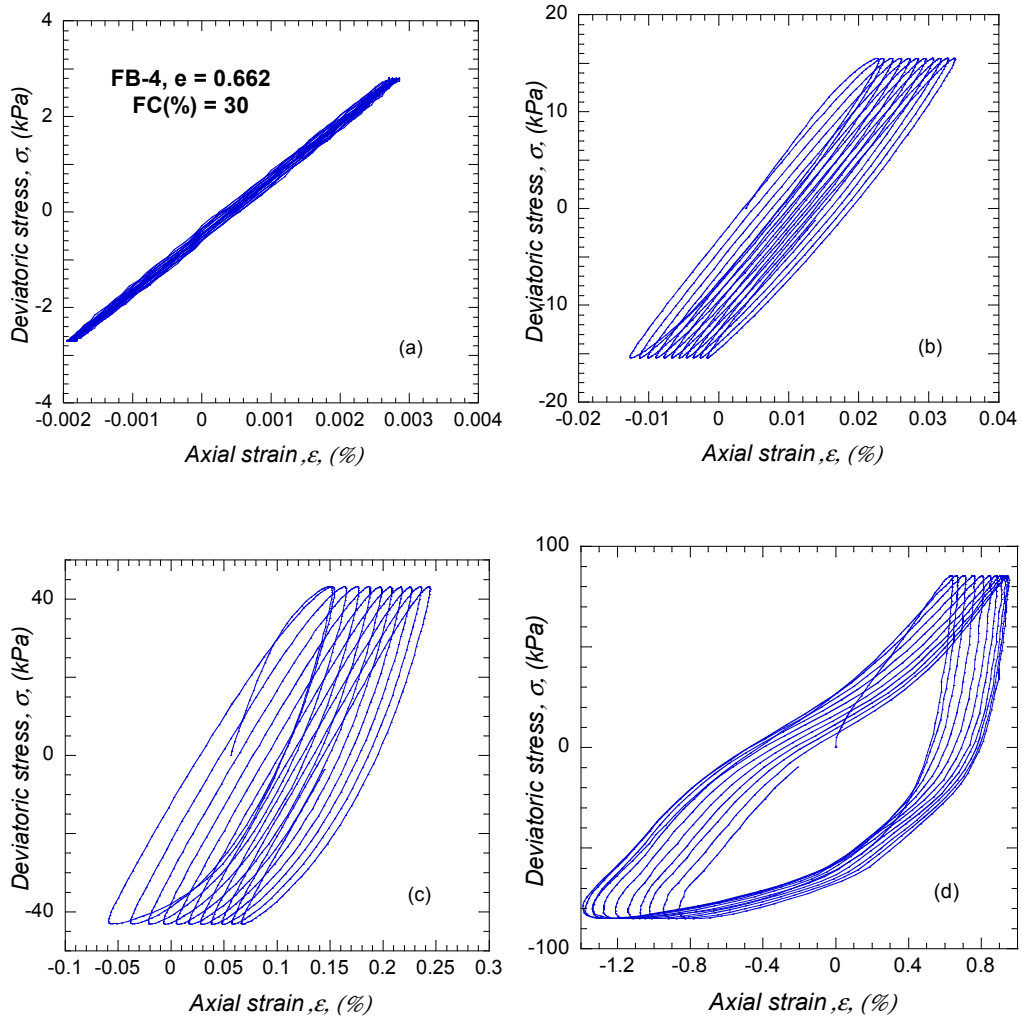

Figure 4-10 Stress-strain curve of FB-4 specimen with FC(%) = 30

4.3.2 Modulus reduction curves

In the case of dynamic loading, the secant Young's modulus is normally approximated over a cycle of loading at a given strain amplitude as explained in Chapter 3. The slope of the line that connects the end points of the generated

hysteresis loop represents the average axial stiffness of the soil, or the secant Young's modulus. For instance, Figure 4-11 depicts the hysteresis loop and the corresponding secant Young's modulus for the 10th cycle of the stage No. 9 loading for the specimen FB-27-10, which is associated to a deviatoric stress level of *40* kPa. The secant Young's modulus decreases with increasing strain amplitude. The relationship between the Young's modulus and the axial strain is called the Young's modulus reduction curve in this thesis.

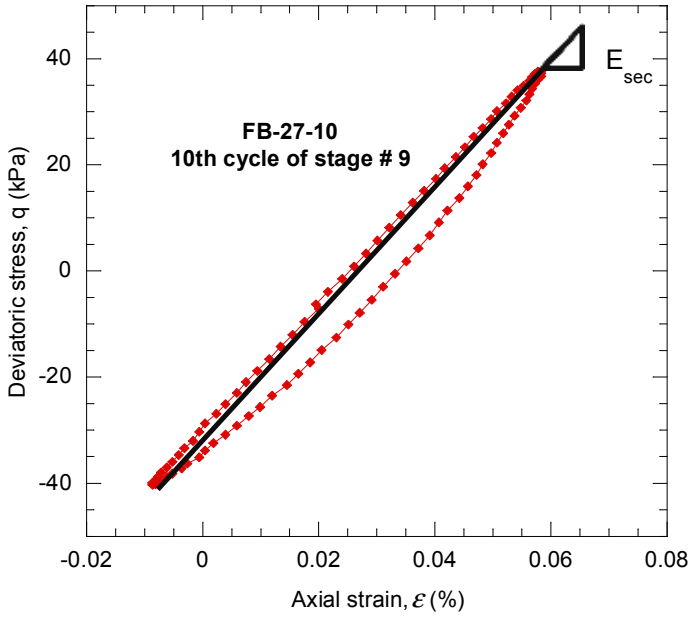

Figure 4-11 Hysteresis loop for FB-27-10 specimen, 10th cycle of stage # 9

4.3.2.1 Effects of density on the modulus reduction curves of FB soils

As discussed in section 4.2.3, for the maximum shear modulus, an increase in soil density results in an increase in soil stiffness. Comparable trends were also expected and observed during the nonlinear cyclic triaxial tests of the FB soils. To illustrate this, the Young's modulus reduction curves of the FB soils with different fines content are compared across varying specimen densities in Figure 4-13. In all tests,

the effective confining pressure was kept constant at $\sigma' = 100\ kPa$ which allows a response comparison at similar loading conditions for samples with different densities and fines content. The reduction curves of several tested specimens of each soil are shown, with the reported density and fines content. The general trend shows that the denser specimens exhibit higher stiffness for strains less than $\varepsilon \sim 0.3\%$ above which soils with different void ratios follow the same pattern.

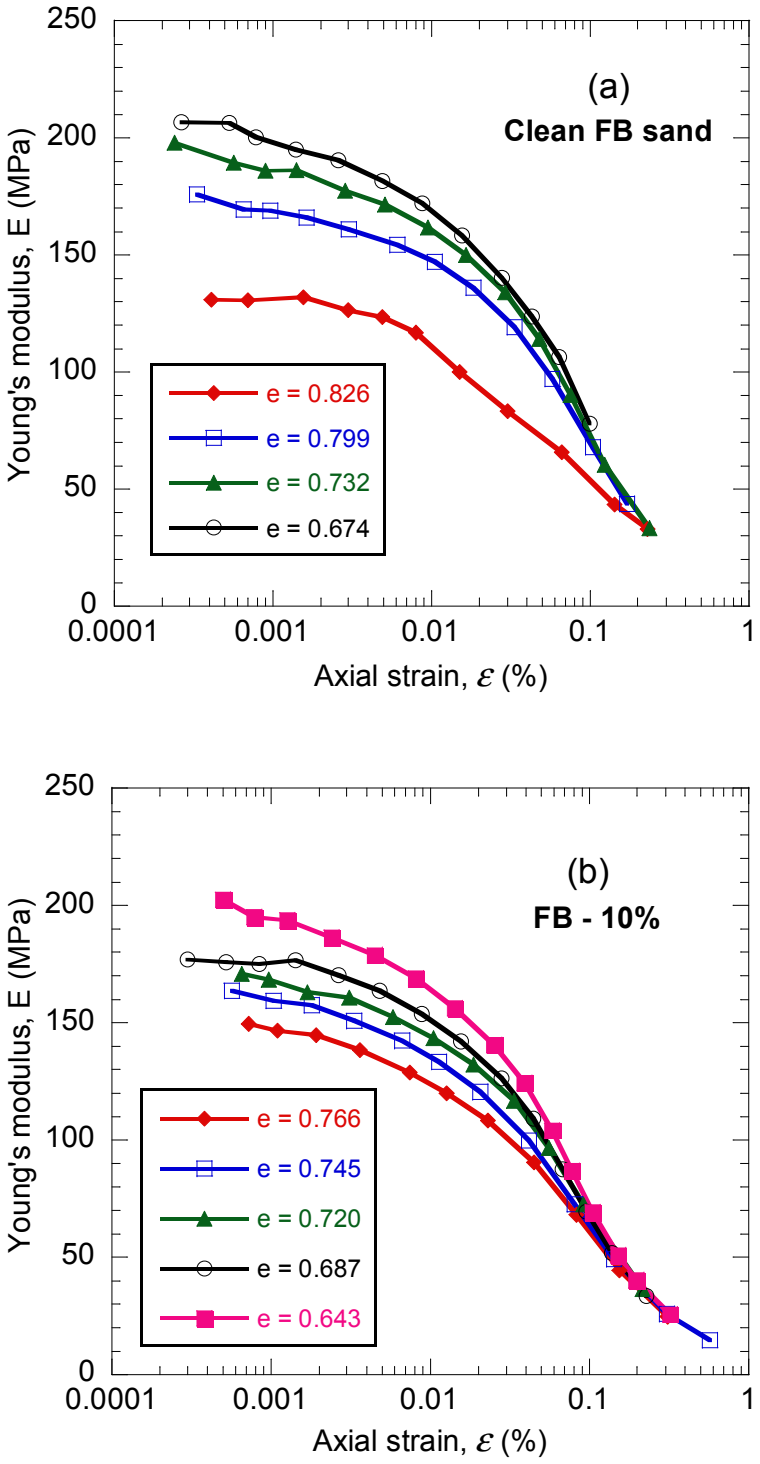

Figure 4-12 Young's modulus reduction curves of FB test specimens with varying fines content (a) FC(%) = 0; and (b) FC(%) = 10

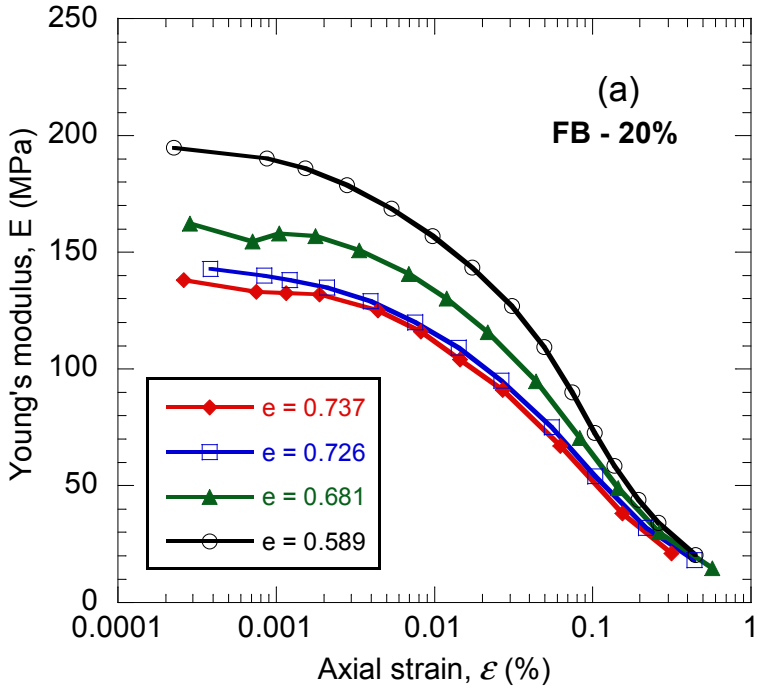

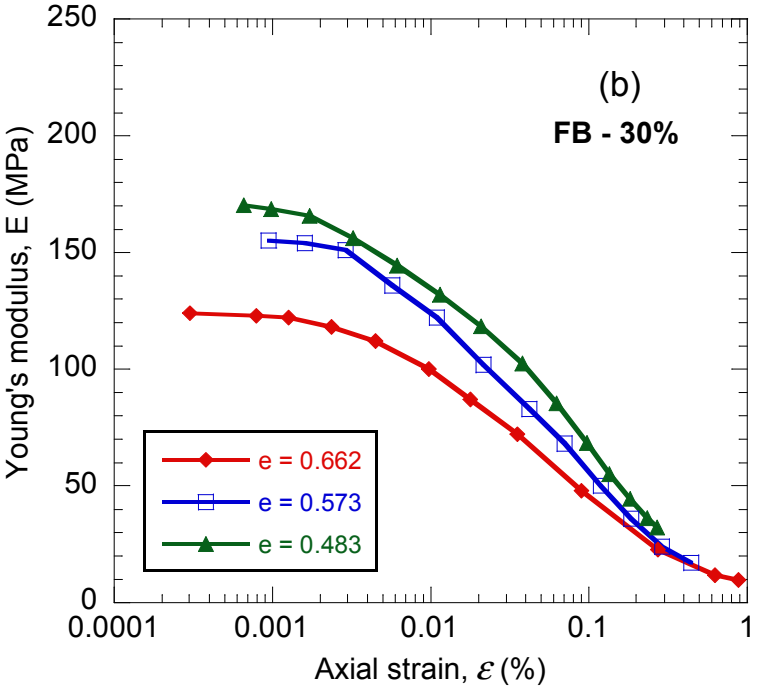

Figure 4-13 Young's modulus reduction curves of FB test specimens with varying fines content (a) FC(%) = 20; and (b) FC(%) = 30

4.3.2.2 Effects of fines on the modulus reduction curves of FB soils

Variation of the fines content of the FB sands was shown in section 4.2.4 to affect the maximum shear modulus. Likewise, it is expected that the fines content has a similar effect on the modulus reduction curves of the FB soils. It was shown in Figure 4-1 that limited values of identical void ratio could be targeted in the preparation of sands with different fines content; this identical void ratio was around $e \sim 0.66$. Figure 4-14 displays the Young's modulus reduction curves of FB soils at the similar void ratio ($e \sim 0.66$). It is clear that the modulus reduction curves of the FB soils with higher fines content have smaller E over a wide range of strains.

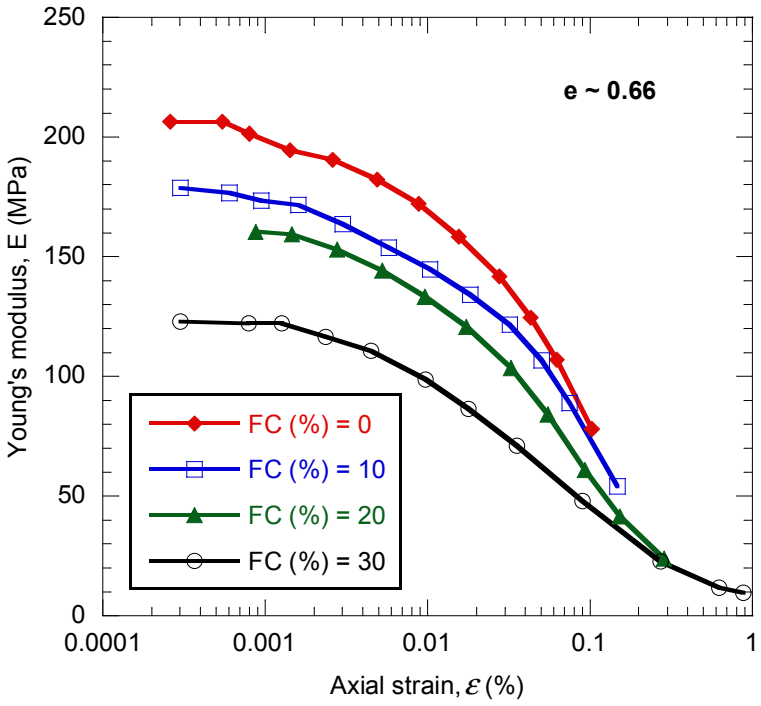

Figure 4-14 Young's modulus reduction curves of FB test specimens with varying fines content at void ratio $e \sim 0.66$

Three different D_r values have also been used to compare the modulus reduction curves of the FB soils – D_r = 45%, 65%, 85%. Note that at a given relative density, the modulus reduction curves for sands with higher fines content have in general

lower secant moduli (Figure 4-15a). Figure 4-15b also shows that the reduction of Young's modulus due to an increase in fines content is dependent to the strain amplitude range ε = 0.001-0.1%. For instance, the Young's modulus of the sand with FC = 30%, is 60-70% is lower than the Young's modulus of clean sand.

As shown in Figure 4-17a, the similarity of the modulus reduction curves for FB soil with FC = 20 and 30% at the relative density of 85% might be due to the uncertainty associated with measuring the maximum and minimum void ratios of silty sands. The G_{max} values of sands with different fines content compared at similar relative densities also showed slight discrepancy. However, the general observed trend means that, for a given density, the FB soils with lower fines contents will have higher stiffness for strains up to ε = 0.3%. Note these were the same effects discussed in section 4.2.4 when comparing the effects of fines on the shear wave velocity of the FB soils. This means that when using void ratio or relative density to characterize the density state of the FB soils, the effects of fines on the shear wave velocity and secant Young's modulus are similar – higher fines content correspond to lower stiffness.

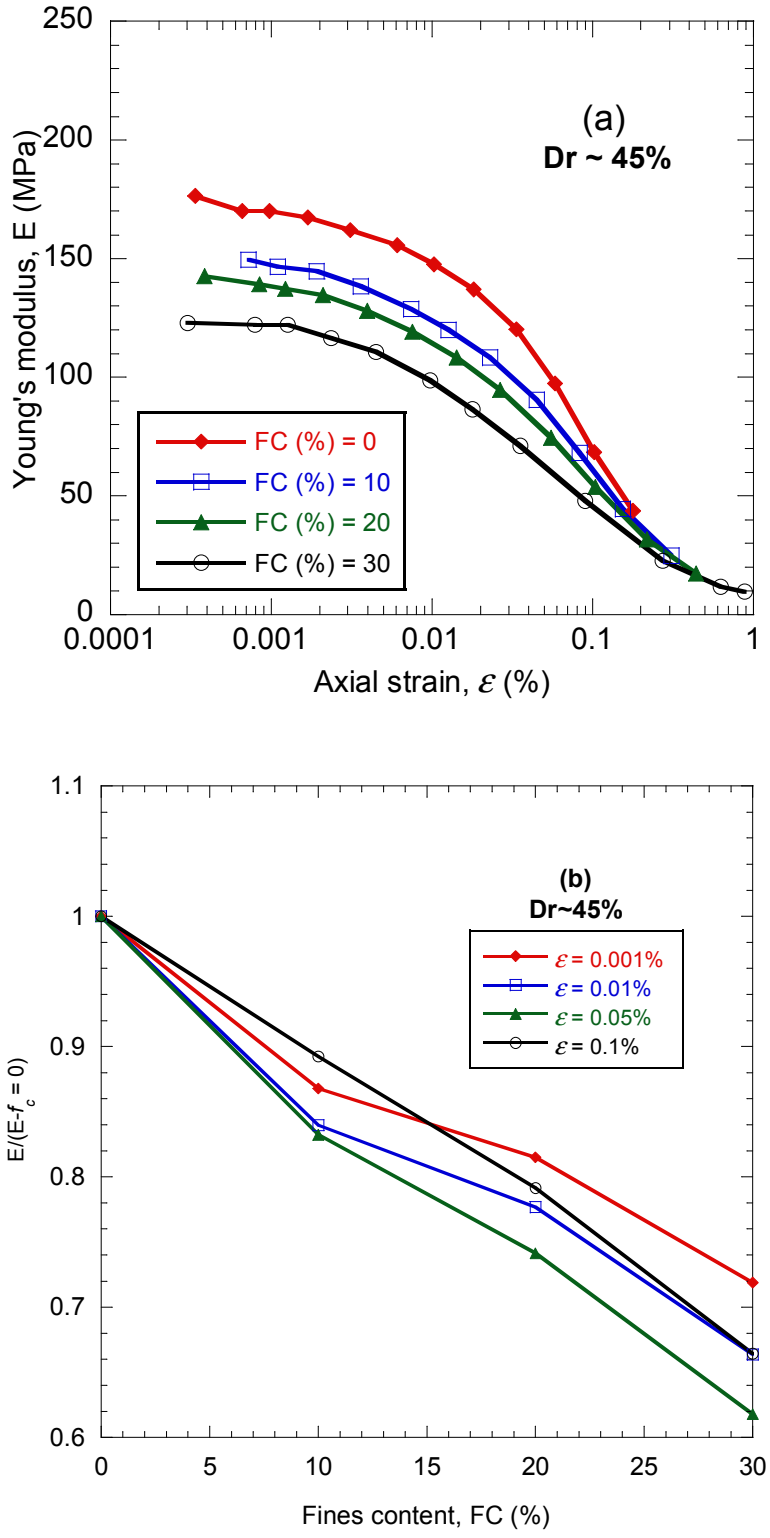

Figure 4-15 (a) Young's modulus reduction curves of FB test specimens with different fines content D_r ~ 45%, (b) The normalized Young's modulus versus fines content for different shear strains.

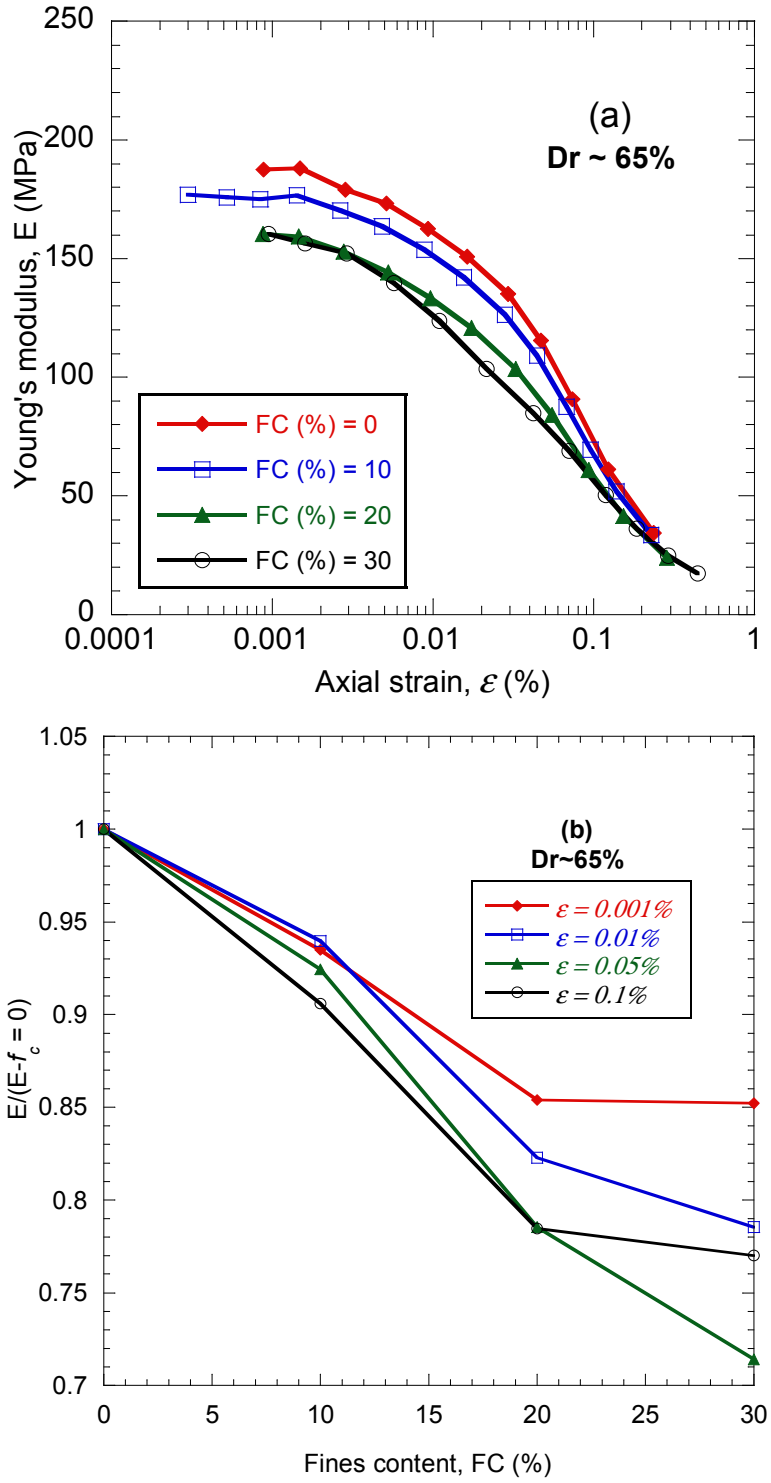

Figure 4-16 (a) Young's modulus reduction curves of FB test specimens with different fines content D_r ~ 65%, (b) The normalized Young's modulus versus fines content for different shear strains.

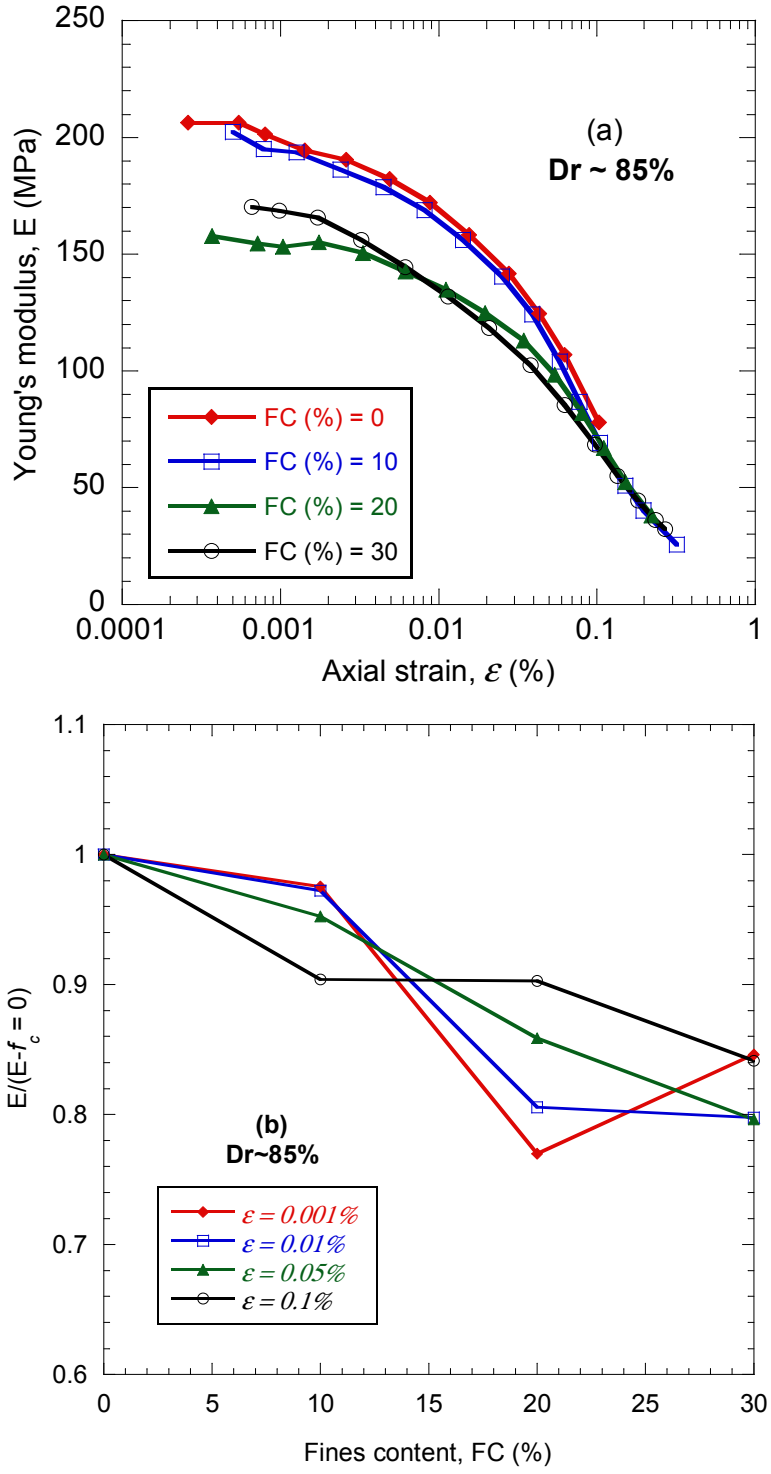

Figure 4-17 (a) Young's modulus reduction curves of FB test specimens with different fines content D_r ~ 85%, (b) The normalized Young's modulus versus fines content for different shear strains.

4.3.3 Normalized modulus reduction curves

As explained in the previous section, soils exhibit nonlinear behaviour upon loading. The secant Young's modulus decreases with increasing strain amplitude as shown in section 4.3.2. Young's modulus at small strains, at which soil behaviour can be considered linear, is referred to as small-strain Young's modulus, E_{max}. The relationship between the secant Young's modulus and strain amplitude is typically characterized by a normalized modulus reduction curve which is the ratio of E/E_{max}. For the sake of consistency, the secant Young's moduli at a strain $\varepsilon = 0.002\%$ were used in lieu of the maximum Young's moduli because it was difficult to accurately measure the latter with the triaxial apparatus. Effects of density and fines content on the shape of those curves are discussed in this section.

4.3.3.1 Effects of density on the normalized modulus reduction curves of FB soils

It has been demonstrated by other researchers (e.g. Darendeli, 2001, Ishihara, 1996) that the value of void ratio has practically insignificant effect on the positions of normalized modulus reduction curves of sandy soils. This independence is verified in Figure 4-18 for the FB sands where normalized modulus reduction curves are plotted for FB sand with different fines content. In each plot the degradation curves are shown for samples with different void ratios.

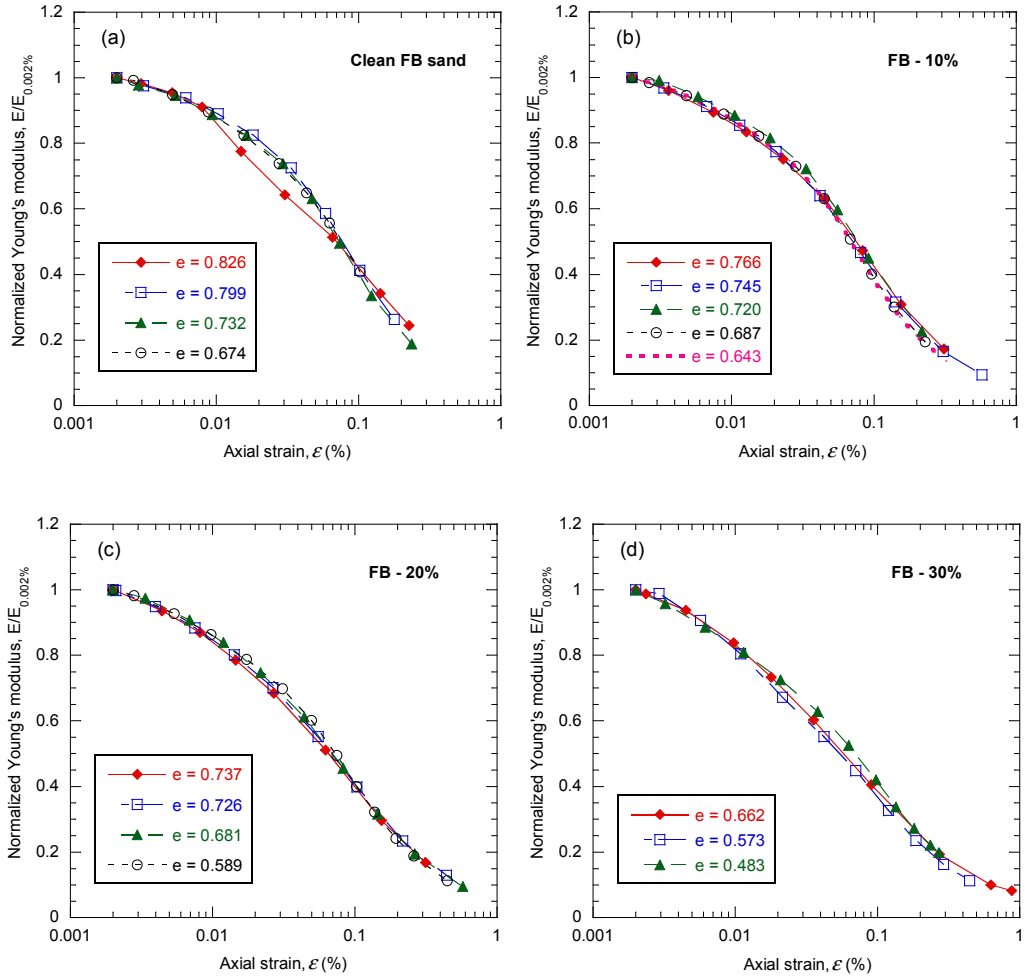

Figure 4-18 Normalized Young's modulus reduction curves of FB test specimens with varying fines content

4.3.3.2 Effects of fines content on the normalized modulus reduction curves of FB soils

The normalized modulus reduction curves are plotted at a given void ratio for the sands with increasing fines content in Figure 4-19. At this level of void ratio (e ~ 0.66), clean sand could be considered as very dense, sand with 10% and 20% fines content as medium dense and, sand containing 30% fines as medium loose (Figure 4-1). It is shown in Figure 4-19 that sands with higher fines content exhibit slightly higher nonlinearity in terms of modulus reduction. In this figure, the clean sand was

prepared at a relative density of D_r ~ 85% which was the maximum achievable density employing the moist tamping method. But the sand containing 30% fines had a relative density of D_r ~ 45% which was the minimum possible density for FB-30; a uniform specimen could not be prepared looser than this density. It is intuitive that stiffer soil shows more linear behaviour than looser samples and therefore, it is more desirable to compare the normalized reduction curves of sand with various fines content at similar relative densities to further investigate the effects of fines on the normalized reduction curve.

The normalized modulus reduction curves are plotted for three distinct relative densities in Figure 4-20, which are medium loose (D_r ~ 45%), medium dense (D_r ~ 65%), and dense (D_r ~ 85%). These curves can give a good indication of how fines content can affect the nonlinearity in the soil, or in other words, the general shape of the modulus reduction curves. It might be noted that the effect of fines on these curves is not significant especially for the denser specimens. A somehow more linear behaviour is apparent for the sand samples with lower fines percentages i.e. slower modulus reduction with the increase of strain level whilst they even have higher void ratios. The general tendency for the modulus reduction curves is in agreement with the trend found for the shear wave velocity correlations with void ratio and relative density. The smaller effects of fines on dense samples might be attributed to a higher likelihood for fines to be active in the stress transfer chains between granular particles. Hence fines containing sands could exhibit similar trends to that of the clean sands. It is also illustrated that for strain levels higher than about ε = 0.2%, the curves converge to a single trend regardless of fines existent in the sand matrix. This means that sands may exhibit similar degradation characteristics independent of the fines content at higher strain levels. At large strain levels, the modulus reduces significantly

to less than 20% of the initial maximum value and therefore the sensitivity of the normalized modulus curve to a change in fines content may decrease too. However, whether this trend is due to low sensitivity to fines content or actual stress-strain behaviour of sands with fines content is not clear.

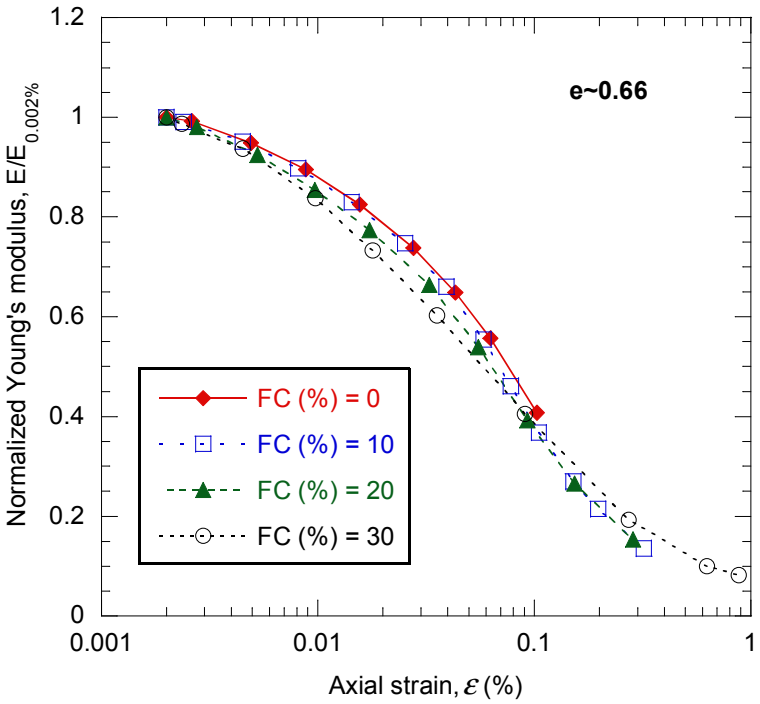

Figure 4-19 Normalized Young's modulus reduction curves of FB test specimens with varying fines content at void ratio $e \sim 0.66$

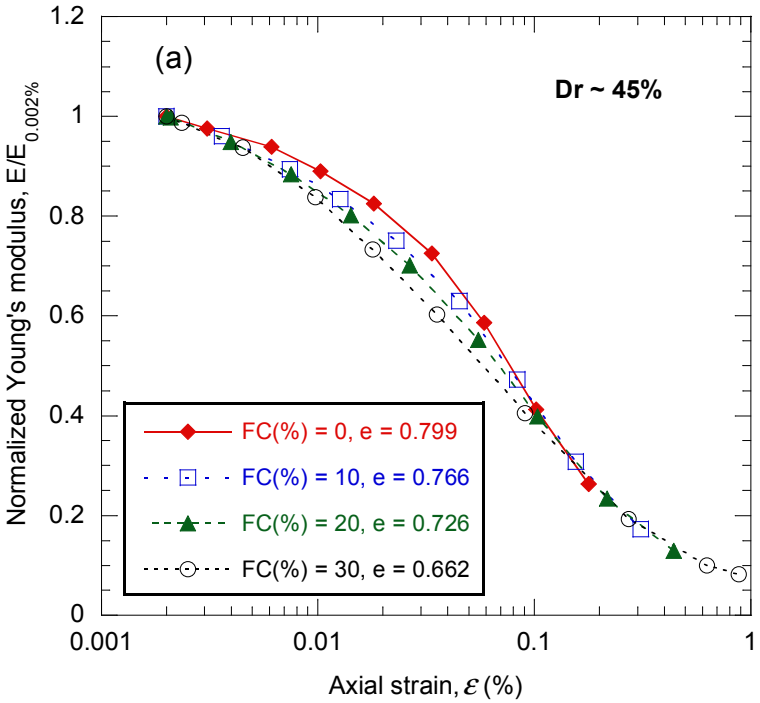

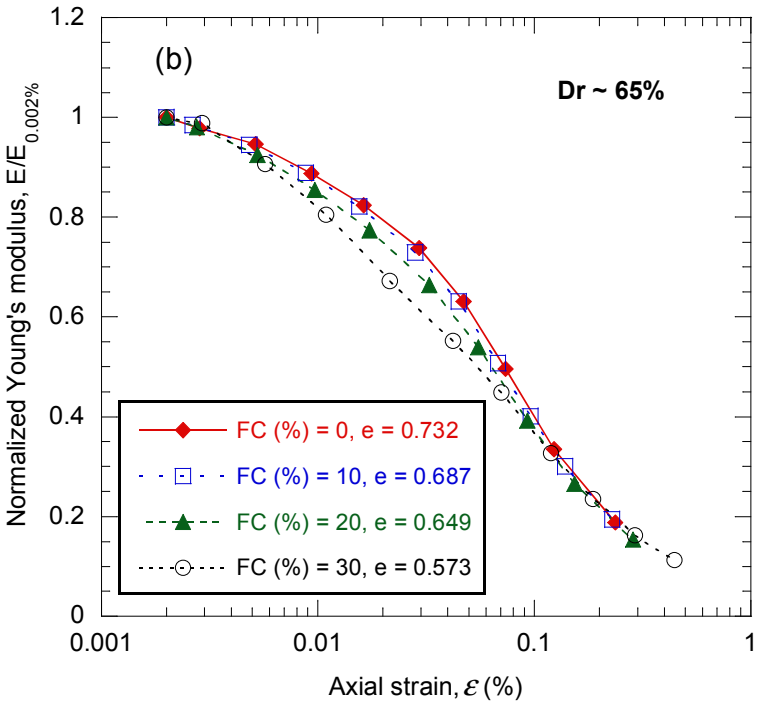

Figure 4-18 Normalized Young's modulus reduction curves of FB test specimens with varying fines content and relative densities (a) Dr ~ 45%, (b) Dr ~ 65%, (c) Dr ~ 85%

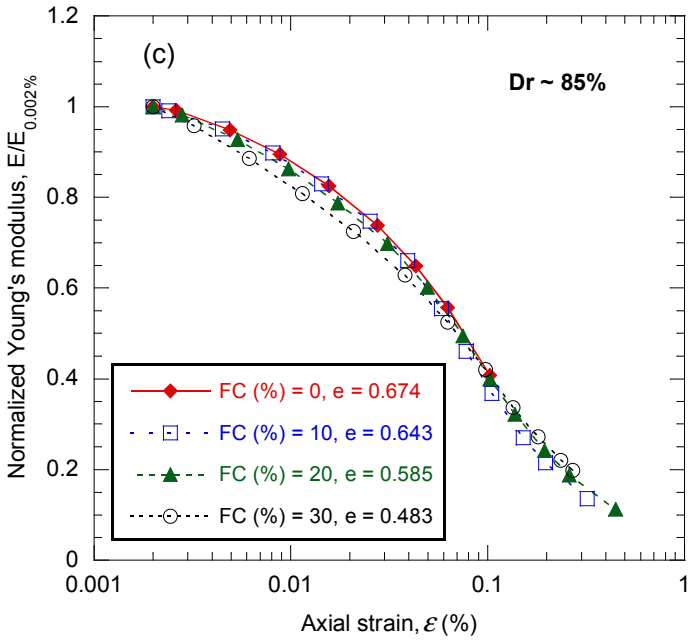

Figure 4-20 Normalized Young's modulus reduction curves of FB test specimens with varying fines content and relative densities (a) Dr ~ 45%, (b) Dr ~ 65%, (c) Dr ~ 85% (Continued)

It was shown in the previous section that void ratio (or relative density) has negligible influence on the general shape of normalized modulus reduction curves. Therefore, in order to investigate the effects of fines on the generic curves associated with each FB sand class, the averages of all the normalized curves of all sands with identical fines content regardless of the measured void ratios are calculated. The computed average curves are shown in Figure 4-21. The slight downward shift of the curves corresponding to the fines-containing sands, or larger degradation, is observed once again, in particular this shift is more evident for low to medium strain levels (γ = 0.004 - 0.04%). Similar trends were found by Darendeli (2001) when the results of clean sand were compared with sands with high fines content. Obviously this larger degradation which is related to exhibiting more nonlinear behaviour for fines containing sands influences the reference strain, ε_r, for each FB sand group. The

reference shear strain, ε_r, is that for which E/E_{max}=0.5. The reference strain decreases slightly with the increase of fines content.

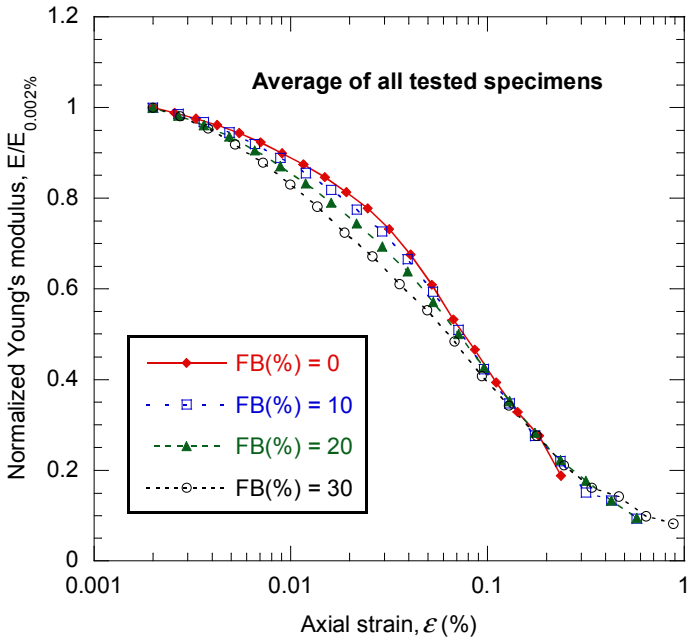

Figure 4-21 Generic normalized Young's modulus reduction curves of FB test specimens at each fines percentage obtained by averaging all curves at each soil class

4.3.4 Damping ratio curves

As discussed in Chapter 3, one convenient method to determine the equivalent damping ratio, *h*, is to use hysteresis loops measured from the laboratory tests on the representative samples. As the strain level increases, the nonlinearity of the soil behaviour would be more pronounced leading to higher values of damping. Using the triaxial tests performed on samples with different fines content and density, values of hysteretic damping for different strain levels are calculated and presented in this section using the procedure outlined in the Japanese Geotechnical Society's standard and described in Chapter 3 (2000).

4.3.4.1 Effects of density on the damping ratio curves of FB soils

In an attempt to identify the strain-dependent damping properties of the FB soil, the values of the material damping ratios of soils with different fines content obtained in the triaxial test series were calculated and are shown in Figure 4-. The presented results were obtained from tests on specimens with different fines content and with different densities, conducted under a confining stress of 100 kPa. The damping ratios after the application of ten cycles are presented in the figures. It is seen from the results, the value of the damping ratio increases with increasing strain and reaches a value of about h = 20% when the axial strain approaches approximately 0.5 per cent. It can also be seen that the relation between the damping ratio and strain amplitude is not affected by the density of the soil as no systematic effects of void ratio are observed, except that slightly higher damping ratio is observed for the looser samples. Obviously the effects of density are either very small or non-existent.

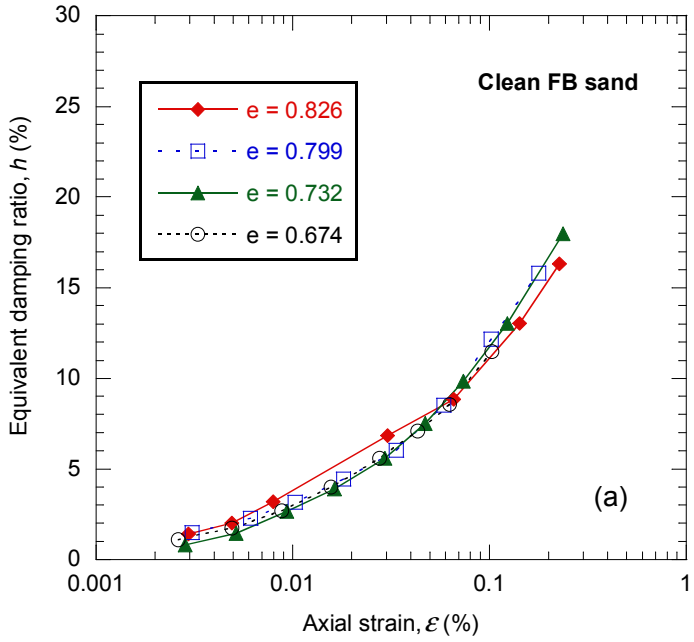

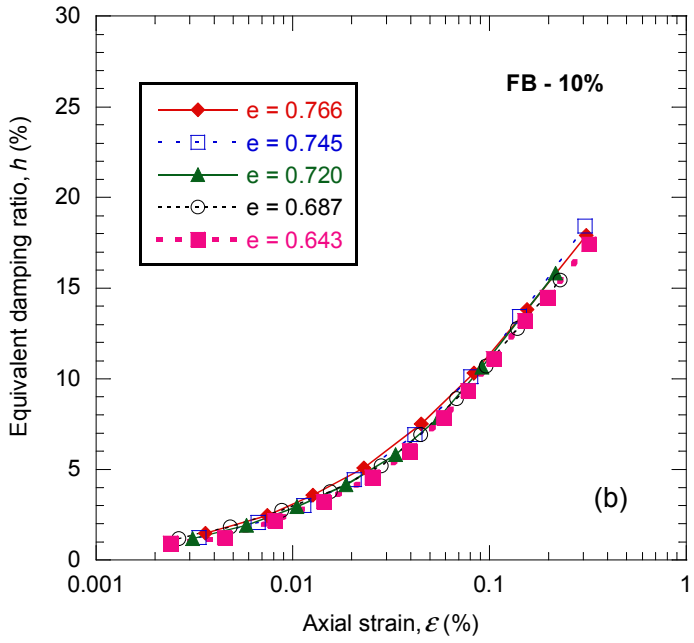

Figure 4-22 Effects of density (void ratio) on damping ratio curves of FB test specimens with different fines content (continued)

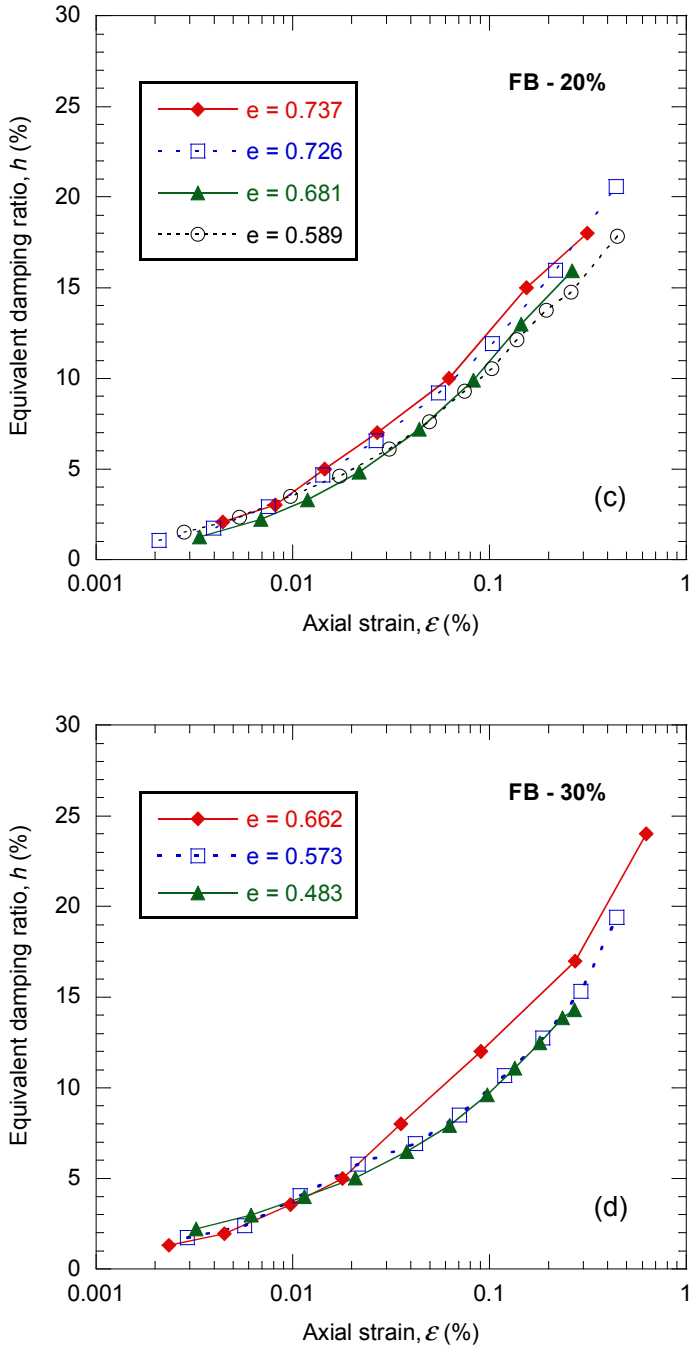

Figure 4-20 Effects of density (void ratio) on damping ratio curves of FB test specimens with different fines content

4.3.4.2 Effects of fines content on the damping ratio curves of FB soils

Typical curves of damping ratio, *h,* versus axial strain amplitude ε are given in Figure 4-23 and 4-22. It was shown in the previous section that generally the damping ratio does not depend on density. A comparison of the damping ratios measured for sands with different fines content also shows that *h* does not significantly depend on the fines content (Figure 4-23). However, fines containing sands exhibit higher damping to some extent, particularly for looser samples. Wichtmann and Triantafyllidis (2010) found that for small confining pressures (< 50 kPa), fines content may exert a great influence on the damping ratio curves whereas for larger pressures the effect of fines content on *h* is less pronounced.

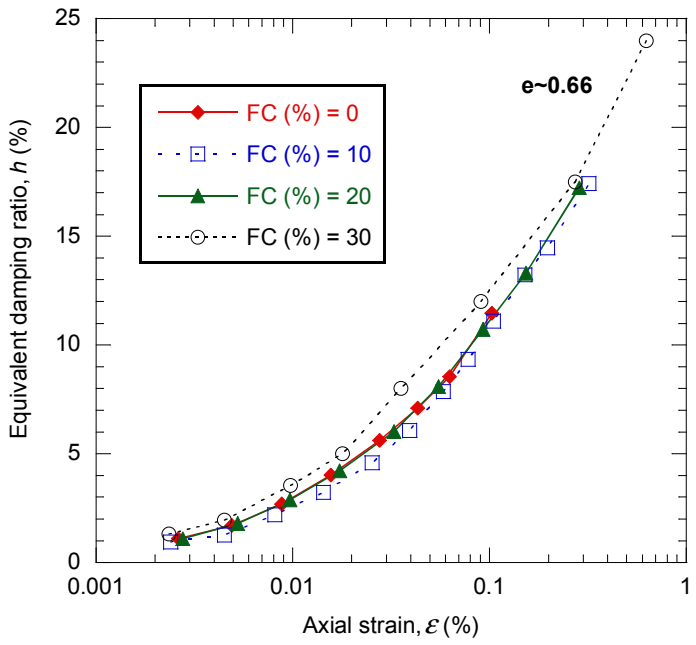

Figure 4-23 Damping ratio curves of FB test specimens with varying fines content at void ratio $e \sim 0.66$

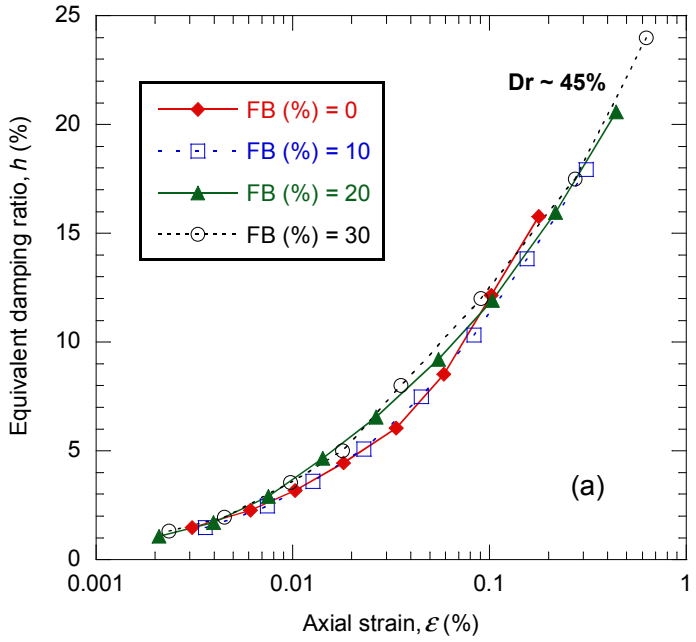

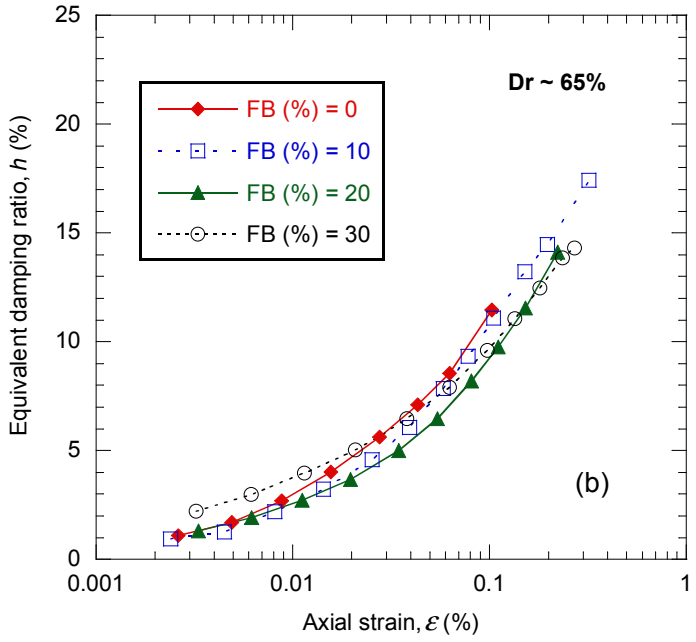

Figure 4-22 Damping ratio curves of FB test specimens with varying fines content and relative densities (a) Dr ~ 45%, (b) Dr ~ 65%, (c) Dr ~ 85%

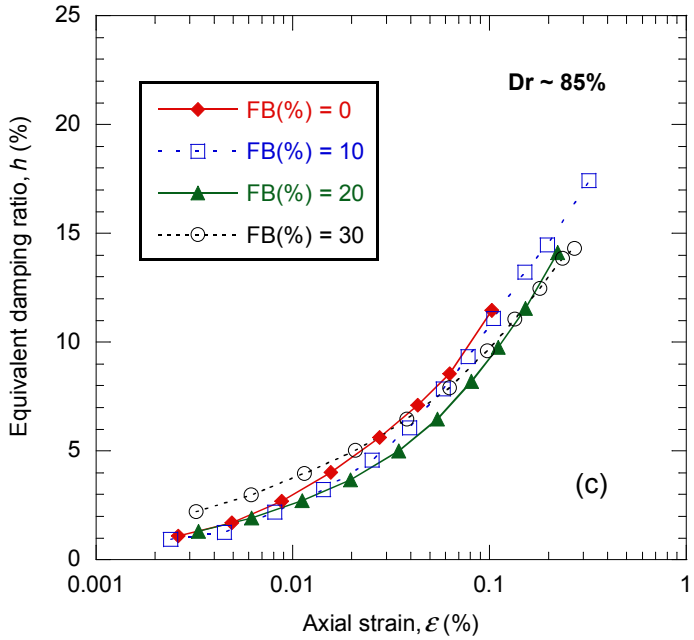

Figure 4-24 Damping ratio curves of FB test specimens with varying fines content and relative densities (a) Dr ~ 45%, (b) Dr ~ 65%, (c) Dr ~ 85% (Continued)

Similar to the modulus reduction curves, it is known that the void ratio (or relative density) has negligible influence on the general shape of the damping ratio curves (e.g. Darendeli 2001). Therefore, in order to investigate the effects of fines on the generic curves associated with each FB sand class, the average curves of all the damping ratio curves of all sands with identical fines content regardless of the measured void ratios were calculated. The computed curves are shown in Figure 4-25. It is noted that the variation in damping ratio can be considered independent from the changes in fines content as well as different void ratios. An average single trend line may be assumed for all the fines-containing sands of FB mixtures in which fines comprise less than 30% of the weight of the specimen. The minimum damping ratio, h_{min} = 0.54%, measured at linear stages of soil testing is obtained by calculating the

mean value of damping ratios of all the tested specimens at the lowest strain which could be measured in the laboratory.

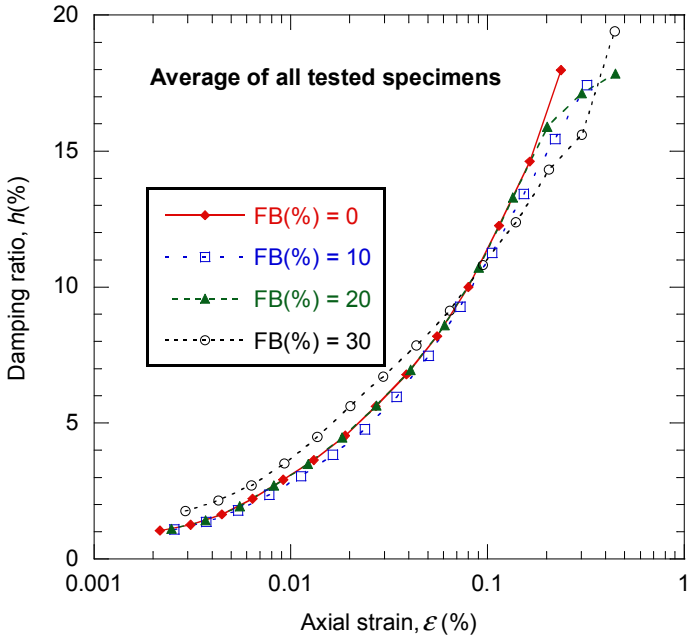

Figure 4-25 Generic damping ratio curves of FB test specimens at different fines content obtained by averaging all curves for each soil class

4.4 Shear modulus – Young's modulus relationship

Shear modulus is the preferred parameter used in the seismic response analyses as compared to Young's modulus. Hence, it is desirable for the site response analyses to convert the latter to the former. The Young's modulus, E, could be evaluated from cyclic triaxial test data at small strains whereas bender element tests results can produce shear modulus, G. These two parameters are related through the following expression:

$$G = \frac{E}{2(\nu + 1)} \tag{4-4}$$

$$\gamma = (1+\nu).\varepsilon$$

where ν is the Poisson's ratio.

The theoretical limits of Poisson's ratio are $-1 < \nu < 0.5$, while in practice for elastic behaviour of soils, this limit is assumed in the range from 0 to 0.5. However, Poisson's ratio is always difficult to establish experimentally and therefore uncertainty remains. Based on experimental studies Hardin (1978), Lade and Nelson (1987) concluded that any value between 0 and 0.2 is accurate enough for most purposes.

Adding one cycle of drained triaxial loading to an undrained series of cycles, Kokusho (1980) employed both the drained and undrained Young's moduli at strains smaller than $\gamma = 0.01\%$, to estimate the Poisson's ratio for several confining pressures. Figure 4-26 illustrates the Poisson's ratio versus shear strain relationship for dense Toyoura sand obtained in Kokusho (1980). It is evident from the graph that the measured Poisson's ratios fall in the narrow band at around $\nu = 0.2$ ascending very slightly with the strain increase. This may imply that an assumption of a constant Poisson's ratio for the entire range of strain amplitudes in converting the Young's modulus curve to the shear modulus curve may be acceptable.

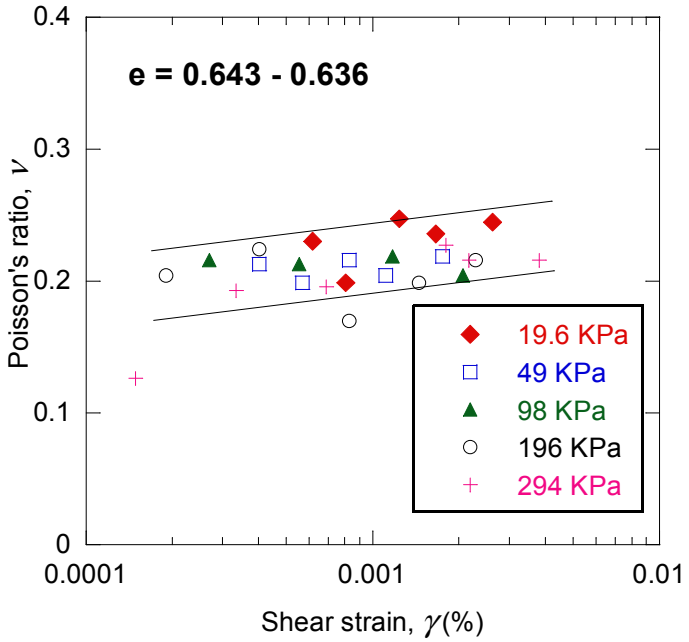

Figure 4-26 ν vs. γ relationships for small strain level with different confining pressures (after Kokusho, 1980)

In this study, the triaxial apparatus was utilised to measure the stress-strain behaviour of sands under cyclic loading for a wide strain range from ε = 0.002% – 0.5%. However, for evaluation of elastic behaviour of soil (ε < 0.001%) bender elements were employed which can estimate the elastic stiffness with higher accuracy. Young's modulus, *E,* can be evaluated from cyclic triaxial tests whereas bender element tests results can produce shear modulus, G_{max}. These two parameters can be related at small strains using equation (4-4).

Alternatively, it is possible to calculate the shear moduli from the triaxial test results assuming variable Poisson's ratios and compare it with G_{max} computed using the shear wave velocity measured in the bender element tests in order to obtain the best match Poisson's ratio. However, it should be emphasized that the bender element tests are carried out at elastic ranges corresponding to strains smaller than 10^{-4}% compared to lowest strains of ε = 0.002% in measured triaxial tests. This means the

shear modulus inferred from bender element tests can be larger than that obtained from triaxial test results due to the difference in the respective shear strains used in the evaluation of G_{max} in these two tests.

Figure 4-27 presents the shear modulus estimated from triaxial test results at ε = 0.002% using two Poisson's ratios, ν = 0.1,0.3, and compares it with the maximum shear modulus measured by the bender element device; the solid lines in this figure represents the 90% deviation. Figure 4-28 shows the same information provided in Figure 4-27 but for each individual fines percentage. It can be inferred that any value between 0.1-0.3 can be a reasonable estimate for Poisson's ratios for soils tested in this study; however ν = 0.1 appear to represent the entire set of the data points. Other researchers have also reported similar range for sands (e.g. Robertson, 2012, Shibuya et al., 1992). The data points in Figure 4-27 also suggest that Poisson ratio is density-dependent; ν increases with decreasing density. This is in agreement with the results presented by Lade and Nelson (1987). According to the theory of elasticity it can be shown that the lateral earth pressure at rest is related to Poisson's ratio based on the following equation (e.g. Davis and Selvadurai, 1996) :

$$K_o = \frac{\nu}{(1-\nu)} \tag{4-5}$$

where K_o is the coefficient of lateral earth pressure. There are several empirical correlations for design values of K_o, including the Jacky's relationship (e.g. Bowles 1997):

$$K_o = 1 - \sin\phi \tag{4-6}$$

where ϕ is the internal friction angle of the soil. Combining equations (4-5) and (4-6), an empirical equation for cohesionless soils can be derived which relates the density to Poisson's ratio. Figure 4-29 shows how Poisson's ratio for denser soils can be lower than for looser soils. It should be noted that Poisson's ratio is defined if soil behaves elastically and therefore when it is used above the threshold strain, as it is shown in Figure 4-27 for γ= 0.002%, it should be acknowledged that the strain level is beyond the elastic behaviour and rigorous application of the Poisson ratio .

Nevertheless, dense samples regardless of fines content tend to deviate from the trend more than that of looser specimens. The deviation present in Figure 4-27 could be explained by the fact that the Young's modulus measured in a conventional cyclic triaxial test may be under-estimated (e.g. Shibuya et al., 1992). The bedding error at the specimen ends can cause this deviation substantial, if the strain is measured by means of the axial displacement of the top cap using a gap sensor (e.g. Kokusho, 1980). Accordingly, the axial deformation is suggested to be locally measured over a central portion of the specimen so as to precisely obtain the deformation properties of soils at small strains (Shibuya et al., 1992). Figure 4-30 illustrates how the presence of loosened soil layers at the ends of the specimen can affect the measurement of the axial displacement using external or local displacement transducers.

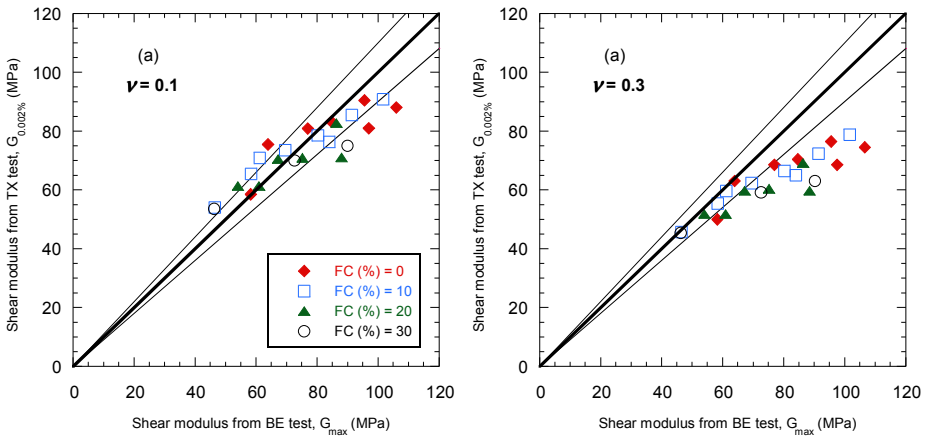

Figure 4-27 Comparison between the maximum shear moduli G_{max} *(MPa)* obtained by the bender element test method and the shear moduli $G_{0.002\%}$ at $\varepsilon = 0.002\%$ estimated by the triaxial test data for (a) ν = 0.1, (b) ν = 0.3

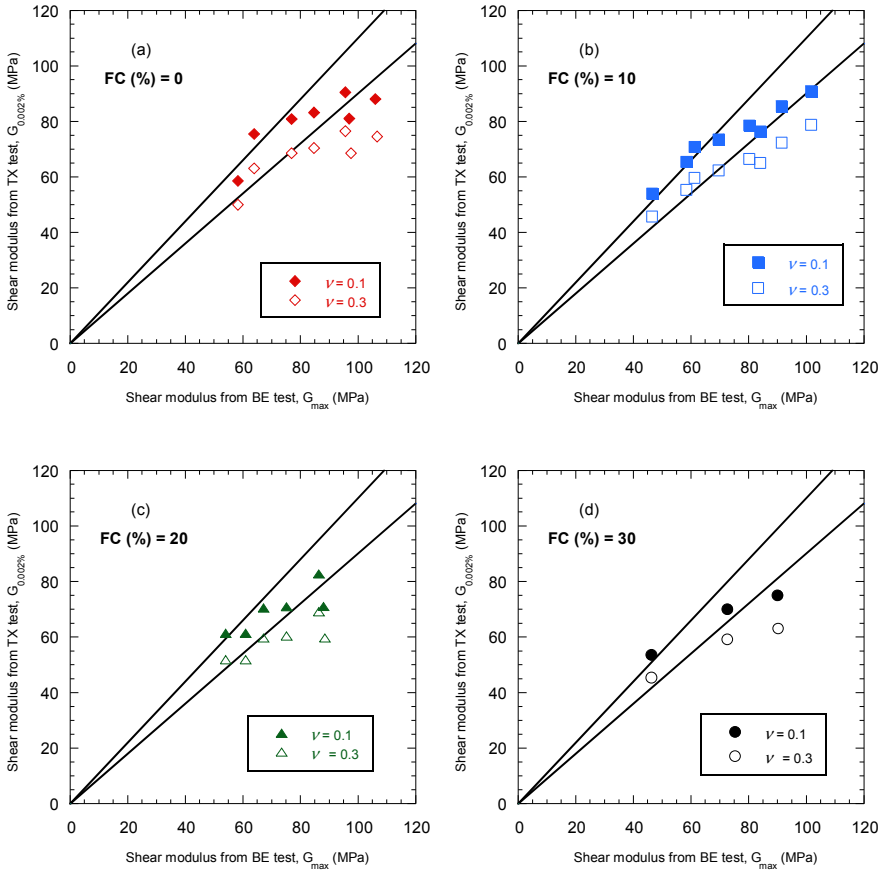

Figure 4-28 Comparison between the maximum shear moduli G_{max} *(MPa)* obtained by the bender element test method and the shear moduli $G_{0.002\%}$ at $\varepsilon = 0.002\%$ estimated by the triaxial test data for ν = 0.1 and ν = 0.2 and different fines content

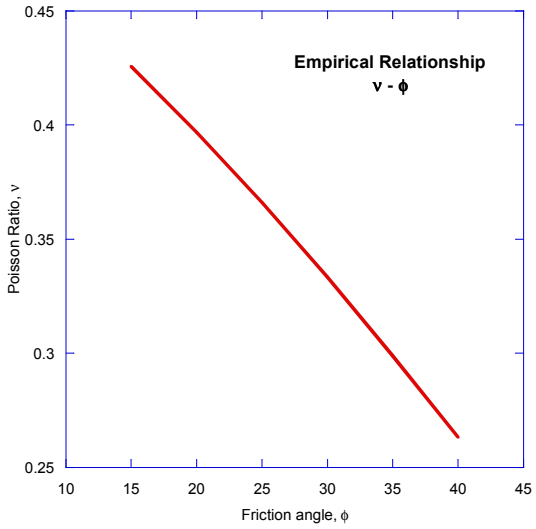

Figure 4-29 Empirical relationship between Poisson's ratio and internal friction angle

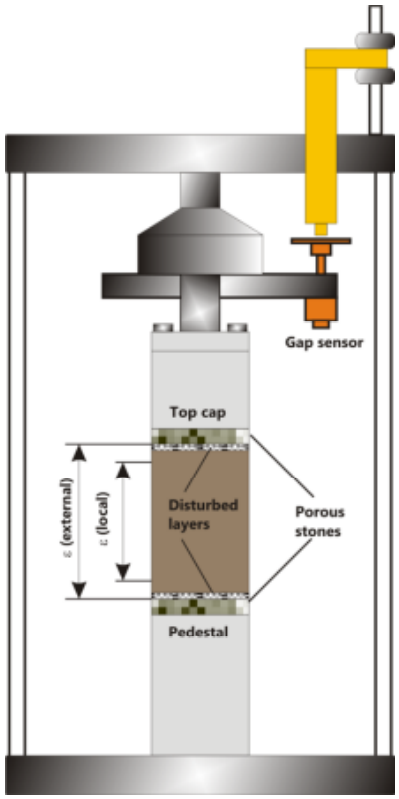

Figure 4-30 Loosened soil layers formed at the ends of triaxial specimens

4.5 Comparison of shear modulus reduction and damping curves of FB clean sand and other sands

Several studies have been undertaken to develop laboratory-based empirical relations for modulus reduction and damping curves. In this section, common families of normalized shear modulus reduction and damping ratio curves developed by several researchers (e.g. Seed and Idriss, 1970, Iwasaki et al., 1978, Darendeli, 2001, Kokusho, 1980) are reviewed and the results for FB sand are compared with these families of curves.

Darendeli (2001) used an extensive database of 110 intact specimens from various research projects to develop the most recent of the families of the normalized modulus and damping curves. The collected data were statistically analysed using First-order, Second-moment Bayesian Method (FSBM) and the effects of various parameters on modulus and damping properties of soils were evaluated and quantified in an empirical framework. This framework is composed of a four-parameter model that can be used to characterize normalized modulus reduction and damping curves. The predicted curves represent average curves while the actual data fall into a band of scatter around the average curve. Therefore, in addition to mean values, associated uncertainty of the empirical curves was also estimated in terms of standard deviation.

Figure 4-31 compares the normalized modulus reduction curves for FB sand obtained in this study as well as the corresponding mean values for non-plastic sand computed by Darendeli's (2001) model. The uncertainty around Darendeli's curve is also shown in terms of a band of standard deviation around the mean values. Note that for the computation of Darendeli's curve, similar test conditions adopted in this study are assumed, i.e. σ'_0 = 100kPa, f = 0.1 Hz and N = 10 cycles. It is shown that under

similar testing conditions, the normalized moduli for FB sand is larger than Darendeli's values for small to intermediate strain ranges. However, this difference decreases for larger strains $\gamma > 0.2\%$.

Many previous studies also characterised the modulus reduction and damping behaviour of sands. Seed and Idriss (1970) summarized a number of studies using different laboratory testing procedures in order to study the sand shear modulus and damping behaviour. The variations of the normalized modulus and damping with shear strain were estimated and approximate lower and upper bounds along with an average relationship was proposed. Based on a comprehensive study, Iwasaki et al. (1978) collected all the average modulus reduction curves proposed by previous studies and compared his resonant-column and torsional-shear test results with those curves. In addition, results of cyclic triaxial tests on specimens of the same saturated clean sand were reported consistent with that of the Iwasaki (1978) curves (Kokusho 1980).

The measured degradation curves from all these studies along with the curves collated by Iwasaki et al. (1978) for sands under σ'_0 = 100 kPa are summarized in Figure 4-32. The average normalized modulus curve for the clean FB sand is also represented by the solid symbols.

It can be concluded that sands show a relatively small variation from one soil to another in terms of moduli and damping curves compared with that of clay soils. However, the normalized modulus reduction and damping curves are found to be somewhat more linear for clean sands compared to those observed for the silty natural sands. This is in agreement with findings of this study which also suggests more linear behaviour for intermediate to large strains for the FB clean sand as compared to

that of silty sand. In general, the laboratory results for the FB clean sand compare very favourably with the Iwasaki et al. (1978) and Kokusho (1980) curves of Toyoura clean sand for confining pressure of 100 kPa. On the other hand, the Seed (1970) and Darendeli (2001) relationships show larger reduction in the shear modulus as compared to that of the FB sand. The average curve suggested by Seed and Idriss (1970) and the curve suggested for sands under σ'_0 = 100 kPa proposed by Darendeli (2001) match very well. It is to be noted that the data which Seed and Idriss (1970) and Darendeli (2001) synthesized are mainly the results of tests performed on silty natural sands.

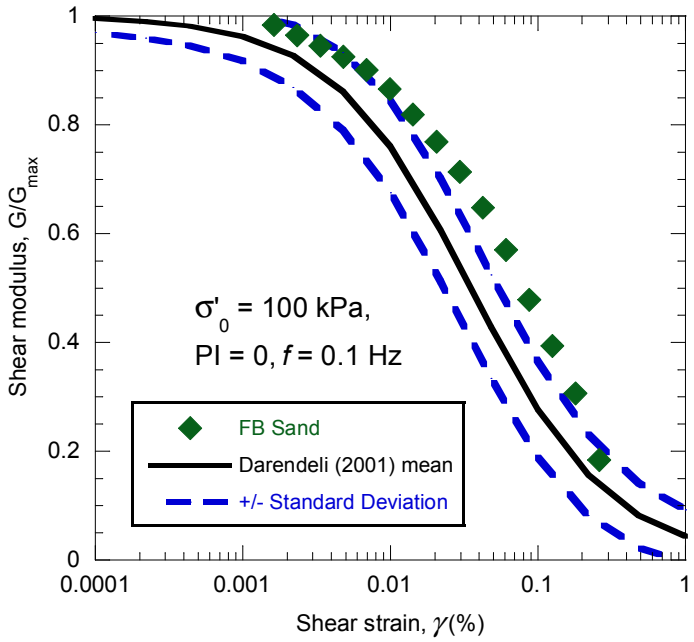

Figure 4-31 Normalized modulus reduction of FB sand and mean values and standard deviations using Darendeli (2001) model

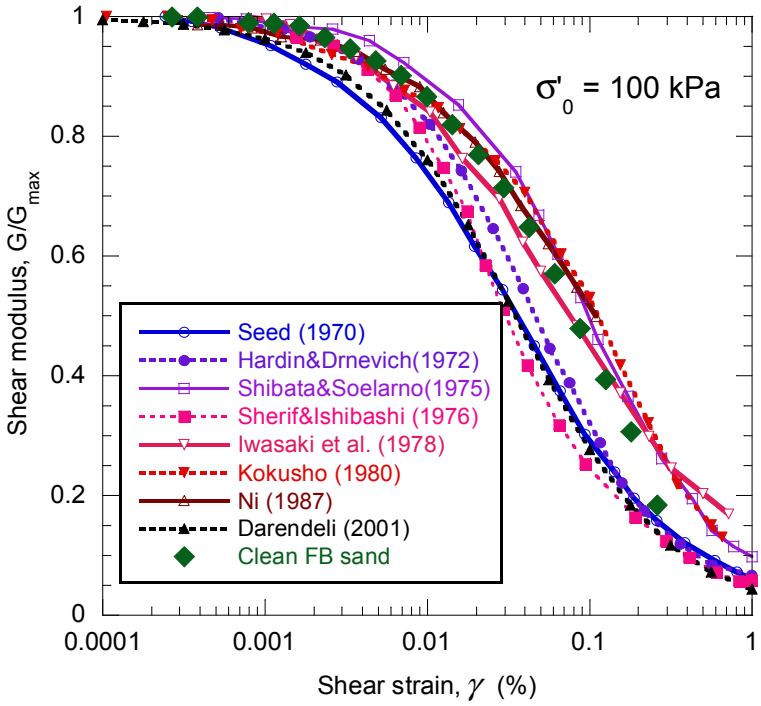

Figure 4-32 Comparison of normalized modulus reduction curves $G/G_{0.002\%}$ with G/G_{max} from different studies.

Figure 4-33 presents the damping curves for FB sand obtained in this study and compares it with the mean damping values computed by Darendeli (2001) model. The upper and lower bounds represent the one standard deviation band around the mean values. It is shown that the standard deviation of Darendeli's model increases with increasing shear strain. Generally, the damping values of FB sand are lower than mean values calculated by Darendeli's relationships. However, the FB sand damping curves are within the median value and lower bounds.

Figure 4-34 shows the upper and lower bounds damping curves suggested by Seed and Idriss (1970) with solid lines as well as an average curve recommended for practical purposes. The mean material damping curve suggested by Darendeli (2001) for sand under a confining pressure of 100 kPa is also presented. The solid symbols represent the average of damping curves for FB clean sand data which indicates the

FB sand damping ratio curves are close to the lower bound value suggested by Seed and Idriss (1970). The FB damping data compare fairly well with Darendeli (2001) curve.

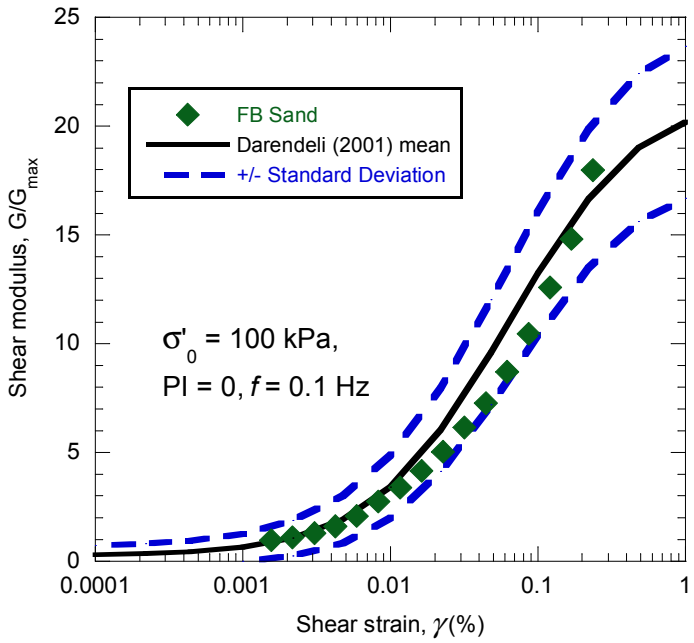

Figure 4-33 Material damping curves of FB sand and mean values and standard deviations using Darendeli (2001) model

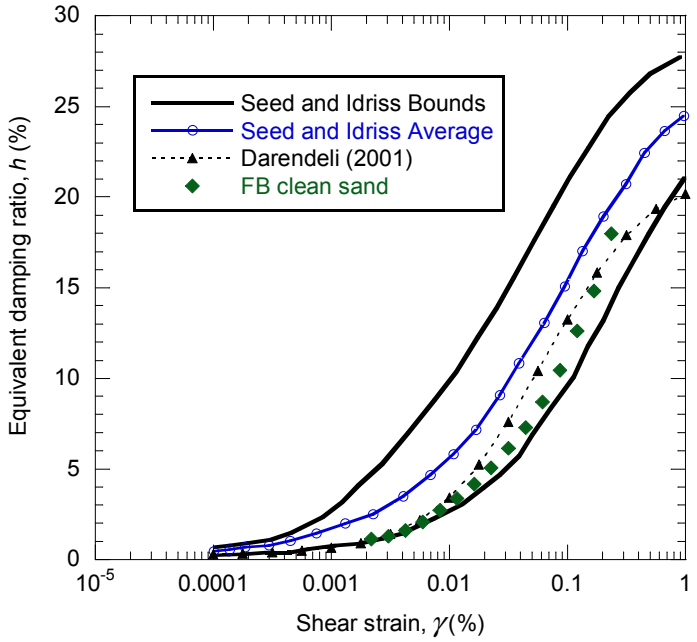

Figure 4-34 Damping ratio curves from different studies.

4.6 Summary

The main focus of this chapter was presenting and analysing the results of bender element and drained cyclic triaxial tests on the four FB sand-fines mixtures. The low-strain stiffness properties of FB soil were firstly discussed in terms of shear wave velocity and maximum shear modulus. It was concluded that at similar void ratios or relative densities, FB sandy specimens with higher fines content exhibited lower stiffness than sands with lower fines content. In other words, there is a reduction of shear wave velocity and shear modulus with an increase of fines content.

The modulus reduction and damping curves of the FB sandy soil were also assessed, using void ratio, e, and relative density, D_r, as the measures of soil density state. It was illustrated that the modulus reduction curves shifted upwards as the specimens densities increased indicating an increase in stiffness at a given strain level.

However, it was found that density had negligible effect on the general shape of the normalized modulus and the damping ratio curves.

Furthermore, it was shown that when using either of these density state measures, the modulus reduction curves of the FB soils located lower as fines content was raised. This was fully in agreement with the low-strain stiffness properties findings explained earlier. Moreover, it was shown that sands with lower fines content exhibited somewhat more linear behaviour than sands with higher fines content, at similar densities. This means the reduction of the normalized modulus curve was more gradual for clean sands than for fines containing sands. This was particularly relevant for looser soil specimens. Modulus reduction curve collapsed to single trends for higher strain levels showing a similar behaviour regardless of fines content at strains higher than ε = 0.2%. The damping ratio curves were found practically unaffected by the density and fines content.

The shear modulus is a more favourable soil parameter; therefore, it is desirable to convert the Young's modulus to shear modulus employing the Poisson's ratio. It was shown that there is a tendency for Poisson's ratio to increase with increasing void ratio. Using the Poisson's ratio, the normalized shear modulus and the material damping curves were then computed and compared with the curves suggested by other studies. It was concluded that the experimental normalized shear modulus reduction curve of FB clean sand compare fairly well with the curves suggested by Iwasaki et al. (1978) and Kokusho (1980) for clean Toyoura sand. The average damping ratio curve of the FB clean sand was similar to the curves presented by Darendeli (2001) and matched better with the lower bound values suggested by Seed and Idriss (1970).

5 Interpretation of the effect of fines on shear modulus using equivalent granular void ratio

5.1 Introduction

Dynamic soil properties such as shear wave velocity, shear modulus and damping characteristics are important factors required for dynamic response analyses of earth structures. In the previous chapter, in order to estimate the dynamic soil properties of the FB sand-fines mixtures, the parameters void ratio, e, and relative density, D_r, were used as state variables. Their application proved to be sufficient to determine the above characteristics for clean sands, but unsatisfactory for the most commonly found silty sands. In addition, it was illustrated that when using the void ratio as a basis for comparison, there is a clear tendency for a decrease in the stiffness of the specimens with increasing fines content. This tendency is similar, though less consistent, when the effects of fines are evaluated based on D_r.

The discussion in the previous chapter suggested that the difference in soil modulus at similar values of the state measures may be due to these measures providing no direct quantification for the effects of fines in the density state of the soil. All particle sizes are assumed to contribute to the overall inter-grain contact density of the soil when using these measures (e.g. Thevanayagam and Mohan, 2000, Cubrinovski et al., 2010), but this assumption may not be physically correct, especially when sand is mixed with fine-grained silt. This shows that void ratio and relative density may not be good measures for characterizing sand with fines. It is desirable to account for the soil fines content by means of a new state measure – one

that differentiates between sand and fines-sized particles, and produces similar soil response at similar values of the measure.

As explained in Chapter 2, an alternative state variable referred to as the equivalent granular void ratio, e^*, has been introduced by Thevanayagam and Mohan (2000) which allows some of the fines-sized particles to be considered in the soil force-chain, rather than either simply neglecting their effects or giving them an equal weight to the sand particles' participation (Thevanayagam and Mohan, 2000). The equivalent granular void ratio, e^*, of sand up to threshold fines content, f_{cth}, is calculated using the following expression:

$$e^* = \frac{e + (1-b) f_c}{1 - (1-b) f_c} \tag{5-1}$$

where f_c is fines content and b represents the fraction of fines that actively participate in the load transfer of the solid skeleton. In this context, the key contribution of the equivalent granular void ratio is that it provides an effective parameter for characterization of the effects of fines on the dynamic behaviour of sands. To calculate the equivalent granular void ratio the term, b, is needed which can be thought of as an influence factor that represents what portion of the fines particles actively participate in the force structure of the sand skeleton during loading. As described in Chapter 2, e^* allows considering either all fines particles as voids ($b = 0$), all fines particles as solids ($b = 1$) or any proportion in between ($0 < b < 1$).

The equivalent granular void ratio, e^*, is used in this chapter to interpret the shear modulus properties of the Fitzgerald Bridge (FB) soils presented in Chapter 4. It was shown that fines content has a small effect on the normalized modulus reduction and negligible effects on the material damping curves whereas the shear wave velocity

and modulus were influenced by fines content significantly. Hence, only the effects of fines content on the shear wave velocity and the absolute values of the Young's and shear moduli are considered in this chapter. A procedure to back-calculate the fines influence factor, *b*, as well as an equation to predict the *b*-value, are also discussed. Finally the effects of fines on the dynamic properties of sandy soils are scrutinized when e^* is used as the measure of soil state.

5.2 Determination of fines influence factor, *b*

Section 2.3.2 presented the equivalent granular void ratio, e^*, concept and discussed the meaning of fines influence factor, *b,* which represents the portion of fines actively participating in the inter-grain contacts during loading. As such, fines that are between coarse particles are in the force chain, whereas fines that are located in the gaps between the coarse grains have little contribution to the force structure. However, the prediction of the *b* value, and thus the determination of the equivalent granular void ratio, is not straightforward. Some methods have been proposed to estimate the value of *b* for a soil based on either material properties or back calculations (e.g. Thevanayagam and Mohan, 2000, Rahman et al., 2008). This section describes and employs both methods to determine *b* values for the dynamic behaviour of FB soils.

5.2.1 Back calculating the *b* value

A back-calculation procedure to determine the *b*-value is detailed below for a given mixture of sand and fines, using an iterative sum of least squares error approach (after Rees 2009). In this method, a constant value of *b*, which is the common assumption in the literature (Cubrinovski and Rees, 2008, Ni et al., 2004), is achieved

for FB soils irrespective of fines content. However, it should be emphasized that the equivalent granular void ratio equation is based on binary packing, therefore discrepancies might arise when such a theory is applied to natural soils simply because all particles are assumed to be spherical in this theory and only two particle sizes are present. In reality, mixtures of sand and fines have variable particle shapes and particle size distribution.

In this section the fines influence factor values for bender element and triaxial test results are calculated separately – this is due to the apparent differences at the small and large strain levels. The objective of the back-calculation procedure is to determine a value of b that lets the dynamic soil response be similar at a constant value of e^*, irrespective of the soil fines content. This means that for instance, if $e^* = 0.8$ and $V_s = 185$ *m/s* for clean sand, then $V_s = 185$ *m/s* when $e^* = 0.8$ for silty sands.

The first step in the back-analysis procedure is to determine the clean sand benchmark response curve. For bender element tests, this is the clean sand shear wave velocity versus void ratio relationship. For triaxial test, the benchmark curve is the clean sand Young's modulus and modulus reduction curve. Mathematical equations are fitted to experimental data points to generate these response curves. A power functional fit is then used for both the shear wave velocity and for the Young's modulus curves as they are correlated through the elastic theory relationships. The power fit was chosen based on Jamiolkowski (1991)'s suggestion for the small-strain shear modulus, G_{max}, and void ratio relationship.

The equivalent granular void ratio, e^*, is computed for all test specimens using $b = 0.0 – 1.0$ in increments of 0.01. In this way, fines activity range from zero to full active can be covered, meaning that all potential values of e^* for the soil are

calculated. For a given *b*-value, the equivalent granular void ratios, *e*,* are evaluated using equation (5-1) given that *e* and f_c are known for each specimen. Note that the *e** values along the benchmark response curve are defined as e^*_b. For the given *b*-value, the distance between the computed *e** for each specimen and the benchmark curve e^*_b is computed as illustrated in Figure 5-1:

$$d = e^* - e^*_b \tag{5-2}$$

The computed values of *d*s are then squared, $d^2 = (e^*_b - e^*)^2$. The squared distances d^2 are summed up for all specimens, and divided by the total number of tests, *n*. This summation gives the mean squared error value, *MSE*, for the given *b*-value. The minimum MSE value identifies the corresponding *b*-value which best fits the computed to the experimental data points. This final step is schematically shown for the FB soil bender element shear wave velocity data in Figure 5-2.

Figure 5-3 shows similar curves for small-strain Young's modulus at $\varepsilon = 0.002\%$ as well as overall shape of modulus reduction curve for the range of ε = 0.002% - 0.1%. A power-function, $E_{0.002\%} = Ae^{-x}$, was also employed as a benchmark to represent the Young's modulus of the clean FB sand. In the case of overall shape of the modulus reduction curve, some 20 data points were extracted within the range, $\varepsilon = 0.002\% - 0.1\%$, for each Young's modulus reduction curve. The *b*-value was then calculated at all data points for all test specimens and mean square error was averaged for the selected strain range. Note that the calculated *b*-values are slightly different from each other nevertheless they are within a narrow range of values.

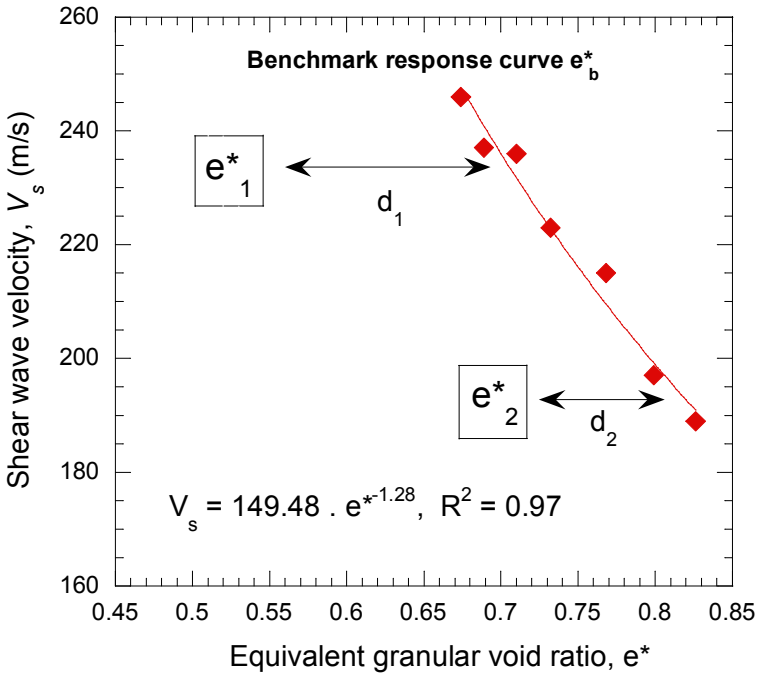

Figure 5-1 Definition of distance of the computed e^* from the clean sand benchmark response curve, $d = e^* - e^*_b$

Once the best fit b-value has been determined, the corresponding e^* values are computed and hence the response curves of all data points for sand with fines can be plotted together. These response curves should come to a single trend with a narrow band surrounding the clean sand data points, indicating that similar values of e^* give similar soil response, irrespective of the fines percentage. The fact that a good correlation based on the least square error is achieved is the main advantage of this method.

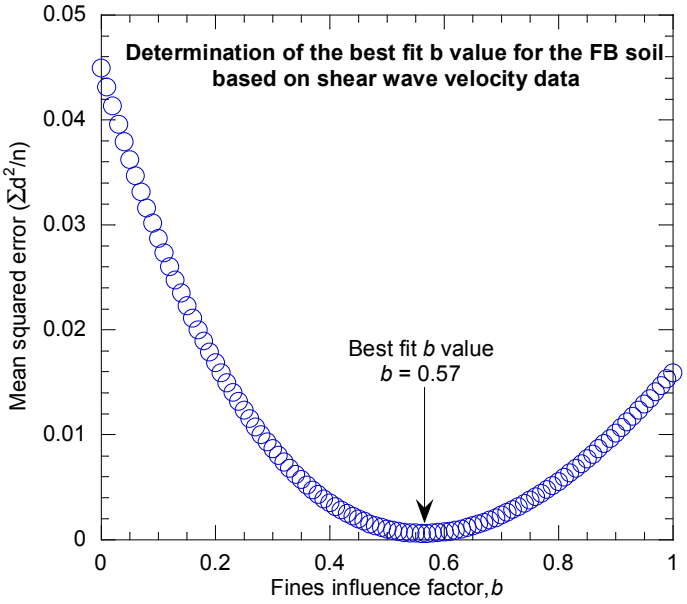

Figure 5-2 Determination of the best fit *b*-value for the FB soil based on shear wave velocity test results

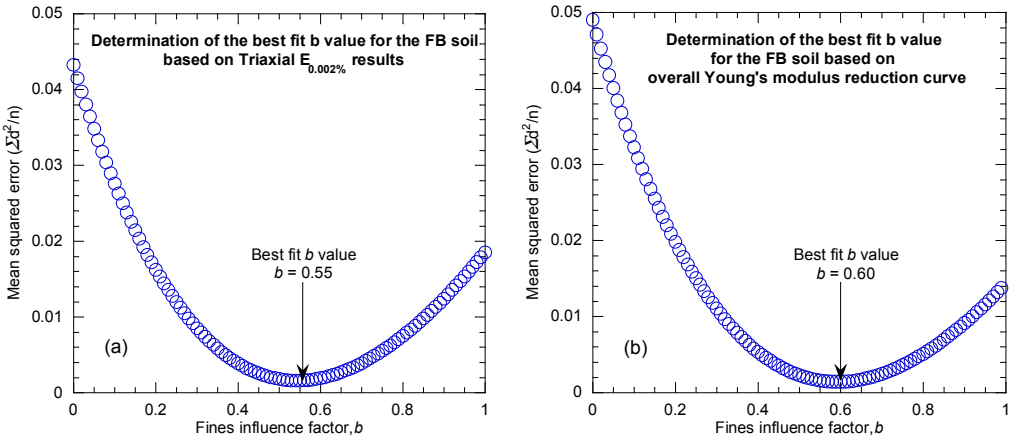

Figure 5-3 Determination of the best fit *b*-value for the FB soil based on triaxial Young's modulus, (a) at small strain Young's modulus $E_{0.002\%}$ (b) for overall modulus curves at strains 0.002%-0.1%.

While the *b* value defines the influence factor, the term $(1\text{-}b).f_c$ gives the quantity of inactive fine particles by weight proportion within the whole specimen. Figure 5-4 illustrates how the $(1\text{-}b).f_c$ term varies with increasing fines content for the FB soil when the shear wave velocity is considered. The line $b = 0$ corresponding to zero

fines influence is displayed for reference, and $b = 1.0$ corresponds to the horizontal x-axis. The line indicating the constant b value and the solid symbols for individual influence factors calculated at each level of fines content are also displayed in Figure 5-4.

It is shown that the required adjustment $(1 - b) f_c$ to the global void ratio in the denominator and the numerator of equation (5-1) increases with increasing fines content, implying the fines affect the response more at higher fines content. In addition, the influence factor can change with a variation in fines content as the relative location of the individual data points to the solid line implies. For instance, the solid symbol at f_c = 10%, lies above the line corresponding to b = 0.57 which means the actual b-value is lower than 0.57 for the specimens with f_c = 10%. However, the solid line in Figure 5-4 shows that using a constant value for the fines influence factor can be a reasonable and useful approximation for the dynamic response of FB soil. Needless to say, this trend should be treated with great caution, as the amount of data to study the effects of fines content on b value is limited for the modulus properties of FB soil.

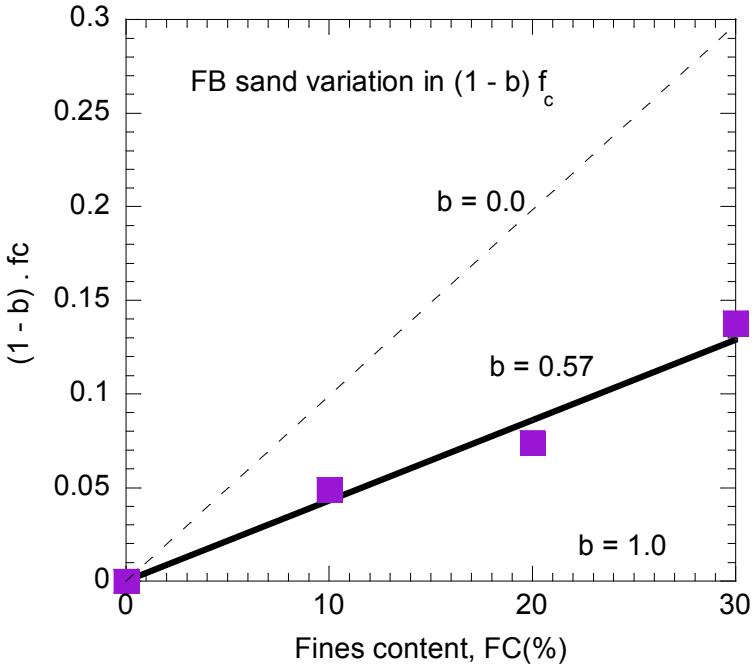

Figure 5-4 Variation in $(1 - b).f_c$ as the fines content of the FB soil is increased

5.2.2 Predicting the *b* value

As was explained in the previous section, the parameter *b* is commonly back analysed in the literature (e.g. Cubrinovski and Rees, 2008, Thevanayagam and Mohan, 2000, Ni et al., 2004) meaning that a single trend is achieved irrespective of fines content among the considered soil responses. However, this procedure does not take into account the effects of physical parameters of soil including fines content, disparity ratio, angularity and coefficient of uniformity. In addition, large amount of test data is required to perform the back calculation. To circumvent some of these limitations, Rahman (2009) developed a semi-empirical equation for predicting the value of *b* so that equivalent granular void ratio, e^*, can be predicted from the void ratio, *e*. The proposed equation by Rahman (2009) is expressed as:

$$b = \left[1 - \exp\left(-\mu \frac{(f_c / f_{cth})}{k}\right)\right]\left(r \frac{f_c}{f_{cth}}\right)^r \tag{5-3}$$

where f_c and f_{cth} = fines content and threshold fines content, respectively; $r = \chi^{-1}$ = d_{50}/D_{10} (where D is the diameter of the coarser grains and d is the diameter of the fines, and subscript 10 and 50 denote 10% lower fractal and median value, respectively), $k = \left(1 - r^{0.25}\right)$ and μ is the calibration constant which is equal to 0.3 for a large dataset (Rahman, 2009). In this context, the b value increases with fines content and disparity ratio, $D_{10,sand}/d_{50,fine}$, also influences the b value. However, the fines content should be less than the threshold fines content, f_{cth}, so the regime of fines-in-sand matrix stands valid and the suggested generalized functional relationship is applicable.

The calculated b value using the above equation for FB soil is shown by solid circles in Figure 5-5. Note that the diameters presented in Table 5-1 have been employed in order to estimate the parameter b at each corresponding fines content value. In order to illustrate how the influence factor varies with the disparity ratio using the above equation, similar plots are presented for slightly different disparity ratios. It is clear that as the disparity ratio decreases, the influence factor increases which is consistent with the binary packing theory. The prediction equation estimates the influence factor, at its highest, to be slightly over 0.40 whereas the back-analysis procedure resulted in higher b values between 0.55 and 0.6. Hence, the use of equation (5-3) for estimating the b-value for FB soil may lead to underestimation of the activity of fines in the force-chain structure.

Table 5-1 Size properties of tested sand and fines

Soil	D_{50} (mm)	D_{10} (mm)
FB sand	0.168	0.089
F fines	0.016	-

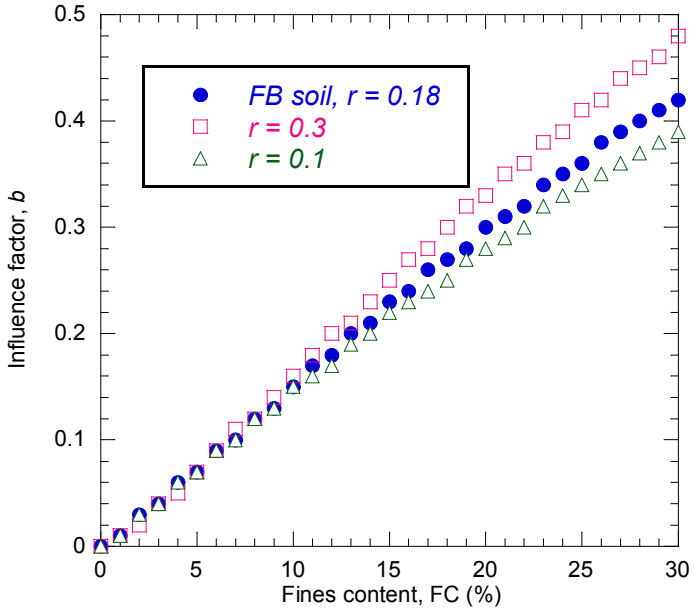

Figure 5-5 Effects of disparity ratio χ on the b-value of different fines content

5.3 Interpretation of effects of fines content on the V_s using the e^*

This section uses the equivalent granular void ratio, e^*, as the soil density state measure to investigate the effects of fines on the shear modulus properties of FB soil. The fines influence factor values, were derived using the procedures described in the previous sections and therefore equivalent granular void ratios can be calculated using equation (5-1). Shear wave velocity is an important parameter required for dynamic

response analyses of earth structures. The shear wave velocity curves of FB soils are presented in Figure 5-6 using the back-calculated value of the fines influence factor and equivalent granular void ratio. The solid line represents the overall trend for all data points using e^*.

Figure 5-6 firstly shows there is significantly less scatter in the shear wave velocity versus the equivalent granular void ratio relationship, as compared to the V_s versus global void ratio relationship as was illustrated in Figure 4-4. This is not surprising given that the value of $b = 0.57$ was back-calculated to best-fit the observed test data, but it does indicate that a constant b value can provide a unique and reasonably accurate V_s-e^* relationship for the FB soils with fines content from 0 to 30%. Based on Figure 5-6, the shear wave velocity of any FB soil with $f_c < f_{cth}$ can be estimated using the equation displayed in this figure or alternatively the clean sand benchmark response curve can be employed for the same purpose. In other words, if the fines content $FC < 30\%$ and the behaviour is characterized based on a sand-matrix, then the effects of fines can be evaluated with reference to clean sand. Hence, the equivalent granular void ratio, e^*, can be a useful density state parameter in order to normalize the effects of fines and establish a unique correlation between the V_s and the modified void ratio irrespective of fines content. This normalisation allows the comparison of the behaviour of the clean and fines-containing sand at an identical density state, e^*.

Using the back-calculated value of the influence factor, $b = 0.57$, also suggests that approximately 60% of the fines added to the clean FB sand actually participate in the soil stress-chain structure, and 40% of the fines simply occupy the voids in the soil matrix without contributing to force transfer. This means that fines can greatly

influence the soil response and therefore this effect needs to be taken into consideration.

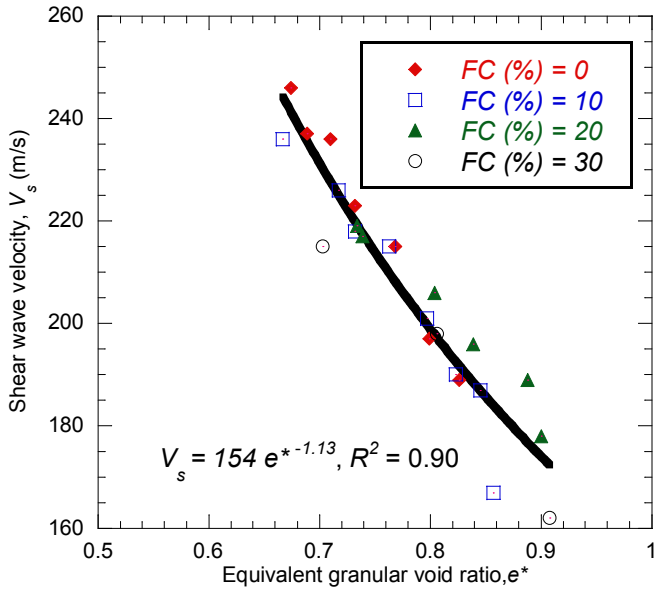

Figure 5-6 Shear wave velocity of the FB soils using the equivalent granular void ratio as the state measure with back calculated *b*-values

The shear wave velocity data points are replotted in Figure 5-7 versus e^* using the *b*-value predicted by equation (5-3). Furthermore, all the data points are represented by a single power-type trend line with R^2 = 0.77. This figure shows a higher scatter compared to the back-calculation method when R^2 was measured as 0.90. One of the great advantages of the back-calculation method is that a good correlation can be achieved based on least mean square method. The trend lines are plotted and compared for both methods in Figure 5-8. Overestimation of equivalent granular void ratio, using the predicted *b*-value, at a constant shear wave velocity is an indication of lower participation factor, *b*, in the calculation of e^*. However if the constant parameter μ in equation (5-3), is recalibrated, on the procedure explained by Rahman (2009), against the FB test results, the prediction equation can calculate the e^* adequately as shown by the dotted curve in Figure 5-9a and b. Therefore for this

method to be useful, the experimental dataset is required beforehand for calibration purposes. This shortcoming puts this method in the same league as the back-calculation method.

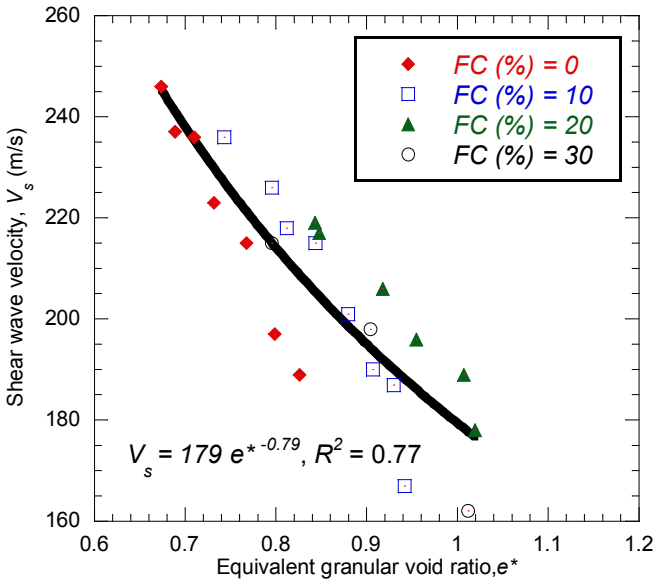

Figure 5-7 Shear wave velocity of the FB soils using the equivalent granular void ratio as the state measure with *b*-value calculated by equation (5-3)

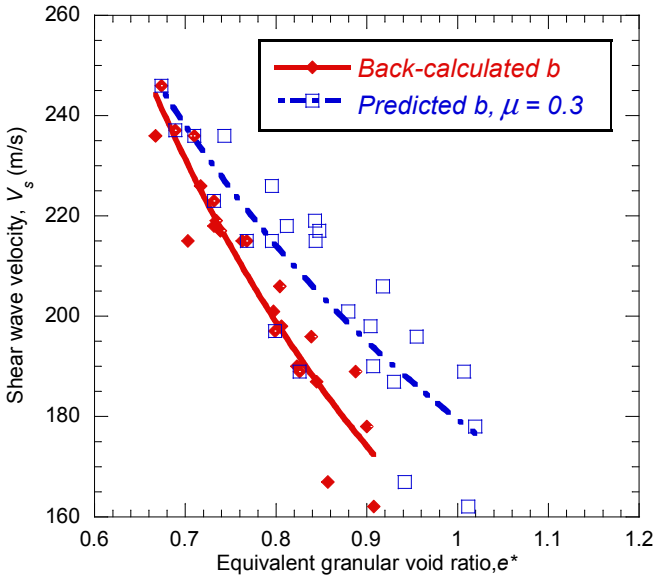

Figure 5-8 Comparison of shear wave velocity versus equivalent granular void ratio, e^*, obtained by back-calculation and prediction equation (5-3)

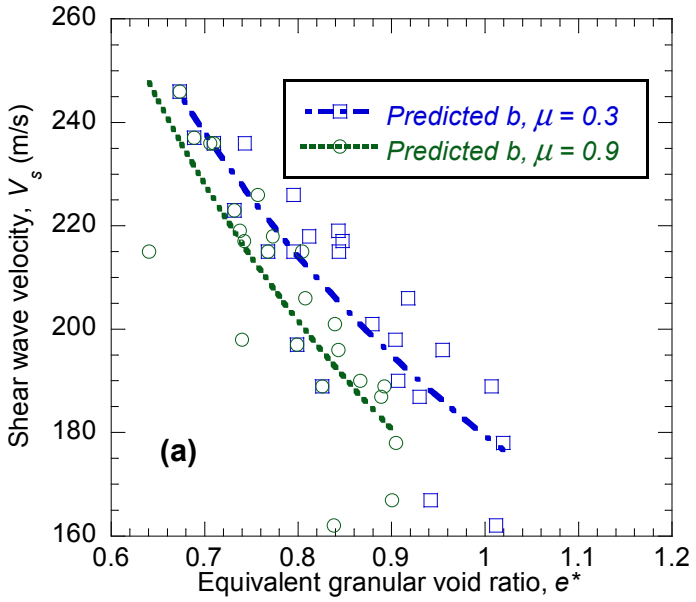

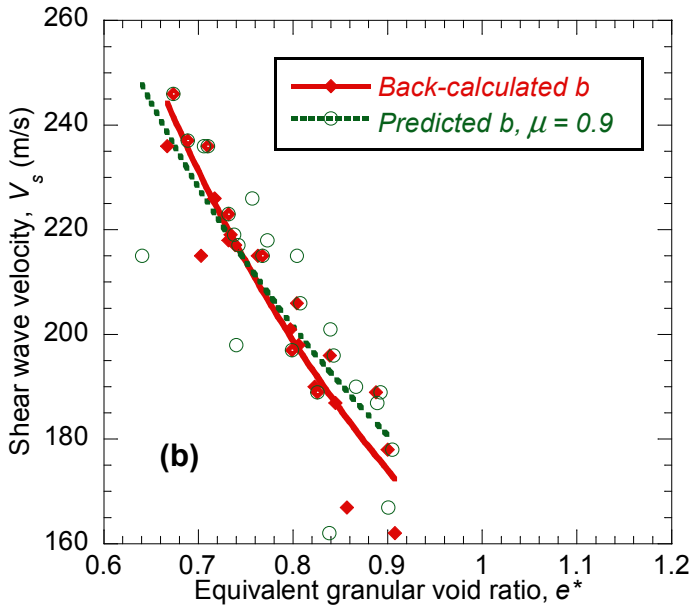

Figure 5-9 (a) Comparison of shear wave velocity versus equivalent granular void ratio, e^*, assuming $\mu = 0.3$ and 0.9 in prediction equation (5-3), (b) comparison of shear wave velocity versus equivalent granular void ratio, e^*, obtained by back-calculation and prediction equation (5-3) using $\mu = 0.9$

5.4 Interpretation of effects of fines content on the G_{max} using the e^*

Likewise, the effects of fines on the shear modulus of the sandy soils can also be interpreted using the equivalent granular void ratio as the density state measure. Figure 5-10 presents the maximum shear modulus curves of the FB soils, with a fines influence factor $b = 0.57$ being back-analysed using the approach described in section 5.2.1. The G_{max} data for all sand/fine mixes collapse into a single narrow band. It correlates better with e^* than with e because the equivalent granular void ratio represents more closely the active contacts than global void ratio. This shows clearly that for the fines-containing sands the direct use of e to estimate G_{max} from maximum shear modulus versus void ratio relationships can be unconservative.

Further, equation (5-3) is also used to predict b-values for different fines content FC using the $\mu = 0.3$ as suggested by Rahman (2009), then the void ratio, e, was converted to e^* using equation (5-1). The computed equivalent granular void ratio were used to re-plot the maximum shear modulus of all experimental data points versus modified void ratio G_{max}-e^* as shown in Figure 5-11. A significant spread is evident in this case with a coefficient of determination R^2 value of 0.69 compared to 0.93 when back-calculation method was used to estimate the b value (Figure 5-12). This clearly shows that the prediction equation (5-3) requires calibration of its parameters for each set of fines-containing sand before it can be used to calculate the b-values.

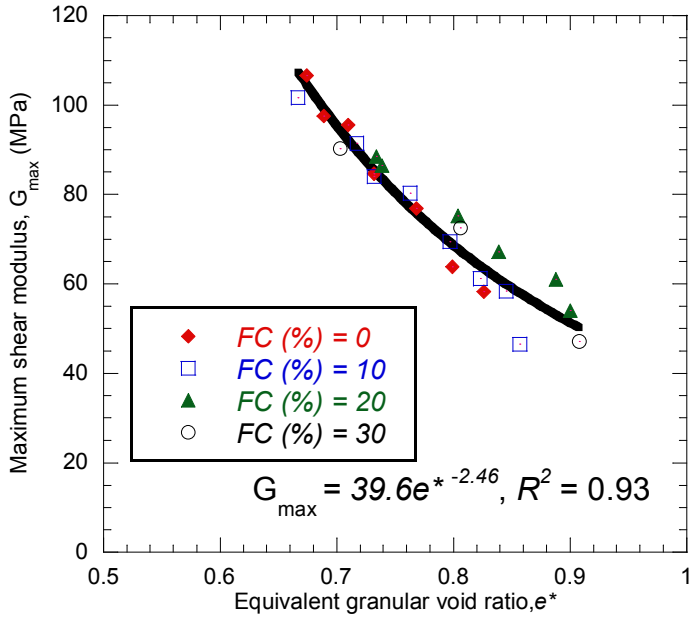

Figure 5-10 Maximum shear modulus, G_{max}, versus estimated equivalent granular void ratio using back-calculated *b*-value

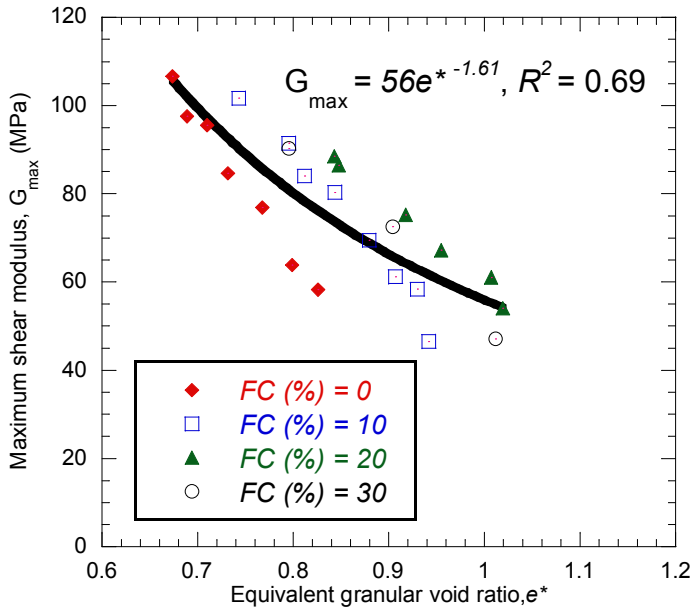

Figure 5-11 Maximum shear modulus, Gmax, versus estimated equivalent granular void ratio using prediction equation (5-3)

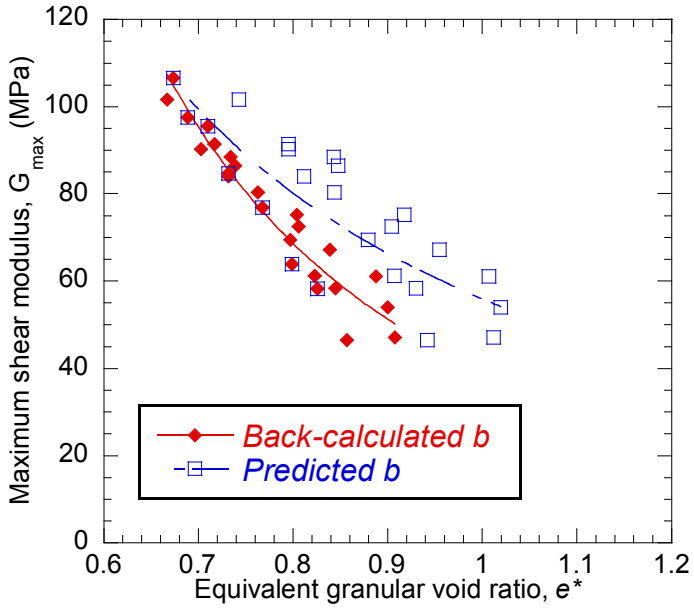

Figure 5-12 Comparison of maximum shear wave moduli versus equivalent granular void ratio, e*, obtained by back-calculation and prediction equation (5-3)

5.5 Interpretation of effects of fines content on the modulus reduction curves using the e*

Previous sections discussed the effects of fines on the low-strain dynamic properties of FB soil using the equivalent granular void ratio. In this section, the effects of fines on the nonlinear modulus reduction curves of the sandy soils are also interpreted using the *e**. Figure 5-13 presents the Young's modulus reduction curves of the FB soils, with a fines influence factor b = 0.6 being back-calculated using the procedure described in section 5.2.1. The modulus reduction curves in Figure 5-13 are located in proximity to one another, close to the FB clean sand curve. The curves suggest that similar values of e* correspond to similar reduction of modulus for the FB soils, as was the case for the stiffness as discussed in the previous sections.

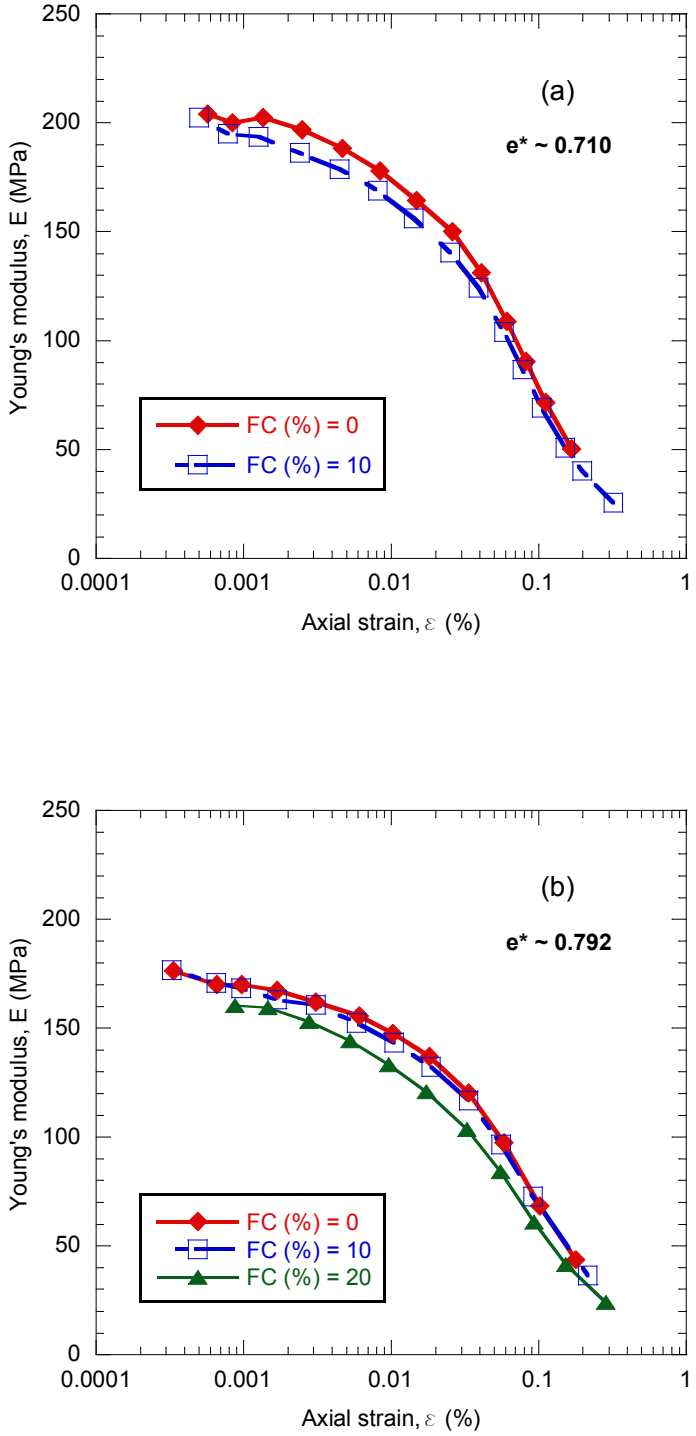

Figure 5-13 Young's modulus reduction curves of various FB sandy soils at similar equivalent granular void ratios, (a) e^* = 0.710 and (b) e^* = 0.792

5.6 Summary

This chapter interpreted the dynamic properties of FB sandy soil using the equivalent granular void ratio, e^*. This parameter differentiates between sand and fines-sized particles and accounts for different levels of fines participation in the soil force transfer during loading. It was shown that both low-strain and high-strain modulus properties are similar when the test specimens had similar values of e^*. It was therefore concluded that e^* could be used as a normalizing parameter for the effects of fines on the dynamic properties if appropriate values of the fines influence factor, b, were used. Such values could be either back-calculated or predicted by semi-empirical equations. For the FB specimens back-calculation resulted to similar b values when different modulus parameters were employed. Interpreting the shear wave velocity the influence factor was back-calculated to be $b = 0.57$, whereas it was $b = 0.55$ and 0.6 when the low-strain Young's modulus and Young's modulus reduction curve were employed, respectively. Discrepancy was observed in the case of employing the generalized function relationships to predict the b value. Data-specific calibration of the input parameters might be required to obtain better correlations. This will negate the predictive capability and will reduce the method to that of back-calculation.

6 Stress-strain model for cyclic response of sands

This chapter discusses modelling of cyclic stress-strain behaviour of soil for total stress seismic site response analysis, in particular, a simple model that can produce a desired stiffness and hysteretic damping for a given strain level as observed in laboratory testing. The constitutive model employs a modified hyperbolic equation as the backbone curve, and uses a modification of the extended Masing unloading-reloading relationship simultaneously leading to correct representation of measured modulus reduction and damping curves, particularly for larger strain levels. A set of cyclic strain loading histories with variable amplitudes are used to demonstrate the model's performance and its capability to allow improved modelling of the magnitude of energy dissipation based on the experimental tests explained in the previous chapters.

6.1 Background

6.1.1 Modulus reduction and damping relationships

The dynamic response of soil deposits at a given site, commonly referred to as site response, has a significant influence on the ground motion hazard of engineered structures. The basic properties that typically need to be determined in order to characterize a particular soil site include the shear modulus, G, and material damping ratio, h, amongst others (e.g. Kramer, 1996). The shear modulus can be prescribed as either: the tangent shear modulus, G_t, or the secant from the origin to a point on the stress-strain curve as illustrated in Figure 6-1 and known as secant shear modulus, G_s. The damping ratio, h, is a measure of the proportion of dissipated energy to the

maximum retained energy during a single cycle of shear deformation as illustrated in Figure 6-1.

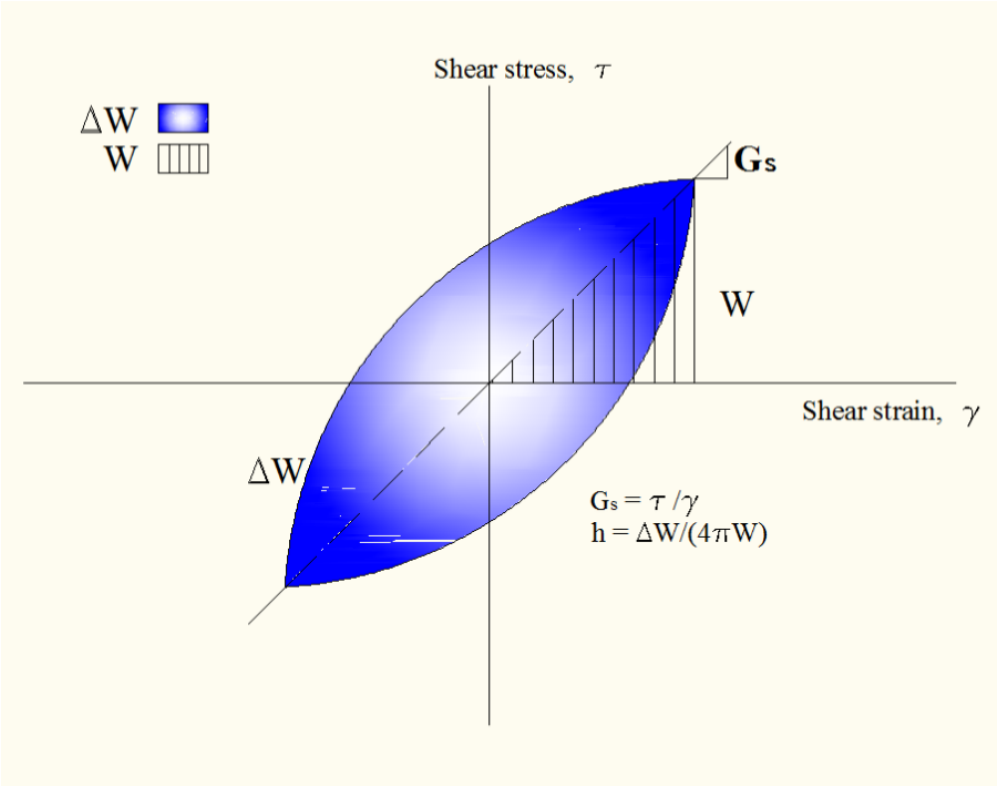

Figure 6-1 Secant shear modulus, G_s, and material damping ratio, h, during cyclic loading

As was explained in previous chapters, the relationship between secant shear modulus, G_s, and shear strain amplitude,γ, is commonly characterised by the normalized shear modulus reduction curve (e.g. Figure 6-2a). For the sake of brevity, secant shear modulus will be denoted by G in the following chapters. Furthermore, the nonlinearity in the stress-strain relationship, which leads to energy dissipation per loading cycle, results in the material damping ratio, h, which increases with increasing shear strain as shown in Figure 6-2b.

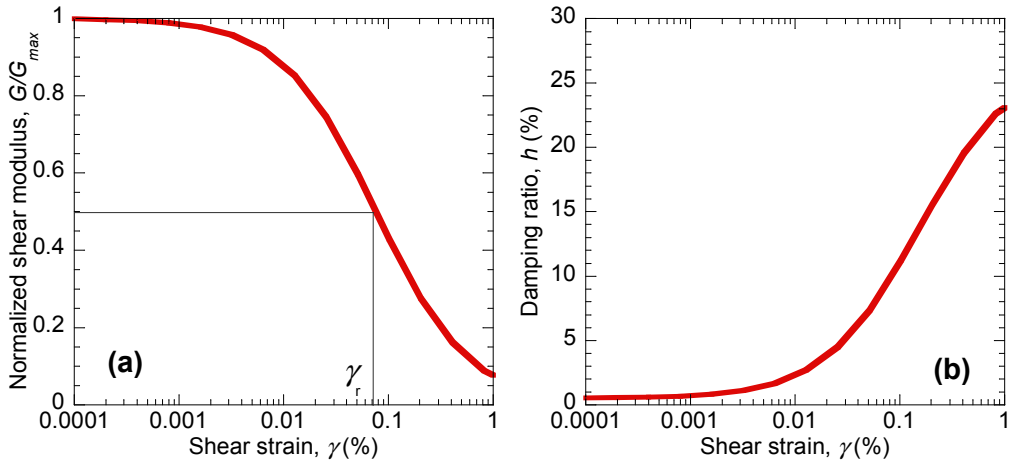

Figure 6-2 (a) Normalized modulus reduction curve and, (b) nonlinear material damping ratio curve. The reference shear strain, γ_r, is that for which $G/Gmax$=0.5.

6.1.2 Site response analysis approaches

In order to predict soil response in future possible earthquake-induced ground shaking, mathematical models are required in order to quantify local site effects via simulation. The constitutive relations of soil are too complicated to be fully described by a single equation. Three general broad classes of soil models have been proposed, namely equivalent linear models (e.g. Schnabel et al., 1972, Kottke and Rathje, 2010), cyclic stress nonlinear models (e.g. Matasovic and Vucetic, 1993, Ramberg and Osgood, 1943, Hashash and Park, 2001), and advanced constitutive models, generally based on plasticity theory (Mroz, 1967, Momen and Ghaboussi, 1982, Dafalias, 1986, Kabilamany and Ishihara, 1990, Cubrinovski and Ishihara, 1998). Equivalent linear analysis is the simplest and most widely employed scheme for 1D analysis, but has several important limitations. On the other hand, plasticity theory-based constitutive models, which are in principle applicable to any arbitrary strain or loading path for 2D or 3D problems, often require numerous parameters which must be determined through laboratory and field tests and this limits their use for many practical problems (Kramer, 1996).

6.1.3 Constitutive models for nonlinear site response analysis

In many practical cases, such as level ground response analyses when pore pressures are not significant, the boundary value problem under study is restricted to one spatial dimension, and the soil is deformed in the simple-shear condition (i.e. 1D wave propagation with horizontally-polarized vertically-propagating shear waves). In such cases it may be more practical to construct a constitutive model which can approximately simulate the nonlinear relationship between the shear stress and strain components involved in the problem, rather than using advanced constitutive models, or simple equivalent linear scheme. The models of this type, referred to herein as 'nonlinear cyclic models', can adequately represent the stress-strain curve of the soil during cyclic loading. A conventional way of constructing a nonlinear cyclic model is based on the concept of a backbone curve which relates the shear stress amplitude, τ, to the shear strain amplitude, γ, during monotonic loading (this gives an equivalent modulus reduction relationship), with general rules for unloading and reloading (which provides an equivalent damping relationship) (e.g. Kramer, 1996).

Generally, the shape of the backbone curve is determined by the maximum shear modulus, G_{max}, shear strength, τ_{max}, and several curve-fitting constants. Matasovic and Vucetic (1998) proposed a modified hyperbolic equation as a backbone curve based on an earlier work by Hardin and Drnevich (1972), which assumes the following form:

$$\mathrm{F_{bb}} = \tau = \frac{G_{\max}\gamma}{1+\beta\left|\frac{G_{\max}\gamma}{\tau_{\max}}\right|^{a}} \tag{6-1}$$

where F_{bb} = τ = shear stress; γ = shear strain, a and β are dimensionless factors which adjust the shape of the curve along the ordinate and control the curvature to represent a wide range of measured soil behaviour. Alternatively, equation (6-1) can be reformatted into the normalized modulus reduction curve as follows:

$$\frac{G}{G_{\max}} = \frac{1}{1+\beta\left|\frac{G_{\max}\gamma}{\tau_{\max}}\right|^{a}} \tag{6-2}$$

In the original form proposed by Hardin and Drnevich (1972) $a = \beta = 1$. In this model, the reference strain is considered a material constant and is defined as:

$$\gamma_r = \frac{\tau_{\max}}{G_{\max}} \tag{6-3}$$

A practical problem with the definition of reference strain, γ_r, is that the shear strength is often not available. Therefore, a pseudo-reference strain is proposed to be used for low to moderate strain levels (Stewart et al., 2008). The pseudo-reference strain is defined from a laboratory modulus reduction curve as the shear strain at which $G/G_{max} = 0.5$, as shown in Figure 6-2a. This definition results from a hyperbolic fit of the modulus reduction curve according to the original form of equation (6-2). The advantage of using the pseudo-reference strain is that in the absence of material-specific tests, empirical relationships exist to predict it from other state parameters such as mean effective stress, plasticity index and, over-consolidation ratio (e.g. Darendeli, 2001). a and β are fitting parameters generally taken as $a \leq 1$ and $\beta > 1$, respectively. If a value is adopted as greater than one, the shear stress reaches a maximum value at $\gamma_m = \sqrt[a]{\frac{\gamma_r^a}{a-1}}$, as shown in Figure 6-3a.

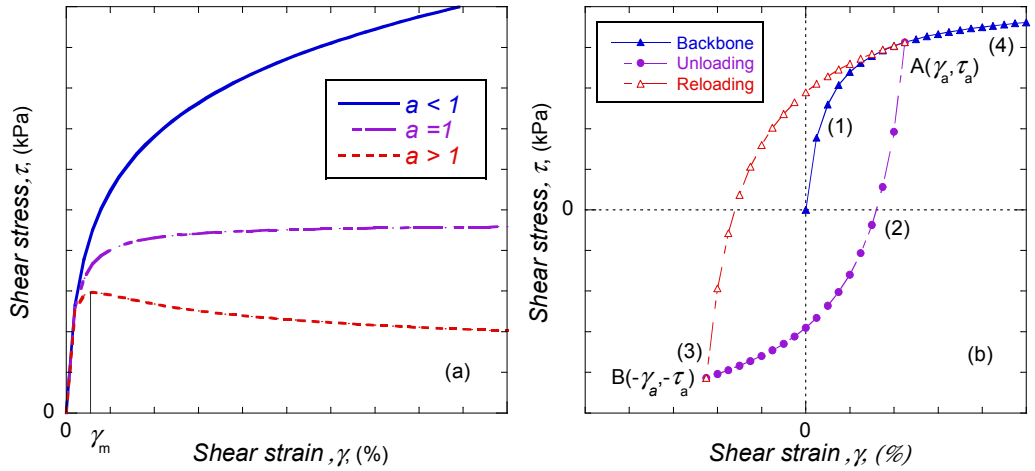

Figure 6-3 (a) Effect of *a* on hyperbolic curve, (b) a hyperbolic backbone curve and Masing unloading-reloading branches

A set of unloading-reloading rules are assumed to describe the hysteresis loop in conjunction with the backbone curve, as shown in Figure 6-3b. These rules generally depend on: the cyclic stress-strain loading history described by the preceding cycles; stiffness degradation caused by previous repetitive loading; and the rate of cyclic straining (e.g. Vucetic, 1990). It has been widely accepted that two rules, originally proposed by Masing (1926), can be used as a basis for modelling the cyclic nonlinear stress-strain behaviour of granular material incorporating the loading history. The first Masing criterion postulates that the tangent shear moduli on each reversal point of the unloading or reloading branches of the loop assumes a value equal to the initial tangent modulus for the backbone loading curve. Furthermore, according to the second criterion, if a stress reversal occurs at a point defined by (γ_a, τ_a) the hysteresis curves are the same as that of the initial backbone curve, except that the scale is enlarged by a factor of $n = 2$, as shown in Figure 6-3b; this is expressed mathematically by the following equation:

$$\frac{\tau-\tau_a}{n}=F_{bb}\left(\frac{\gamma-\gamma_a}{n}\right) \tag{6-4}$$

Pyke (1979) appended an additional two rules to the Masing rules for irregular loadings. In the first, if the unloading or reloading curve exceeds the maximum past strain, and intersects the backbone curve, it follows the backbone curve until the next reversal point. In the second, if an unloading or reloading curve intersects previous unloading or reloading curves, the path follows that of the previous curve. Pyke (1979) noted that these four rules are applicable only to the behaviour of a material with non-degrading strength properties. Collectively these four rules are often referred to as the 'extended Masing rules'.

6.1.4 Implied damping using the extended Masing rules

The adequacy of the mathematical modelling of unloading/reloading can be examined by comparing the observed and modelled damping ratio with shear strain. By applying Masing rule to a hyperbolic model the damping ratio at each strain level can be shown to have the following expression (e.g. Ishihara 1996):

$$h=\frac{4}{\pi}\left[1+\frac{1}{\frac{\gamma_a}{\gamma_r}}\right]\left[1-\frac{\ln\left(1+\frac{\gamma_a}{\gamma_r}\right)}{\frac{\gamma_a}{\gamma_r}}\right]-\frac{2}{\pi} \tag{6-5}$$

It can be seen that damping ratio converges to a limiting value of $2/\pi = 0.637$ when shear strain amplitude becomes infinitely large. However, experimental evidence suggests that the maximum values of damping ratio for sands are in a vicinity of 0.3 or considerably smaller than the value resulting from the Masing rule (e.g. Hardin and Drnevich, 1972, Ishihara, 1996, Darendeli, 2001, Stewart et al., 2008). Figure 6-4 schematically shows that the application of Masing's rule leads to

values of damping ratio which significantly differ from corresponding experimental values, specifically an overestimation of damping at relatively large shear strains. The overestimation of hysteretic damping induced by employing Masing criteria can unconservatively lead to underestimation of some of the seismic response parameters (e.g. Silva et al., 2000, Stewart et al., 2008). Therefore, the application of Masing's rules does not provide an adequate approximation for both shear modulus and damping ratio, particularly at large strains.

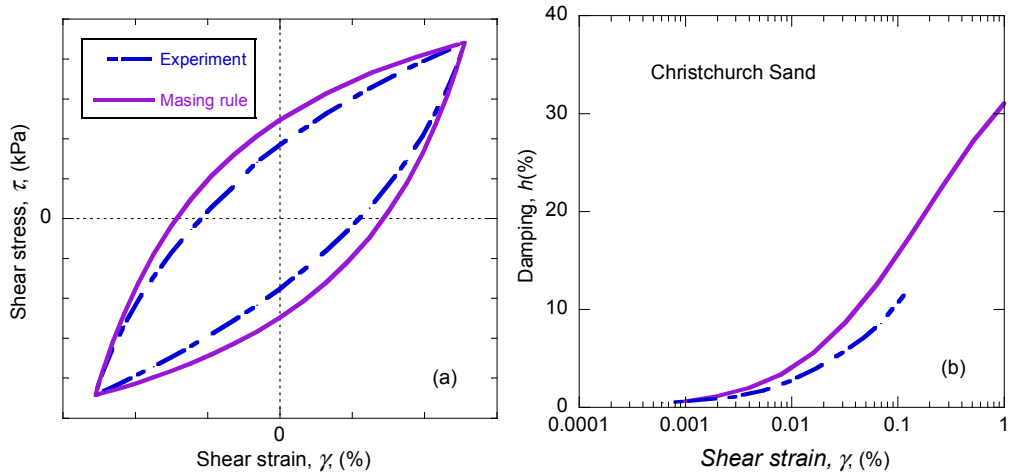

Figure 6-4 Comparison of experimental and Masing-based calculated hysteresis loop (a), damping ratio curve (b)

6.1.5 Modifications to Masing rules to achieve consistent damping

The issue of how to simultaneously approximate both the shear modulus and the damping ratio has been address by Muravskii (1998), but that proposed model was rate dependent. Later Osinov (2003) followed a similar approach to develop unloading-reloading curves which were independent from the backbone curve. Another solution of the aforementioned damping problem with Masing criteria has been proposed by Phillips and Hashash (2009). Based on an earlier work by Darendeli (2001), Phillips and Hashash (2009) developed a reduction factor to modify the unloading-reloading equations from those of the Masing criterion. Equation (6-6)

presents the functional form for the damping reduction factor proposed by Phillips and Hashash (2009).

$$F(\gamma_m) = p_1 - p_2\left(1 - \frac{G_{\gamma_m}}{G_{\max}}\right)^{p_3} \tag{6-6}$$

where $G_{\gamma m}$ is secant modulus corresponding to the maximum shear strain level, γ_m; and p_1, p_2 and p_3 are non-dimensional coefficients selected to obtain the best possible fit with the target damping curve. This damping reduction factor given by equation (6-6) is used in the unloading-reloading relationship given by equation (6-7) (Hashash et al., 2010):

$$\tau = F(\gamma_m)\left[2\frac{G_{\max}\dfrac{\gamma-\gamma_a}{2}}{1+\beta\left(\dfrac{\gamma-\gamma_a}{2\gamma_a}\right)^a} - \frac{G_{\max}(\gamma-\gamma_a)}{1+\beta\left(\dfrac{\gamma_m}{\gamma_a}\right)^a}\right] + \frac{G_{\max}(\gamma-\gamma_a)}{1+\beta\left(\dfrac{\gamma_m}{\gamma_a}\right)^a} + \tau_a \tag{6-7}$$

While functional form in equations (6-6) and (6-7) provide consistency between the experimental and mathematical damping curves, the tangent modulus at the point of reversal is not equal to G_{max}, because of the use of the reduction factor. This is inconsistent with experimentally recorded hysteresis loops which illustrate that the tangent modulus immediately after load reversal is approximately equal to the low-strain modulus for a wide variety of soils under cyclic loading and moreover should be independent of the strain amplitude of the loop (e.g. Hardin and Drnevich, 1972a, Hardin, 1978). A similar shortcoming is observed for the model proposed by Osinov (2003). Moreover, equation (6-7) is highly dependent on the use of the Darendeli (2001) model which relates the damping ratio curve to that of normalized shear modulus. As a consequence, arbitrary normalized shear modulus and damping curves may not be simulated adequately using the model of Phillips and Hashash (2009).

Given a soil model for symmetrical loadings, Pyke (1979) proposed an alternative unloading-reloading rule in which the Masing coefficient n can deviate from 2, in order to extend the Masing model for use with irregular loadings. A factor $n > 2$ allowed simulation of cyclic hardening, while cyclic softening could be modelled by assuming a value of $n < 2$ (Lo Presti et al., 2006). This same idea can be employed to simulate any target damping ratio curve by modifying the Masing criterion, and is the approach developed further in the remainder of this section.

6.2 Modelling concept of the stress-strain relationship

The hysteresis curve for the stress-strain relationship developed herein is constructed in such a way that it produces both the required modulus reduction and damping ratio as functions of the strain amplitude for soil under cyclic loading. The backbone describing the monotonic stress-strain curve is modelled using the modified hyperbolic relationship stated in equation (6-1). The cyclic behaviour, or unloading-reloading branches, is modelled using a modified version of Masing criterion. An empirical parameter, ϕ, is introduced for the unload-reload curves. Moreover, the parameter, n, is allowed to vary depending on the desired level of hysteretic damping.

6.2.1 Modulus degradation curve

In order to simulate the experimental modulus reduction curves with the hyperbolic function given by equations (6-1) and (6-2), G_{max} and γ_r are measured from experimental tests. The least square error method is employed to estimate the fitting parameter, a, in the hyperbolic model; while the β factor is considered to be equal to 1. Therefore a set of parameters, (G_{max}, γ_r, a), for the modified hyperbolic equation are computed for experimental tests in order to determine the backbone curve. It is further

explained in Appendix A that the best-fit curvature coefficient, a = 0.98, for all the tested specimens in this study. The fitted hyperbolic relationships for experimental cyclic loading data for Fitzgerald Bridge (FB) sand are shown in Figure 6-5. The plots show the stress-strain curves obtained in tests with different combination of void ratio and fines content. It can be seen that the hyperbolic relationship is able to accurately model the stress-strain response over a wide range of shear strain with considerable accuracy (given the limited number of model parameters).

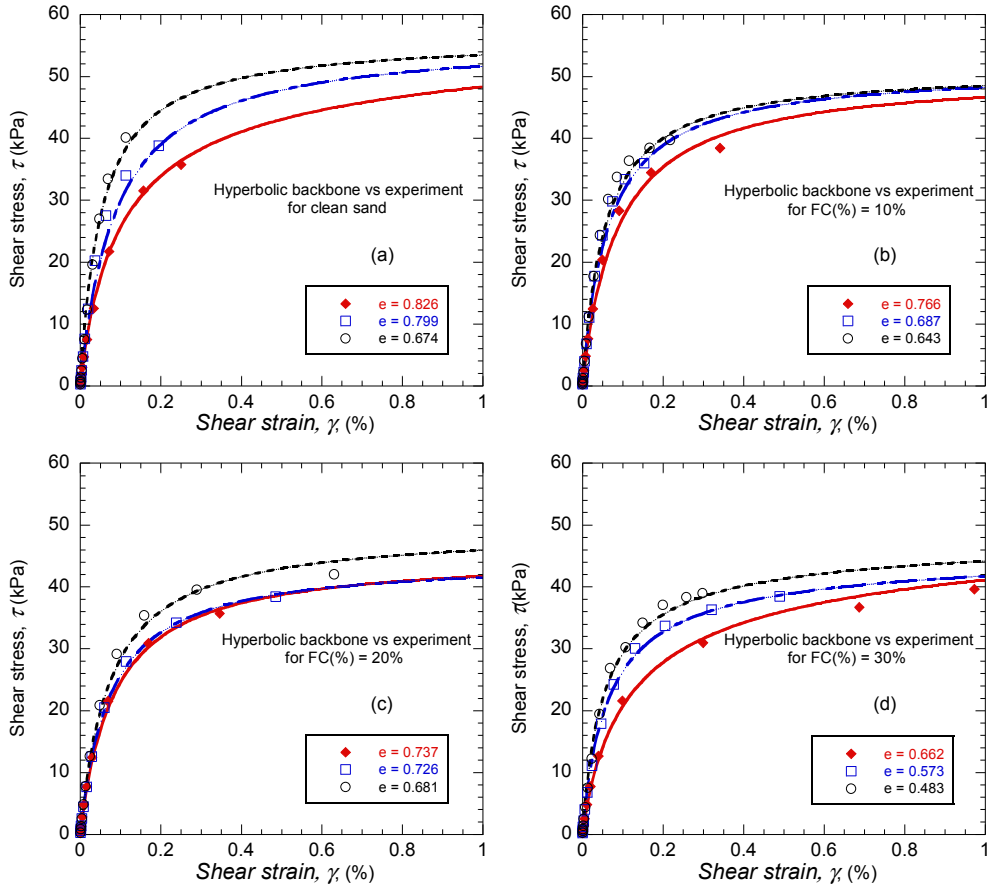

Figure 6-5 Comparison of hyperbolic stress-strain skeleton curve with experimental test results for FB sand with different fines content. The experimental results are for drained cyclic triaxial tests with the effective confining stress 100 kPa, number of cycles N = 10

It is important to note that the hyperbolic stress-strain relationship best-fit to FB sand experimental data shown in Figure 6-5, are valid for only the considered shear

strain levels in the laboratory. As the proposed model may be used for ground response subject to earthquake motions, which induce large shear strain in the soil profile, the stress-strain relationship should be extrapolated for larger strains to capture the shear strength as well; this is further explained in Chapter 7.

6.2.2 Unloading-reloading cycles

As was explained in previous sections, the Masing rule allows the construction of hysteresis loops from a given backbone curve without resort to any functions. On the other hand, as damping characteristics of Masing's model result completely from the backbone curve and constructed hysteresis loops, they cannot be controlled independently. This leads, in most cases, to an over-prediction of damping, especially for large strain amplitudes. This comment is generally true, even if the backbone curve approximates the cyclic stiffness degradation of the soil satisfactorily (e.g. Muravskii and Frydman, 1998, Stewart et al., 2008, Ishihara, 1996). Therefore, it is necessary to have unloading/reloading rules which can be tailored to fit a given soils damping characteristics independent of the backbone curve.

The main feature of the present model in comparison to conventional models is that the damping ratio produced by unloading/reloading can be prescribed independently of the backbone curve. To preserve the simplicity of the solution proposed by Masing (1926), as well as achieving a better agreement between the experimental and modelled hysteretic damping, two conditions need to be satisfied:

1. When unloading is followed by reloading of the same amplitude, the stress-strain state should return to the same state ('reversal point') where the unloading began (similarly to the classic Masing's model) forming a closed loop for any level of shear strain.

2. The tangent shear modulus on each reversal point should assume a value equal to the initial tangent modulus for the initial loading curve, G_{max}.

To meet the first condition, antisymmetry should be satisfied, namely the two points A(γ_a , τ_a) and B(-γ_a, -τ_a) in Figure 6-3 should fall on the unloading and reloading branches. The unloading-reloading equation should contain as a parameter the absolute value of strain, γ_a, at which the point (γ, τ) leaves the backbone curve because of either unloading or reloading. This parameter remains unchanged until the point (γ, τ) intersects the backbone curve and afterwards abandons it at a new value, -γ_a. Introducing the power factor ϕ and substituting equation (6-1) into equation (6-4) yields the following expression for the general unloading-reloading function:

$$\frac{\tau-\tau_a}{n}=\frac{G_{\max}\dfrac{\gamma-\gamma_a}{n}}{\left(1+\left|\dfrac{\gamma-\gamma_a}{n\gamma_r}\right|^a\right)^{\phi}} \tag{6-8}$$

It is obvious that points *A* and *B* in Figure 6-3 both fall on the above curve considering a Masing coefficient $n = 2$ and $\phi = 1$. However, this may not be true for an arbitrary value of *n*. Rearranging equation (6-8) for ϕ, and for a general *n*-value, and entering point *B* in the equation yields:

$$\phi=\frac{\ln\left(1+\left|\dfrac{\gamma_a}{\gamma_r}\right|^{\alpha}\right)}{\ln\left(1+\left|\dfrac{2\gamma_a}{n\gamma_r}\right|^{\alpha}\right)} \tag{6-9}$$

Therefore, any adopted combination of ϕ and *n* which satisfies equation (6-9) will result to a closed loop hysteresis.

It can be shown that the derivative of the unload-reload equation at the reversal points is equal to the initial tangent modulus and hence the second condition remains valid; this was not the case for the Phillips and Hashash (2009) formulation.

The value of n in equations (6-8) and (6-9) controls the damping ratio of the cyclic response (i.e. recall that $n = 2$ for Masing rule). Substitution of equation (6-9) in equation (6-8) yields the unloading/reloading equation that can be solved iteratively for the *n*-value as a function of shear strain amplitude. Thus, the *n* value can readily be obtained by matching the damping ratio from experimental test results and the one calculated by the given closed loop. Once *n* is adopted, the curvature variable, ϕ, can be obtained using equation (6-9). Figure 6-6a and b illustrate the hysteresis loops corresponding to function (6-8) for values of cyclic strain amplitudes of γ_a = 0.4 and 0.8%, respectively. It can be observed that any target damping ratio can be simulated after computing the parameters *n* and ϕ.

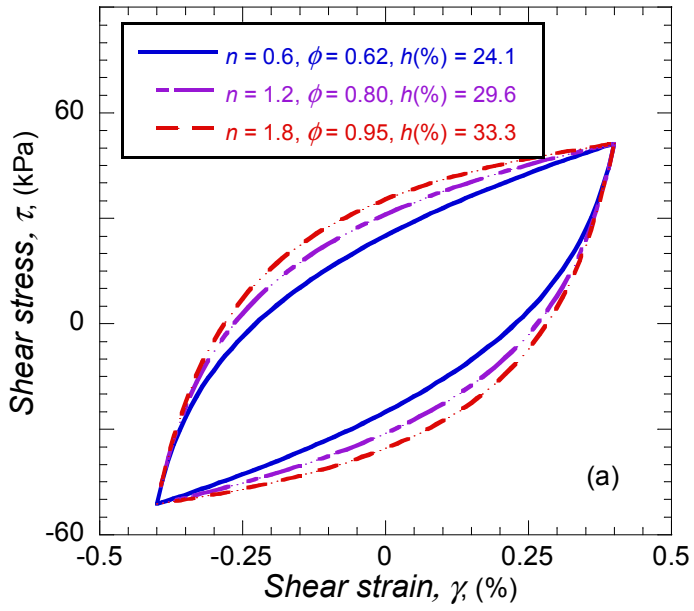

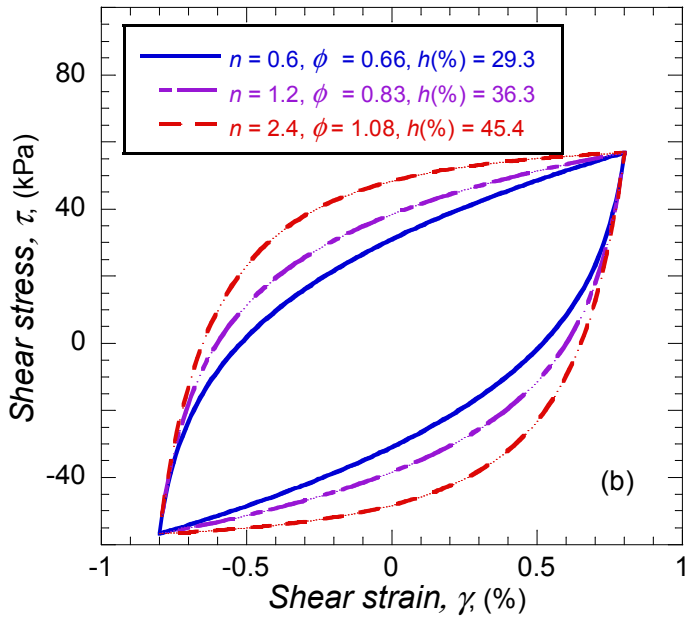

Figure 6-6 Varying the Masing coefficient, n, and curvature parameter, ϕ for two values of amplitude, (a) $\gamma_a = 0.4\%$; and (b) $\gamma_a = 0.8\%$

Hence to summarise, the proposed constitutive model utilizes equation (6-1) for the monotonic behaviour and equations (6-8) and (6-9) for the unloading-reloading equations in order to improve the match between the experimental and modelled hysteretic damping. Figure 6-7 shows the flowchart of the proposed procedure for the calculation of the model parameters. The calibration of model parameters is discussed in the subsequent section.

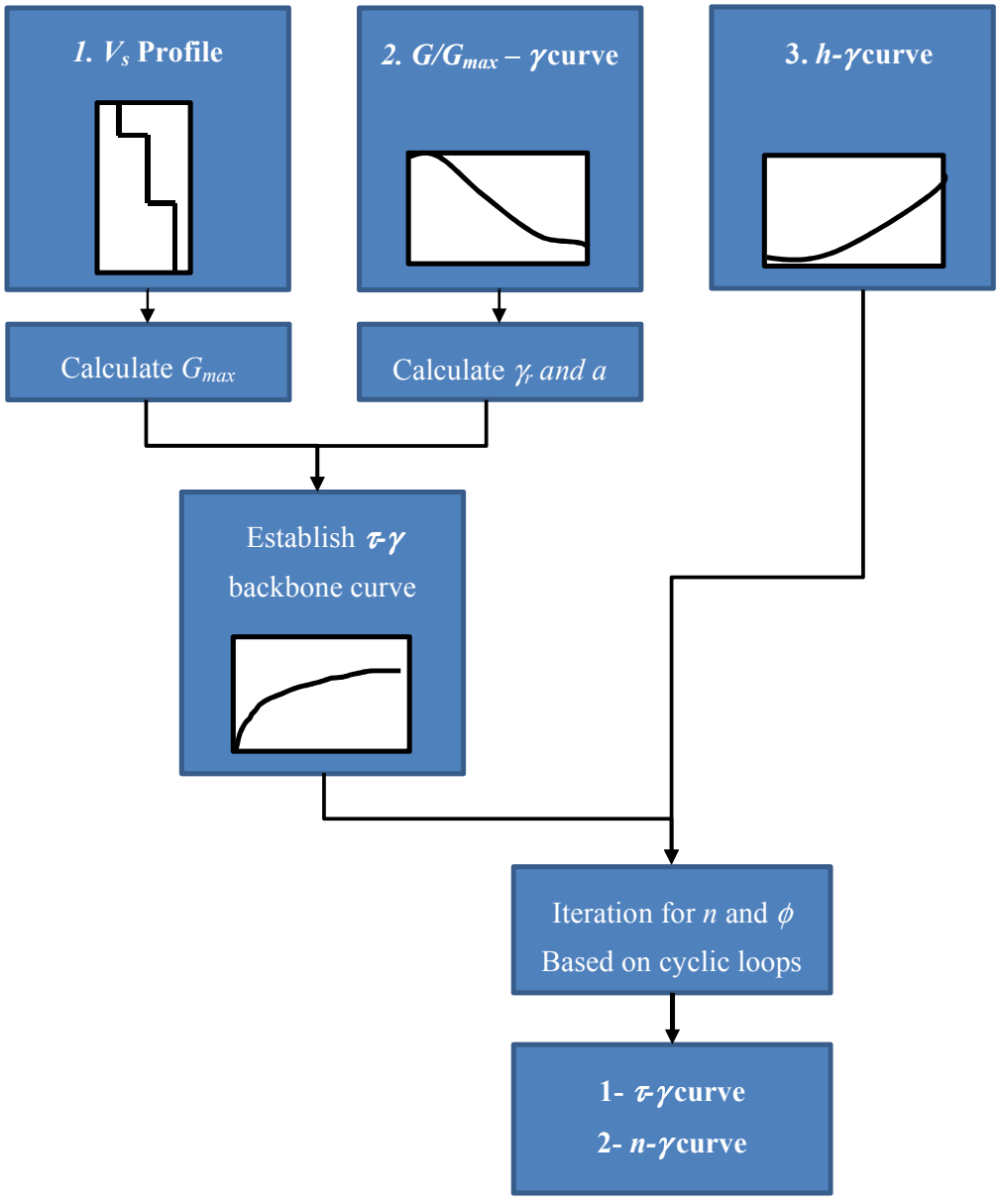

Figure 6-7 Flowchart of the proposed model

6.3 Model calibration: Experimental versus simulated damping

6.3.1 Modulus reduction calibration (parameters G_{max}, γ_r, a)

In order to illustrate the application of this model, its parameters are subsequently calibrated using measured modulus reduction and damping data from triaxial tests on FB sand samples under confining pressure of 100 kPa described in previous chapters.

The first step is the determination of the modulus reduction parameters (G_{max}, γ_r, a) based on the experimental results (extracting the backbone results from cyclic testing). This calibration is simply performed by least squares fitting as discussed with reference to Figure 6-5.

6.3.2 Unloading/reloading calibration (n)

The second step is the determination of the parameter, n, which controls the unloading/reloading response. A symmetrical cyclic shear strain time series was employed to evaluate the performance of the proposed model against the observed behaviour during laboratory testing. Similar to the experimental procedure, each strain cycle is obtained as twice the amplitude of the previous cycle. Based on the imposed shear strain time series in Figure 6-8a, the shear stress response in Figure 6-8b was computed for each specimen using the procedure explained in the previous sections.

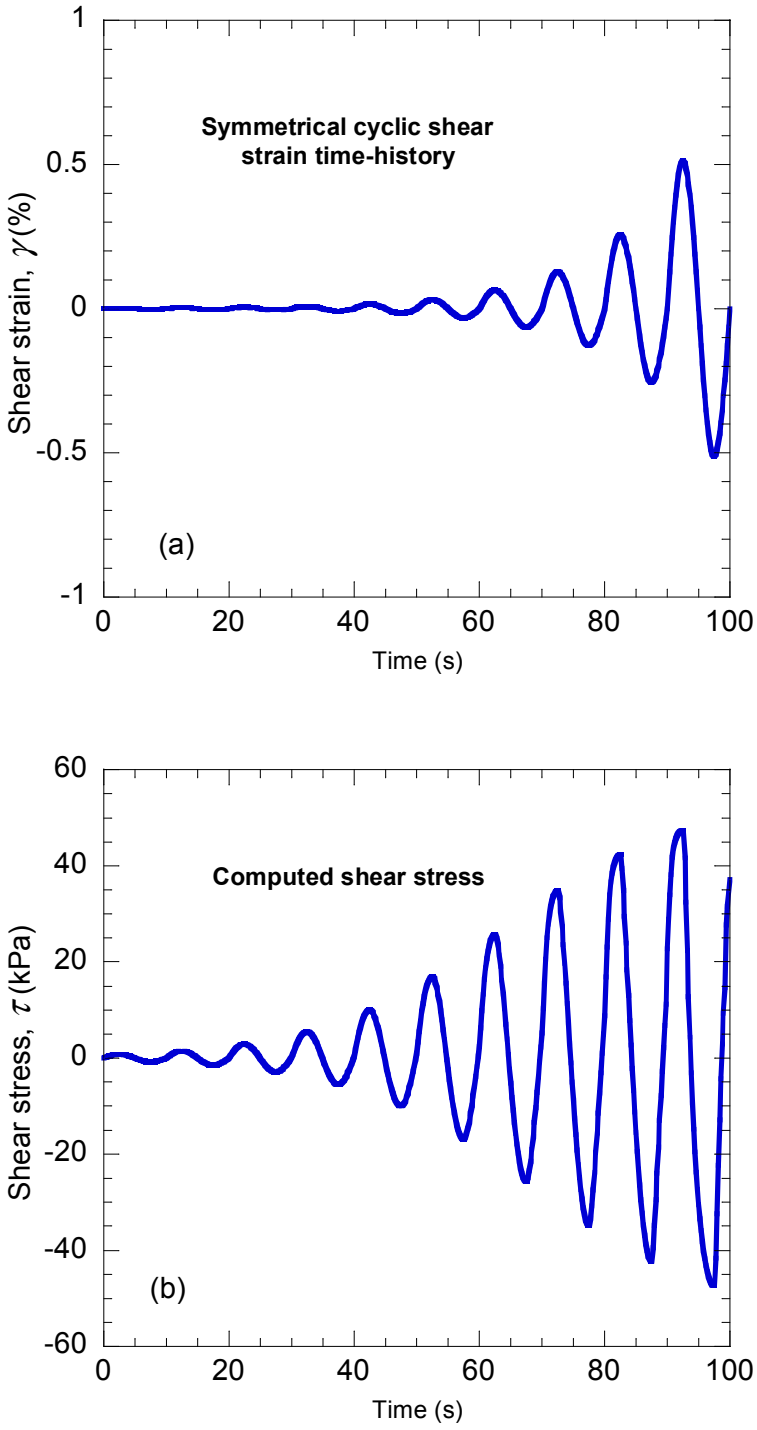

Figure 6-8 (a) Input shear-strain time history, (b) computed shear stress time history

The bisection method is employed to estimate the *n*-value through iteration steps. The starting interval is assumed to be n = [0.001, 2]; then the predicted damping ratios are compared with that observed in the experiment. The bisection algorithm modifies *n*-value until convergence to the desired damping ratio is achieved. Figure 6-9a shows the computed values of n with respect to the iteration number at the cyclic strain amplitude γ= 0.2%. At each strain amplitude level, the same procedure should be applied to compute the strain-dependent *n*-value. Figure 6-9b presents how the residual damping, which is the difference between the computed and the experimental damping ratio, reaches to zero after ~7 iterations. The sensitivity of computed damping with respected to the *n*-values is further presented in Figure 6-10.

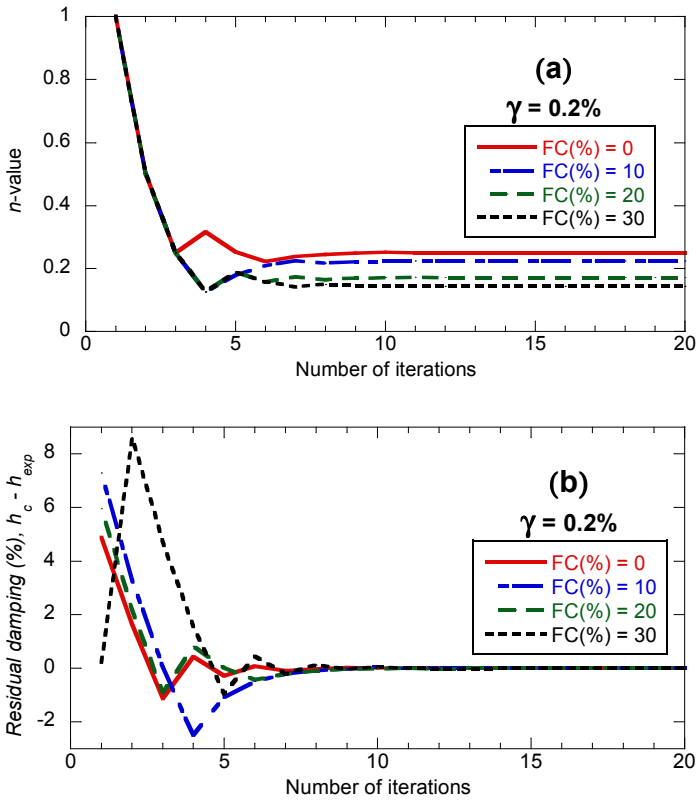

Figure 6-9 (a) The convergence of *n*-value with iterations (b) The variation of residual damping (%), the difference between computed damping ratio, h_c, and the experimental damping ratio, h_{exp}, for FB sands with variable amounts of fines content

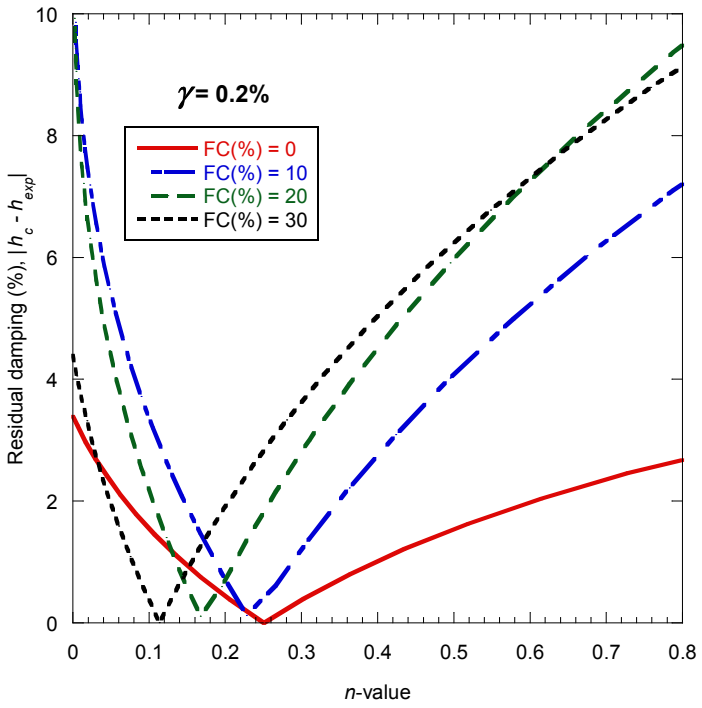

Figure 6-10 The variation of absolute value of residual damping (%), the difference between computed damping ratio, h_c, and the experimental damping ratio, h_{exp}, for FB sands with variable amounts of fines content

Figure 6-11 presents the stress-strain hysteresis loops generated by employing the Masing criteria and the proposed model explained above. The solid line represents the proposed behaviour developed here and the dashed line of the conventional Masing rule. It is illustrated that the breadth of the loops for higher strain levels are smaller for the modified relationships than the conventional Masing rule, implying lower hysteretic damping. This difference between the two methods in damping is explicitly illustrated in Figure 6-11b, d and f, which also illustrate the obtained damping ratios from experimental test results. It can be seen that the proposed model is capable of capturing the experimental damping ratios well over a wide range of shear strain amplitudes. In contrast, while a good match is obtained between Masing formulation and laboratory damping ratio when the strain amplitude is low, the Masing formulation over predicts the damping at larger strains, as previously elaborated upon.

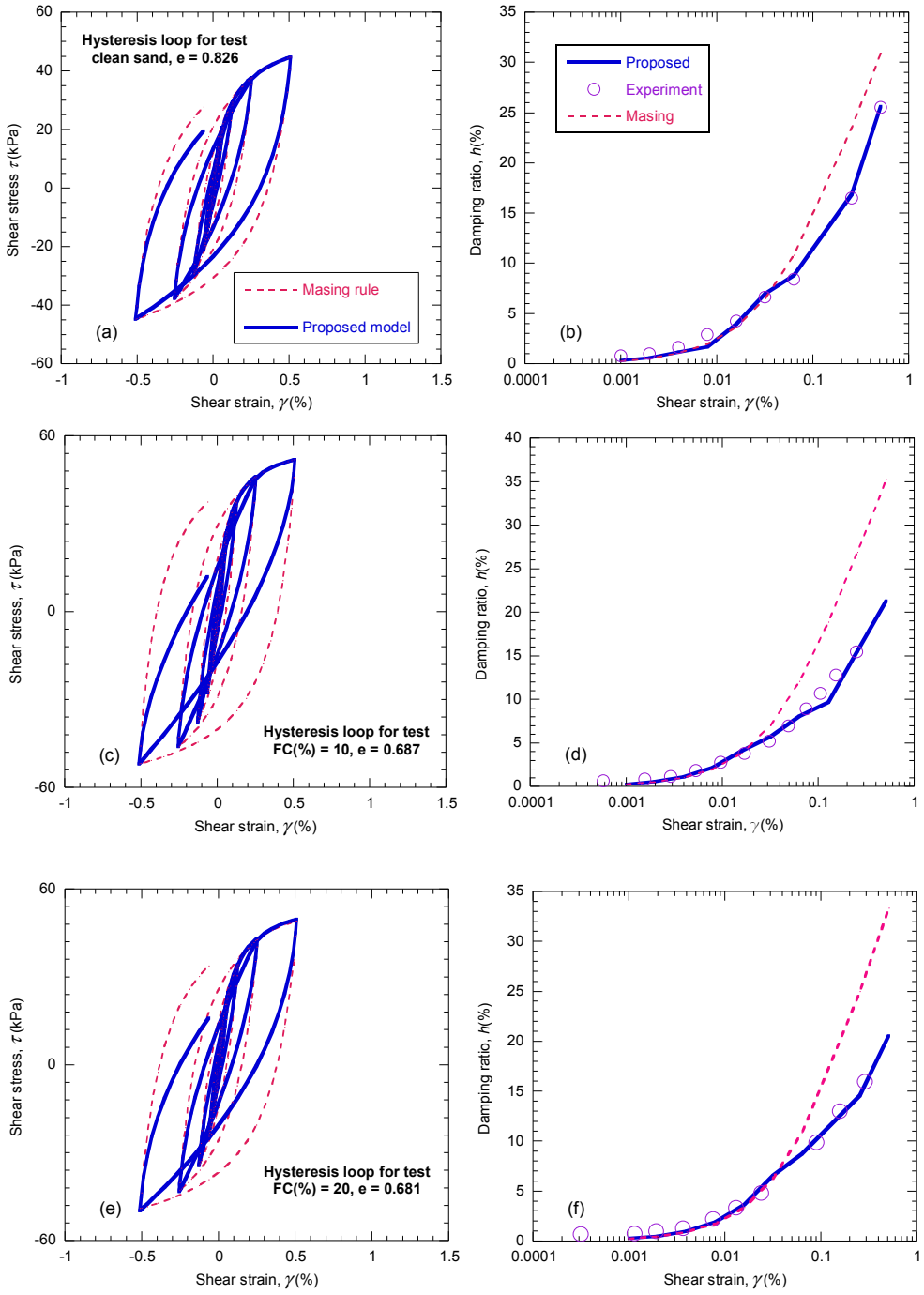

Figure 6-11 Comparison of stress-strain loops and damping curves using Masing and the proposed model for specimens with different fines content and void ratio

The performance of the proposed model with regard to variation in the mean effective stress is also investigated. Darendeli (2001) proposed an empirical model by which the normalized modulus and damping curves can be computed. Figure 6-12a and b present the damping curves for different mean effective stresses. The dotted and solid lines represent the damping produced by Masing and the proposed model, respectively. It is clear that the proposed model can produce the target damping curve very well. Figure 6-12c and d illustrate the corresponding hysteresis loops computed by the Masing and proposed model. The larger loops correspond to Masing model which results in higher hysteretic damping and larger energy dissipation.

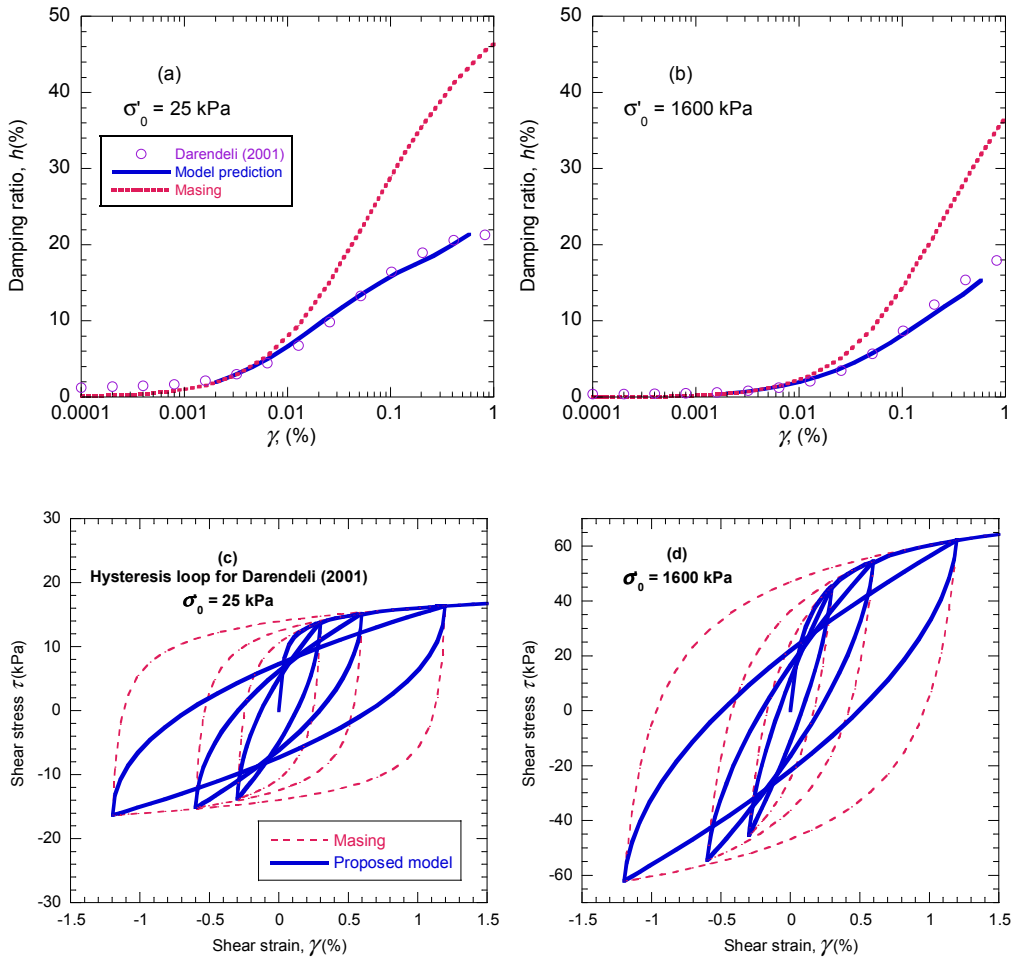

Figure 6-12 Comparison of stress-strain hysteresis loops and material damping ratio curves using Masing criteria and the proposed model for different mean effective stresses based on Darendeli (2001) model.

6.3.3 Dependence of parameter *n* on shear strain

In the proposed formulation (i.e. equations (6-8) and (6-9)) the Masing coefficient, n, is shear strain dependent and therefore is updated at every cycle with the change of shear strain level. This implementation is in contrast to the common Masing rule implementation where $n = 2$. It is desirable to compute the variation of n-value for experimental results explained in previous chapters. It was shown in Chapter 4 that the normalized modulus reduction curves of sandy soil can be slightly influenced by the percentage of fines content; however, the material damping curves were very similar and independent of fines content. In order to observe the implications of the proposed model to simulate the experimental modulus reduction and damping curves simultaneously, the average material damping curve for all tested soil specimens along with individual normalized modulus reduction curves for each percentage of fines are used.

In Figure 6-13a, b, n-values are plotted against shear strain for sands of variable fines content; power function fits to n-values are also presented with solid lines. The power function is fit to data points with shear strains larger than 0.05% because below this level, the overestimation of damping by the Masing rule is not significant. $n < 2$ is required to circumvent the overdamping issue introduced by employing Masing criterion. Despite similar material damping curves, it is noted that different n-value curves are produced; due to different modulus reduction curves. The slope and intercept of the linear fit to data points shown in Figure 6-13b are determined (Table 6-1) for each set of material damping curve and are employed to express n as a parametric function of γ. In addition to the errors associated to the numerical

calculations, the computation of the damping based on the power fit to the n-γ variation introduces further error which is examined later in section 6.4.2.

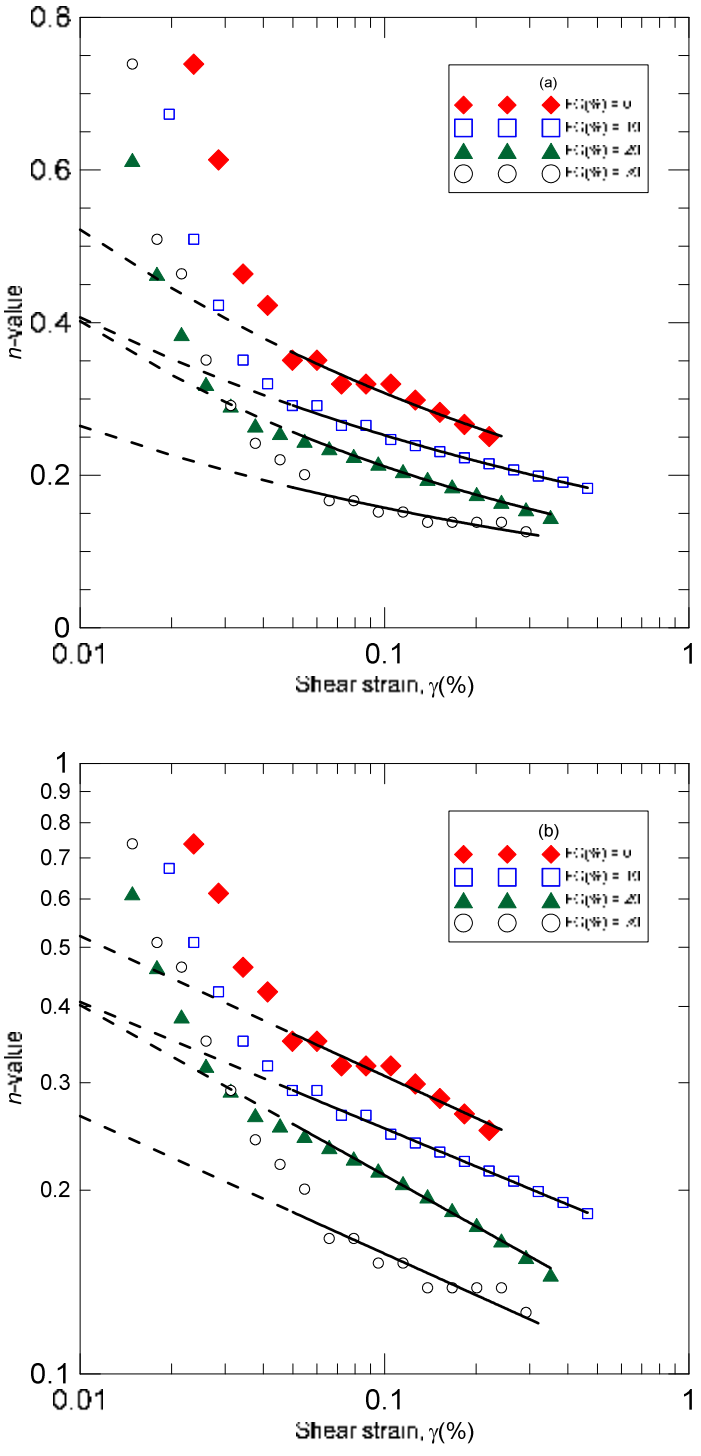

Figure 6-13 (a) n-value versus shear strain level (linear scale) (b) n-value versus γ (log scale) for FB sands with variable fines content

Table 6-1 The fitted power function to the computed n-γ curves

Fines content FC(%)	Power function $0.1 < n < 2$	Coefficient of determination R^2
0	$n = 0.181\gamma^{-0.223}$	0.94
10	$n = 0.157\gamma^{-0.207}$	0.99
20	$n = 0.111\gamma^{-0.270}$	0.99
30	$n = 0.094\gamma^{-0.226}$	0.89

The variation of n-value with regard to loading conditions is also investigated. As certain loading conditions were not considered in the experimental study presented in the previous chapters, empirical equations in the literature are used. Darendeli (2001) proposed a framework by which a family of normalized modulus and material damping curves can be computed at specified loading conditions and soil type. Figure 6-14 illustrates the material damping curves for sandy soils at various confining pressures. The simulated damping ratios calculated assuming the Masing criteria are also plotted in this figure. Employing the proposed formulation in this chapter, the variation of n-value for sandy soils under different confining pressures can be computed. Figure 6-15a shows the variation of n-value with respect to shear strain amplitude; the power function fits to the n-values are also illustrated by solid lines. The slope and intercept of the linear fit to curve shown in Figure 6-15b are also the coefficient and exponents of the power function fit in Figure 6-15a. Table 6-2 lists the power function fit to the material damping curves using least-square-error method.

The coefficient of determination is also presented in this table. The high values for R^2 implies that the power function is a good representative of the variation of n-value with the shear strain amplitude. Once a functional form is obtained for n-value in terms of shear strain for each target material damping curve, the fitted equations can be directly used in numerical site response analyses, as discussed subsequently.

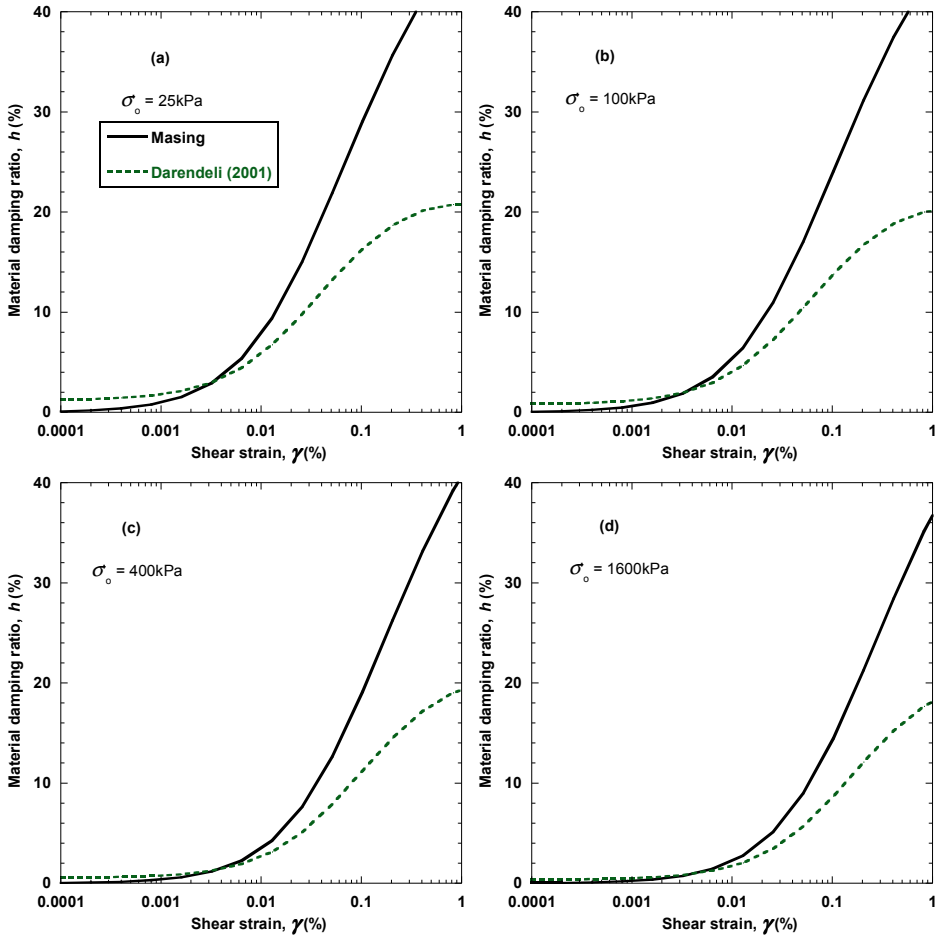

Figure 6-14 Effect of mean effective stress on material damping curves of nonplastic soils and simulated damping curves employing Masing criteria

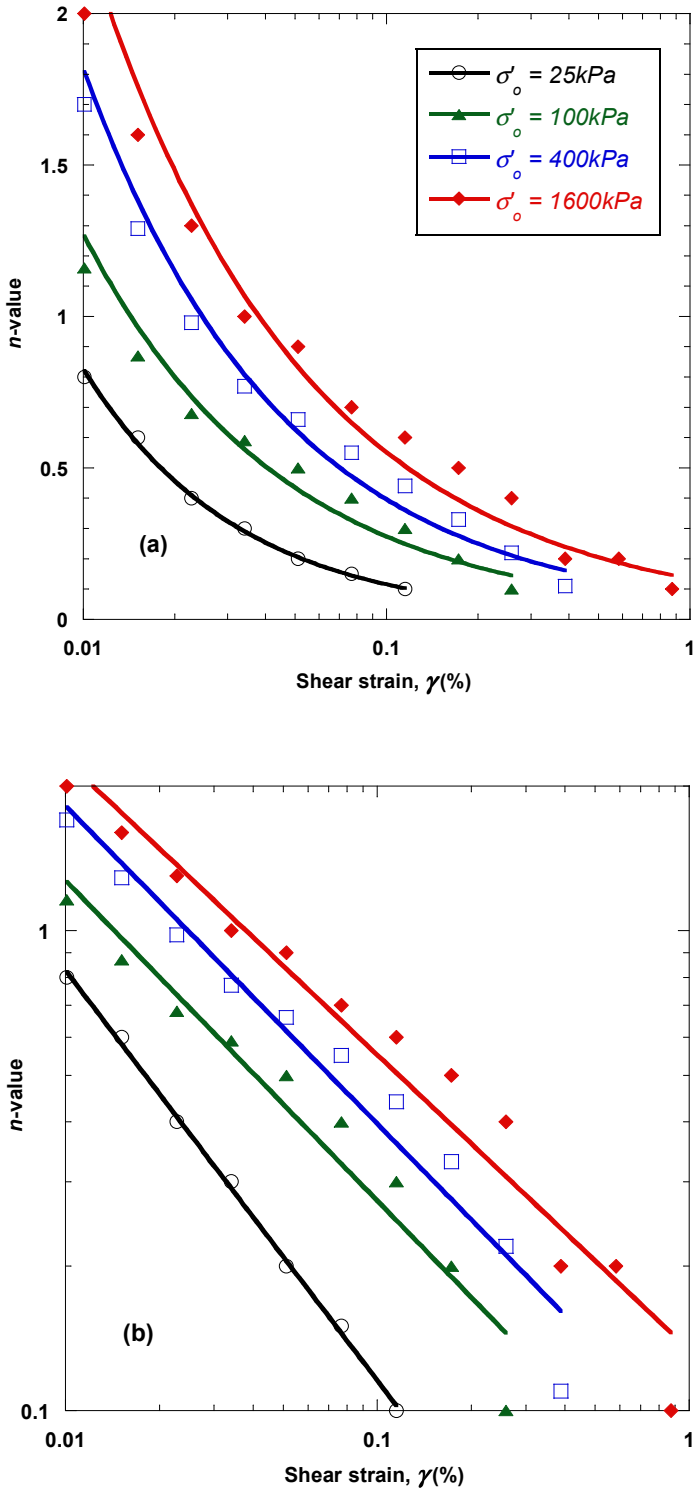

Figure 6-15 (a) n-value versus shear strain level, γ (linear scale) (b) n-value versus shear strain level, γ (log scale) for sands with variable confining pressures. Darendeli (2001) modulus reduction and damping ratio curves have been used to evaluate n-values

Table 6-2 The fitted power function to the computed *n*-γ curves for sands under different confining stresses

Confining stress (kPa)	Power function ($0.1 \leq n \leq 2$)	Coefficient of determination R^2
25	$n = 0.0162\gamma^{-0.855}$	0.99
100	$n = 0.0589\gamma^{-0.668}$	0.98
400	$n = 0.0862\gamma^{-0.663}$	0.99
1600	$n = 0.1340\gamma^{-0.615}$	0.98

6.4 Verification of the new formulation through element testing

The hierarchical nature of the OpenSees' platform structure (McKenna and Fenves, 2001) allows new material models to be conveniently added to the framework. Therefore, the new material procedure was implemented into OpenSees. By keeping element and material implementations separate in this software, the new material model can be used in an existing element without modifying the element implementation. The programming language C++ supports the data encapsulation and run-time binding necessary to achieve this complete separation of material from element (McKenna and Fenves, 2001). The proposed simple constitutive model was considered to simulate uniaxial material which provides the interface for one-dimensional stress-strain behaviour. Nevertheless, it is possible to extend the same formulation to NDmaterials which are multi-dimensional generalization of UniaxialMaterials.

Prior to the simulation of the horizontally stratified soil deposits using the proposed model, it is important to verify the constitutive model implementation to ensure that soil behaviour is implemented as expected, therefore element test simulations of the implementation of the model are performed in this section. A series of analyses corresponding to different loading patterns (monotonic, simple cyclic and irregular loadings) are presented to verify the new unloading-reloading formulation and evaluate its impact on non-linear cyclic loading. A shear strain history is specified and a shear stress history from the model is calculated. The set of element testing combinations explained herein are suggested by Stewart et al. (2008).

6.4.1 Loading histories

Firstly monotonic behaviour with small reversal of loading is examined. The purpose of including the small reversal is to test for any potential numerical instability brought upon by a small reversal and also to ensure that the third modified Masing rule is followed. It is observed in Figure 6-16c that with the increase of shear strain amplitude, shear stress also increases following a hyperbolic path. Keeping the shear strain amplitude constant at the end of loading does not change the shear stress value as shown in Figure 6-16b. Figure 6-16c also shows that the stress path follows the backbone curve once the maximum past shear strain amplitude is exceeded. Figure 6-16d illustrates the second type of test which consists of loading the element to γ= 0.8%, unloading to γ = -1% with a small reversal in the unloading path, and then reloading to γ= 1%, ensuring that the third and fourth Masing criteria are followed in the negative direction of computed stresses.

Four types of cyclic loading histories are further assessed. The first type is a symmetrical sinusoidal and harmonic strain input with constant amplitude. The

analysis can be repeated with different cyclic strain amplitudes. The purpose of using such loading is to ensure whether or not any stress accumulates in one direction under symmetric loading. Figure 6-17a-c shows that the predicted stress history is sinusoidal, constant amplitude and in-phase with the imposed strain history showing that unlike Pyke (1979) model, the predicted hysteresis loops do not change with repeated cycles. The second type of harmonic loading history gradually increases in amplitude to 1% (Figure 6-17, right frame). It is seen that the unloading-reloading curve follows the backbone curve once the maximum past shear strain is exceeded. The third type of loading is similar to the second type except that after reaching 1% of shear strain, the amplitude gradually decreases back to zero as shown in left frame of Figure 6-18. This is to test constitutive behaviour for successive cycles of different amplitudes. The predicted stress histories are in-phase with the imposed strain history and the change in the stress amplitude follows the trend of strain amplitude. Lastly, a constant-amplitude sinusoidal loading with biased straining in positive strain direction is imposed. As shown in the right frame of Figure 6-18, stress amplitude is modelled as expected even the time history of the input strain is asymmetrical.

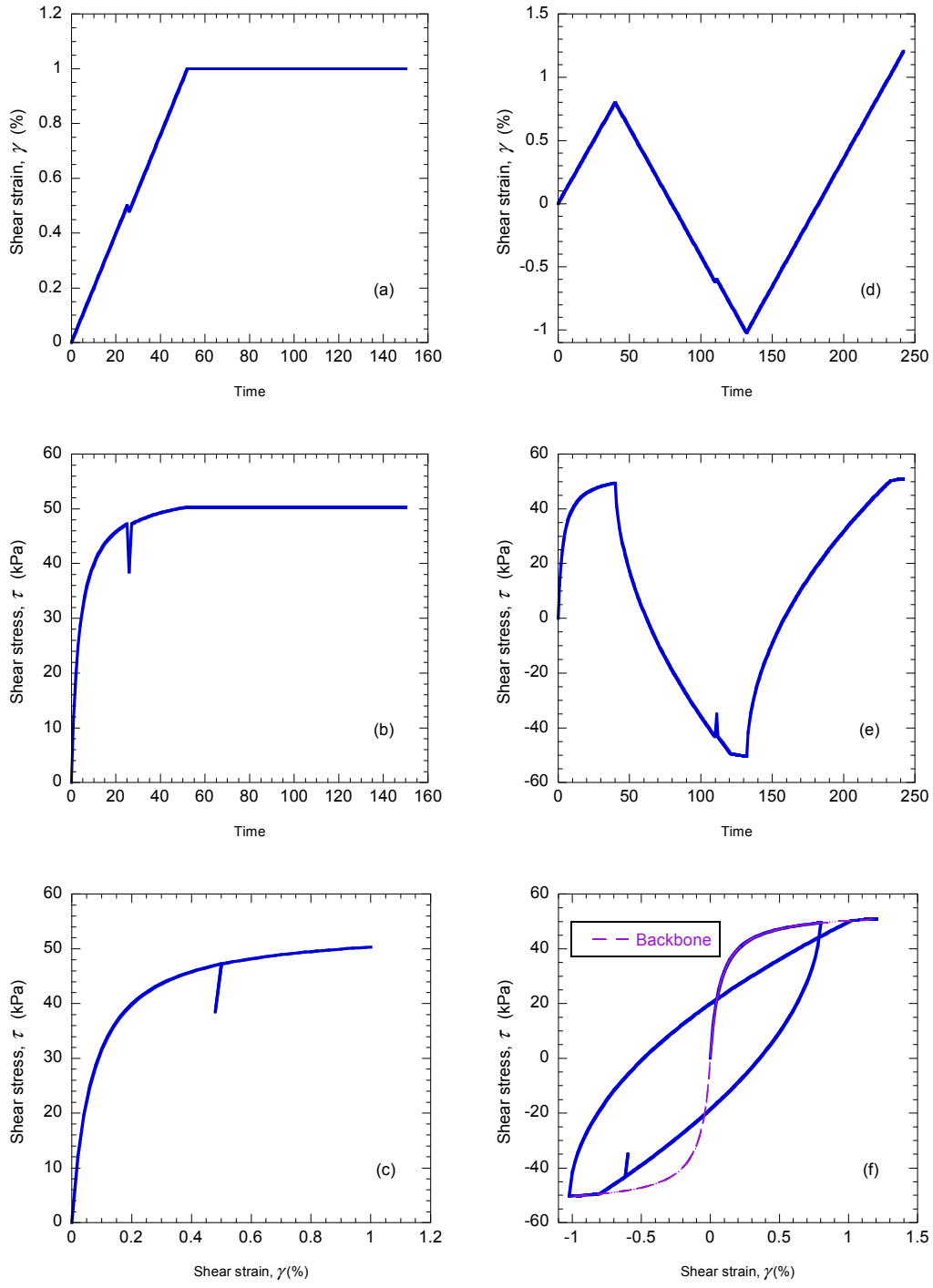

Figure 6-16 Results of monotonic with a small reversal loading stress-strain (a-c); non-symmetrical cycle with irregular loading (d-f)

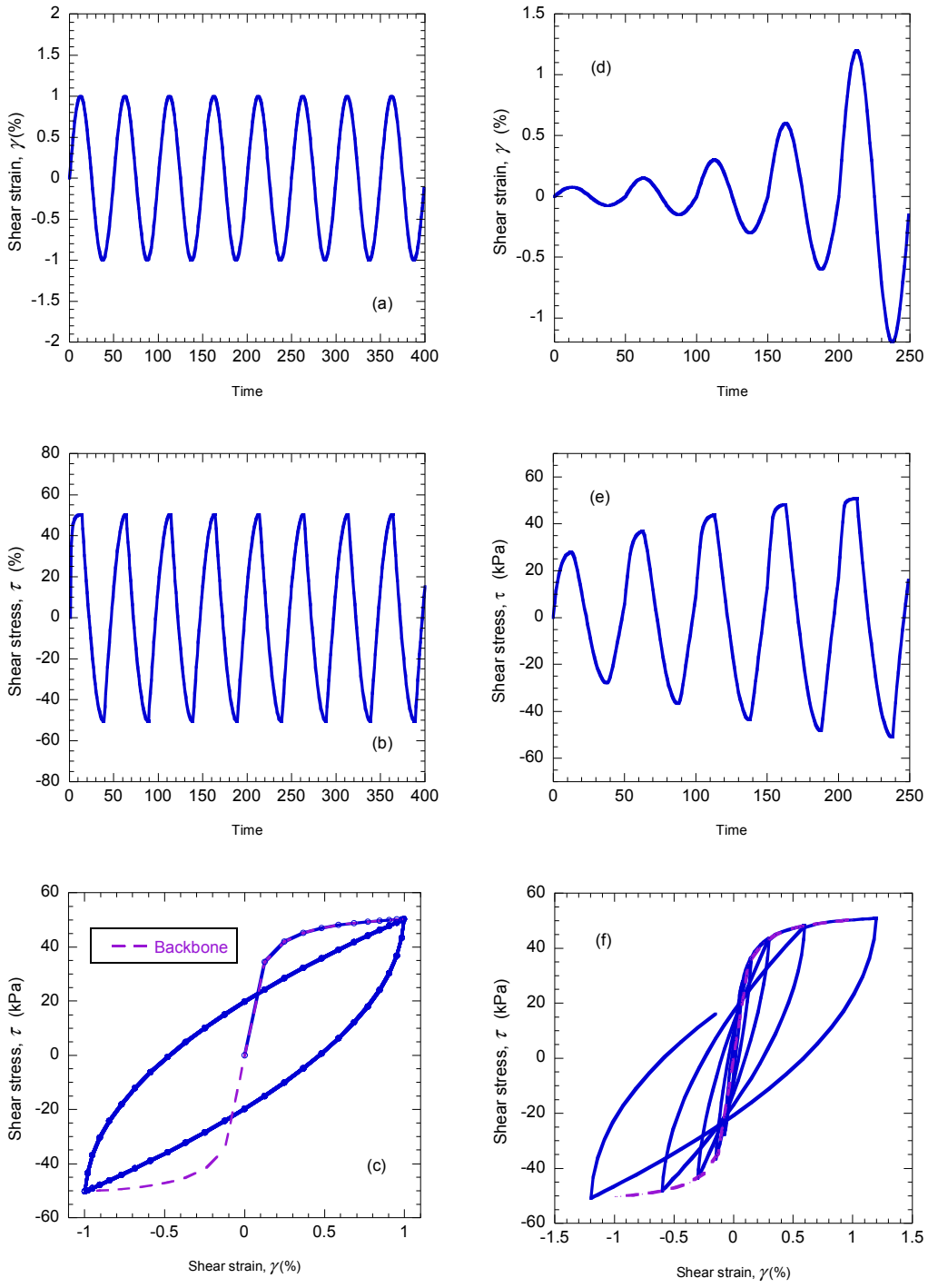

Figure 6-17 Results of symmetrical loading with strain at a constant amplitude (left), with increasing strain amplitude (right)

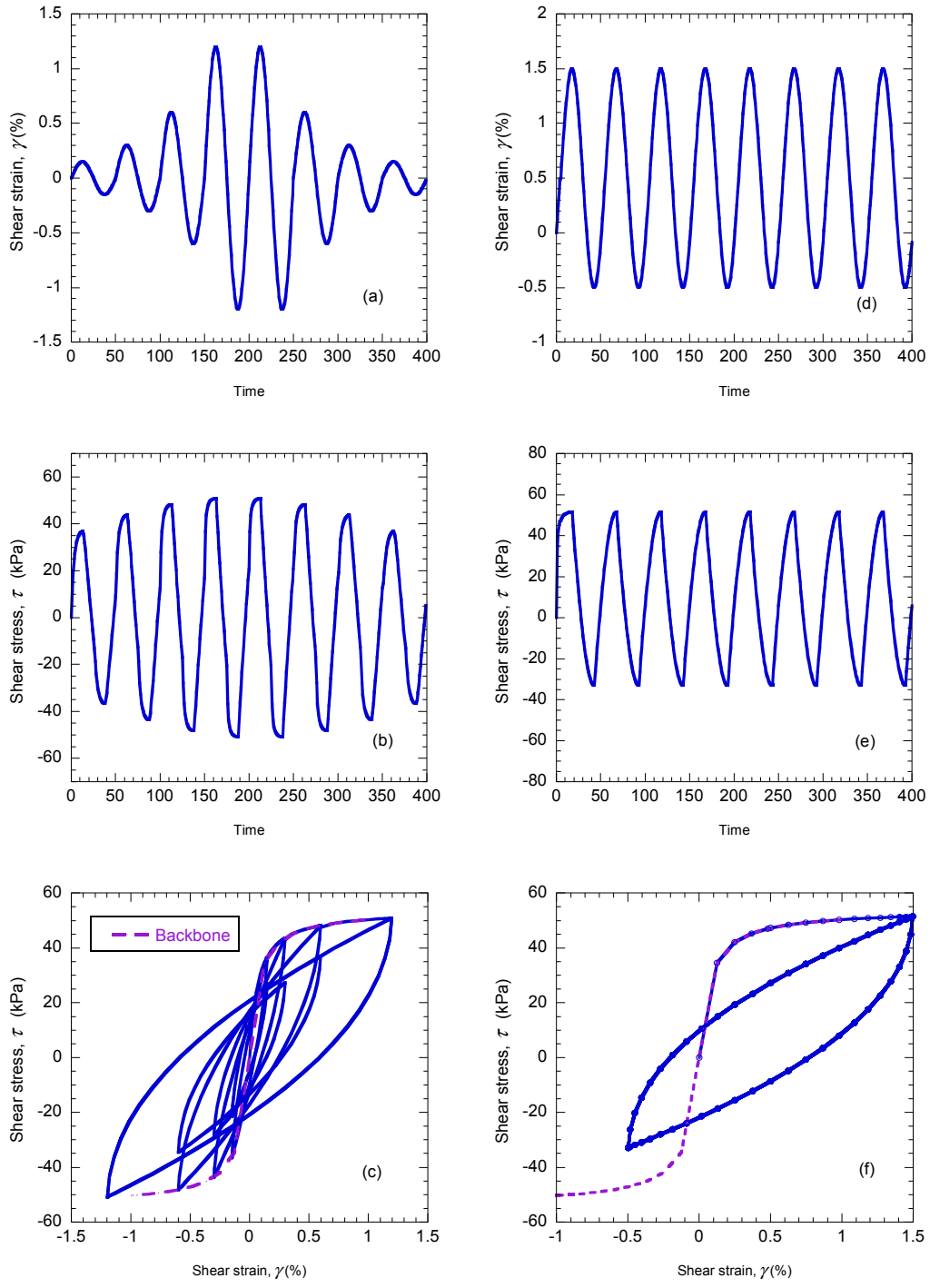

Figure 6-18 Results of symmetrical loading with varying strain amplitude (left), and asymmetrical loading (right)

6.4.2 Validation of the simulated damping with experimental results

It is important to validate the model's predicted damping with that obtained from experimental tests. Figure 6-19 presents the comparison between the experimental and the modelled damping curves using the power function fit to *n*-value variation. These curves are presented for different levels of fines content. The average material damping ratios presented in Chapter 4 for each level of fines content are compared with the simulated damping ratios employing the proposed formulation for soil elements subject to cyclic loading. The solid line and the circles represent the mathematically-modelled and experimentally-measured damping ratios, respectively. The dotted lines represent the damping curves computed based on the Masing rules.

It is clear that the simulated damping for medium to high strain levels can be accurately represented by the proposed formulation. However, slight underestimation of the actual damping may occur for low-strain range and overestimation at strains larger than 0.1%. The former is due to the fact that at small-strains the simulated hysteretic damping is close to zero similar to conventional nonlinear cyclic models. Whereas the latter is considered to be the result of approximating the *n*-value variation with power fit function. Despite these small variations between the modelled and experimental damping, it can be seen that the proposed model allows regulating independently the damping characteristics and modulus reduction and hence reflects more precisely experimental results on cyclic loading of soils.

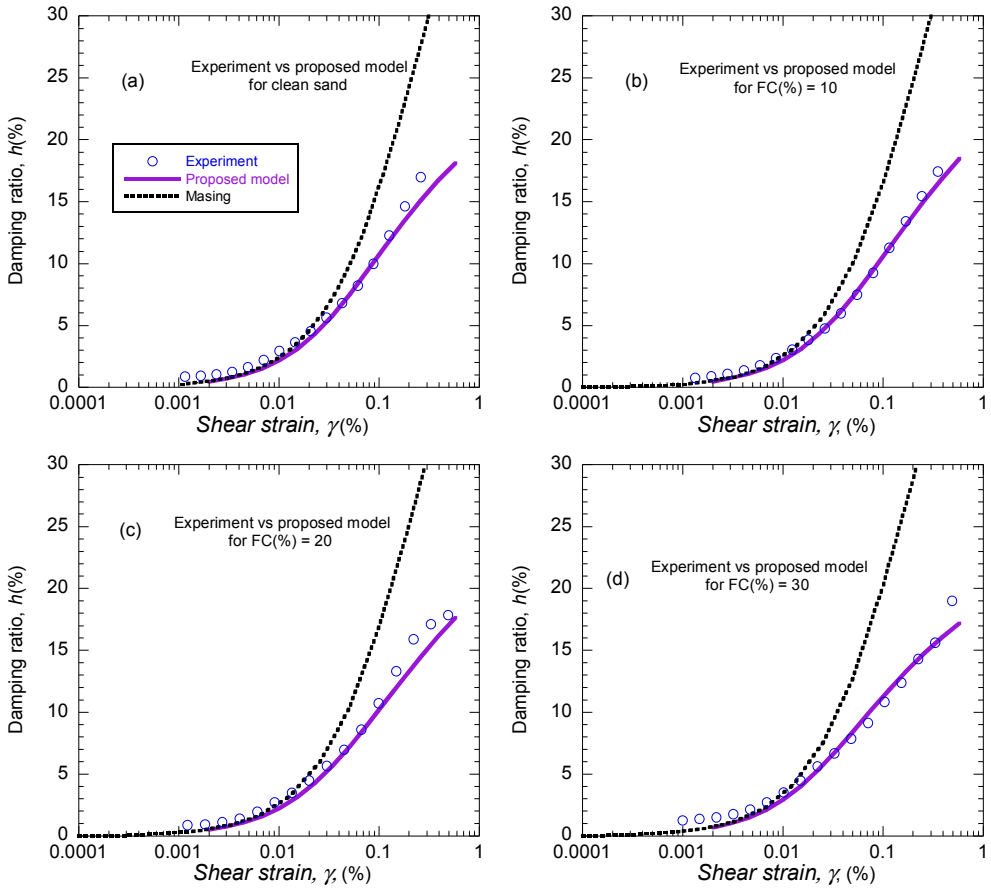

Figure 6-19 Comparison of the computed damping curves using the proposed model and the hyperbolic experimental input damping curve

6.5 Summary

A new formulation was proposed for modelling of unloading-reloading branches of cyclic stress-strain hysteresis loops for sandy soils within nonlinear total-stress site response history analysis. The proposed model uses the modified hyperbolic model as the backbone to represent the modulus reduction curve, and a modification of Masing's unloading/reloading rules, specifically via a coefficient, n. It was shown that the formulation is capable of capturing any desired level of energy dissipation, measured in laboratory cyclic loading tests, as a function of shear strain; in contrast to conventional models which tend to overestimate damping. A parameter n, can be obtained for any given shear strain amplitude in order to match the damping produced

by the numerical model with the observed behaviour in the laboratory. Therefore, both the modulus reduction and damping curves can be simulated simultaneously without compromising the accuracy of one over the other. It was illustrated that the coefficient, n, should be smaller than 2, in order to match the hysteretic damping with the measured strain dependent damping. The model was validated via comparison of the model performance against experimental data presented in earlier chapters.

7 One-dimensional site response analyses using the nonlinear stress-strain model

This chapter presents the results of site response analyses using the proposed model as well as the conventional Masing-type approach. First, the mathematical representation of the soil columns using the program OpenSees (McKenna and Fenves, 2001) for modelling 1D nonlinear analysis is presented. Second, the nonlinear time-domain model is calibrated based on the linear exact solutions computed by the equivalent linear software Strata (Kottke and Rathje, 2010). Then several strong motion stations, which recorded the 2010-11 Canterbury earthquake sequence, are introduced for site response analysis purposes in this chapter. The procedure to compute the required input ground motion for site response analyses at the selected strong motion stations is also explained. The results of using the proposed model are compared with the results of employing conventional Masing-type model. Lastly, the calibration of model parameters at one of the selected strong motion station sites is further investigated and the results are compared with the recorded motions.

7.1 Nonlinear site response modelling

The set of dynamic ground response analyses to be conducted in this study is to be performed using the fully nonlinear code OpenSees (McKenna and Fenves, 2001), incorporating the proposed model in Chapter 6. The software architecture and open-source approach of OpenSees provides many benefits to simulate geotechnical systems with models of nonlinear behaviour. While OpenSees can perform both effective and total stress dynamic analyses, only total stress analyses are performed in this study.

For the purpose of numerical analysis, the soil column is divided into a series of discrete sublayers with depth-dependent dynamic properties. One degree-of-freedom in the horizontal direction is considered for each sublayer using a series of lumped masses. The lumped masses are interconnected by springs and viscous dashpots which correspondingly model the stiffness and small-strain damping of the soil deposit during horizontal movement. The non-linear springs were defined by either the non-linear constitutive relation proposed in Chapter 6 or the conventional Masing-type constitutive model, in order to represent the hysteretic behaviour of the soil during cyclic loading. The system of coupled equations is discretized temporally and a time-stepping scheme (e.g. Newmark β method) is employed to directly solve the system of equations. The control motion is specified at the bottom of the soil column. For the analyses considered herein, the required soil profile properties for each layer include:

- Parameters to define the backbone curve: G_{max}, γ_r, and constant a
- Coefficient of Masing factor n and its relationship with shear strain
- Layer thickness and density
- Viscous damping ratio for low-strain damping

It was explained in section 2.4.2 that the finite rigidity of the underlying material can be simulated using either rigid or visco-elastic medium. Both methods will be employed in the following sections and they will be compared against exact solutions computed by the linear frequency-domain solution.

7.2 Calibration of the nonlinear soil model

Calibration of the 1D lumped-mass system is performed by comparing results of linear time-domain analyses performed by OpenSees (McKenna and Fenves, 2001) to an exact solution from linear frequency-domain analyses using Strata (Kottke and Rathje, 2010). A one-dimensional single layer with shear wave velocity of 100m/s and thickness of 15m was considered. Two assumptions were taken into account for modelling the base layer in the time-domain analyses. First, the half-space was modelled as a linear visco-elastic medium with V_s = 450m/s and a velocity time series was applied to the model as shown in Figure 7-1a. In the second analysis, the base layer was assumed rigid and an acceleration time series was employed at the interface of soil layer and half-space as illustrated in Figure 7-1b. The equivalent viscous damping ratio used in the frequency-domain analysis was 2%. A parametric study was undertaken to first obtain the best damping ratio for simulating small-strain damping in the time-domain analyses, and second, to scrutinize whether the compliant or rigid base assumption is a better representation in time domain.

The East-West component of the RHSC station which recorded the 2010 Darfield earthquake was used as the input ground motion (GeoNet, 2012). It was found that 2% viscous damping for the stiffness-proportional Rayleigh formulation in the time-domain using a compliant base and a velocity time history input resulted in the best match with the exact solution computed by Strata in the frequency domain. Figure 7-2 shows the response spectra computed at the surface of the two models using the RHSC motion at the base of each soil column. Despite the negligible mismatch in the period range 0.1-0.2s, the overall similarity of the spectral accelerations in the high- and low-frequency ranges appears promising. On the other hand, the assumption of a

rigid base with ground motion input in the form of an acceleration time series significantly overestimated the spectral response for periods, $T < 0.2$s. This is in agreement with the benchmark studies conducted by Stewart et al. (2008). Considering different combinations of input motion and base conditions, they showed that for the common case in which the input motion is recorded as outcropping, the input motion should be applied without modification for time-domain analyses with an elastic base layer.

It was further found that an increase in the stiffness of the base layer in the linear soil models and a larger viscous damping ratio in time-domain can result in similar response spectra for all three approaches. However, in order to simulate the in-situ soil stratigraphy using realistic assumptions, the models in this study employ a dashpot and apply a shear stress boundary condition at the base of the soil column that is proportional to the velocity time series of the motion (Joyner and Chen, 1975, McGann and Arduino, 2012). Hence all the acceleration input time series considered were integrated to obtain the velocity time series to be utilized at the compliant base of each modelled soil column.

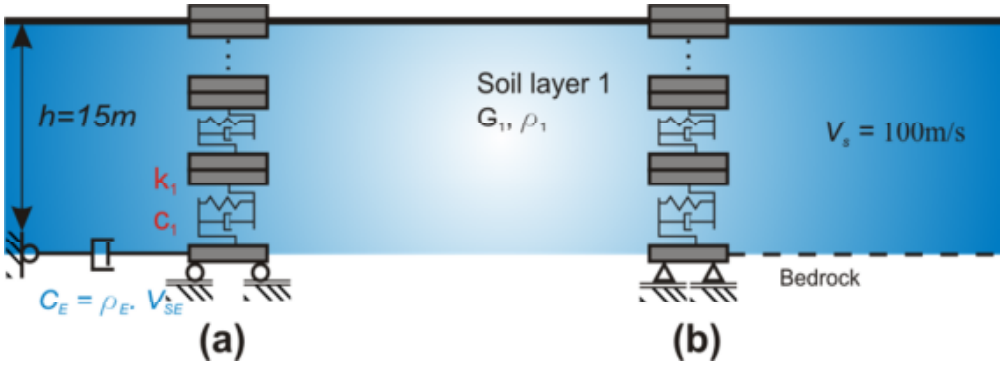

Figure 7-1 Schematic representation of the 1D site response model, (a) visco-elastic base, (b) rigid base. Lumped masses interconnected with springs.

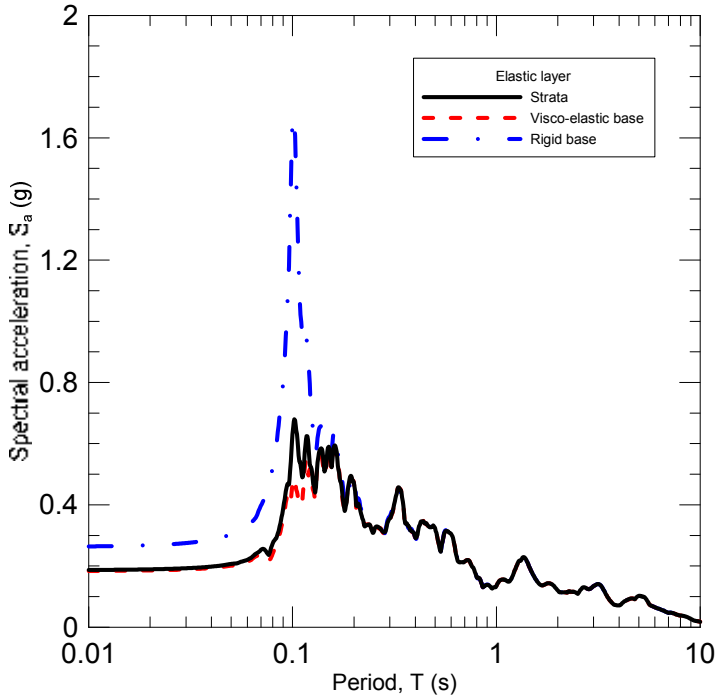

Figure 7-2 Comparison of 5% damped response spectra for an arbitrary single-layer soil site for Strata and OpenSees assuming rigid and compliant base

The adopted single-layer soil column with the visco-elastic base was employed in order to verify the overdamping of the conventional Masing rules. The normalized modulus reduction curve for clean Fitzgerald Bridge (FB) sand illustrated in Figure 7-3a was employed to simulate the backbone curves in both soil layers using Masing and the proposed model. The material damping ratio in the Masing formulation is not prescribed in advance and is calculated mathematically during the analysis as illustrated by the solid line in Figure 7-3b. However, the proposed model requires the material damping curve as a basis to define the hysteresis cycles. The damping ratio curve for clean FB sand under 100 kPa of confining stress was employed in this case as shown in Figure 7-3b.

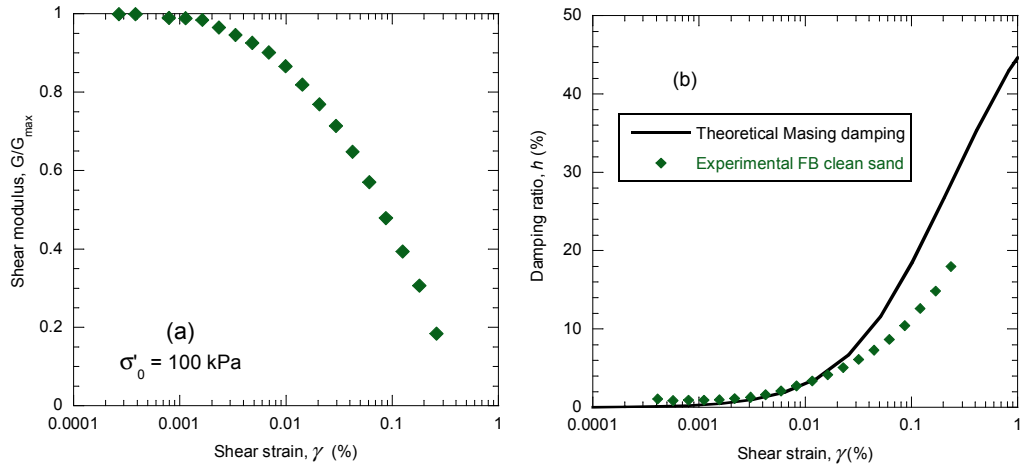

Figure 7-3 (a) Normalized modulus reduction curve and, (b) damping ratio curve for clean Fitzgerald Bridge (FB) sand

Figure 7-4 shows the pseudo-acceleration response spectra for the two models for different scaling factor of the input ground motion. The input motion at the bottom of the soil column was scaled to induce larger shear strains in the soil profile. It is apparent in this figure that for periods less than 0.1s, the Masing rule results in an insignificant difference compared with the more accurate constitutive relationship. However at longer periods ($T > 0.9s$) the response is often underestimated significantly, which may be regarded as a direct consequence of the overestimation of material damping. This difference between the proposed model and Masing criterion becomes excessively larger for stronger input motions. This implies that for the case of stronger input motions (or softer soil deposits), in which soil may exhibit larger shear strains, the underestimation of response parameters can be even more significant. Note that employing the proposed formulation for weak ground motions, which induce small shear strains (γ<0.1%), results in similar spectral amplitudes as the adoption of Masing rules. This suggests that the overestimation of damping, induced by Masing rules, exert a great influence on the response only if the maximum shear strain exceeds a certain level of strain (e.g. Hashash et al., 2010).

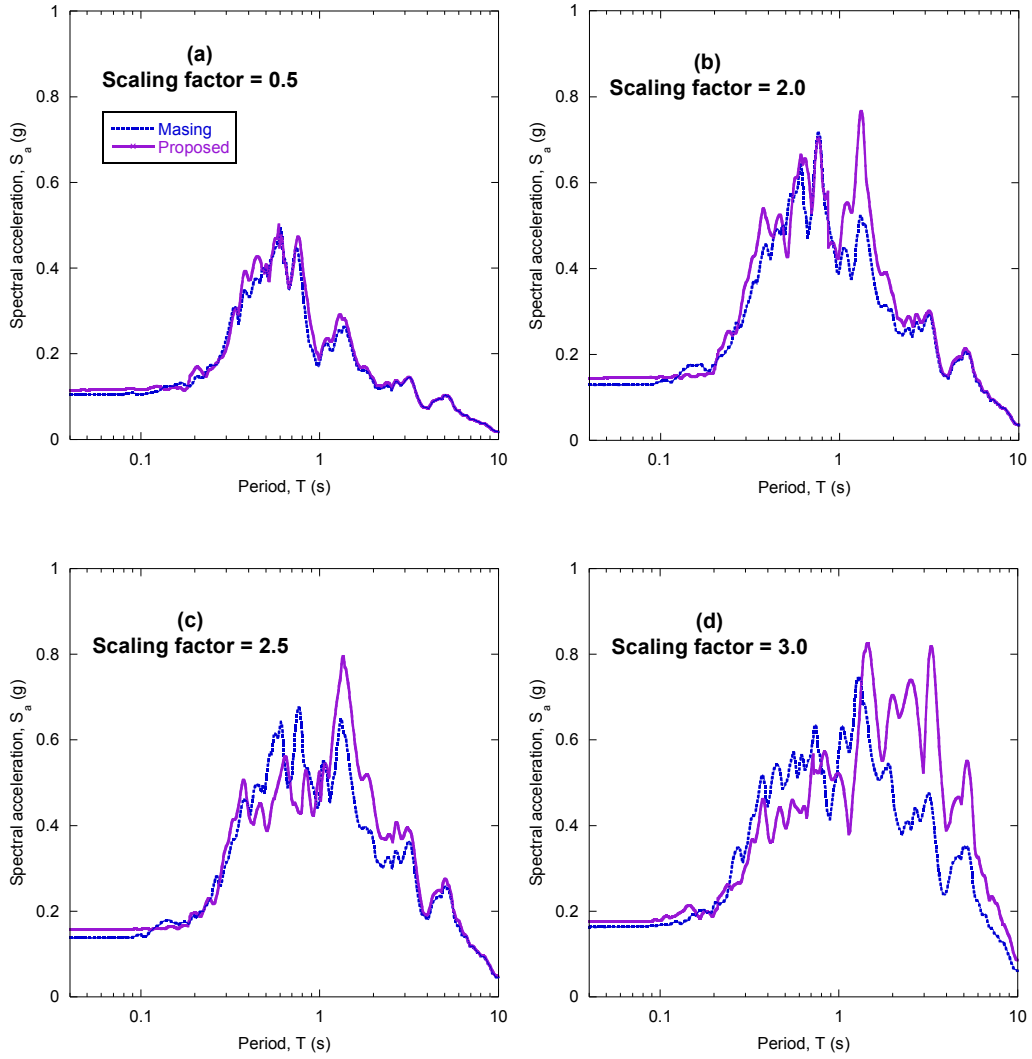

Figure 7-4 Comparison of 5% damped response spectra for an arbitrary single-layer soil site for the proposed model and the Masing criteria assuming a compliant base layer for different scaling factor of the input ground motion

Figure 7-5 shows the spectral ratios of the computed accelerations by the proposed model and the Masing model corresponding to Figure 7-4. Each curve corresponds to each ground motion scaling factor introduced earlier. It is clear that for periods, $T > 1$s, as the scaling factor increases, the spectral ratio computed by the proposed model increases by more than 50%. However for scaling factor, $SF < 2.5$, the spectral ratios approach to unity in the long-period range. In the mid-period range, $0.1\text{s} < T < 1\text{s}$, higher amplification by the proposed model is only observed for $SF <$

2. As the input motion becomes stronger and the induced shear strain increases, deamplification relative to the Masing-type spectra occurs; this deamplification is persistent for SF = 3.0. This deamplification might be due to the lower tangent stiffness in the proposed model.

Maximum single-amplitude, γ_{SA}, maximum double amplitude, γ_{DA}, and residual, γ_{res}, shear strains are also computed at mid-height of the soil profile. The open and solid symbols in Figure 7-6a represent the results for the maximum single- and double-amplitude, respectively. It is apparent that there is a tendency for the proposed model to predict the single- and the double-amplitude shear strains higher than the Masing model. For larger input ground motion, this overestimation is even larger as shown in Figure 7-6. In contrary, the residual strains are slightly larger for the Masing model as shown in Figure 7-6b. Smaller computed residual strain using the proposed model is consistent with the variation of tangent stiffness of the unloading-reloading branches of stress path. It was shown in the previous chapter that the tangent stiffness of the unloading-reloading branches of the proposed model rapidly decreases in comparison to the Masing rules.

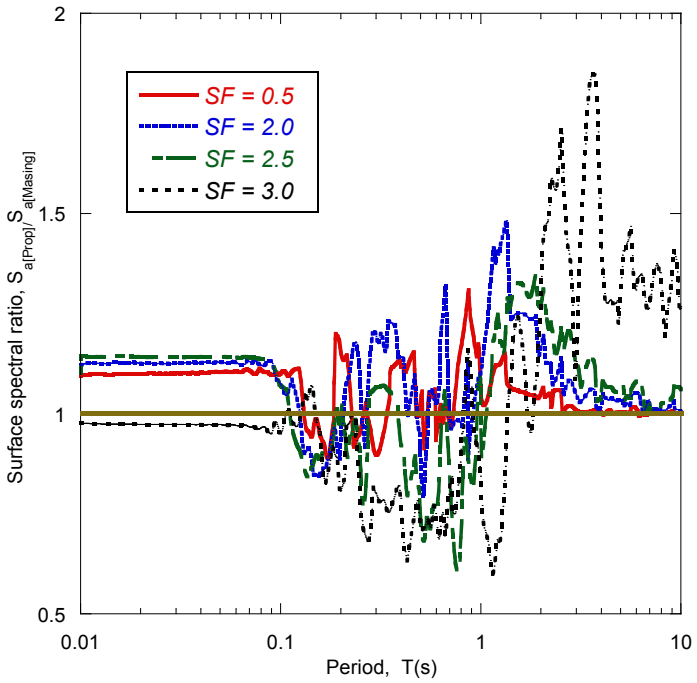

Figure 7-5 Comparison of ratios of the computed spectral accelerations of the proposed model and the Masing rule

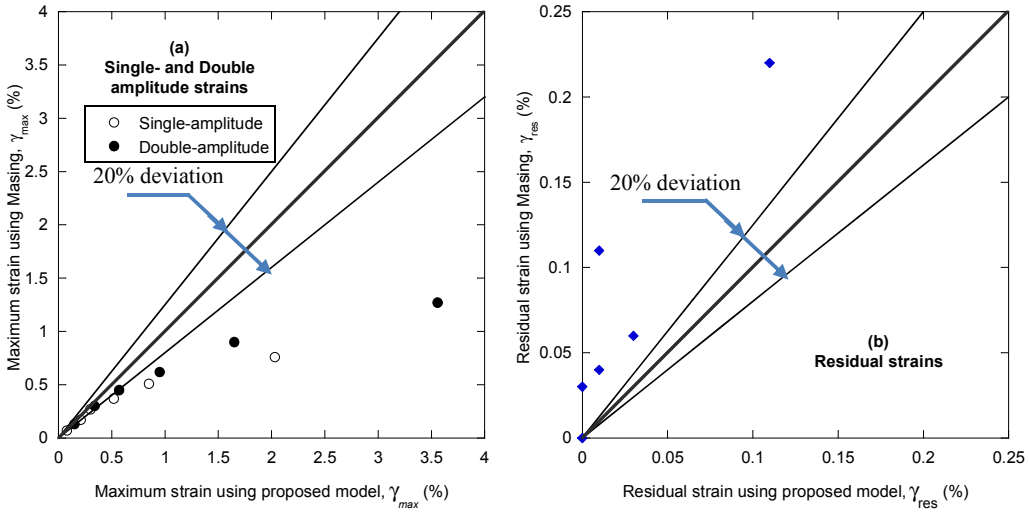

Figure 7-6 Comparison of (a) the single-amplitude, the double-amplitude and, (b) the residual strains computed using the proposed and Masing models

In order to examine whether the trends in Figure 7-5 to 7-6 are specific to the particular ground motion considered, a set of 20 strong ground motions with M = 6-7 and R_{rup} = 0 – 40km were used from PEER ground motion database (PEER, 2013). The nonlinear response analyses with the aforementioned single layer soil profile were repeated for this set of records uses as input motions. Figure 7-7a and 7-7b show the computed response spectra at the surface of the single-layer soil model using the Masing and the proposed model, respectively. The bold lines in the figure represent the average of the computed spectra for each set of nonlinear analysis. Figure 7-8 shows the ratio of the spectral accelerations of the proposed model to Masing; the mean of the spectral ratios are also presented in this figure. It is clear that for periods T > 1 s, the mean of spectral ratios of the 20 ground motions is more than one, implying that using Masing criteria over-estimates the damping in this period range. The similarity of the proposed and Masing models for period range, T < 1 s, might be due to the fact that the high-frequency content can be attributed to small cycles which are simulated similarly using the two models. Figure 7-9 compares the computed maximum shear strain in the soil profile. Similar to Figure 7-6, it appears that the proposed model predicted larger shear strains in the soil profile compared to Masing predictions.

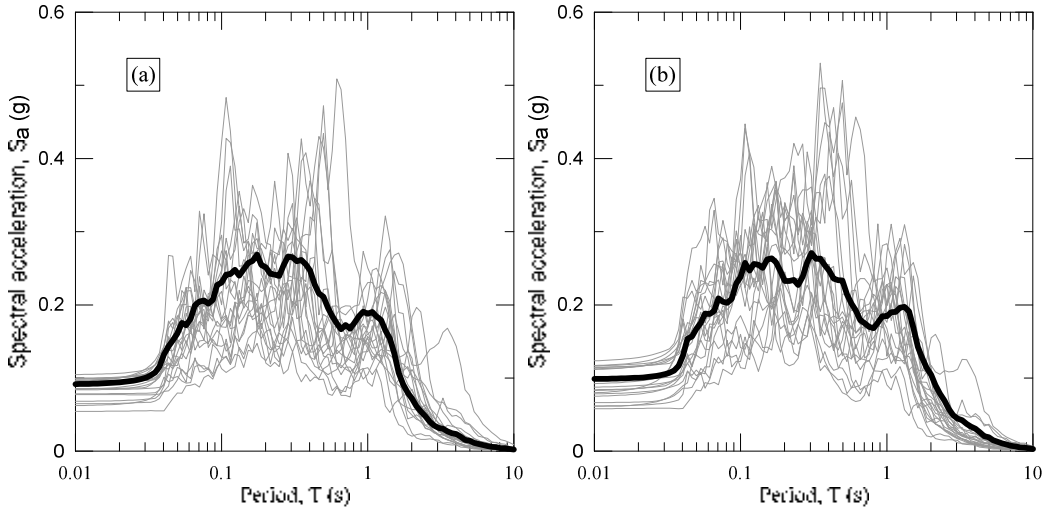

Figure 7-7 Computed 5% damped response spectra for a set of 20 ground motions, using (a) Masing and, (b) the proposed model. Solid lines represent the average

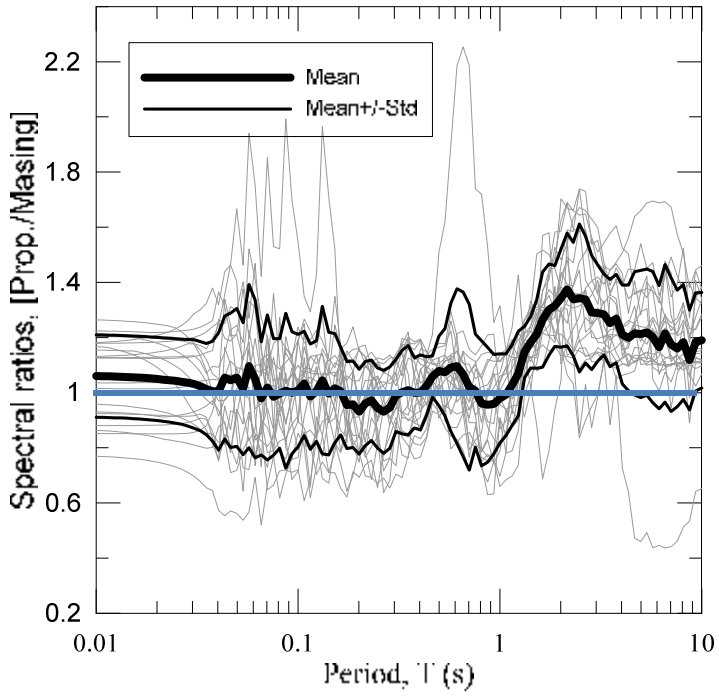

Figure 7-8 Computed spectral ratios of the proposed and the Masing model for the set of 20 ground motions. Solid lines represent the mean and mean±std

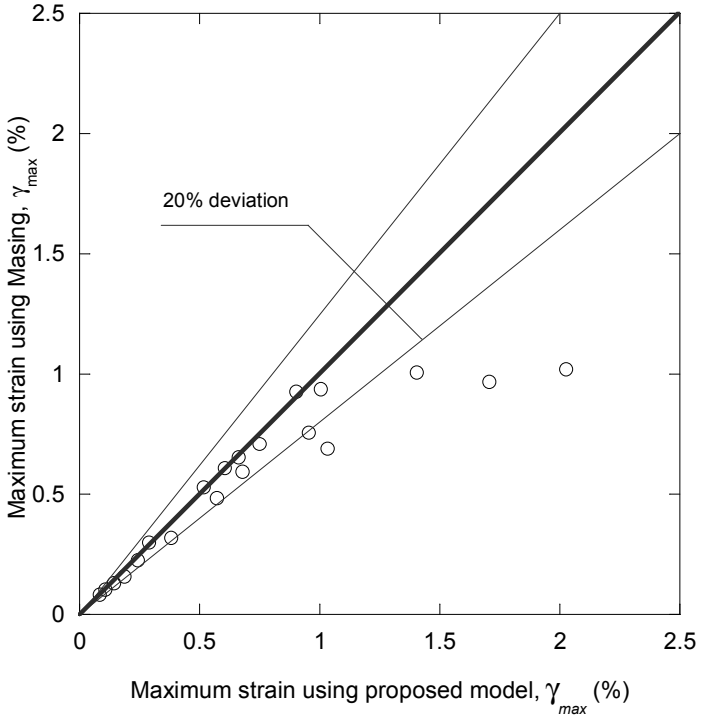

Figure 7-9 Comparsion of the maximum single-amplitude computed using the proposed and the Masing model for the 20 ground motions

7.3 Strong ground motion stations and input ground motions

7.3.1 Strong ground motion stations

GeoNet is a strong data collection and analysis system consisting of national and regional-scale sensor networks for New Zealand (GeoNet, 2012). Strong motion records from the GeoNet ground motion stations provided valuable new information during the 2010-11 Canterbury earthquakes sequence. Four of these stations, which are located in Christchurch, are selected in this study to further investigate the performance of the proposed constitutive model in predicting the site response. Figures 7-10 and 7-11 show the locations of the selected sites for the purpose of site response analysis in this study. Table 7-1 lists the sites used in this study and their

corresponding NZS 1170.5 (2004) site classification. With the exception of the RHSC site, all other sites are located in Christchurch CBD.

The specification of input for modelling in the nonlinear dynamic analyses involves:

1) generation of the V_s profile using site-specific data and/or correlation equations;

2) incorporation of the appropriate strain- and depth-dependent normalized shear modulus and material damping curves; and

3) determination of the representative rock/soil motion for use as input half-space excitation.

The details of calculating the dynamic soil properties of Christchurch soil as well as the stratigraphy and mechanical characteristics of the selected strong ground motion stations are introduced in Appendix A. The determination of the input motion for site response analysis purposes in this study will be described briefly in the following subsections.

Figure 7-10 Geographical distribution of the selected strong motion stations across Christchurch city

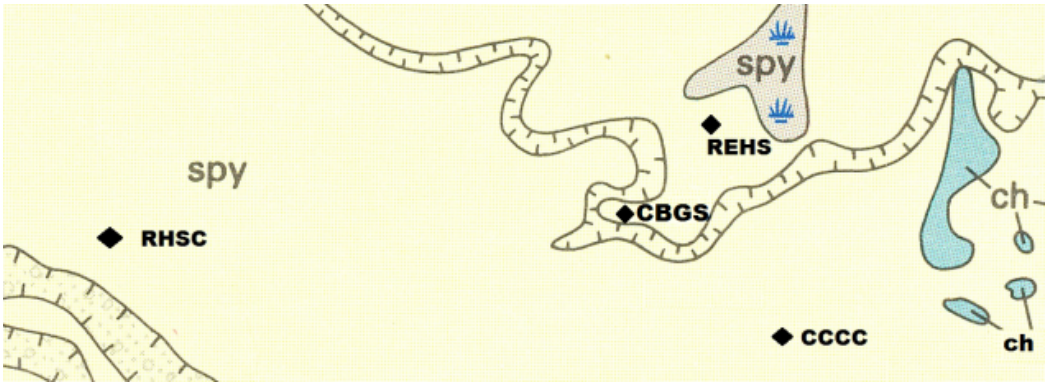

Figure 7-11 Geology of the selected stations in the Waimakariri river floodplain. Spy: Springston formation: dominantly alluvial sand and silt overbank deposits; ch: Christchurch formation (modified after Brown and Weeber, 1992)

Table 7-1 Selected strong motion stations and ground subsoil categories defined based on NZS1170.5(2004)

Site symbol	Station name	R_{rup} (km)	Site subsoil category
RHSC	Riccarton High School	10	D
CBGS	Christchurch Botanic Gardens	14.4	D
CCCC	Christchurch Cathedral College	16.2	D
REHS	Christchurch Resthaven	15.8	D

R_{rup}: Closest distance from fault plane of the 4 September 2010 Darfield earthquake to each site

7.3.2 Input ground motions

In addition to representative dynamic soil properties at the sites, requisite input for the analyses of seismic soil response includes suitable input strong motion records (input time series). A common practice to assess the base rock incident motion is by using the given motion specified at the surface of the soil and employing the equivalent linear approach which relates the response at any point of the deposit to the response at any other point within the deposit. This deconvolution procedure is

particularly useful in the interpretation of ground motions recorded on the surface of other soil deposits. Because of existence of dense gravelly layers underlying very thin shallow soft soils, the level of nonlinearity in the RHSC station is expected to be much lower than the other stations; hence the recorded motion at the surface of the RHSC is base-line corrected and deconvolved, and then is used as input ground motion for other soil sites.

Figure 7-12 schematically illustrates the deconvolution procedure in which the surface motion at site A (RHSC strong motion station) is known. To specify the corresponding parameters at the surface of the other sites of interest (CCCC, REHS and, CBGS), the time series of ground surface motion recorded at point A is used. This motion is then deconvolved through RHSC soil profile to determine the time series of outcropping firm ground motion at point B. Equivalent linear analyses in conjunction with the dynamic properties of RHSC soil profile were employed for this purpose. The computed outcropping motion then was used at the interface between the firm ground and local soil deposit (point D) of the soil profile at the site of interest. A conventional ground response analysis is then performed to propagate the input motion up through the soils to predict the motion at the surface of the soil profile of interest (point E).

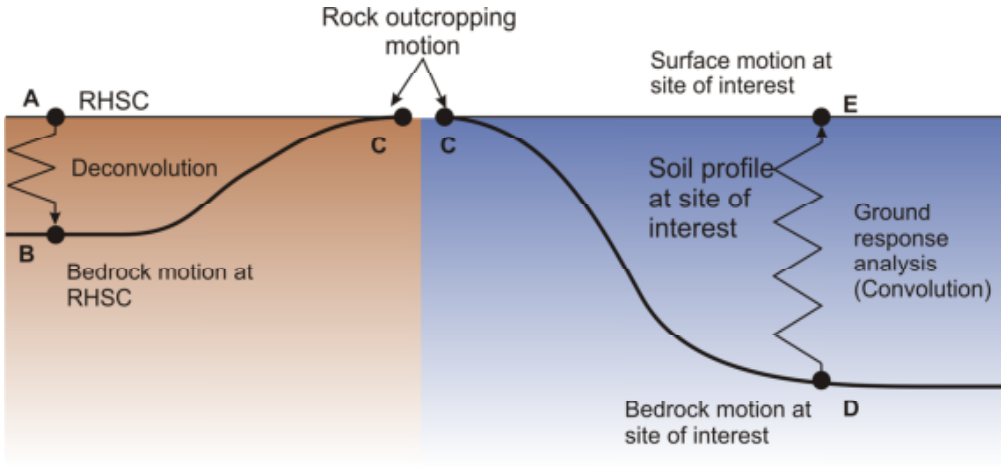

Figure 7-12 Procedure for modifying ground motion parameters using the deconvolution method in the RHSC site and conventional site response analysis in the site of interest (modified after Kramer, 1996)

Although the deconvolution of a linear elastic system should theoretically produce a unique solution and additionally be consistent with the motion at the surface, some practical issues have to be resolved. Some of these may be of a computational nature, particularly when iteration toward strain-compatible soil properties are required and the shaking is severe (Roesset, 1977, Towhata, 2008). Others are related to limitations in the accuracy of the assumption that all motion results from vertically propagating plane shear waves (Kramer, 1996, Silva et al., 1988). Silva et al. (1988) suggested filtering and scaling of the surface input motion may be essential in practice otherwise the analysis may not converge and excessively high acceleration may be developed at half-space level. This amplitude overestimation was regarded to be due to either the amplification of high frequency noise or deficiencies in the modelling of in-situ modulus reduction and damping curves (Silva et al., 1988). The sample rate of recorded motions in this study was reduced in the frequency domain. As a result much of the high frequency content was removed during signal processing (Cousins, 2013, Hodder, 1983).

In addition to the above, in order to eliminate potential variability between recorded and computed ground motions in each station, every pair of as-recorded ground motion components were rotated to East-West (EW) and North-South (NS), through rotating the coordinate system with an angle θ about the origin according to following equation:

$$\begin{bmatrix} a_{1,\theta}(t) \\ a_{2,\theta}(t) \end{bmatrix} = \begin{bmatrix} \cos(\theta) & \sin(\theta) \\ -\sin(\theta) & \cos(\theta) \end{bmatrix} \begin{bmatrix} a_1(t) \\ a_2(t) \end{bmatrix} \tag{7-1}$$

The shear wave velocity profile and the soil type stratigraphy of the RHSC station are presented in Figure 7-13. The shear wave velocities which are measured by Multi-Channel Analysis of Surface Waves (MASW) are obtained from Wood et al. (2011). Using MASW, it is conventional to report a constant shear wave velocity value for each corresponding soil layer; this implies that the stiffness of the soil layer does not increase with larger overburden pressure. This is in contrast with general trends like equation (2-4) which suggests that the modulus is proportional to confining stress. Hence, the V_s profile measured by Wood et al. (2011) is corrected to follow a depth-dependent pattern (e.g. Robertson, 2012). In this context, it is assumed that the reported shear wave velocities in Wood et al. (2011) are the averages of V_s in each soil layer and they increase with depth according to the following equation:

$$V_s = A.\left(\frac{\sigma'_{vo}}{P_a}\right)^{0.25} + B \tag{7-2}$$

where σ'_{vo} and P_a are in-situ effective vertical stress and atmospheric pressure in the same unit, respectively; A and B are the fitting parameters for the shear wave velocity at mid-point of each soil layer to be equal to reported V_s in Wood et al. (2011).

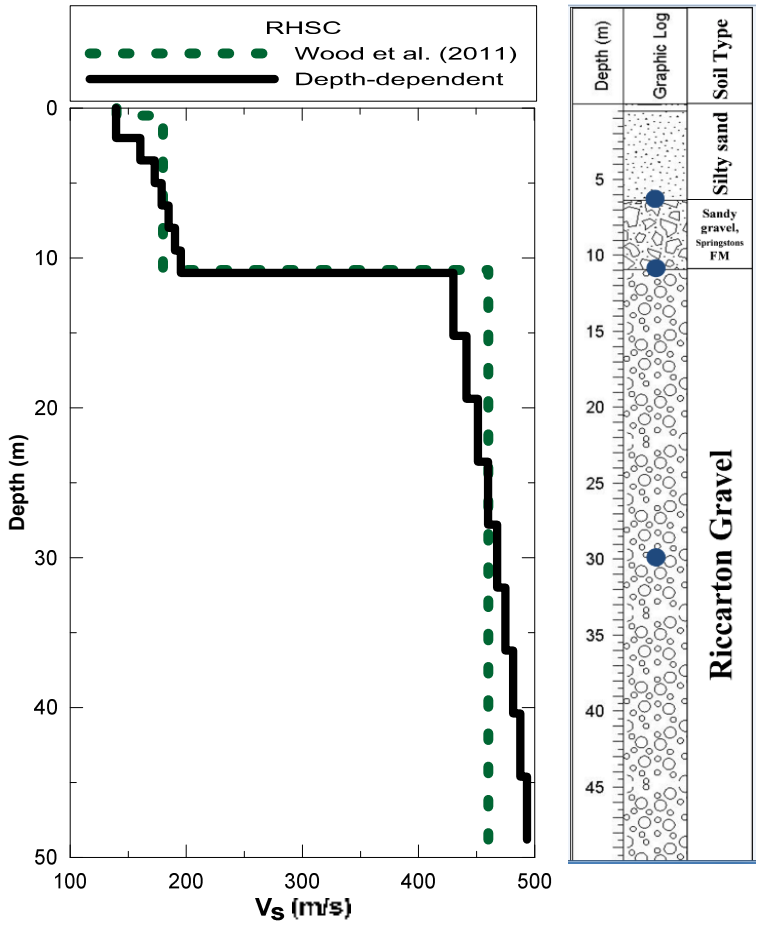

Figure 7-13 Shear wave velocity profile utilized in this study (left) and stratigraphy (right) profile at the RHSC station (modified after Wood et al., 2011, Wotherspoon, 2013)

The two components of the recorded motion at the RHSC strong motion station during the 4 September 2010 Darfield earthquake was deconvolved to be used as the input motion for the soil models. The North-South component (approximately fault-normal) and the East-West component (approximately fault-parallel) will be used throughout this chapter. Figure 7-14 shows the response spectra of the deconvolved motion at depths H = 6.4, 10.8 and 30m in RHSC station for two horizontal components. It appears that the deconvolved motion at depths H = 10.8 and 30m are very similar as both lie in the Riccarton gravel layer. These deconvolved motions at

depths H = 10.8 and 30m will be used in this study as input for site response analyses and computation of the ground motion at the surface of the selected station in Christchurch CBD. Each strong motion station profile is used to systematically compare results between Masing-type and the proposed formulation.

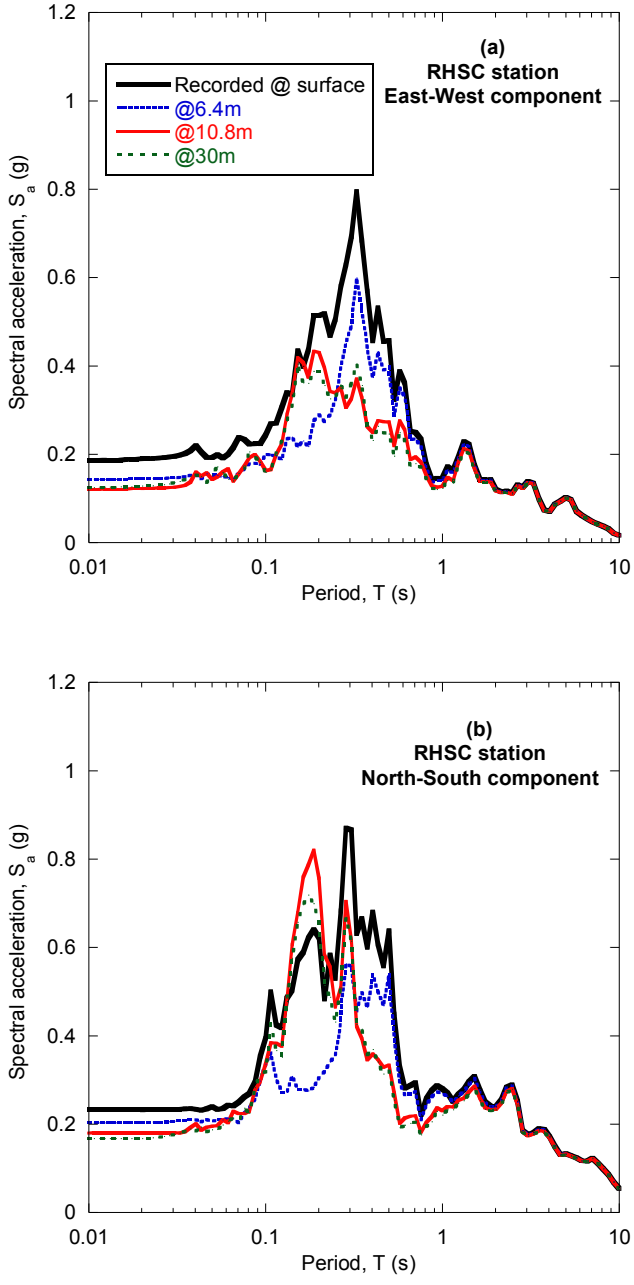

Figure 7-14 The 5% damped response spectra of the recorded at surface and deconvolved motions at depths H = 6.4m, 10.8m and, 30m at RHSC strong motion station: (a) East-West direction, (b) North-South direction

7.4 Results of nonlinear analyses at the strong motion stations

The Masing-type and the proposed formulation explained in Chapter 6 will be utilized in this section to model the soil profiles underneath the selected strong motion stations which recorded the Canterbury earthquake sequence. As such, the performance of the proposed formulation can be verified in the modelling of real soil deposits. First, each soil column is modelled elastically in time-domain OpenSees and frequency-domain Strata, in order to obtain the viscous damping ratio for the simplified Rayleigh damping (stiffness-proportional) in the time-domain analyses. Using the computed viscous damping, the soil columns are modelled in OpenSees using the Masing and the proposed models.

The measured normalized modulus and damping ratio curves of Christchurch sand obtained during the laboratory testing is employed to simulate the deformational properties of the soil profiles selected in this section. In order to model other soil types and/or soils under different confining stresses, the modulus reduction and damping relationships proposed by Darendeli (2001) are used. It was shown in Chapter 4 that the effects of fines on the normalized modulus reduction curves were not significant while their influence on damping curves were negligible. Therefore, the effects of fines on the seismic response of soil profiles are not considered in this section. The results of site response analyses are presented in terms of pseudo-acceleration response spectrum, spectral ratios and, maximum shear strain profile.

7.4.1 REHS

The top 20m of the REHS soil profile is first modelled elastically using the shear wave velocity and stratigraphy shown in Figure 7-15. The Riccarton Gravel substratum was assigned a shear velocity of 460 *m/s* and a density of 2.1 t/m^3. A

more detailed description of the site stratigraphy is described in Appendix A. In order to better represent the variation of the shear wave velocity with overburden stress, a depth-dependent shear wave velocity profile based on the measured values are adopted (e.g. Robertson, 2012).The soil profile was analyzed employing Strata, with exact solution in the frequency-domain, and OpenSees, with integrated solution in the time-domain; the purpose was to determine the suitable viscous damping ratios for time-domain analyses. The damping in the linear frequency domain was set to minimum damping ratio at each layer, ranging from h_{min} = 0.5 – 1.5%. This can be inferred from material damping ratio curves presented in Figure 7-17b. In addition the damping of half-space was considered 1%. Figures 7-16a and 7-16b compare the 5% damped acceleration response spectra of surface motions from Strata with results from OpenSees. It was found that the 0.4% damping ratio in both directions for the simplified Rayleigh formulation for viscous damping in time-domain analysis provide the best match with the exact solution provided by Strata.

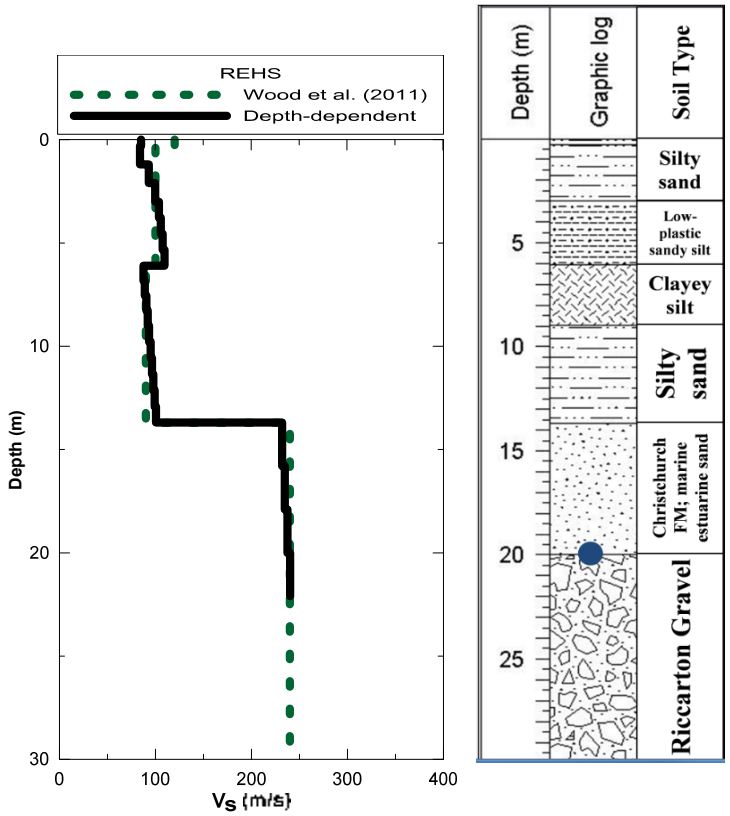

Figure 7-15 Shear wave velocity (left) and stratigraphy (right) profile at the REHS station (modified after Wood et al., 2011, CERA, 2013)

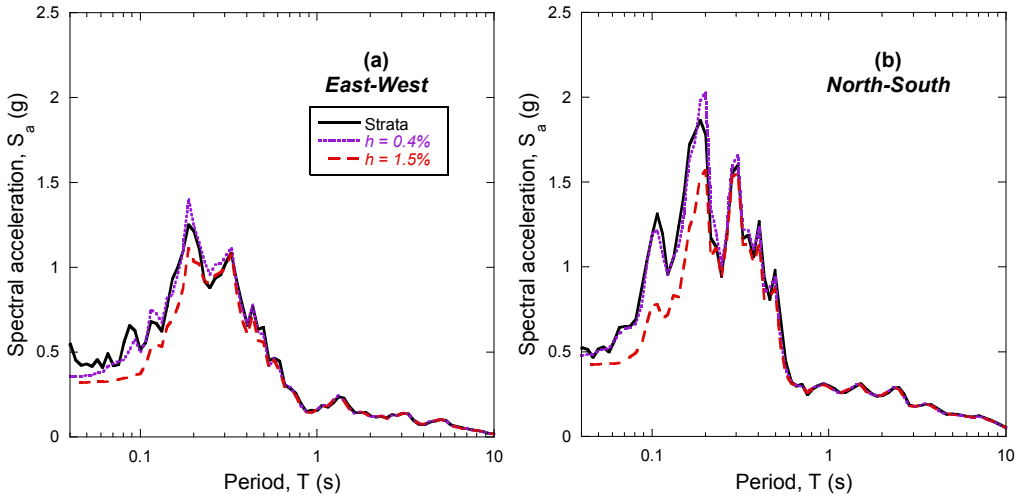

Figure 7-16 Comparison of 5% damped response spectra for the REHS strong motion soil site using elastic frequency-domain with that of time-domain for (a) East-West (approximately fault-parallel) and (b) North-South (approximately fault-normal) components

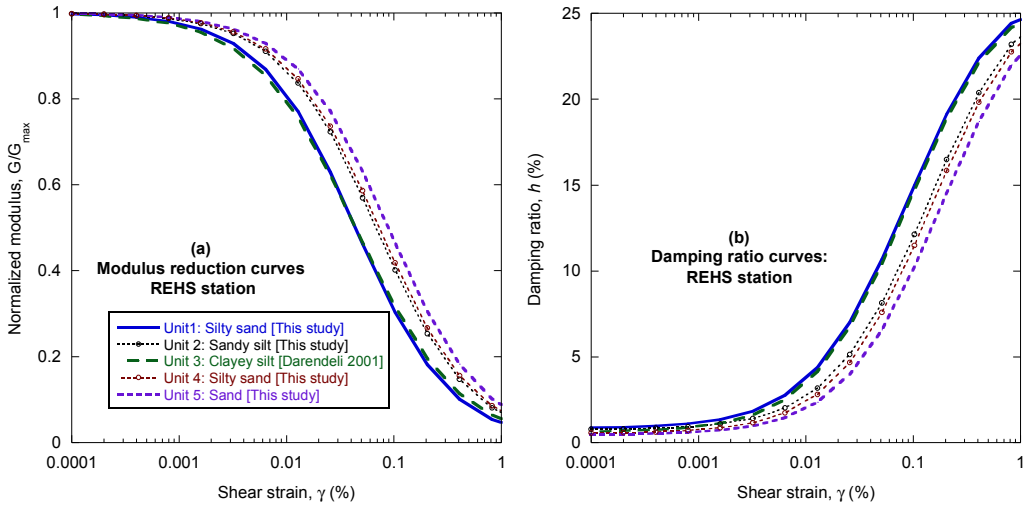

Figure 7-17 Modulus reduction and damping ratio curves for REHS station soil profile. For soil types and/or confining stresses that no laboratory tests were conducted in this study, Darendeli (2001) family of modulus and damping ratio curves have been used.

7.4.1.1 Nonlinear site response analyses of REHS station

Nonlinear time-domain analyses were also carried out using the Masing and proposed formulations for modelling the nonlinear stress-strain relationships of soils. The nonlinear model parameters were computed based on the modulus reduction and damping curves presented in Figure 7-17. The stiffness-proportional Rayleigh damping was obtained, h_{min} = 0.4%, from elastic analyses and this viscous damping ratio was adopted at the corresponding natural frequency of the top 20m of the REHS station, $f \sim$ 1.9 Hz.

The difference between the two models can be observed by examining the computed surface acceleration time history and response spectra shown in Figures 7-18 to 7-21. The soil motion are estimated at different depths, i.e. H = 0, 5, 10 and 16m below ground level; these depths correspond to vertical effective stresses of σ'_v = 0, 70, 120 and 180 kPa, respectively. Figure 7-18 and 7-19, present the acceleration time history results of the simulations at different depths. Each plot compares the time

histories computed by stress-strain relationships using Masing rule and proposed model. It is obvious that the predicted waveforms for both methods are very similar. The computed time histories show that although the calculated PGAs occur at almost the same time the absolute values are slightly different. It is also indicated that peak ground acceleration increases as the wave propagates to ground surface. This amplification of peak acceleration is observed for both models.

Further, the computed pseudo-acceleration response spectra at the surface of the REHS station for the two components of the Darfield earthquake are also compared for the two employed models. In the East-West (EW) direction, the spectra are very similar for both models; however, the Masing solution slightly underestimates the motion relative to the proposed formulation; meaning the spectral amplitudes are less amplified by this model. The solid line in Figure 7-21 clearly illustrates this underestimation of the response, by showing the spectral ratios between the proposed model and the Masing model. Similar behaviour is also observed in the NS direction. However, in NS direction, for mid-period range, $0.1 < T < 0.4$s, this trend is reversed and the Masing criteria results in larger spectral amplitudes.

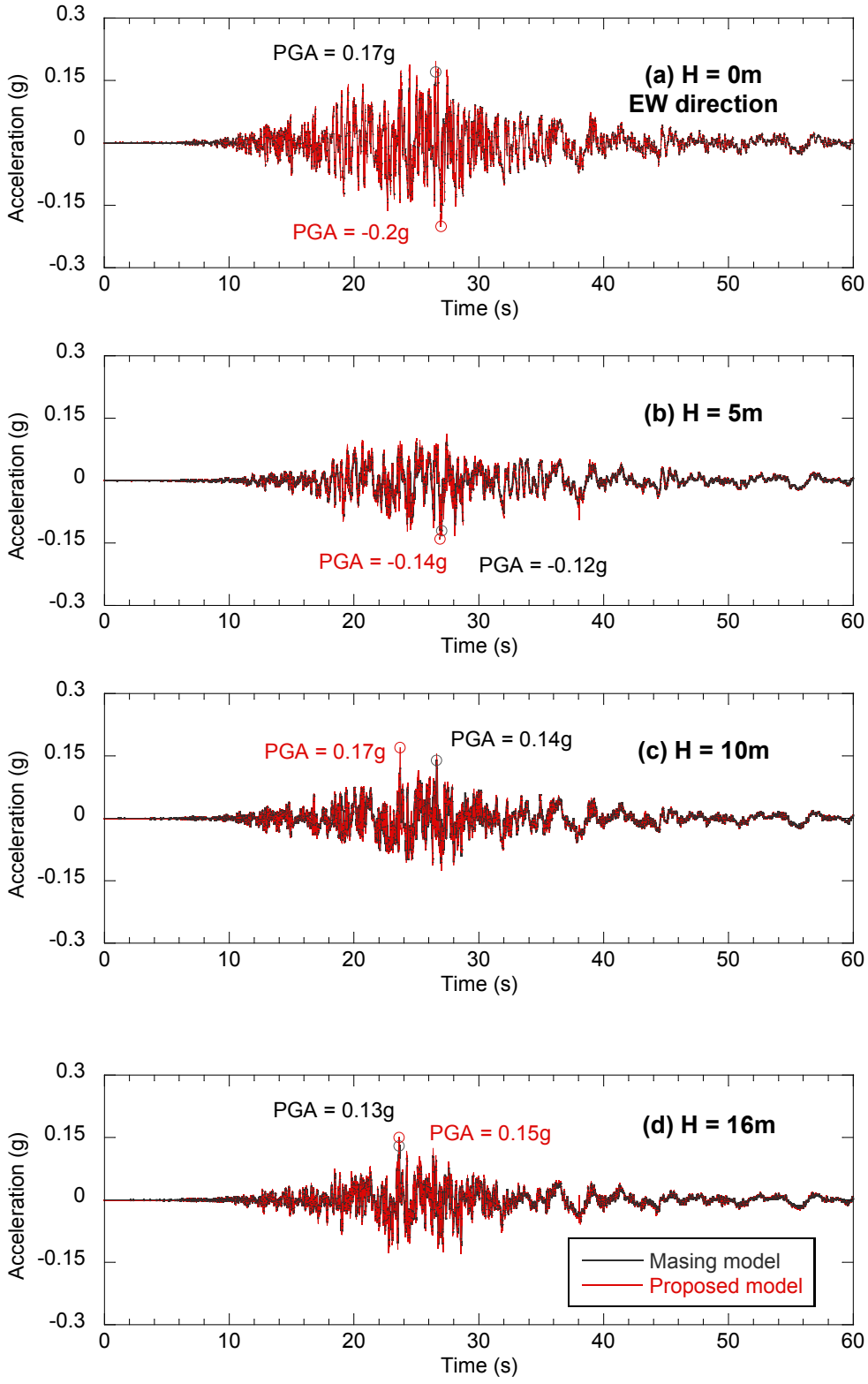

Figure 7-18 Computed time histories at the surface and depths of H = 5, 10 and 16m of the REHS station using the proposed and Masing models in East-West direction

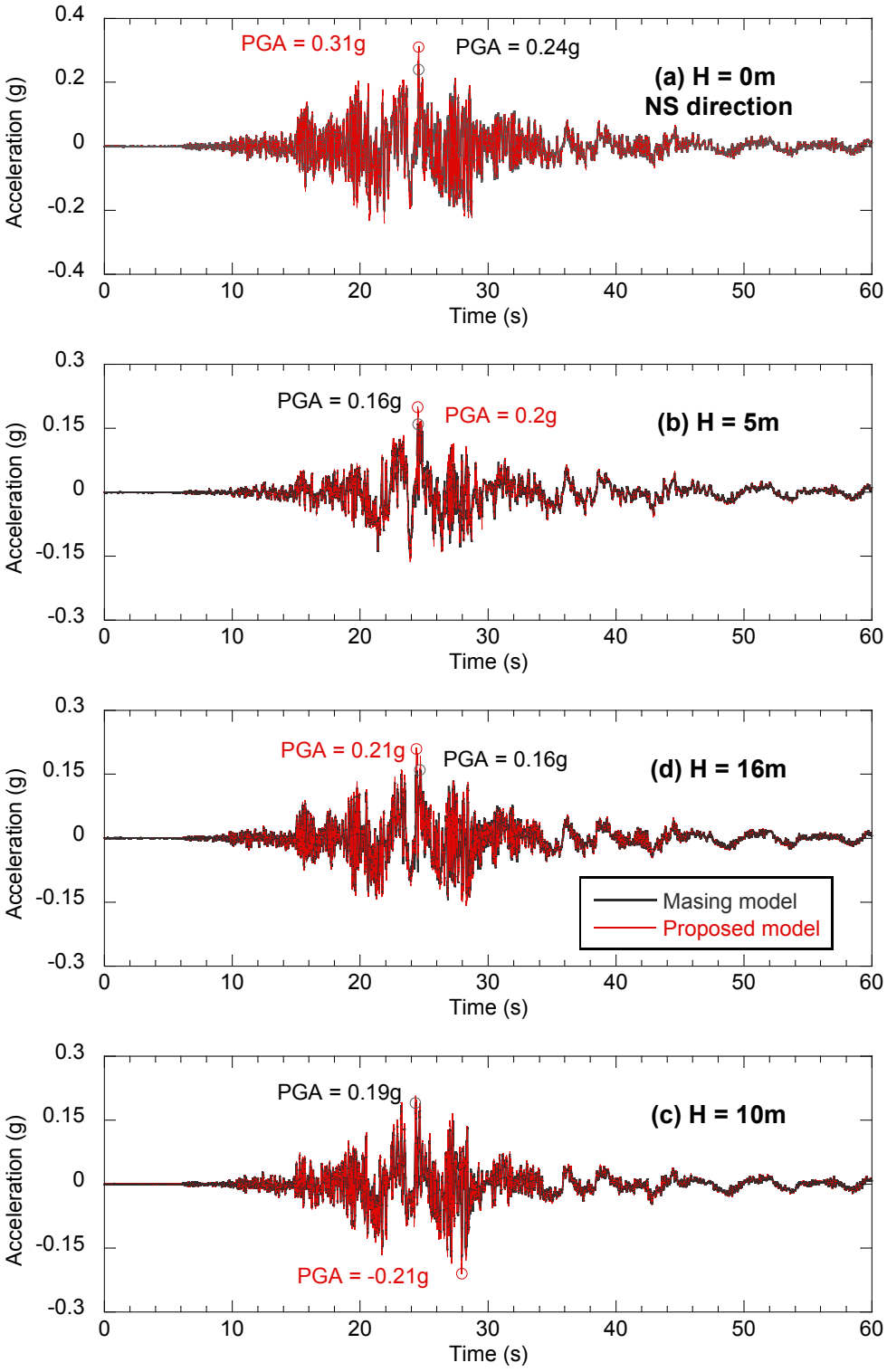

Figure 7-19 Computed time histories at the surface and depths of H = 5, 10 and 16m of the REHS station using the proposed and Masing models in North-South direction

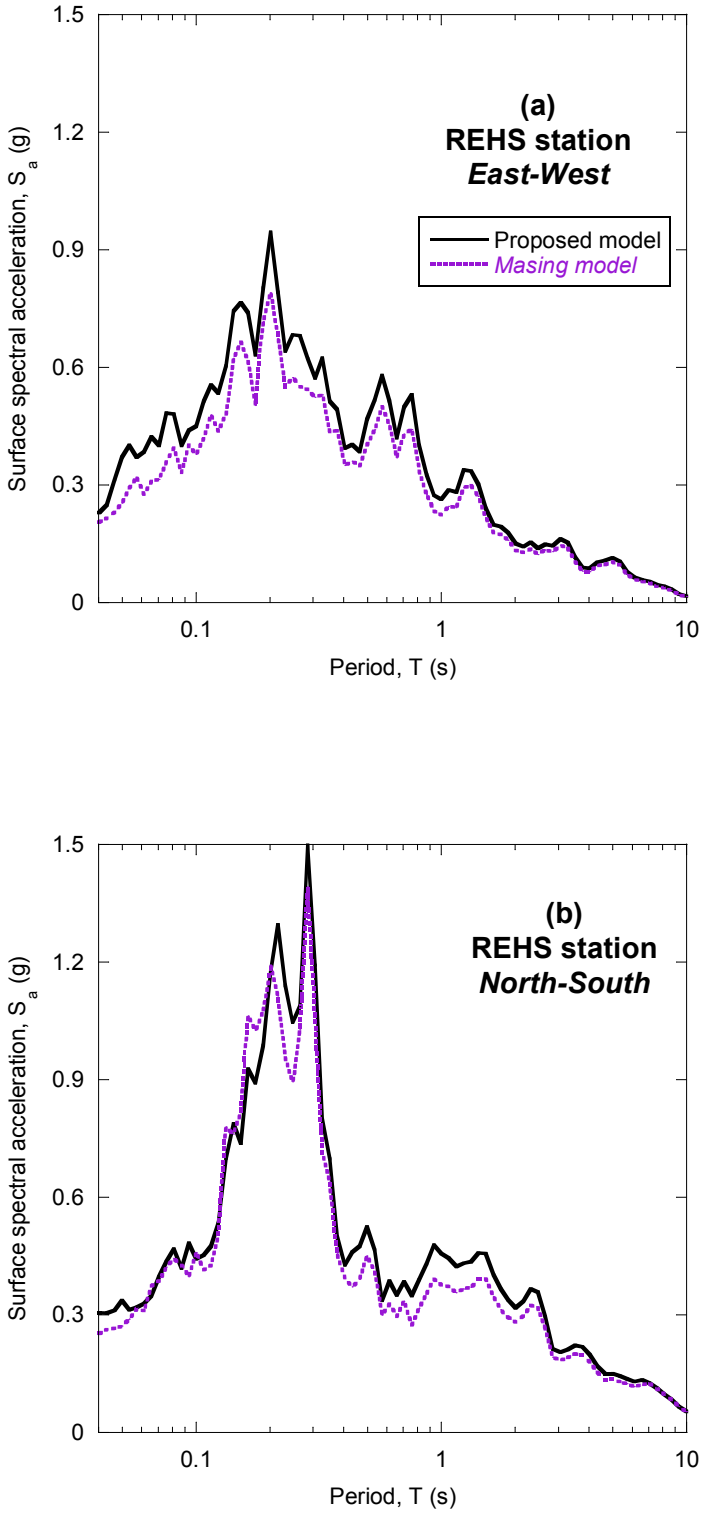

Figure 7-20 Comparison of 5% damped response spectra for the REHS soil site using the proposed formulation (solid line) and Masing criteria (dotted line) for (a) EW (approximately fault-parallel) and (b) NS (approximately fault-normal)

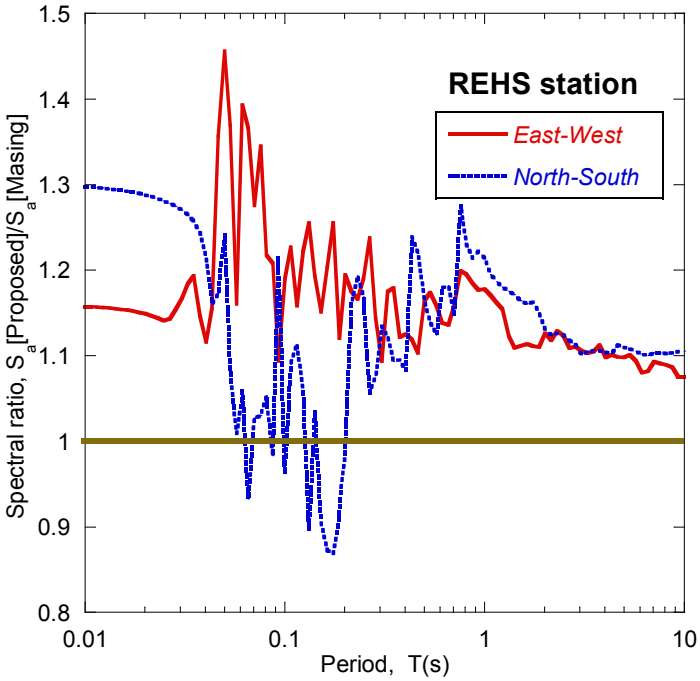

Figure 7-21 Comparison of ratios of the computed spectral accelerations of the proposed model and the Masing rule for East-West and North-South directions

Figure 7-22 presents the maximum shear strain profile for this strong motion station using the proposed and the Masing model. It appears that the maximum shear strains are computed consistently smaller by Masing rule than it is computed by the proposed model. This difference is more pronounced in NS direction where the computed strains are larger compared to EW direction. Note that in the NS direction the maximum shear strain exceeds 0.4% at the depth, H = 12.5m. The shear stress-shear strain hysteretic loops are presented for the depth, H = 13m, in Figures 7-23 and 7-24. Excessive hysteretic damping dissipated using the Masing model is clearly shown in Figure 7-23 for East-West component of the input ground motion. For the Masing model, a larger residual shear strain is also observed for this strong motion station as illustrated in Figures 7-22e and 7-23f. Similar trend is observed for stress-strain behaviour at other depths as shown in Figures 7-25 and 7-26. It is seen that at depths, H ~ 16m below ground level where induced shear strains are lower, the stress-

strain relationships simulated by Masing and proposed model are quite similar. For shallower soil layers where shear modulus is lower and induced shear strains are larger, the difference in the two modelling approaches is most significant and may alter the ground response substantially affecting the stress-strain curves, damping ratios and response spectra.

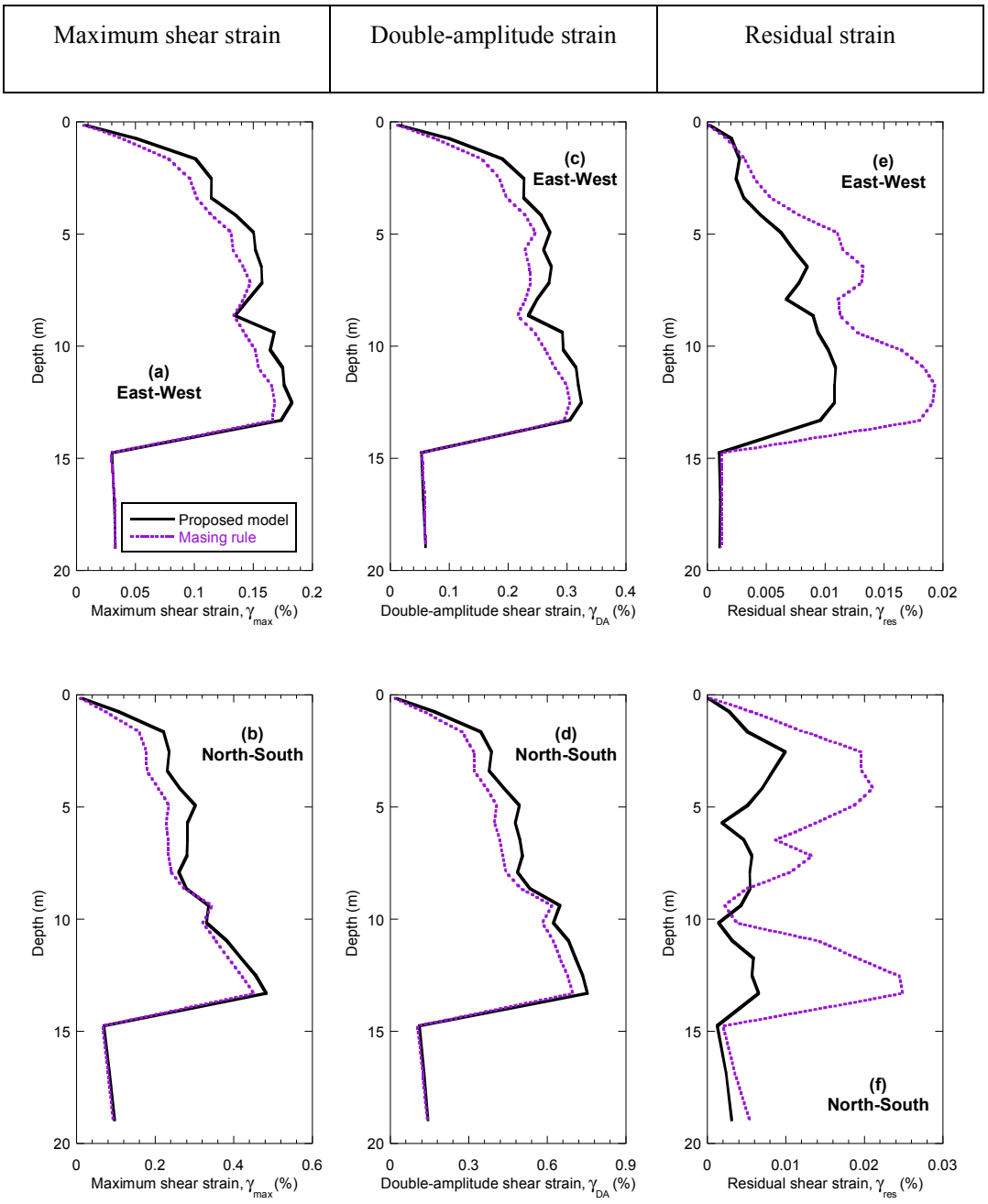

Figure 7-22 Maximum and residual shear strain profiles for REHS with simplified Rayleigh viscous damping in (a) East-West and (b) North-South directions. Note that the strains are not plotted in the same scales

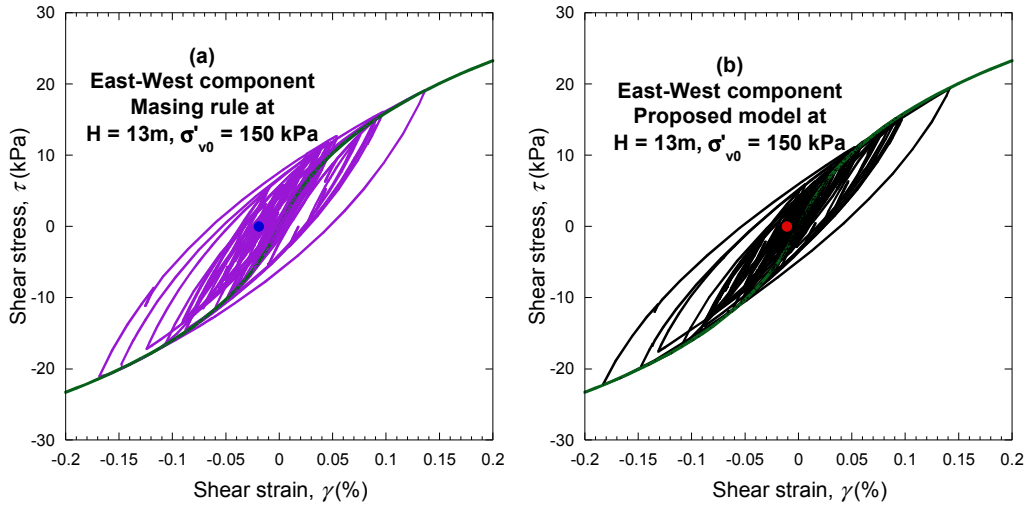

Figure 7-23 Computed stress-strain behaviour in EW direction of REHS for: (a) Masing; (b) proposed models. The green solid line represents the backbone curve

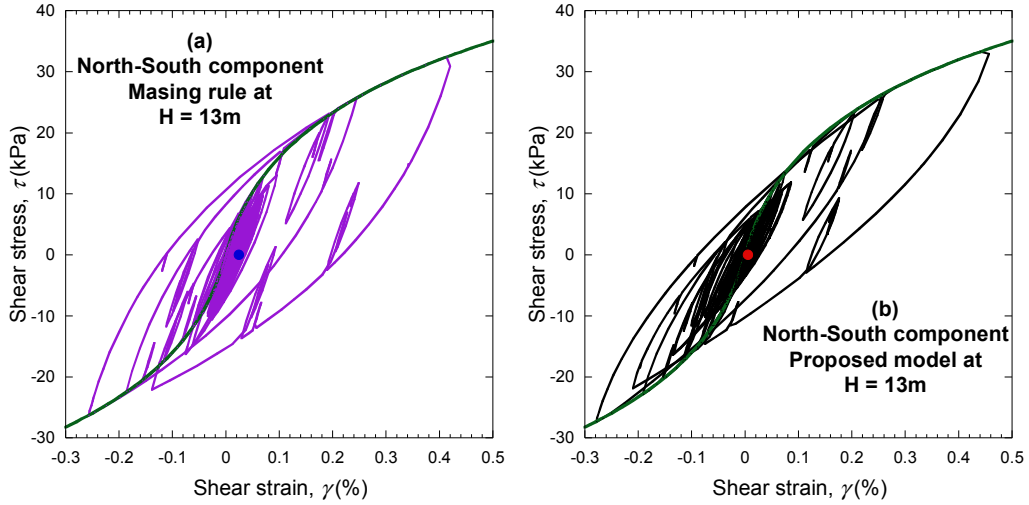

Figure 7-24 Computed stress-strain behaviour in NS direction of REHS for: (a) Masing; (b) proposed models. The green solid line represents the backbone curve

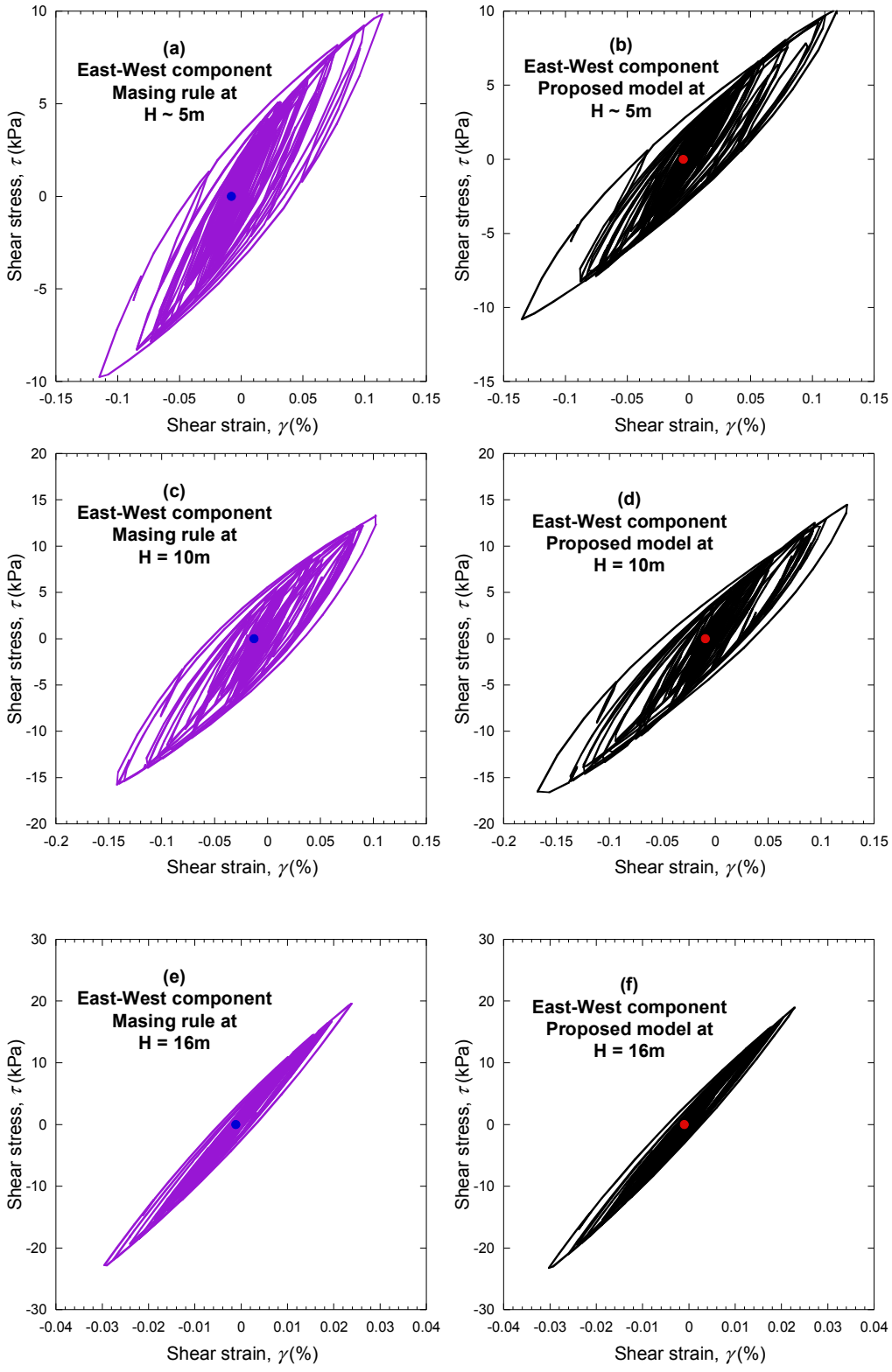

Figure 7-25 Computed stress-strain behaviour in EW direction of REHS for depths H = 5, 10, 16m below ground level

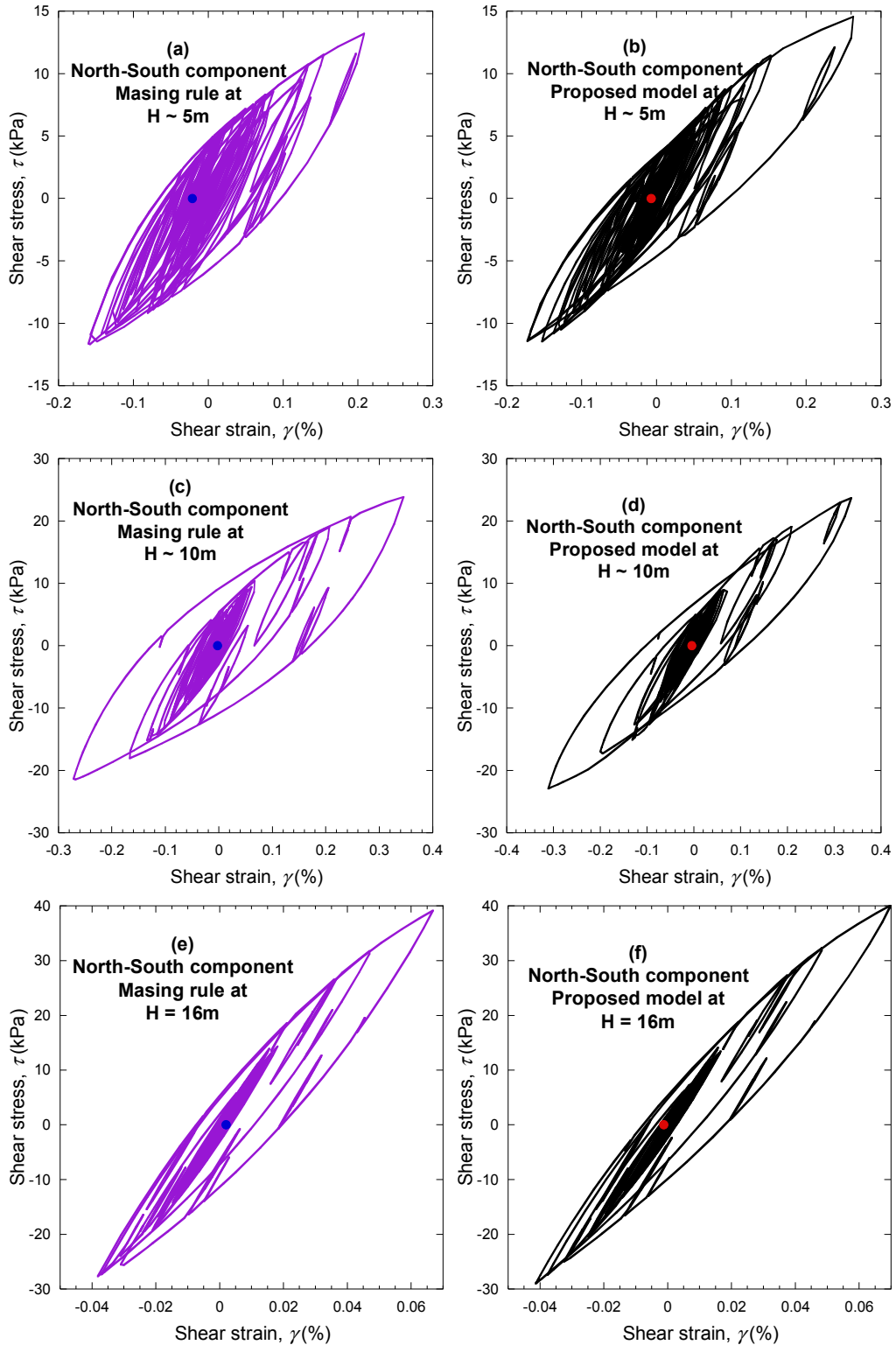

Figure 7-26 Computed stress-strain behaviour in NS direction of REHS for depths H = 5, 10, 16m below ground level

7.4.2 CCCC

The CCCC site is a soft soil to a depth of 18 to 25m over a stiff layer of Riccarton Gravel (Figure 7-27), with a gradual transition to competent bedrock at >500m in depth. Elastic modelling of the top 18m of the CCCC strong motion station shows that 0.4% damping ratio in both directions for the viscous damping in time-domain analysis provide a good match with the results of the exact solution provided by Strata. Figure 7-28 presents a comparison between the computed surface response spectra from linear frequency domain (exact solution) and time domain solution (simplified Rayleigh damping) for the CCCC station soil profile. Using the computed low-strain viscous damping and the deconvolved ground motions at 18m depth, surface ground motions were calculated. The modulus and damping properties which were used in nonlinear analyses are presented in Figure 7-29.

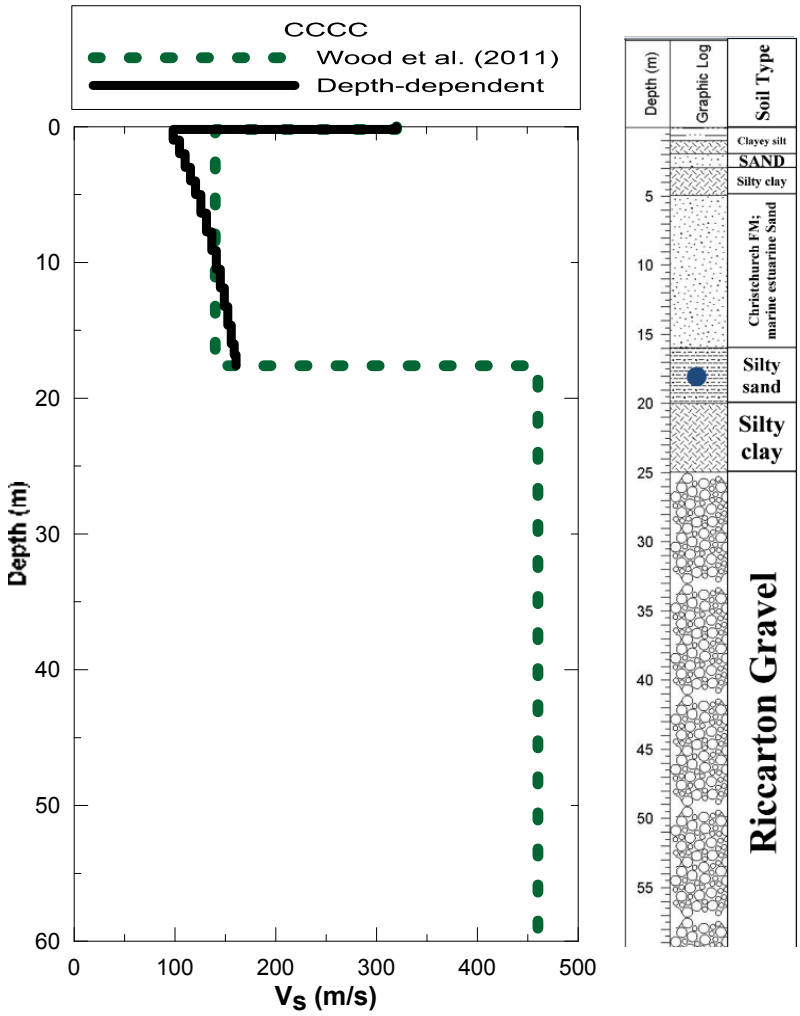

Figure 7-27 Soil type index (top), shear wave velocity (left) and stratigraphy (right) profile (modified after Wood et al., 2011, CERA, 2013, Stephenson et al., 2010)

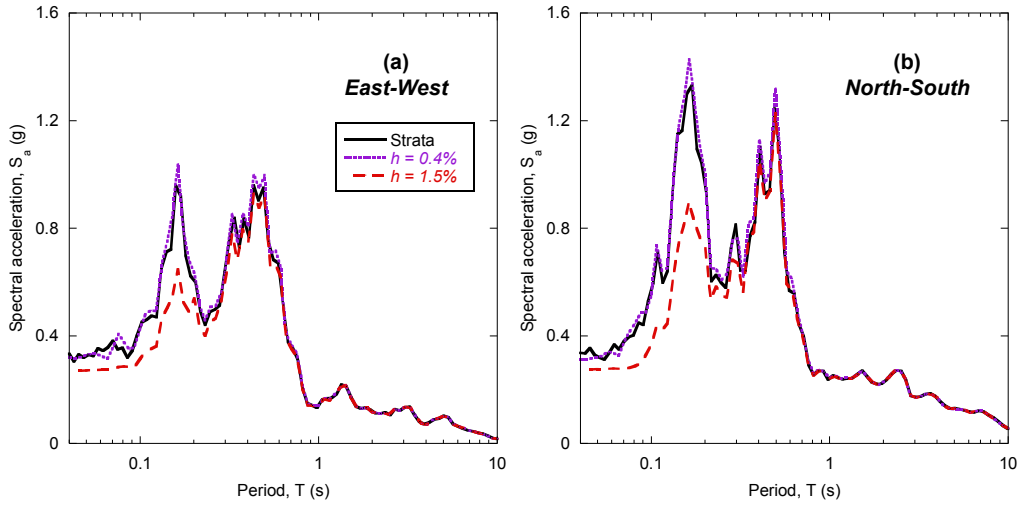

Figure 7-28 Comparison of 5% damped response spectra for the CCCC strong motion soil site using elastic frequency-domain with that of time-domain for (a) East-West (approximately fault-parallel) and (b) North-South (approximately fault-normal) components

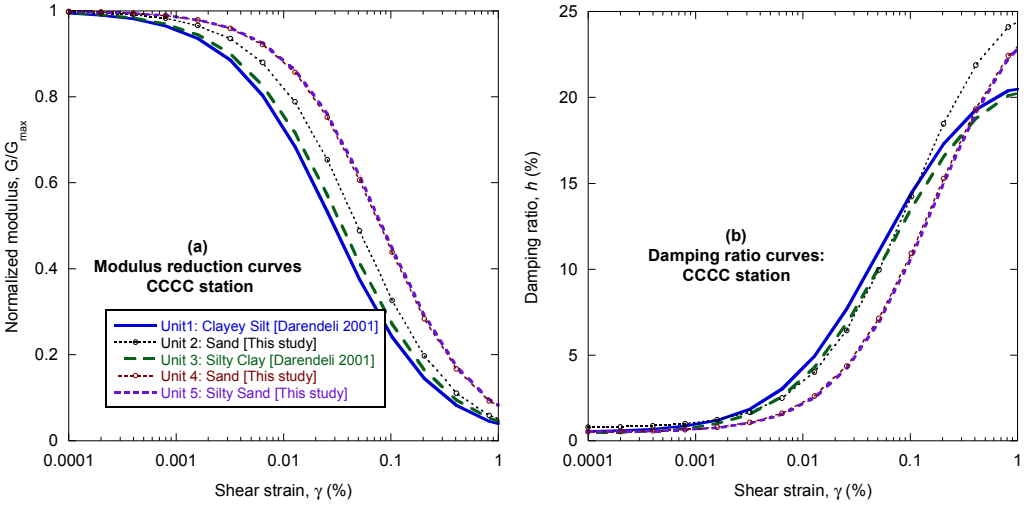

Figure 7-29 Modulus reduction and damping ratio curves for CCCC station soil profile. For soil types and/or confining stresses that no laboratory tests were conducted in this study, Darendeli (2001) family of modulus and damping ratio curves have been used

7.4.2.1 Nonlinear site response analyses of CCCC station

Consider the results of calculations for the input motions shown in Figures 7-27 to 7-29. The pseudo-acceleration response spectra at the surface of the CCCC station for the two components of the Darfield earthquake are computed and compared using

the two soil models. In the EW direction, the Masing solution slightly underestimates the motion; this underestimation is less than 20% for a wide period range as is seen in Figure 7-32. This small variation between the two models might be due to small maximum shear strain in the soil profile as shown in Figure 7-33a.

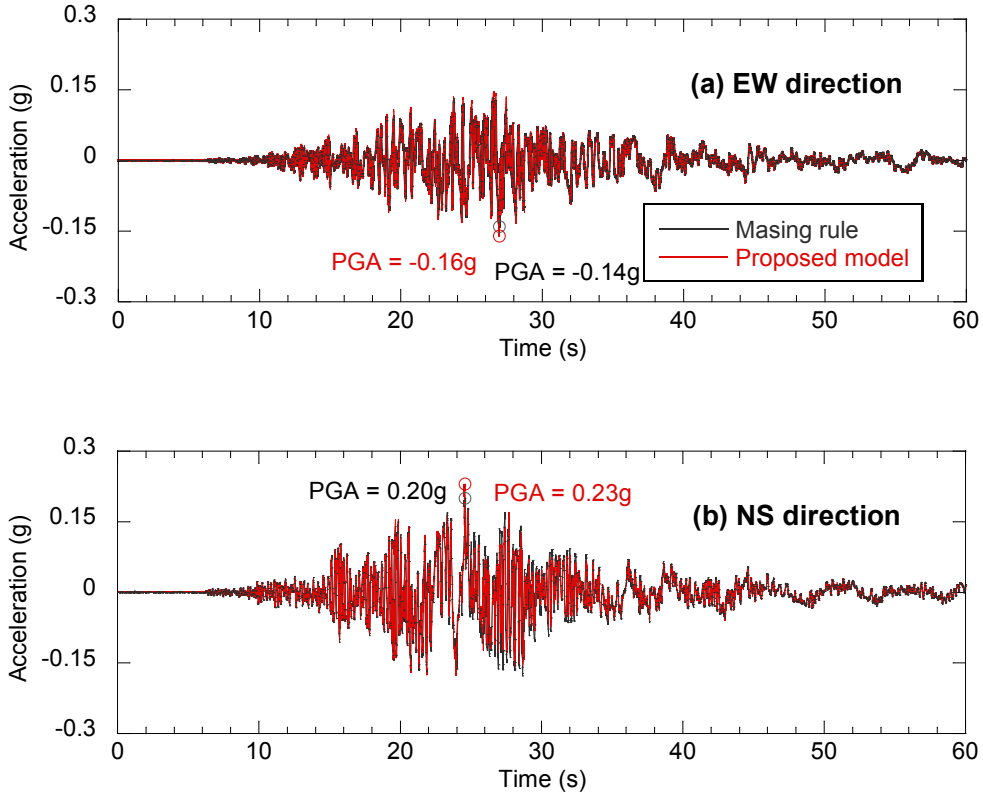

Figure 7-30 Computed time histories at the surface of CCCC strong motion station using the proposed and Masing model

In the NS direction the underestimation of spectral acceleration computed by Masing model occurs in the high-period range (T > 0.2s). The over-prediction of the response by Masing model in the mid-period range is similar to what is observed for the arbitrary single layer explained in section 7.2. The maximum shear strain profile is presented in Figure 7-33b. The proposed model consistently predicted higher shear strains across the profile depth as shown before.

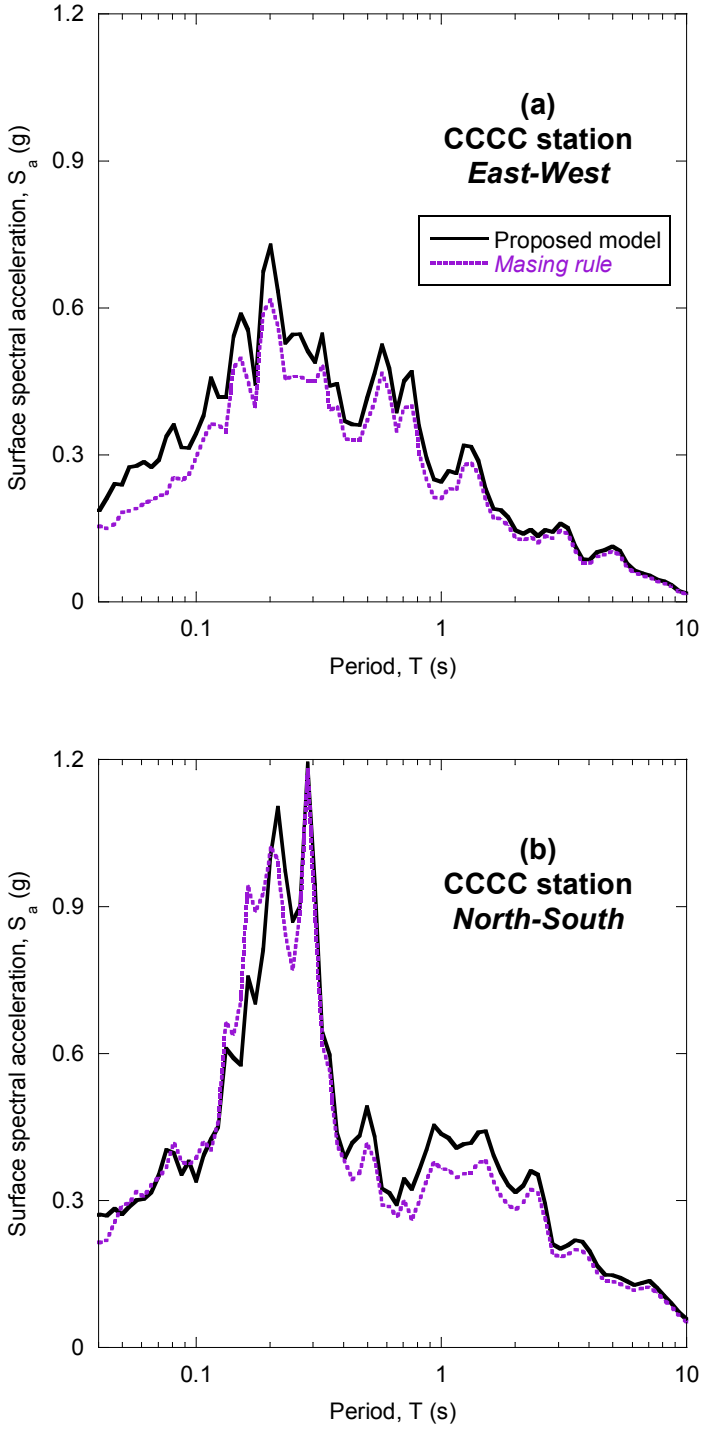

Figure 7-31 Comparison of 5% damped response spectra for the CCCC soil site using the proposed formulation and Masing criteria for (a) EW and (b) NS components

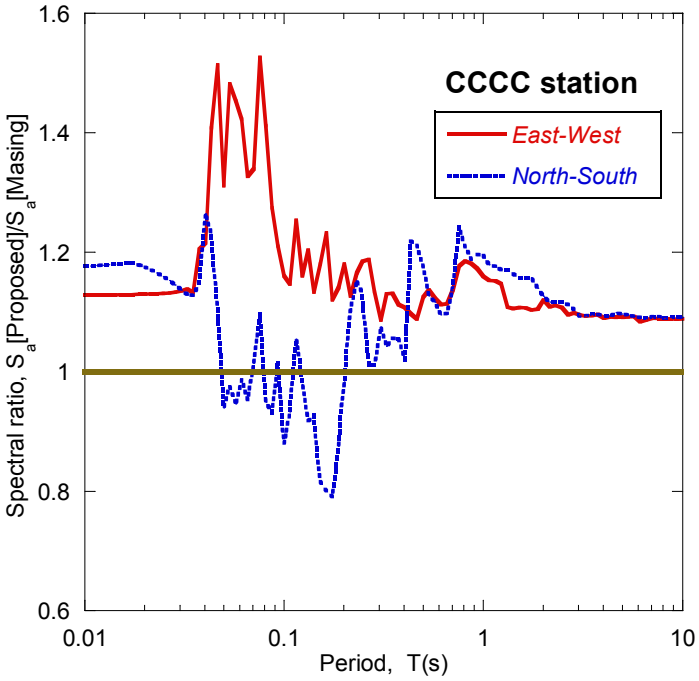

Figure 7-32 Comparison of ratios of the computed spectral accelerations of the proposed model and the Masing rule for East-West and North-South directions

The other significant difference between the proposed model and Masing is the computed residual shear strain. For instance, Figure 7-33e and 7-30f, plot the residual strains across the profile depth. It is shown that the Masing model predicts larger residual strains compared to the proposed model. This behaviour can be also observed in Figure 7-35 by comparing the computed hysteretic loops of the two models at H = 14m. This can be regarded an attribute of the proposed model as the unloading-reloading stiffness is lower than the Masing one.

Figure 7-34 and Figure 7-35 illustrate the stress-strain hystereses computed at the depth H = 14m, for East-West and North-South directions, respectively. It appears that both in the East-West (EW) and the North-South (NS) direction, predicted maximum shear strains are very similar and the computed hysteretic damping by the proposed model appears lower than the one computed by Masing model.

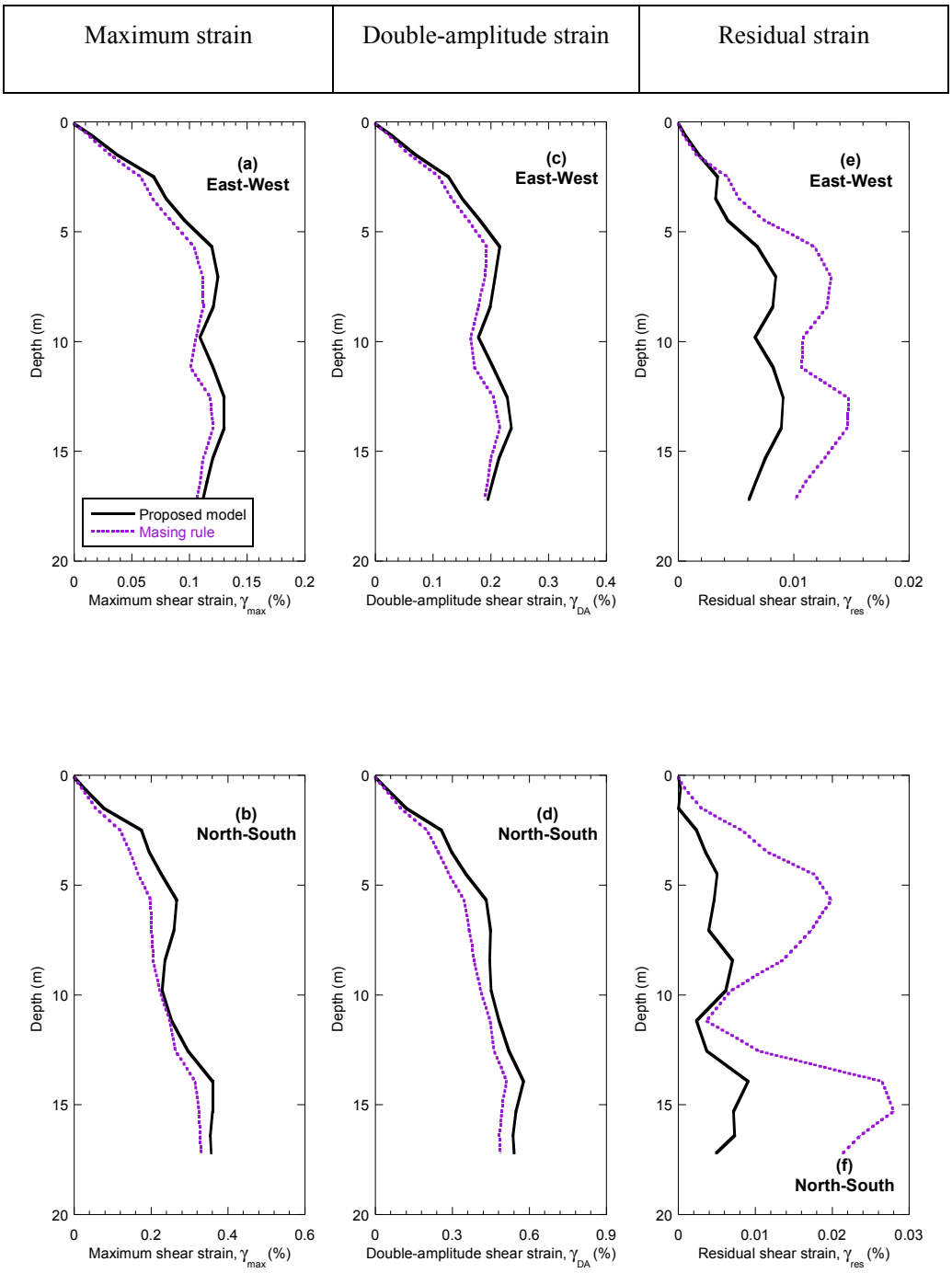

Figure 7-33 Residual and maximum shear strain profile for CCCC site response analysis with simplified Rayleigh viscous damping in (a) East-West and (b) North-South directions. Note the scale is different for each set of shear strain profiles

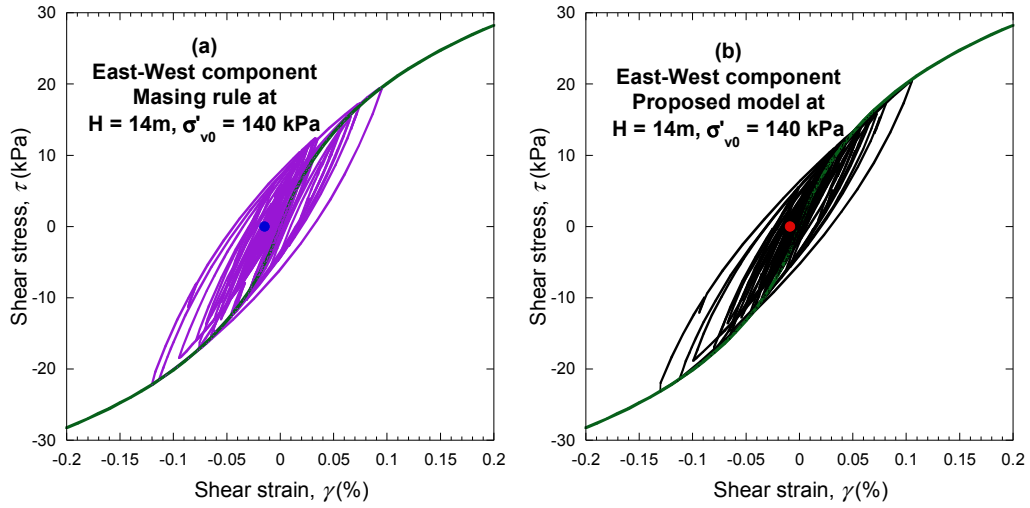

Figure 7-34 Computed stress-strain behaviour in East-West direction of CCCC station for: (a) Masing criteria; (b) proposed model; The solid circle represents the residual strain

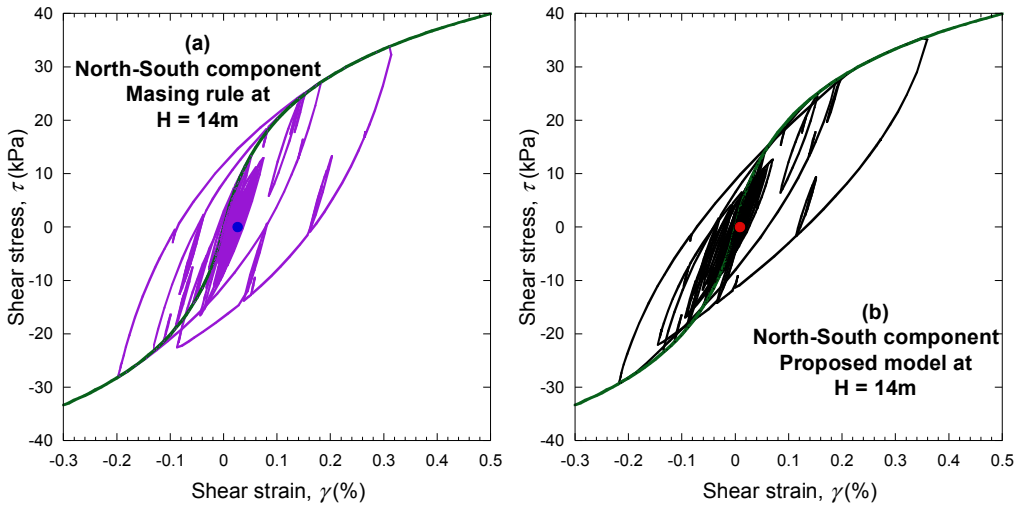

Figure 7-35 Computed stress-strain behaviour in North-South direction of CCCC station for: (a) Masing criteria; (b) proposed model; The solid circle represents the residual strain

7.4.3 CBGS

The CBGS strong motion station has a 20-m layer of shallow soil that overlies stiffer Riccarton Gravel. The shear wave velocity profile and the stratigraphy of this station soil profile are illustrated in Figure 7-36. The normalized modulus reduction

and damping ratio curves employed in site response analyses are also presented in Figure 7-37. Figure 7-38 compares the 5% damped acceleration response spectra of surface motions of linear analysis using Strata and OpenSees. It was found that the 0.4% damping ratio in both the EW and the NS directions for the stiffness-proportional viscous damping in time-domain analyses provide the best match with the exact solution provided by Strata.

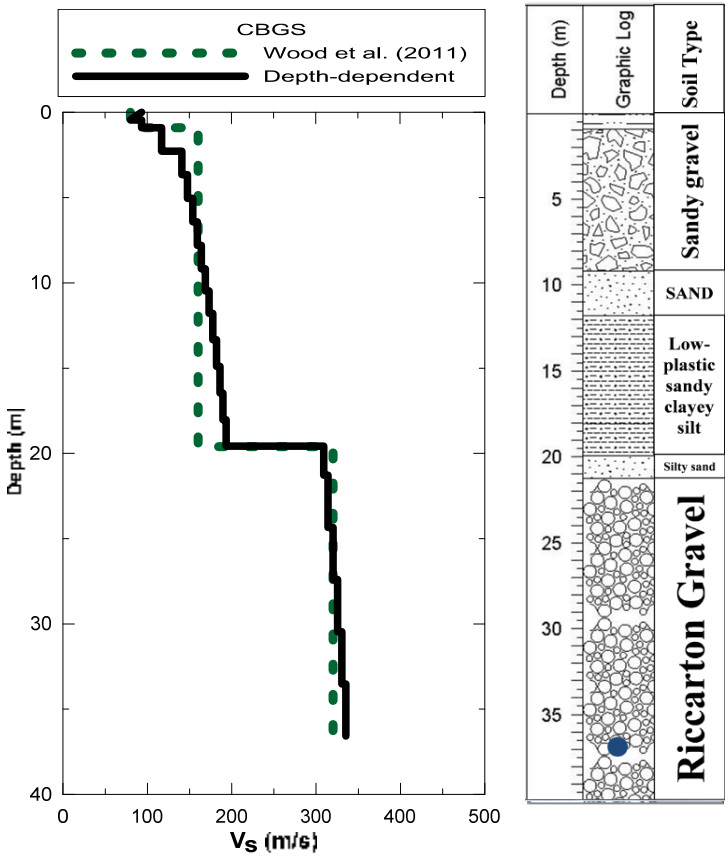

Figure 7-36 V_s (left) and stratigraphy (right) profile at the CBGS station (modified after Wood et al., 2011, CERA, 2013, Stephenson et al., 2010)

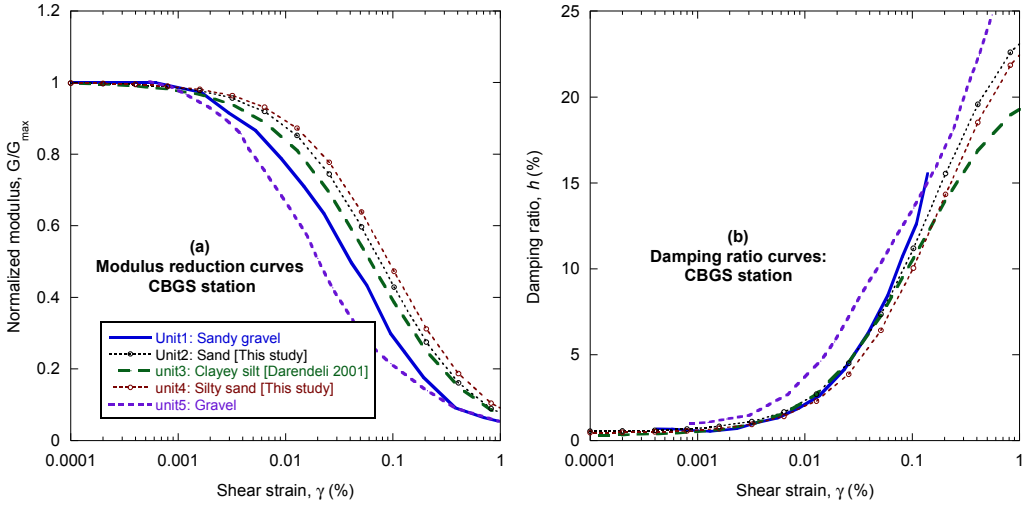

Figure 7-37 Normalized modulus reduction and damping ratio curves of soil unit in CBGS station soil profile. For soil types and/or confining stresses that no laboratory tests were conducted in this study, Darendeli (2001) family of modulus and damping ratio curves have been used.

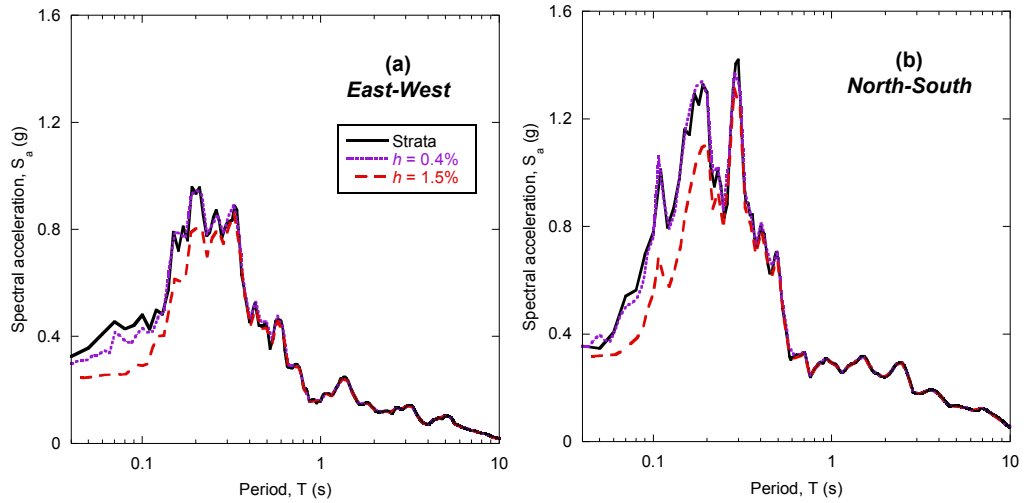

Figure 7-38 Comparison of 5% damped response spectra for the CBGS strong motion soil site using elastic frequency-domain with that of time-domain for (a) East-West (approximately fault-parallel) and (b) North-South (approximately fault-normal) components

7.4.3.1 Nonlinear site response analyses of CBGS station

Nonlinear time-domain analyses were also carried out using the Masing and the proposed formulation. The nonlinear model parameters were computed based on the modulus reduction and damping curves presented in Figure 7-37. The computed target

small-strain damping ratios from elastic analyses were used at the corresponding natural frequency of the top 36m of the CBGS station, $f \sim 1.38$ Hz. Consider results of calculations for the input motions shown in Figures 7-39 and 7-40. The pseudo-acceleration response spectra at the surface of the CBGS station for the two components of the Darfield earthquake are computed. In Figure 7-40a, the proposed model spectra are larger than the spectral acceleration for Masing criteria at $T > 0.1$s and $T < 0.03$s, which is expected and which was consistently observed in the spectra computed at other stations. Although this pattern is also followed in the NS direction, the overestimation of spectral acceleration computed by the Masing model in intermediate periods, is persistent across a wider period range, $0.03\text{s} < T < 0.3\text{s}$ (Figure 7-41).

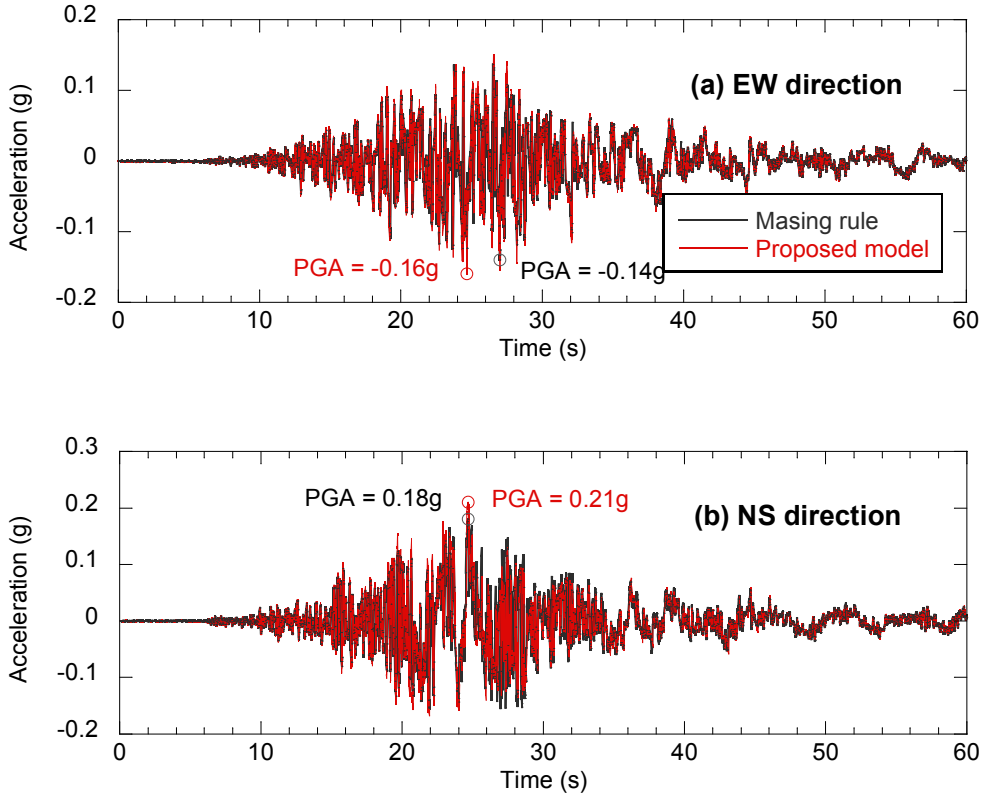

Figure 7-39 Computed time history at the surface of the CBGS station, (a) East-West direction and (b) North-South direction

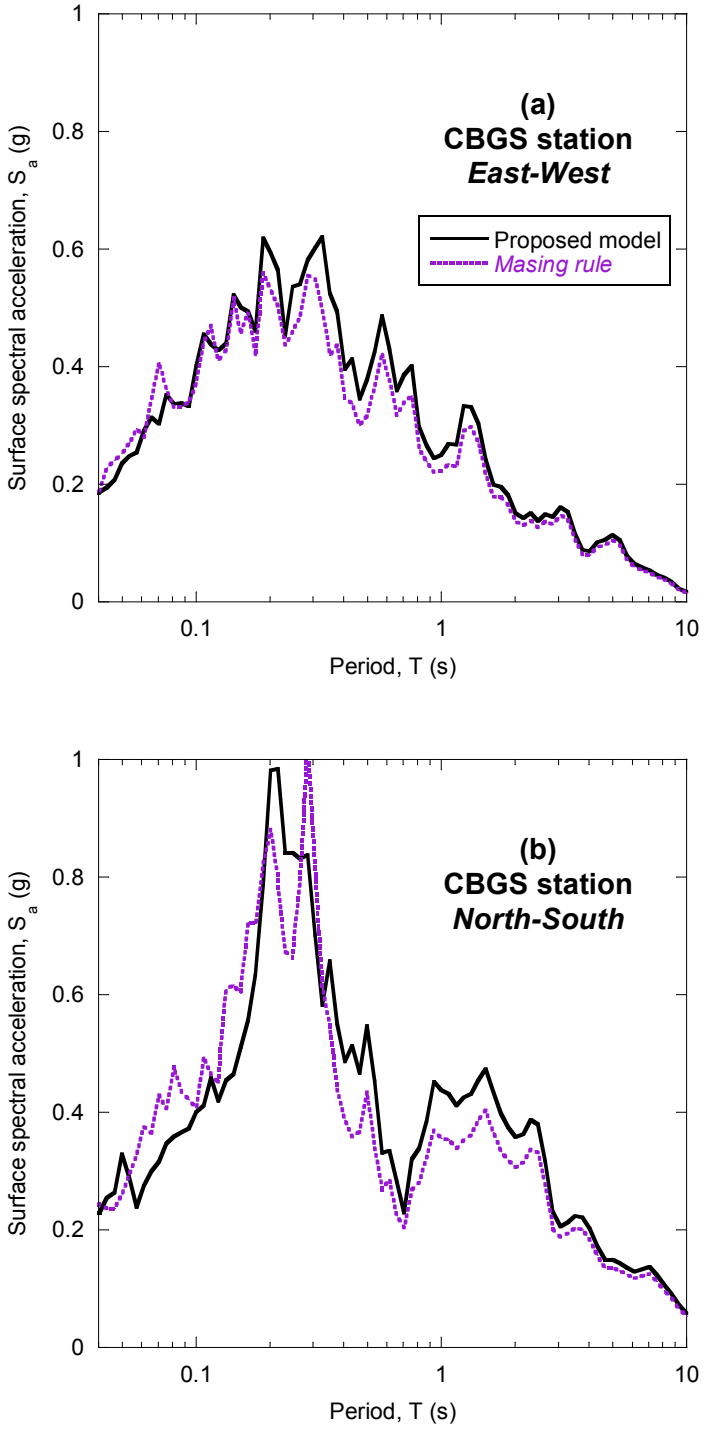

Figure 7-40 Comparison of 5% damped response spectra for the CBGS strong motion soil site using the proposed formulation and Masing criteria for (a) East-West (approximately fault-parallel) and (b) North-South (approximately fault-normal) components

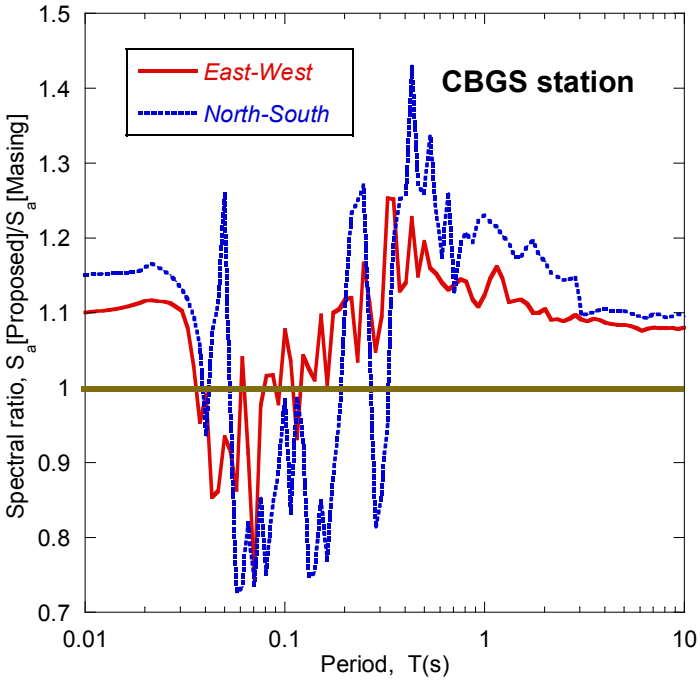

Figure 7-41 Comparison of ratios of the computed spectral accelerations of the proposed model and the Masing rule for East-West (solid line) and North-South (dotted) directions

The maximum shear strain profiles are presented in Figure 7-42 for the CBGS soil column. It is apparent that the maximum shear strain profiles computed by the proposed model is larger compared to what is computed by the Masing model. However, the residual shear strains computed by Masing are larger than the residual strains computed by the proposed model.

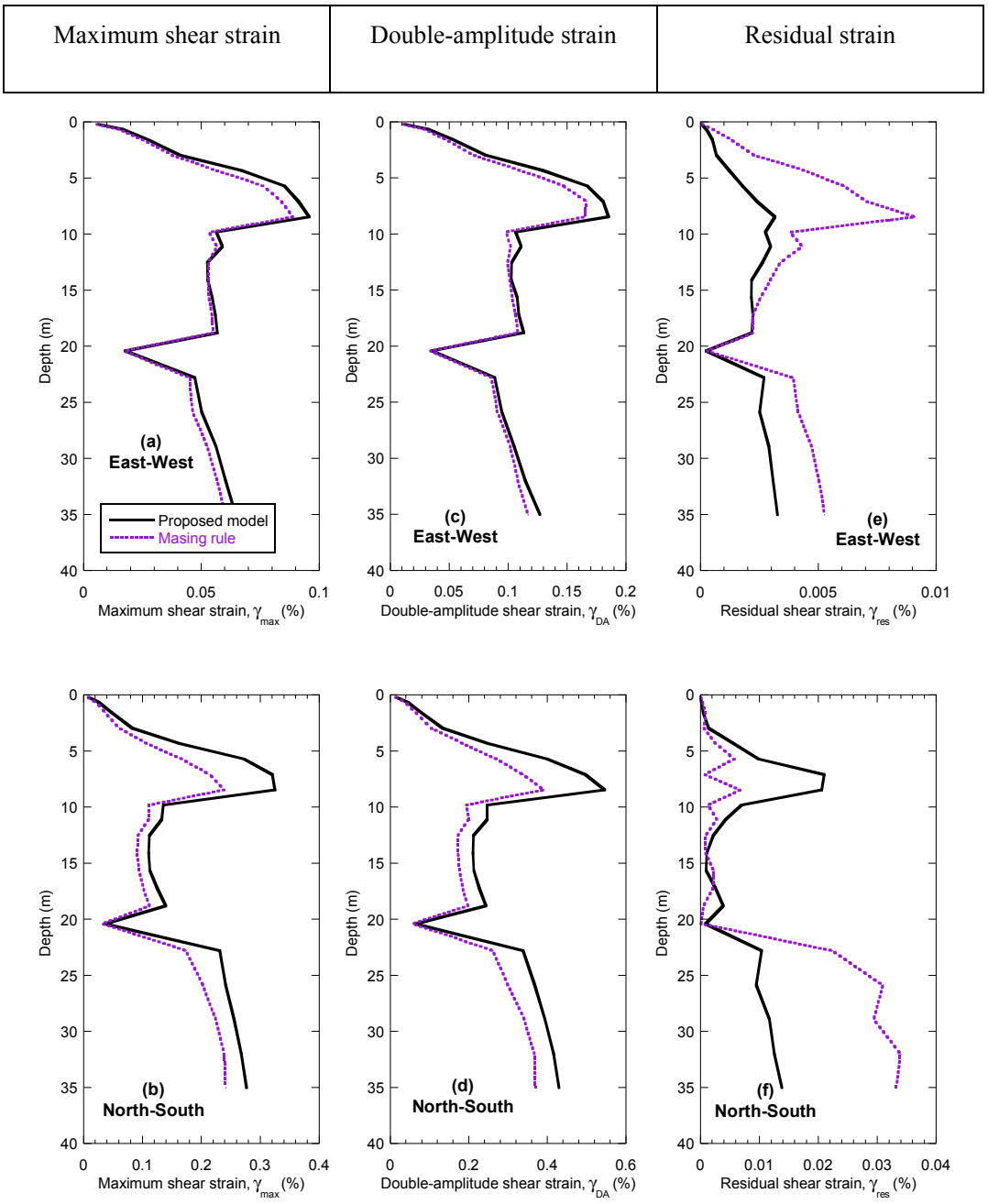

Figure 7-42 Maximum shear strain profile for CBGS site response analysis with simplified Rayleigh viscous damping in (a) East-West (approximately fault-parallel) and (b) North-South (approximately fault-normal) directions

7.5 Comparison of the estimated with the observed ground motion for the 2010 Darfield earthquake

It is desirable to compare the computed motions using the proposed model with the actual motions recorded during the 2010 Darfield event. During the M7.1 Darfield, Canterbury earthquake of 4 September 2010, several strong motion stations recorded the ground motions. In this section, one of these strong motion stations is selected to further investigate this comparison. The results in the form of ground-surface response spectra are compared to the actual recordings. Additional ground response analyses were performed with the program Strata for equivalent linear modelling of the selected soil profile. The computer program Strata computes the response for vertical propagation of horizontally polarized shear waves through a site with horizontal layers. For linear elastic, one-dimensional wave propagation, the soil is assumed to behave as a visco-elastic Kelvin-Voigt medium, in which the dynamic response is described using a purely elastic spring and a purely viscous dashpot (Kottke and Rathje, 2010). It performs equivalent linear site response analysis in the frequency domain using time domain input motions.

In the equivalent linear analyses presented in this chapter, a cut-off frequency of 25 Hz was used, and the effective strain in equivalent linear analyses was chosen to be 61% (Idriss and Sun, 1991). The spring and dashpot constants were related to the same set of G-γ and h-γ curves used for the fully nonlinear analysis. Thus, the same fundamental stress-strain relations were obtained for both sets of results, the difference lying in the way the solutions were computed. But firstly, in order to ensure that the modulus reduction properties at small to intermediate strain levels as well as

the strength properties at larger strain are captured properly, a parametric study is first conducted in this chapter.

7.5.1 Simulation of backbone curve using normalized modulus reduction curve and shear strength

It has been noted (e.g. Stewart et al., 2008) that the hyperbolic backbone curve defined by G_{max}, γ_r and, a, is capable of capturing stress-strain behaviour of soil within small to moderate strain levels. However, using the reference strain, γ_r, obtained from laboratory G/G_{max} curves, may not capture the actual strength of the soil at larger strains. This is because the reference strain is generally determined based on the normalized modulus reduction curves for strains less than 1% whereas the shear strength is typically mobilized at larger strain levels. This problem is further investigated by examining the degree to which the computed shear strength by the proposed model is different from the actual shear strength of the soil for several shear wave velocities and confining stresses.

A hypothetical element of soil with a given shear wave velocity (V_{s1}) at confining pressure of σ'_{v0} = 100kPa is considered. Note that employing equation (7-3), the shear wave velocities at different confining pressures can be also calculated. The simulated shear stress using the hyperbolic model is then computed at a large strain level (e.g. at γ= 5%) using the confining-stress-dependent reference strain, γ_r.

$$V_s = V_{s1}\left(\frac{\sigma'_{v0}}{p_a}\right)^{0.25} \tag{7-3}$$

$$\tau_m = \frac{\rho V_s^2 \gamma}{1 + \left(\frac{\gamma}{\gamma_r}\right)^a}$$

The actual shear stress τ_r, at the assumed large strain level (e.g. γ= 5%), is also calculated based on a fraction of the critical state strength of soil, $\tau_f = \sigma'_v \tan(\phi'_{cs})$. The reference stress, τ_r, at the assumed strain level, γ= 5%, is assumed to be 90% of the residual strength at critical state based on experimental tests on Toyoura sand (e.g. Cubrinovski, 1993). Figure 7-43 compares how accurately the model can capture the actual shear stress at this large strain level. It is shown that for small shear wave velocities, the shear strength is highly underestimated using the hyperbolic model with the given set of parameters based on target G/G_{max} curve which are calculated using a = 0.98. However, this bias disappears with an increase in the shear wave velocity.

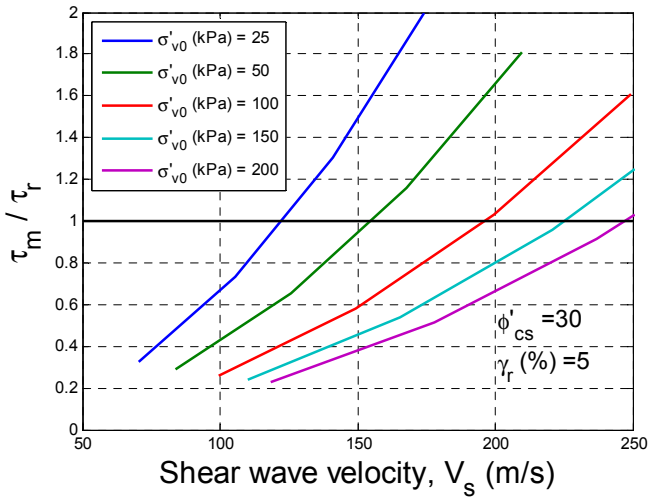

Figure 7-43 Comparison of the ratio of simulated shear strength, τ_m, and actual shear strength, τ_r, at γ= 5% versus shear wave velocity of the soil profile

For large-strain problems, where a fraction of the critical state strength is used to define the hyperbolic model parameters, the curvature coefficient, a, needs to be re-calibrated in order to realistically simulate the large strain stress-strain behaviour. However, the computed modulus reduction curve may deviate from the target G/G_{max} curves because of different curvature coefficients. Figure 7-44 illustrates if the large-strain properties are used to calibrate the hyperbolic model, what curvature coefficient needs to be employed with the depth-dependent reference strain, γ_r. It appears that the required curvature coefficient to capture the actual strength properties, can be different from a = 0.98 used for the target curves. Figures 7-45 and 7-46 compares how the normalized and absolute stress-strain relationships for $V_{s1} < 150\, m/s$ are simulated if large strain properties are used to calibrate the curvature coefficient. The misfit of the computed modulus reduction curve and target G/G_{max} curves are presented in Figure 7-47 if the curvature coefficients in Figure 7-44 are employed. It appears that poor match is obtained for V_s < 100 m/s at overburden pressures σ'_{v0} > 50 kPa.

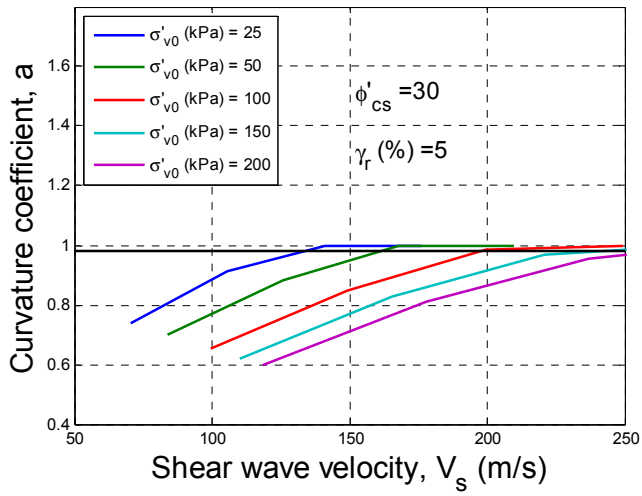

Figure 7-44 Comparison of the curvature coefficients, a, to capture the reference stress, τ_r = 0.9 . τ_f, at γ_r = 5% versus shear wave velocity of the soil profile

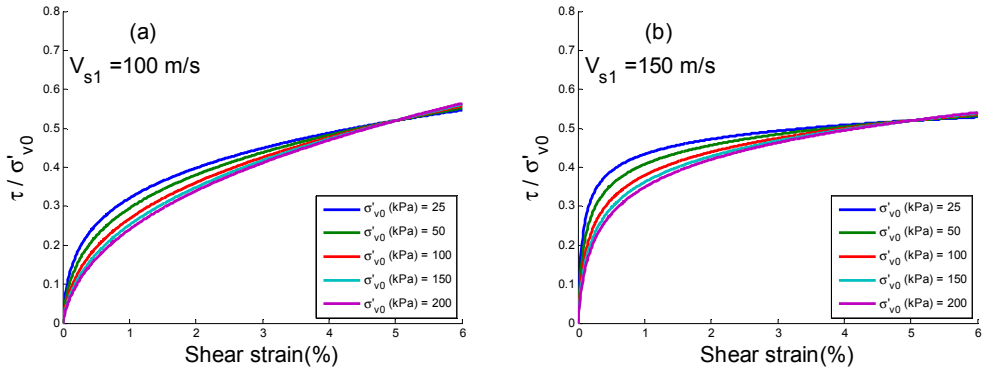

Figure 7-45 Influence of vertical effective stress on the simulated normalized stress-strain curve (a) V_{s1} = 100 m/s and, (b) V_{s1} = 150 m/s

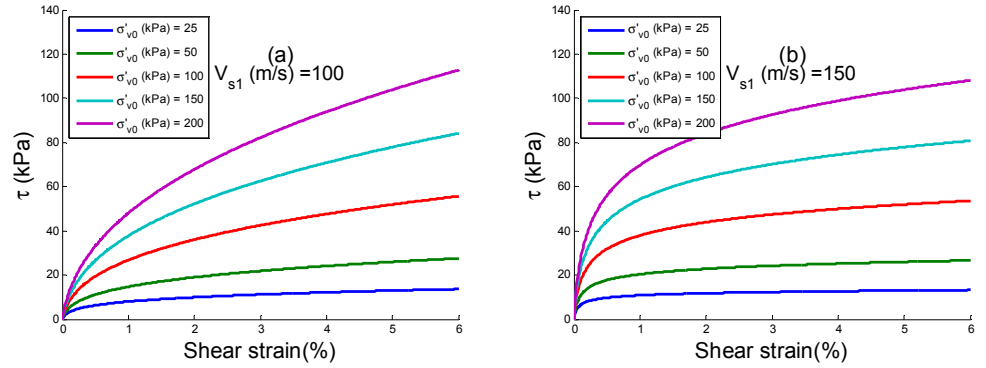

Figure 7-46 Influence of vertical effective stress on the simulated stress-strain curve (a) V_{s1} = 100 m/s and, (b) V_{s1} = 150 m/s

It was shown in Chapter 6 that the material damping curve can be simulated independent from the backbone curve for any desired target values. To illustrate the sensitivity of the computed site response to the selection of model parameters based on target modulus reduction curve (strains less than 1%) and strength properties (strains larger than 1%), the two sets of assumptions will be employed in the site response analyses in REHS station. The main difference would be the use of curves constrained by the shear strength or the target modulus reduction curve.

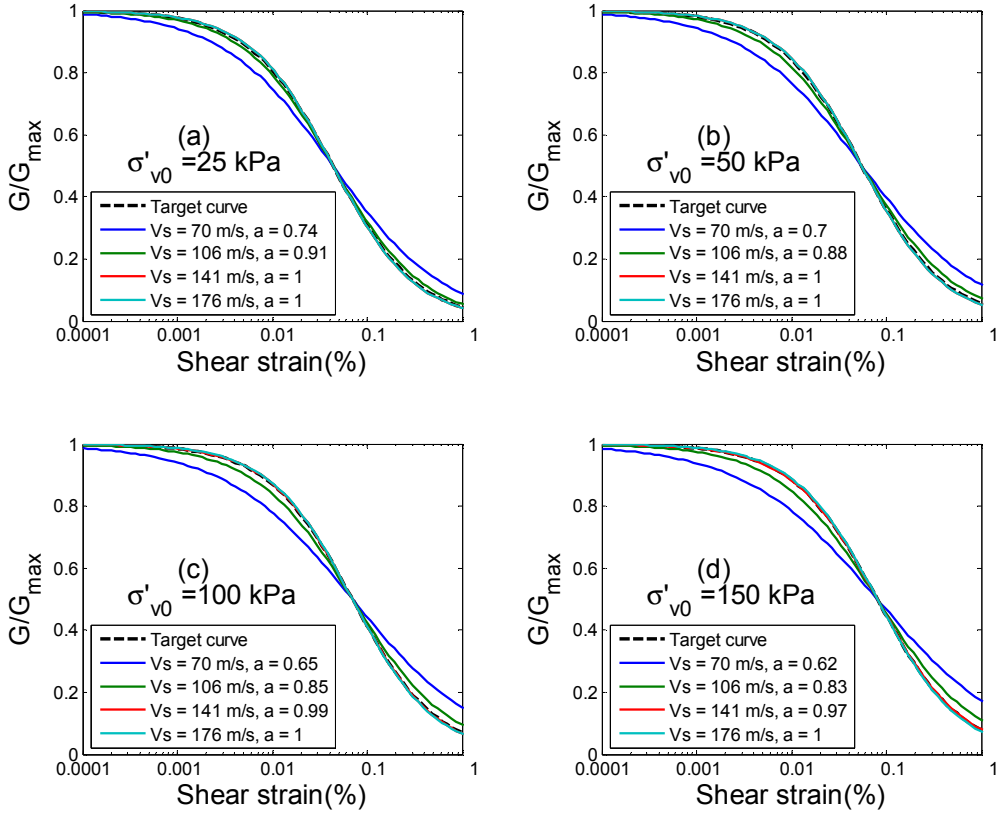

Figure 7-47 Comparison of the target modulus reduction curve with the simulated G/G_{max} curves using the large-strain strength properties

7.5.2 Comparison to the observed ground motion

A set of 1D site response analyses employing the equivalent linear and nonlinear analyses is carried out at REHS station under a base motion corresponding to the horizontal components of the deconvolved motion of the RHSC record of the 2010 Darfield earthquake. As shown in Figure 7-48, the RHSC station is approximately located 10km away from the fault plane which created 2010 Darfield event and 6km distant from REHS station. The computed results using the two approaches are then compared with the recorded motion at the surface REHS station.

Figure 7-48 Approximate location of the considered strong motion station relative to the Darfield earthquake plane. The approximate fault trace and the REHS station are indicated by the solid red line and the black circles, respectively (after maps.google.com 2013)

In this subsection, a sensitivity analysis is first performed based on the results of previous section on simulation of G/G_{max} curves at small- to intermediate strains and stress-strain behaviour at large strain. As noted previously, the backbone relationship of each soil layer can be simulated using exact match of target G/G_{max} curve or large-strain strength properties; alternatively a balance between the two approaches can be adopted. An exact match of target curves in this study, implies a constant curvature coefficient, a = 0.98. Whereas depth-dependent strength behaviour results in layer-dependent a as shown in the previous section. Figure 7-49 illustrates the computed response spectra adopting two different assumptions of constant a = 0.98 and depth-dependent a. The measured shear wave velocity profile by Wood et al. (2012) is used for calculations of response spectra. Targeting G/G_{max} curve for the entire strain range with (a = 0.98), results in de-amplification of motion in low to mid period ranges. Whereas, improved amplification is predicted if depth-dependent strength properties are employed. The de-amplification of motion shown by blue-dashed line can be a direct consequence of shear strength underestimation. As shear strains in the soft layers develop excessively and soil is yielded, the computed accelerations decrease

due to induced nonlinearity. Figure 7-49 shows that capturing shear strength of the soft soil layers can improve the predicted motion in a great extent.

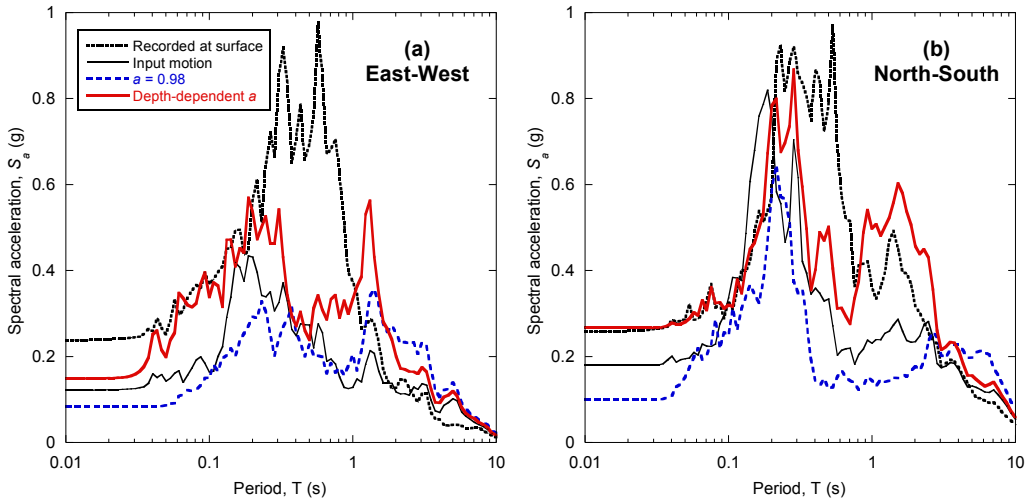

Figure 7-49 Influence of backbone simulation using the G/G_{max} curve or large-strain stress-strain relationship, (a) East-West and (b) North-South direction 5% damped response spectra at REHS station

Since shear wave velocity is expected to increase with an increase in confining stress, Vs is corrected for the effects of the overburden (e.g. Robertson, 2012). Two different shear wave velocity profiles were estimated. Profile 1 captures the softer layer between 6 – 13m and Profile 2 increases without any reduction to lower depths. Profile 1 is first adopted to investigate the effect of shear wave velocity changes with depth. Figure 7-51 shows the computed response spectra employing this soil profile. Note that depth-dependent model parameters are calculated and employed for this purpose. Although, in NS direction, the two profiles result in different spectral values at longer periods (T>1s), the spectra are very similar in EW in a wide period range.

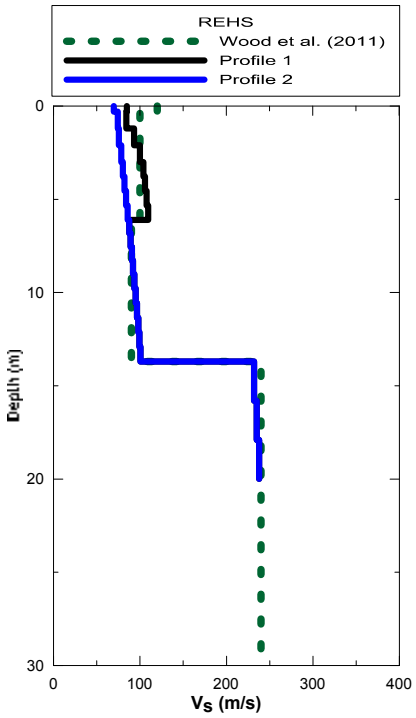

Figure 7-50 Depth-dependent shear wave velocity at REHS station

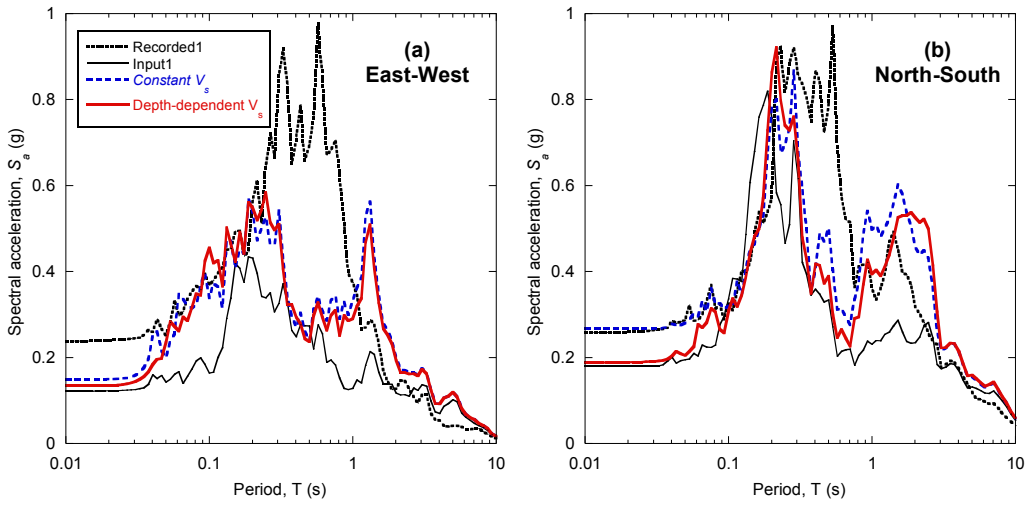

Figure 7-51 Influence of variation of shear wave velocity with depth, (a) East-West and (b) North-South direction in 5% damped response spectra at REHS station

The computed response based on analyses using Profile 1 and Profile 2 is further investigated. Figure 7-52 shows how variation of shear wave velocity in REHS station can affect the surface response. In EW direction, the spectral acceleration is greatly

improved in comparison with the recorded motion at surface. The amplification of spectral values for periods T < 1s, is seen in Figure 7-52a. In the NS direction, however, the response is no different in period range 0.1 < T < 0.3s for the two V_s profiles.

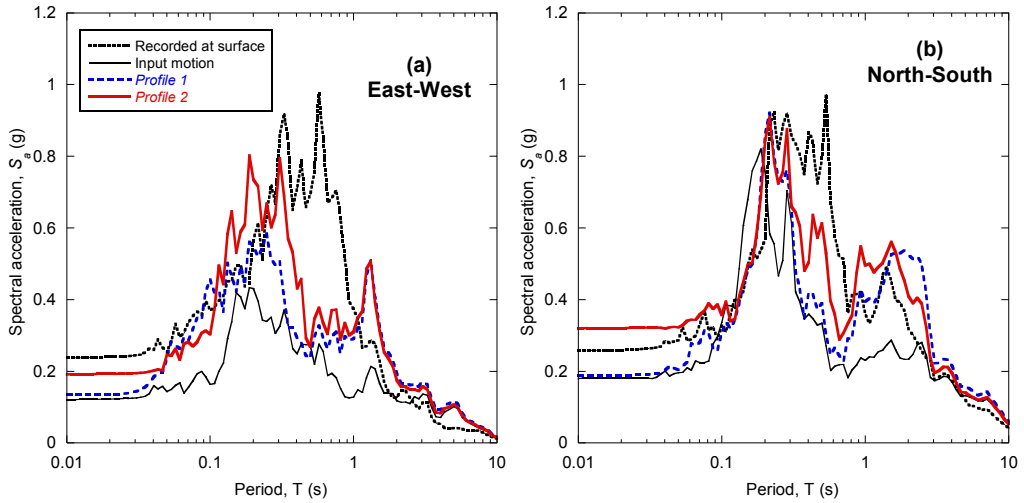

Figure 7-52 Influence of shear wave velocity profile on the computed spectral acceleration at surface, (a) East-West and (b) North-South direction on 5% damped response spectra at REHS station

The computed acceleration time histories using the nonlinear and the equivalent linear methods are also presented in Figures 7-53 and 7-54. The observed ground motion recorded at surface is also illustrated in these figures. It appears that the levels of acceleration amplitudes are larger using the equivalent linear scheme compared to the nonlinear method. Figure 7-55 shows the 5% damped surface response spectra for non-linear time domain analyses using the program OpenSees and the equivalent-linear analyses employing Strata. Qualitatively, larger spectral amplitudes employing EQL method is also clear in this figure, particularly in NS direction. In East-West direction, there was not much difference between the two sets of predictions in the low- and high-period ranges (T<0.1s and T>2s). Figure 7-56 shows that in the NS

direction, the proposed model provides an improved matched with the observed motion for low-period ranges.

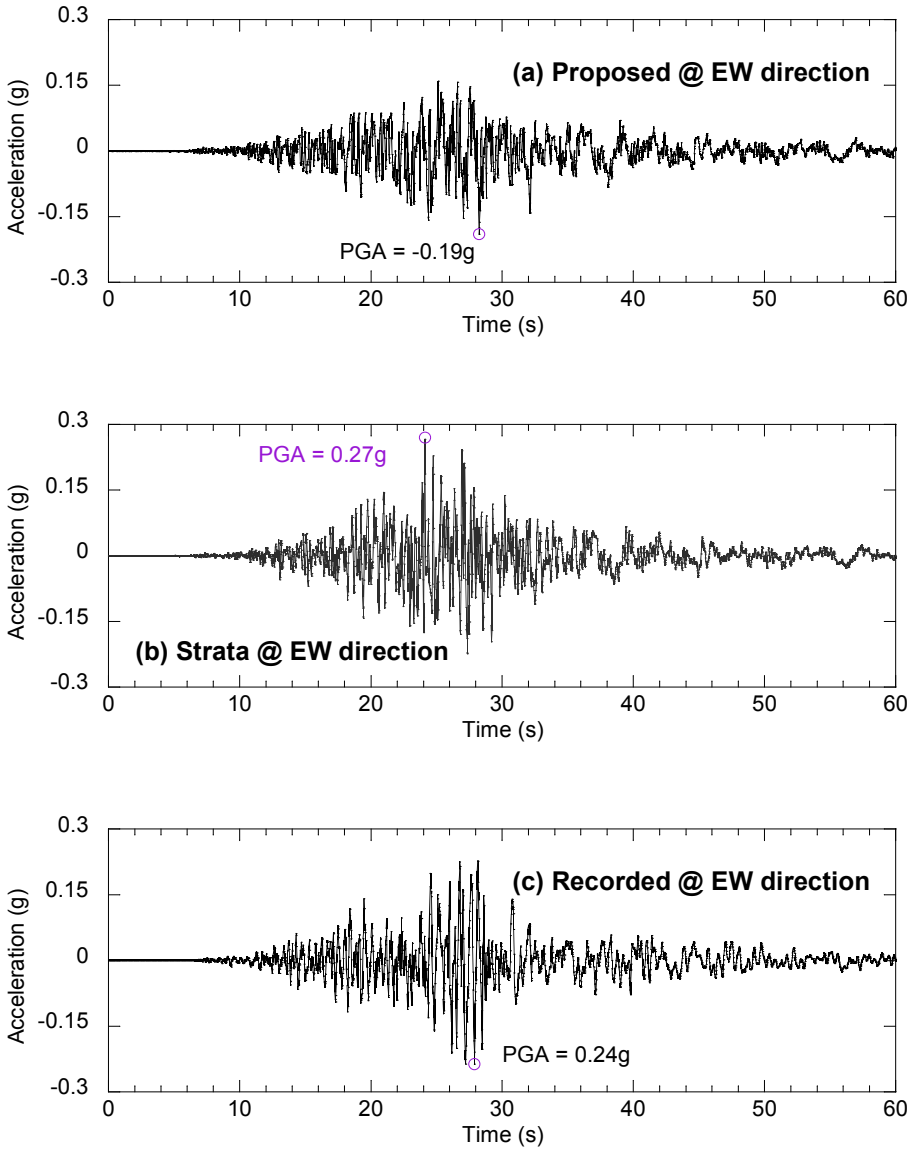

Figure 7-53 Surface acceleration time series in East-West (EW) direction at REHS strong motion station, (a) computed by the proposed and (b) Strata, (c) Recorded

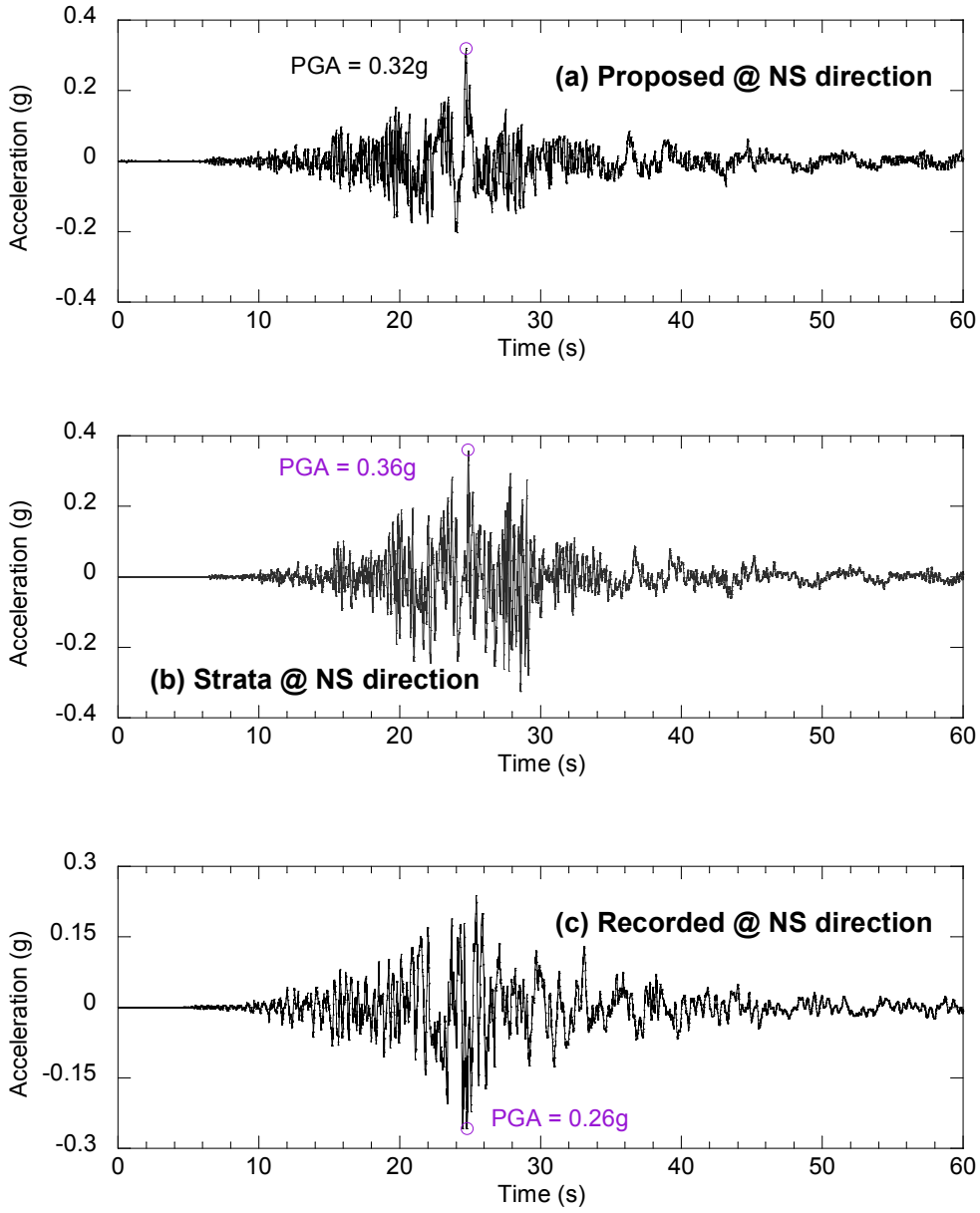

Figure 7-54 Surface acceleration time series in North-South (NS) direction at REHS strong motion station, (a) computed by the proposed and (b) Strata, (c) Recorded

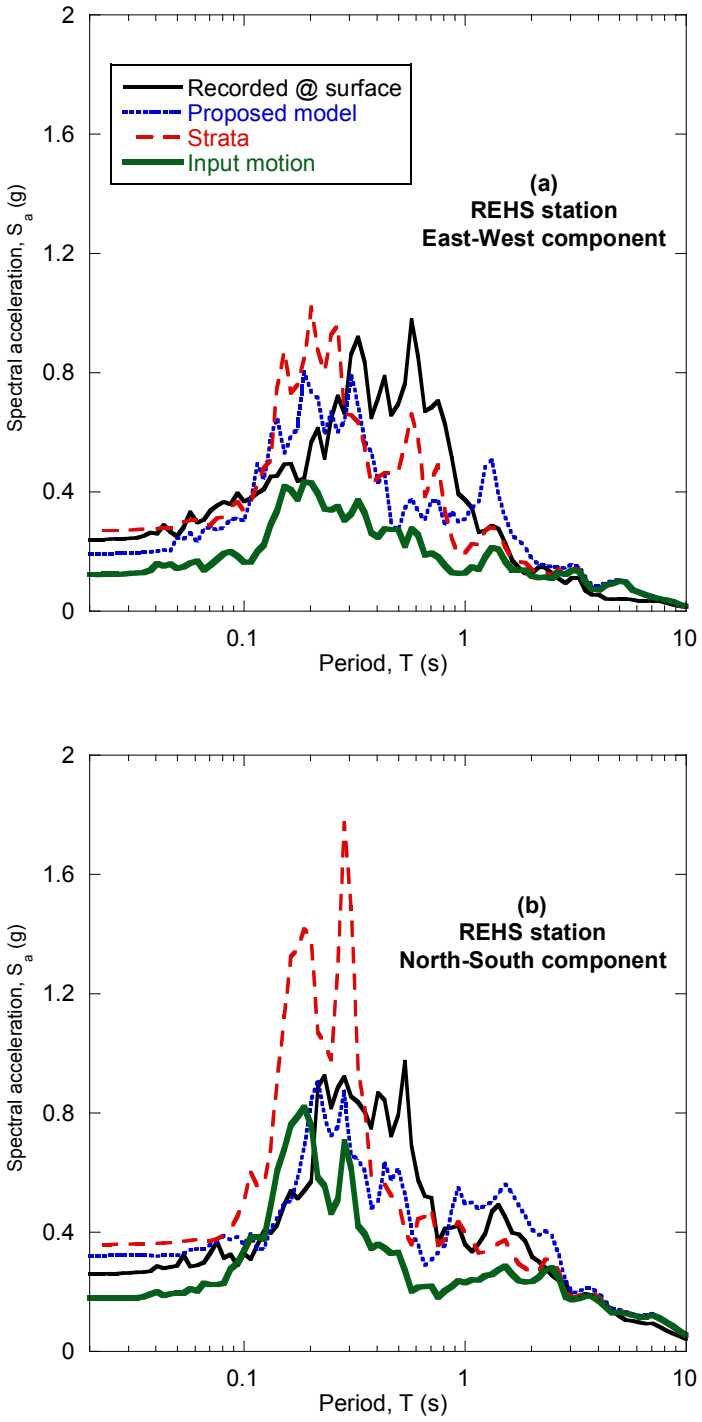

Figure 7-55 5% damped surface acceleration response spectra for the recorded motion, the proposed hysteretic and the equivalent linear model for (a) East-West (approximately fault-parallel) and (b) North-South (approximately fault-normal) components

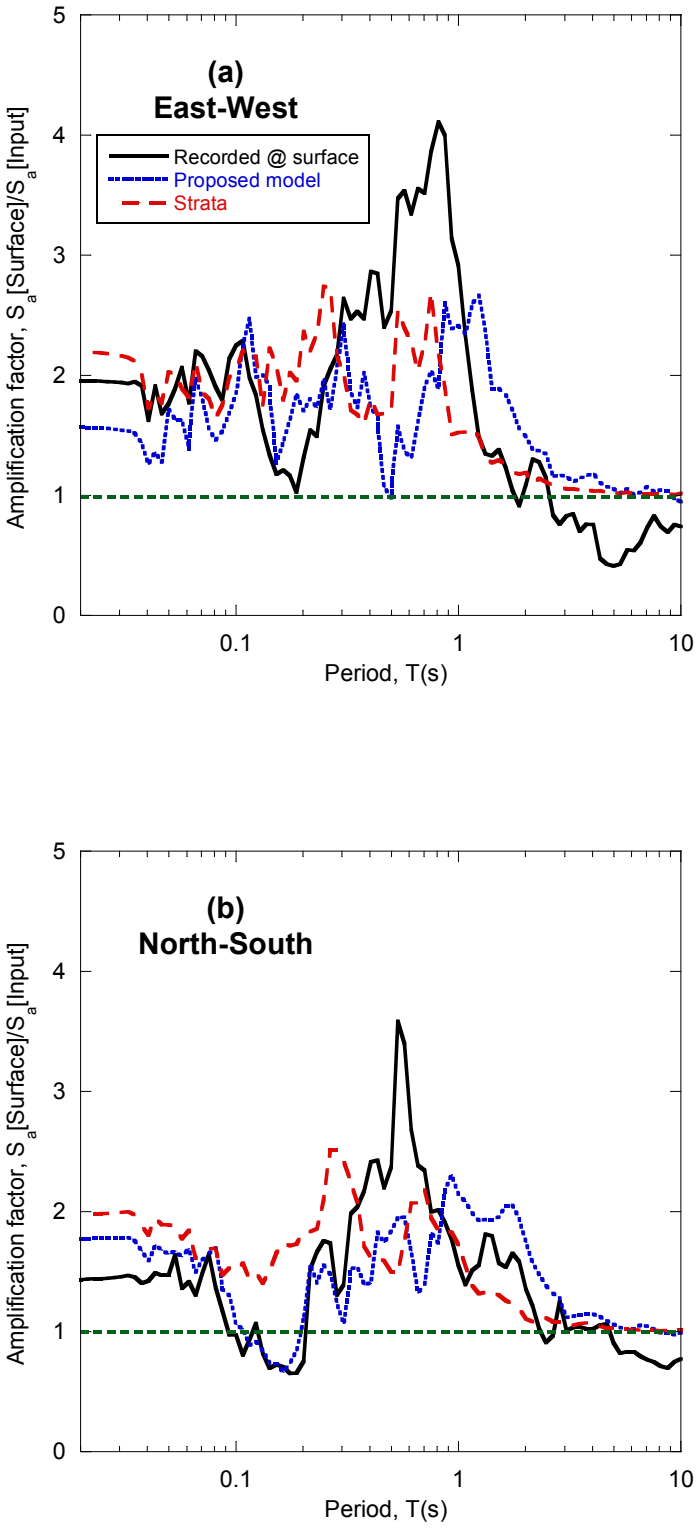

Figure 7-56 Amplification functions for the REHS strong motion station (a) East-West direction, (b) North-South direction

7.6 Summary

This chapter has presented the results of using 1-D nonlinear site response analyses. The proposed model for simultaneous simulation of the modulus and the damping was compared with the conventional Masing-type solution. Based on the observation in this chapter, the results suggest that except for mid-period range, the Masing model under-predicts the spectral acceleration due to larger hysteretic damping. The proposed model was shown that can capture the modulus reduction and the damping ratios simultaneously. Further, the maximum shear strains in the profile were computed larger for the proposed model. The reason the proposed model results in larger shear strains may be due to the different induced damping and also different stiffness degradation in unloading stages of the soil elements. However, the residual strains followed the opposite trend with Masing rule providing larger values; this could be attributed to larger stiffness in unloading branch of stress-strain hysteresis.

A parametric study on elements of soil was performed to investigate the simulation of backbone curve using small to intermediate G/G_{max} curve and large-strain strength properties or alternatively a combination of the two approaches. It was shown that for soft soils (e.g. V_s < 150 m/s), the adoption of G/G_{max} curve to determine the hyperbolic model parameters may underestimate significantly the shear strength resulting in smaller response parameters such as acceleration at surface. On the other hand, the determination of model parameter based on strength properties may lead to misfit of target G/G_{max} curve. It was shown that this misfit for (V_s > 150 m/s) is negligible but can be significant for soft soils under high confining pressures.

Nonlinear and equivalent linear response analyses were performed further for selected strong motion stations. Nonlinear results were compared to those obtained

using equivalent linear approach. The results of each method were compared in terms of the spectral ordinates, spectral amplification factors, and maximum shear strain profiles. Generally equivalent linear analysis had a tendency to give larger peak acceleration compared to the nonlinear model. This could be attributed to modelling of hysteretic damping by the nonlinear method. Further comparison of the computed motion with the set of recorded accelerograms revealed that the calibration of the model parameters exert a great influence on the prediction of the recorded motion. For the REHS station, it was shown that much of the spectral accelerations induced during the 2010 Darfield earthquake cannot be explained by the 1D nonlinear analyses.

8 Summary and conclusions

This chapter summarizes the key findings and conclusions of this study. Firstly, it presents the results from laboratory investigations including the effects of fines content and density on the stress-strain behaviour of sands as represented through maximum shear modulus, G_{max}, the shear modulus reduction, G-γ and, the material damping, h-γ, relationships. Then, nonlinear mathematical modelling of the stress-strain behaviour with target modulus and damping based on experimental G-γ and h-γ curves is presented. Finally the incorporation of the proposed model in the context of total stress one-dimensional site response analysis is scrutinized. Limitations of this research are highlighted and used to propose further work.

8.1 Effects of fines on shear modulus and damping ratio of sands

The effects of fines were investigated by measuring shear wave velocity, V_s, shear modulus, and material damping ratio during testing of reconstituted samples of Christchurch sand. A cyclic triaxial soil testing system using samples with height of $h \approx 100mm$, and diameter of $d \approx 50mm$ was employed. The testing system included a pair of bender elements for the measurement of shear wave velocity, V_s. Twenty-seven tests were carried out under different values of density ($e= 0.483 – 0.826$) fines content (FC = 0 – 30%), and shear strain amplitude (γ= 0.0001% - 0.8%). All tests were conducted on isotropically consolidated samples at p' = 100kPa; the tests were stress-controlled with a sinusoidal shape of cyclic loading and frequency of 0.1 Hz. The results provided the basis for determining effects of fines content on the dynamic properties of some Christchurch sandy soils. The investigations on V_s focused on explorations of the effects of void ratio and fines content following equations of the

form introduced by Jamiolkowski (1991). The effect of fines on V_s, G_{max}, G-γ and, h-γ was first interpreted using void ratio and relative density. The results of the experimental study can be summarized as follows:

- The shear wave velocity determined using bender element tests showed decrease in V_s with increasing void ratio. For clean sands, the shear wave velocity decreased from 240m/s to 180m/s for specimens having void ratios e = 0.674 and 0.826 (D_r ~ 85% and 35%) respectively. Similar trends were also found for fines-containing sand with $FC \leq 30\%$.

- It was found that void ratio/density had negligible effect on the shape of the normalized modulus reduction and damping ratio curves.

- Comparisons between clean sands and fines-containing sands showed that, when the void ratio (e) or relative density (D_r) were kept constant, the shear wave velocity decreases with the fines content. For example, at void ratio of e = 0.65 the shear wave velocity was 220, 200, and 170m/s for FB-10, FB-20 and, FB-30 (i.e. sands with 10%, 20% and 30% fines) clearly showing decrease in V_s with an increasing fines content.

- The normalized Youngs modulus reduction curve was shown to be marginally affected by the addition of fines content in clean sand. A small increase in the nonlinearity was observed with increasing fines content from FC = 0 to 30%. In other words, the reduction of the normalized modulus curve was more gradual smaller for clean sands than for fines containing sands.

- The equivalent Young's modulus reduction curve collapsed into a single curve at higher strain levels showing a practically identical behaviour

regardless of fines content at strain larger than ε = 0.2%. The secant modulus reduces significantly at this strain range and therefore the effects of fines may not be discernible.

- The material damping curves were found to be independent of fines content in the investigated range of FC = 0 - 30% and densities D_r = 35 – 85%. In other words, practically unique $h - \gamma$ curve was observed for all tests.

- Poisson's ratio of each specimen was computed to relating the shear modulus measured using bender elements to equivalent Youngs modulus measured by triaxial apparatus. It was shown that Poisson ratio is density-dependent and there is a tendency for Poisson's ratio to increase with increasing void ratio. This was indicated to be in accordance with the other experiments and also elasticity theory.

- It was concluded that the experimental normalized shear modulus reduction curve of FB clean sand compares fairly well with the curves suggested by Iwasaki et al. (1978) and Kokusho (1980) for clean Toyoura sand. It is shown that under similar testing conditions, the normalized moduli for FB sand is larger than Darendeli's values for small to intermediate strain ranges. Generally, the damping values of FB sand are lower than mean values calculated by Darendeli's relationships. However, the FB sand damping curves are within the median value and lower bounds. Further, the FB damping ratio curves matched better with the lower bound values suggested by Seed and Idriss (1970).

Equivalent granular void ratio, e^*, was then used as a density state measure to study the effects of fines on the shear wave velocity and shear modulus. The concept of e^* is based on the participation of fines-sized particles in the internal soil force-chain during loading and it allows to interpret the soil stiffness, irrespective of the fines content below the threshold value, f_{cth}. By back-calculating and/or predicting the participation factor of fines, b, the equivalent granular void ratio, e^*, was used to characterize and quantify the effects of fines on the dynamic sand properties. In this context, the following results were obtained:

- The fines influence factor values for bender element and triaxial test results were back-calculated separately due to the apparent differences at the small and large strain levels. It was found that the computed b-values were within a narrow range. The b-values were b = 0.57, 0.55 and, 0.6 for shear wave velocity, Young's modulus and modulus reduction curve, respectively. It can be argued that participation of fines content in the transfer of shear can be different at different strain levels.

- The b-value was also predicted using Rahman (2009) formulations. It was shown that a large discrepancy may exist between this approach and back-calculation. The prediction equation estimated the influence factor, at its highest, to be slightly over 0.40. Hence, estimating the b-value for FB soil may lead to underestimation of the activity of fines in the force-chain structure. Data-specific calibration of the input parameters of the proposed equation reduces the method to that of the back-calculation scheme.

- Adjusted power-fit equations (e.g. Figure 5.6) were proposed to relate the equivalent granular void ratio with shear wave velocity. This equation allowed predicting the shear wave velocity of sand independent of fines content utilizing the concept of *b*-value (b = 0.55 – 0.60) or contribution of fines content in the load transfer chain.

8.2 Development of simple shear stress-shear strain model to simulate modulus and damping curves

Accurate simultaneous simulation of the normalized modulus reduction and damping ratio curves was targeted. A simple total stress constitutive model was proposed to model the stress-strain behaviour of soil represented through the normalized shear modulus reduction and material damping curves. The proposed method uses a modified hyperbolic formulation, including a power term, *a*, for the backbone curve (Matasovic and Vucetic, 1993). In addition, the second Masing (1926) rule is modified to account for modelling of the material damping measured in the laboratory. That is the coefficient, *n*, in the original Masing rule is not a constant but a function of the shear strain amplitude, γ. The following results were obtained from this analytical study:

- The modified hyperbolic equation was shown to be adequate to model the stress-strain behaviour of soil within the strain range addressed in the experimental phase of this study.
- It was shown that the proposed model is capable of capturing any desired level of energy dissipation measured in laboratory cyclic loading tests as a function of shear strain. However, in order to match the mathematical and

the experimental damping, the proposed model requires iteration at the end of each cyclic loop to compute the Masing parameter n. The iteration in the model could potentially lead to slow computing time in site response analyses. Hence, the iterations were performed in advance for various cyclic strain amplitudes and for several loading conditions to derive mathematical forms for the required parameter, n. The strain dependent n values were then employed as input and used in the analyses to compute the unloading-reloading hysteresis loops that accurately simulate given target laboratory G-γ and h-γ curves.

- It was shown that the Masing coefficient n, should be strain-dependent in order to simulate the material damping ratio measured in the laboratory. Generally, $n < 2$ and decreases with increasing cyclic strain amplitudes.

The simple stress-strain model was incorporated into the OpenSees (McKenna and Fenves 2001) computational platform and was applied to site response analyses. Semi-infinite horizontally stratified soil layers were modelled as one-dimensional multi-degree-of-freedom lumped mass system. The proposed model was used to scrutinize the effects of damping on one-dimensional seismic site response analysis which involved the computation of the response of a layered deposit overlying a uniform half-space subjected to vertically propagating shear waves. The following conclusions were drawn from site response study:

- It was shown that for a wide period range, the computed response in terms of spectral accelerations is larger for the proposed model as compared to the conventional Masing model. This could be associated to modelling excessive damping by Masing model. However, for mid-period range the

proposed model may underestimate the response relative to the spectral acceleration computed by the Masing model.

- The tangent stiffness of the unloading-reloading branches of the proposed hysteretic model decreases with a higher rate in comparison to the Masing model. This could potentially result in larger maximum calculated shear strains in the soil profile for the proposed model.

Issues were also identified by using the proposed method in 1D site response analyses:

- It was shown that in modelling of soil layer parameters, care needs to be taken for modelling $G/G_{max} - \gamma$ curves so that realistic modelling of large strain strength is also obtained. For soft soils (e.g. $V_s < 150$ m/s), a simple extrapolation of the adopted G/G_{max} curve for the determination of the hyperbolic model parameters could significantly underestimate the shear strength resulting in substantially lower stresses and accelerations at surface and unrealistic response. Therefore a layer-dependent curvature coefficient, a, and careful calibration of the model over the entire range of strains anticipated in the ground response analysis is required.

- On the other hand, the determination of model parameter based on strength properties may lead to misfit of the target G/G_{max} curve. It was shown that this misfit for ($V_s > 150$ m/s) is negligible but can be significant for soft soils under high confining pressures. Therefore, a reasonable balance of modelling normalized modulus reduction curve and strength properties should be achieved.

- The model's predictive capacity through simulations of observed ground motion records during the 2010 Darfield earthquake was examined. It was shown that accurate interpretation of in-situ properties as well as calibration of the model parameters can greatly influence the end result.

8.3 Application of the Research Findings

The experimental study presented in Chapters 4 and 5 established modulus and damping properties of Christchurch FB sand. The modulus reduction and damping curves of Christchurch sand were compared to that of Darendeli (2001) curves which were obtained based on a large database of different soil types. It was shown that the Christchurch FB sand exhibit slightly less nonlinearity in comparison to the mean curves proposed by Darendeli (2001). Effects of fines content on the deformation properties were also discussed. It was shown that fines content has small effect on the shape of normalized modulus reduction and damping curves but can exert a great influence on the shear wave velocity and maximum shear modulus of silty sand. Employing a suitable means for evaluation of stiffness properties of silty sand, i.e. e^*, is imperative in quantifying the level of participation of fines content in the shear transfer between the granular particles. Assessing the contribution of fines content in linear and non-linear ranges helps to understand how fine particles can contribute to transfer of load at different levels of strains.

Evaluation of the deformational properties is imperative to estimate response of soil sites under seismic actions. Therefore, presented curves may be used to estimate seismic response of soil profiles. Although, the effects of fines content on the G/G_{max} – γ and h - γ of sandy soils could be ignored, it was shown V_s and G_{max} can be greatly influenced by fines content. The presented modulus reduction and damping curves

were developed for soils under p' = 100kPa, but it was illustrated from literature that the confining stress can exert a great influence on the shape of these curves. Moreover, accurate evaluation of the shear wave velocity as a function of confining stress is paramount in seismic response analyses. As presented in Chapter 4, the proposed curves are applicable only for similar sand and fines content to that of Christchurch FB sand. Nevertheless, the modulus reduction and damping properties of sand were found to fall within a narrow bound.

Using the proposed stress-strain model in this study, concurrent simulation of the modulus reduction and damping ratio curves was shown to be adequate across all relevant strains. The site response analyses of a hypothetical soil column as well as selected strong motion stations in Christchurch indicated that the conventional Masing criteria may result in lower response parameters due to excessive damping at medium to large strains. This underestimation of response parameters is unconservative in particular if the induced shear strain strains are computed large across the soil column. However, at large strains a reasonable balance of modelling normalized modulus reduction curve and strength properties can be a challenge. Using a strain-dependent Masing coefficient which varies with depth can circumvent this shortcoming and moreover the mathematical damping can be matched with that of experimental values.

8.4 Limitations of the research and recommended further work

In retrospect there are perhaps inevitably both limitations of this study and additional questions which arise from the interpretation of results and implementation of the mathematical model. This section concludes the thesis by specifically identifying limitations in this context and proposing further work:

- Effects of plastic fines on the dynamic sand properties were not considered in this experimental study. Whilst, low-plastic fines content exist in the surficial fluvial layers of Christchurch. Tests need to be conducted on a range of sands mixed with plastic fines to determine how plasticity affects G-γ and h-γ curves.

- To avoid bedding error in the cyclic triaxial tests, it is recommended to use local strain gauges attached to each specimen. This could enable the bender element results be combined with the triaxial data in order to evaluate the Poisson's ratio of drained tests with a higher accuracy.

- The proposed soil model was developed for one-dimensional problems using spring (truss) elements. It is desirable to extend the same concept to two-dimensional models using four-node quad elements in OpenSees. Unlike one-dimensional lumped-mass system, continuum discretized quad elements use plain strain and distributed mass formulation which idealize the layered soil column in a better fashion.

- Stiffness degradation caused by previous repetitive loading and strain rate effects were not considered in the proposed constitutive model. These effects can be significant especially for plastic soils including clays and silts. Moreover, experimental test data on Christchurch plastic soils are required to calibrate the degraded backbone curves.

- Further 1D site response analyses using the proposed model at the strong motion stations which recorded the 2010-11 Canterbury earthquake sequence can help to understand the efficiency and limitations of the proposed model for a range of site soil profiles.

Appendix A: Local site conditions and dynamic soil properties

In this appendix, the inferred dynamic soil properties of Christchurch soil are presented. The stratigraphy and mechanical characteristics of the selected strong motion stations are also introduced.

A.1 Dynamic properties of Christchurch sand

In order to complement the limited number of dynamic tests conducted in this study and extrapolate for cases where no test data is available, the model developed by Darendeli (2001) is employed in this appendix. After the Canterbury earthquake sequence, extensive in-situ testing was undertaken in Christchurch in order to characterize the nature and variability of the geotechnical conditions present within the city boundary. Seismic geophysical techniques as well as penetration testing methods were employed to assess the geotechnical characteristics of shallow soil layers (e.g. Wood et al., 2011, CERA, 2013). The collected data were used to define the in-situ small-strain properties such as V_s in several sites including the strong motion stations. Moreover, the publicly available information (CERA, 2013) provided the opportunity to review the existing empirical correlations between V_s measured by geophysical techniques and the penetration resistance. These correlation studies are discussed in the following subsections.

A.1.1 Recommended normalized modulus and material damping curves

Based on the limited number of dynamic test data available for FB soil samples, the effects of confining stress and plasticity index on the dynamic soil properties of Christchurch sand was not considered. Hence the model recommended by Darendeli

(2001) was employed to extrapolate the effects of those factors. This subsection first briefly describes the framework suggested by Darendeli (2001) and finishes with calibration of this model using the FB sand results.

Darendeli (2001) proposed model

Darendeli (2001) developed an empirical framework in order to create a set of normalized modulus reduction and material damping curves. This framework is composed of a four-parameter model that can be used to characterize normalized modulus reduction and material damping curves. The model incorporates the key factors that control nonlinear behaviour of soils. The expression for modulus reduction curve proposed by Darendeli (2001) is based on the hyperbolic soil model originally developed by Hardin and Drnevich (1972). The basic hyperbolic relationship between stress and strain is slightly modified in order to accommodate a better fit to the modulus reduction curves in the laboratory (e.g. Matasovic and Vucetic, 1993). The form suggested for normalized modulus reduction curve is:

$$\frac{G}{G_{\max}} = \frac{1}{1+\left(\frac{\gamma}{\gamma_r}\right)^a} \tag{A-1}$$

where γ_r , reference strain corresponds to the strain amplitude when shear modulus reduces to one half of G_{max}. The coefficient, a, has an impact on the curvature of the normalized curve.

Impacts of soil type and loading conditions on nonlinear soil behaviour are structured considering several parameters, ϕ_i's. These parameters are calibrated based on the experimental observations. The resulting equations can then be utilized to estimate the mean normalized modulus reduction curves for a given soil type and

loading conditions. The two parameters in the above equation, γ_r and a, are related to soil type and loading conditions as follows:

$$\gamma_r = (\varphi_1 + \varphi_2 \times PI \times OCR^{\varphi_3})\sigma'^{\varphi_4}_o$$
$$a = \varphi_5 \tag{A-2}$$

where: σ'_o = mean effective confining pressure (atm), PI = soil plasticity (%), OCR = overconsolidation ratio, and ϕ_1 through ϕ_5 = parameters that relate the normalized modulus reduction curve to soil type and loading conditions.

The equation for the material damping curve is related to the shape of the modulus reduction curve assuming the validity of Masing behaviour combined with two modifying parameters. To start, Masing rules are used to calculate material damping by evaluating the hysteresis loops that should form for a given modulus reduction curve and two-way stress reversals (e.g. Ishihara, 1996). Masing-type damping can be expressed in terms of strain amplitude as:

$$h_{\text{Masing}} = \frac{4}{\pi} \frac{\int \frac{\gamma}{1+\left(\frac{\gamma}{\gamma_r}\right)^a} d\gamma - \frac{1}{2} \frac{\gamma^2}{1+\left(\frac{\gamma}{\gamma_r}\right)^a}}{\frac{\gamma^2}{1+\left(\frac{\gamma}{\gamma_r}\right)^a}} \tag{A-3}$$

The Masing-type material damping curve is modified using two parameters to fit the laboratory data (Darendeli 2001):

$$h = F \times h_{Ma\sin g} + h_{\min}$$
$$F = b \times \left(\frac{G}{G_{\max}}\right)^{0.1} \tag{A-4}$$

where F is a function that adjusts damping at high strains, h_{min} is small-strain material damping ratio, and b is a parameter that control the behaviour of this function. The two parameters in this format (h_{min} and b) are related to soil type and loading conditions as follows:

$$\begin{aligned} h_{\min} &= (\varphi_6 + \varphi_7 \times PI \times OCR^{\varphi_8})\sigma'^{\varphi_9}_o \left[1 + \varphi_{10} \times \ln(f)\right] \\ b &= \varphi_{11} + \varphi_{12} \ln(N) \end{aligned} \tag{A-5}$$

where f = loading frequency, N = number of loading cycles, and ϕ_6 through ϕ_{12} = parameters that relate material damping curve to soil type and loading conditions.

Calibration of Darendeli (2001) model using TX test results

FB soil test data are utilized to calibrate some of the parameters of the model developed by Darendeli (2001). The equation 2 can model the shifting of the normalized modulus reduction curve with increasing soil plasticity, overconsolidation and confining pressure. The parameters ϕ_1 is equal to reference strain at σ'_o = 100 kPa and therefore it is readily available from *TX* test data on *FB* soil. The parameter ϕ_5 can be obtained by employing least-square-error method to best-fit the hyperbolic equation to the experimental test results. The other three parameters which relate to the effects of plasticity index, overconsolidation ratio, and confining pressure were not considered in this study and the values recommended by Darendeli (2001) are utilized in site response analyses. Furthermore, ϕ_6 and ϕ_{11} were also computed based on triaxial tests on FB sand, as the former is related to the minimum damping ratio measured at low-strain levels and latter can be computed based on least-square error method to fit the adjusted damping curves to the experimental test results on FB soil.

Table A.1 lists all the required parameters to describe adequately the normalized modulus reduction and material damping curves for site response analyses in this study. The grey cells indicate the parameters which were suggested by Darendeli (2001) based on extensive statistical analyses of a large database of dynamic behaviour of natural soils and the white columns are calibrated values based on the TX test results of FB soil groups. Figure A.1 illustrates the recommended curves computed based on Darendeli (2001) framework calibrated by the cyclic triaxial test results of Christchurch sand at the loading frequency f = 0.1 Hz. Note that, in this figure, the normalized modulus reduction and material damping curves corresponding to σ'_o = 100 kPa is the average curves of the experimental results of dynamic tests on FB sand, which were explained in Chapter 4.

Table A.1 Parameters relating the normalized modulus and damping curve to soil type and loading conditions

ϕ_1	ϕ_2	ϕ_3	ϕ_4	ϕ_5	ϕ_6
0.07913	0.001	0.3246	0.3483	0.98	1.586
ϕ_7	ϕ_8	ϕ_9	ϕ_{10}	ϕ_{11}	ϕ_{12}
0.0129	-0.1069	-0.2889	0.2919	0.6849	-0.0057

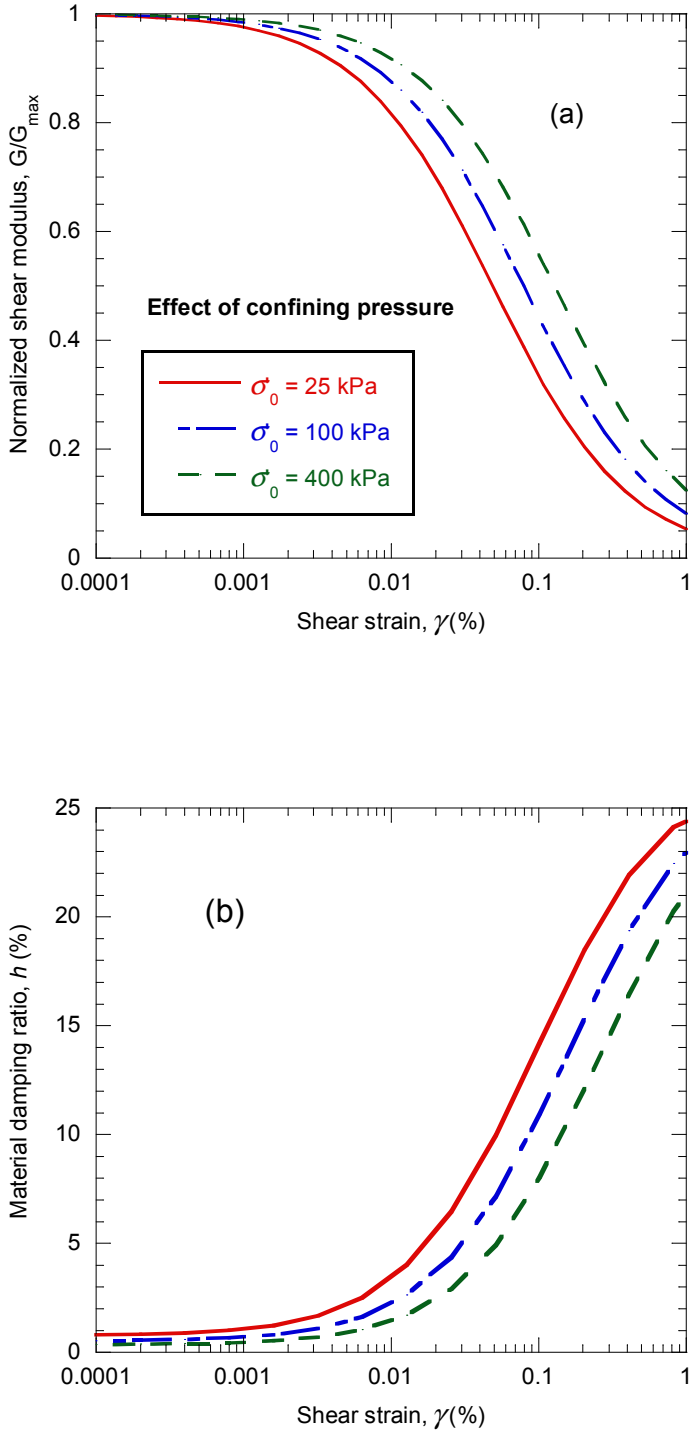

Figure A.1 Recommended normalized modulus reduction curve (a), material damping ratio curves for Christchurch sand (b); f = 0.1 Hz

A.1.2 Correlations of seismic properties with engineering properties

One of the most commonly cited V_s correlations for cohesionless soils is that with the penetration resistance, q_c, obtained from the cone penetration test (CPT). Numerous studies have established the relations between the cone penetration resistance, q_c, and the shear wave velocity, V_s (e.g. Robertson, 1990, Baldi et al., 1989, Rix and Stokoe, 1991). However, the inherent difficulty of correlating a small strain parameter such as V_s with penetration parameters that relate to much larger strains is problematic. Small strain modulus and penetration resistance depend on the state of stress and density to different degrees, making a unique semi-empirical correlation between them difficult.

In an effort to review the correlations found in the literature for the evaluation and modelling of shear wave velocities of sandy soil units in Christchurch, data has been collected from CERA database (CERA, 2012). Correlations between the measured shear wave velocities and penetration resistance of local sandy soils were established and regression analyses were performed to obtain best fit relationships. These relationships were also compared to existing shear wave velocity correlations. This subsection attempts to summarize the findings for developing empirical correlations between V_s and penetration resistance, both of which were measured during post-earthquake site investigations performed in Christchurch CBD (CERA, 2012).

In-situ methods

The collated shear wave velocity measurements, represented in CERA database, were made using multi-channel analysis of surface waves (MASW) method. MASW analyses the dispersion of surface waves in order to identify the thickness and shear

wave velocity of the subsurface layers but does not provide any information regarding the soil types.

On the other hand, penetration test methods are the oldest commonly used in-situ tests in geotechnical engineering field and are the most popular field tests for the assessment of the deformation characteristics of soils. While these tests are used to measure high-strain characteristics of soil, their results have also been correlated to low-strain soil properties to indirectly determine some of the deformation properties of soils. The Cone Penetration test (CPT) method was employed extensively in the Christchurch CBD to characterize the nature of geotechnical conditions underneath the city. The near continuous nature of the CPT test results provides valuable information about soil variability.

Data gathering

Christchurch City Council and Tonkin & Taylor Ltd were engaged to undertake an extensive in-situ testing to characterize the nature and variability of the geotechnical conditions present within Christchurch CBD and to make this information publicly available to assist with the post-earthquake recovery process. The data presented in this section pertaining to the shear wave velocities and the engineering parameters of the soil were obtained from an online database comprising these test results (CERA, 2012). The Canterbury geotechnical database, made possible by CERA, provided this opportunity to review the existing empirical correlations between properties such as V_s measured by MASW technique with the penetration resistance, q_c.

The shallow alluvial soils in Christchurch are substantially variable within short distances, both horizontally and vertically. Hence, in order to establish meaningful

correlations, only recorded CPTs and MASWs conducted in the close proximity to each other (< 10m) were collected from the database. In this way, the soil heterogeneity due to different locations at which the V_s and the q_c were recorded could be minimized. As such data from a total of 49 sites in the Christchurch CBD were incorporated. Distinctions were made between the fill and native materials by removing the upper two meters at each soil profile from the database. Since the range of soil properties determined at each site could vary considerably, only sandy soils were analysed in this study.

One of the major applications of the CPT has been the determination of soil stratigraphy and the identification of soil type; this provided the opportunity to identify sandy layers. A popular CPT soil behaviour chart based on normalized CPT data is that proposed by Robertson (1990). A parameter, I_c, was identified in which the CPT results for most young, un-cemented, insensitive, normally consolidated soils will plot despite some expected overlaps in some zones. The parameter, I_c, is defined as follows:

$$I_C = \left((3.47 - \log Q_t)^2 + (\log F_r + 1.22)^2 \right)^{0.5} \quad \text{(A-6)}$$

where Q_t is dimensionless normalized cone penetration resistance $= (q_c - \sigma_{v0})/\sigma'_{v0}$ and F_r is normalized friction ratio $= f_s/(q_c - \sigma_{v0})$. The normalization of the penetration resistance and the sleeve friction are due to the variation in effective overburden stress for very shallow and/or very deep soundings. Vertical effective stresses were calculated using assumed total unit weights of 17 kN/m^3 and 19 kN/m^3 above and below the ground water table respectively. In this way, the commonly marine and alluvial sandy layers in Christchurch CBD were identified through the index, I_c (1.31

< I_c < 2.1) as shown for a sample site in Figure A.2. The average tip resistances were computed over the depth of the layer for which V_s was measured by MASW. All the layers with shear wave velocities more than 250 *m/s* were removed from the database in order to make sure that only Holocene-aged soils were included in the analysis.

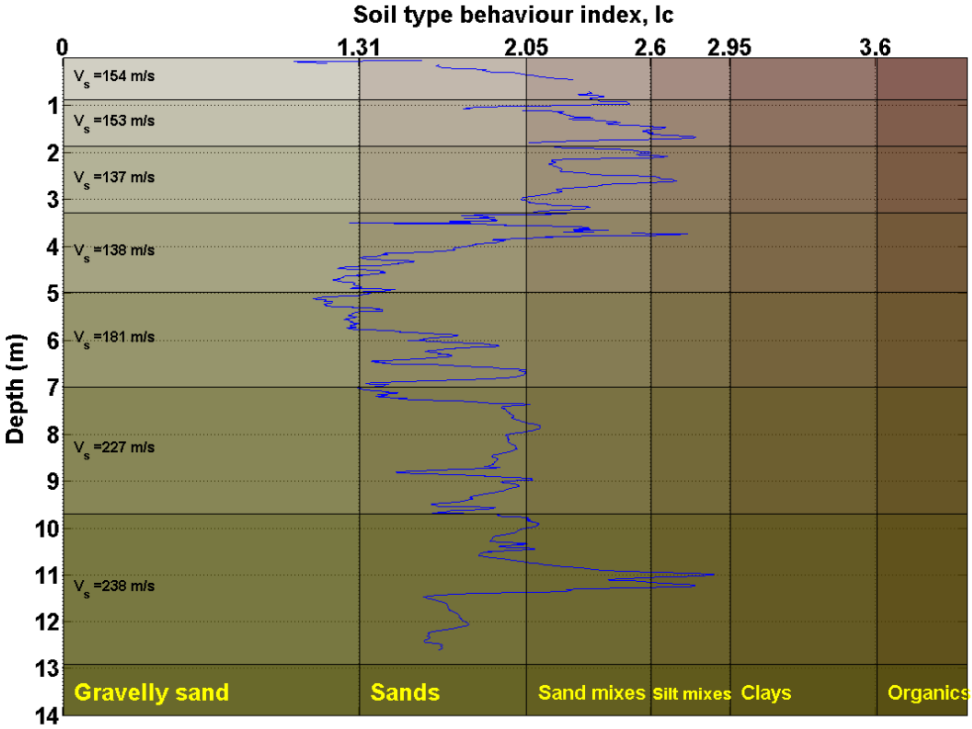

Figure A.2 Example profile for soil index at a site in Oxford Terrace, Christchurch

Correlation studies

A number of empirical relationships between low-strain stiffness and CPT penetration resistance have been developed (e.g. Lo Presti and Lai 1988; Baldi et al 1989; Rix and Stokoe 1991; Robertson and Cabal 2010; Wair et al. 2012). Based on the in-situ CPT and MASW test results conducted on Christchurch CBD, two of the more widely published empirical relationships between penetration resistance and V_s values were reviewed in this section. Based on earlier works, Wair et al. (2012) suggested a correlation relationship for V_s-q_c in the form expressed in the following equation:

$$\log V_s = \log A + b.\log(q_c) + c.\log(\sigma'_v) \quad \text{(A-7)}$$

where σ'_v = vertical effective stress (MPa) and A, b, and c = constants which are computed based on regression analysis. Coefficient of determination (R^2) was used to assess the strength of the relationship between the variables; higher R^2 indicating greater agreement between the variables. Employing this equation to predict the shear wave velocity using penetration resistance resulted in coefficient of determination R^2 = 0.63. The low value of R^2 shows the significant scatter in the data; however the trend represented by the power functions seems to fit the data in a tolerable fashion. Wair et al. (2012) also listed similar R^2 for this relationship using sandy soils. Figure A.3 illustrates the measured V_s versus the calculated V_s using the power form of the equation 7. Figure A.4 shows that the residual of the measured and the predicted values are smaller for mid-height layers.

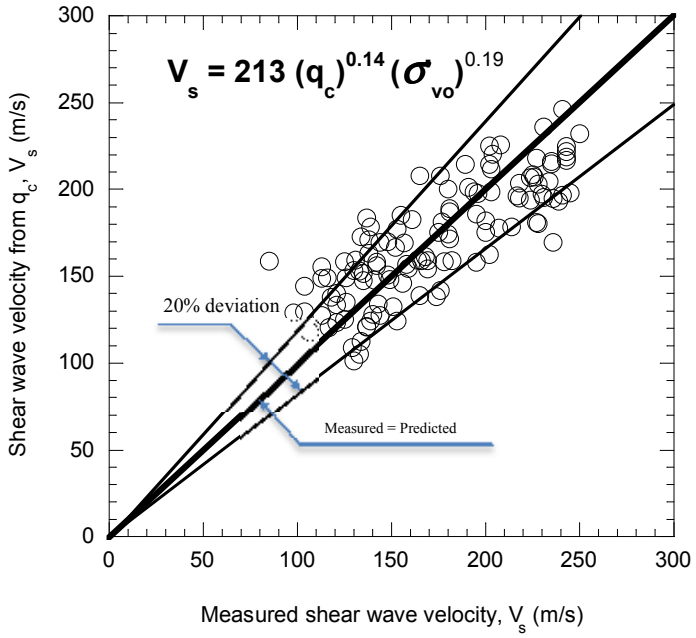

Figure A.3 Shear wave velocity (m/s) of Christchurch CBD from q_c (MPa) vs. that measured

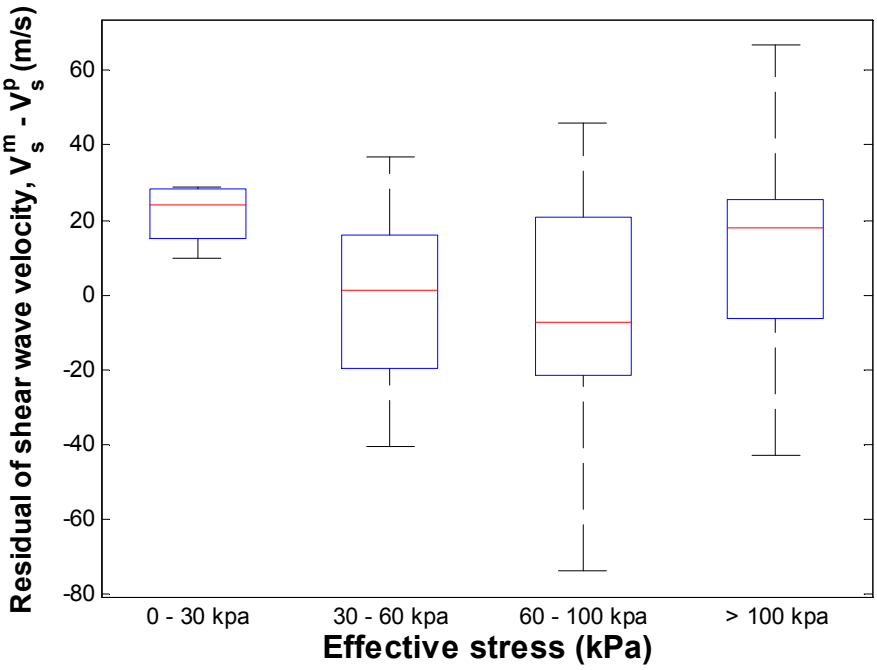

Figure A.4 Residual of shear wave velocity versus vertical effective stress, boundaries represent ±25% percentile

Based on extensive in-situ tests combined with published data for a wide range of soils, Robertson (2009) developed a set of contours of normalized shear wave velocity, V_{s1}, on the normalized penetration resistance, Q_{tn}, and friction ratio, F_r. The contours of V_{s1} are approximated using the following equation:

$$V_{s1} = [\alpha_{vs} Q_{tn}]^{0.5}$$
$$\alpha_{vs} = 10^{(0.55 I_C + 1.68)} \quad \text{(A-8)}$$

The shear wave velocity, V_s, can be obtained as:

$$V_{s1} = V_s \left(\frac{P_a}{\sigma'_{vo}} \right)^{0.25} \quad \text{(A-9)}$$

where σ'_{vo} and P_a are in-situ effective vertical stress and atmospheric pressure in the same unit, respectively. Figure A.5 illustrates the results of employing Robertson

(1990) equation to predict the shear wave velocity using penetration test results compared with the measured V_s using MASW method. It seems larger scatter exists in this figure (R^2 = 0.46) compared to the equation proposed by Wair et al. (2012).

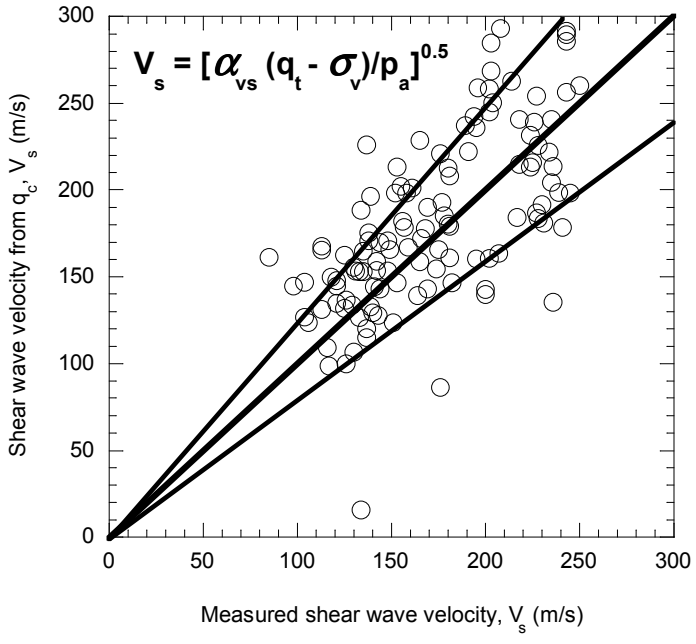

Figure A.5 Shear wave velocity of Christchurch CBD from Robertson (2012) equation vs. that measured

The preceding V_s – q_c relationships have been investigated to aid in the characterization of sandy materials located at sites in the CBD of Christchurch for studies involving seismic response analysis.When making estimates of V_s for a given soil layer, it is highly recommended that a number of estimation methods or relationships be employed before selecting the value or range of values to be used in the analyses and that the predicted values be regarded as only preliminary estimates for in-situ conditions.

A.2 Strong motion stations

The city of Christchurch is situated on nearly 1 km of Quaternary alluvial sediments and volcanic rock overlying greywacke basement (Brown and Weeber, 1992). In the vicinity of Christchurch, water wells have been drilled to prove a complex sequence of gravels interbedded with silt, clay, peat, and shelly sands down to 400m. The postglacial marine transgression and progradation made the depositional environments beneath the city quite complicated. However, the gravel strata and interbedded fine grained sediments have been grouped into formations related to climatic stages of the Quaternary. The immediate subsoil under the surface of the city of Christchurch, which is significant to engineering works, includes the Springston and Christchurch Formations (Brown and Weeber, 1992).

Springston Formation is postglacial fluvial sediment comprised of well sorted, rounded gravel with dominantly sand matrix with local lenses of silt. It is the dominant surface layer in the western part of the city to within approximately 5km of the eastern coastline, where it becomes interspersed with the Christchurch Formation. Christchurch Formation is also a postglacial formation, created by beach, lagoonal, dune, and coastal swamp sediments (Brown and Weeber, 1992). Riccarton Gravel is commonly the uppermost gravel immediately underlying the predominantly fine sediments of Springston and Christchurch formations. Deeper formations are beyond normal depth of concern for engineering purposes.

Each of the four sites investigated consists near surface soils which are different in each case. The general information regarding each strong motion station site was obtained from the Geonet website. In order to identify the stratigraphy of the top soil layers, the penetration test results and boreholes conducted nearby the strong motion

stations were also downloaded from CERA database (CERA, 2013). The shear wave velocity profiles used, were based on MASW test data from Wood et al. (2011) and estimated from V_s-q_c correlations explained earlier. For the examples presented in this study, the density of soil, ρ, in the soil column was assumed to be of those suggested by Elder et al. (1991).

A.2.1 Riccarton high school: RHSC

The RHSC strong motion station is located on Quaternary fluvial sand and silt deposits at approximately 17 m above sea level. Near-surface gravel bed (Springston Formation) is found at depths > 5m. Riccarton Gravel underlies the Springston Formation gravel at ~10 m below ground surface. The water table is 4-5m below the ground surface (CERA, 2013). The liquefaction susceptibility was considered to be low in this location (e.g. Elder et al., 1991); this was confirmed during the Darfield and Christchurch earthquakes as no liquefaction was observed. Station site class according to NZS 1170.5 (2004) was site class D (GeoNet, 2012). Shear wave velocity measurement was made by Wood et al. (2011) and Stephenson et al. (2010) and portrayed in Figure A.6. Also shown in Figure A.6 is a final soil type stratigraphy based on a SPT borehole (Wotherspoon, 2013), conducted at ~30m away from the station, and other sources (e.g. Brown and Weeber, 1992, Elder et al., 1991). The data from RHSC sensors, which is still functioning, has been recorded by CSI CUSP3C SENSOR 10405 accelerometer.

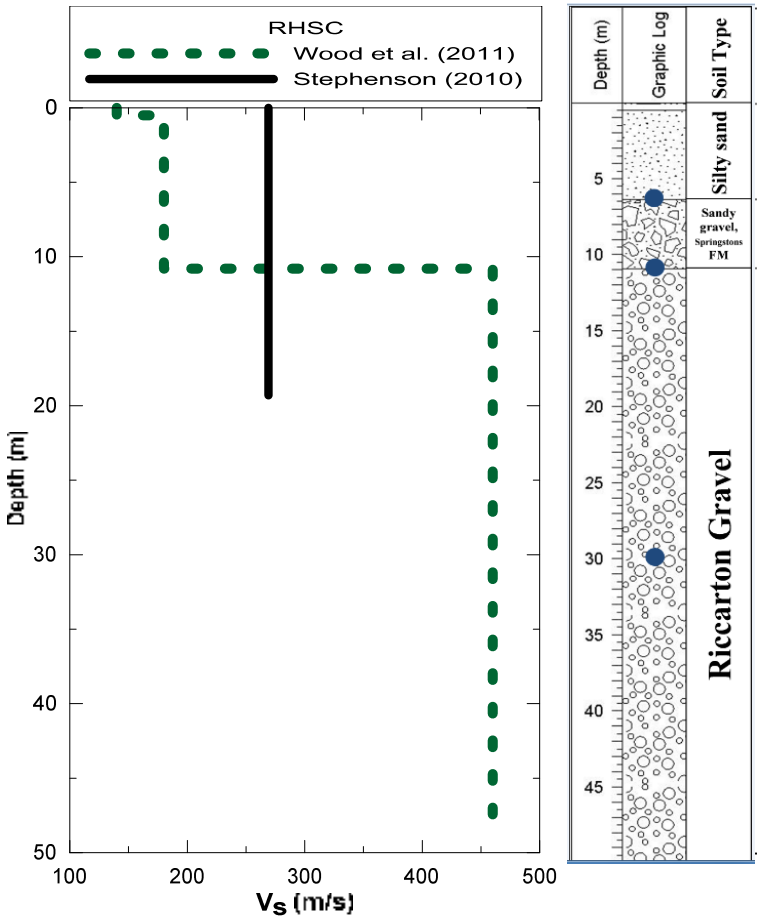

Figure A.6 Shear wave velocity profile utilized in this study (left) and stratigraphy (right) profile at the RHSC station (modified after Wood et al., 2011, Wotherspoon, 2013)

A.2.2 Christchurch Botanic Gardens: CBGS

The CBGS strong motion station is located in the middle of Hagley Park, resting on Quaternary fluvial deposits. Riccarton Gravel underlies the Springston Formation at ~25 m below ground surface. Depth to water table is reported to be ~1 m below ground level (Brown and Weeber 1992). The liquefaction susceptibility is considered to be low in this location; this was confirmed during the Darfield and Christchurch earthquakes as no liquefaction was observed. (CERA, 2013). Station site class

according to NZS 1170.5 (2004) was site class D before the Canterbury earthquake sequence (GeoNet, 2012).

A borehole was drilled close to the station and through the surface gravels; a CPT test was then conducted through the sand/silt layers. The top layers of the site appear to be mainly gravelly. Based on the CPT test, the soil type index profile was computed for lower layers, and is illustrated in Figure A.7. Shear wave velocity measurement was made by Wood et al. (2011) using MASW method and is compared in Figure A.7 with prediction equations explained earlier in this chapter. It appears that, albeit slight overestimation, the prediction equations match well with the MASW data. Also shown in is a final soil type stratigraphy based on the borehole drilled close to the CBGS station (Wotherspoon, 2013).

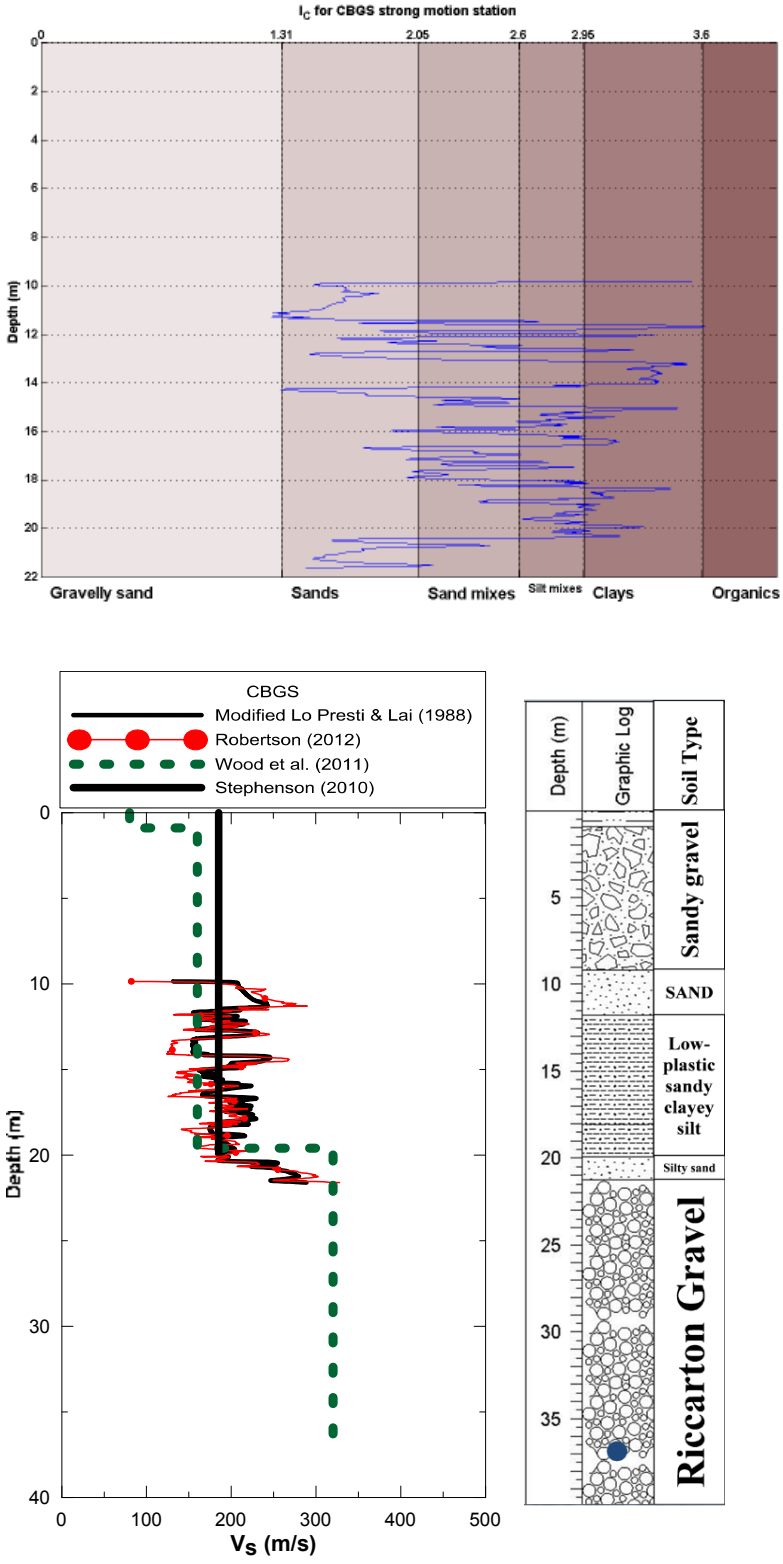

Figure A.7 Soil type index (top), shear wave velocity (left) and stratigraphy (right) profile at the CBGS station (modified after Wood et al., 2011, CERA, 2013, Stephenson et al., 2010)

A.2.3 Christchurch Cathedral College: CCCC

The GNS-owned CCCC strong motion station is located on fluvial sandy silt deposits at ~4 m above sea level. Riccarton Gravel underlies the Springston and Christchurch Formation at ~25 m below ground surface (~20 m below mean sea level). Depth to water table is reported to be ~1 m below ground level (Brown and Weeber 1992; CERA 2012). The liquefaction susceptibility is considered to be medium to high in this location (e.g. Elder et al., 1991), nevertheless minor liquefaction was observed during 22 February 2011 Christchurch earthquake and minor quantities of ejected materials was reported during 13 June 2010 aftershock; no liquefaction was observed during the 4 September 2010 Darfield earthquake (CERA, 2013). Aerial photography interpretations infer that the site subsided about 0.2 – 0.3 m after the Canterbury earthquake sequence (CERA, 2013). Station site class according to NZS 1170.5 (2004) was site class D before the Canterbury earthquake sequence (GeoNet, 2012).

Based on a CPT test conducted at ~40m away from the station the soil type index was computed and is illustrated in Figure A.8. The top layers of the site appear to be mainly silty sand interbedded with low-plasticity clayey silt layers. Shear wave velocity measurement was made by Wood et al. (2011) using MASW method and are shown in Figure A.8 along with prediction equations explained earlier in this chapter. A good match between V_s measurement and predictions is observed only for the top 5m. Also shown in Figure A.7 is a final soil type stratigraphy based on all the information collated around CCCC station from several sources. The sensors in this station are CSI CUSP3B SENSOR 331 seismometers.

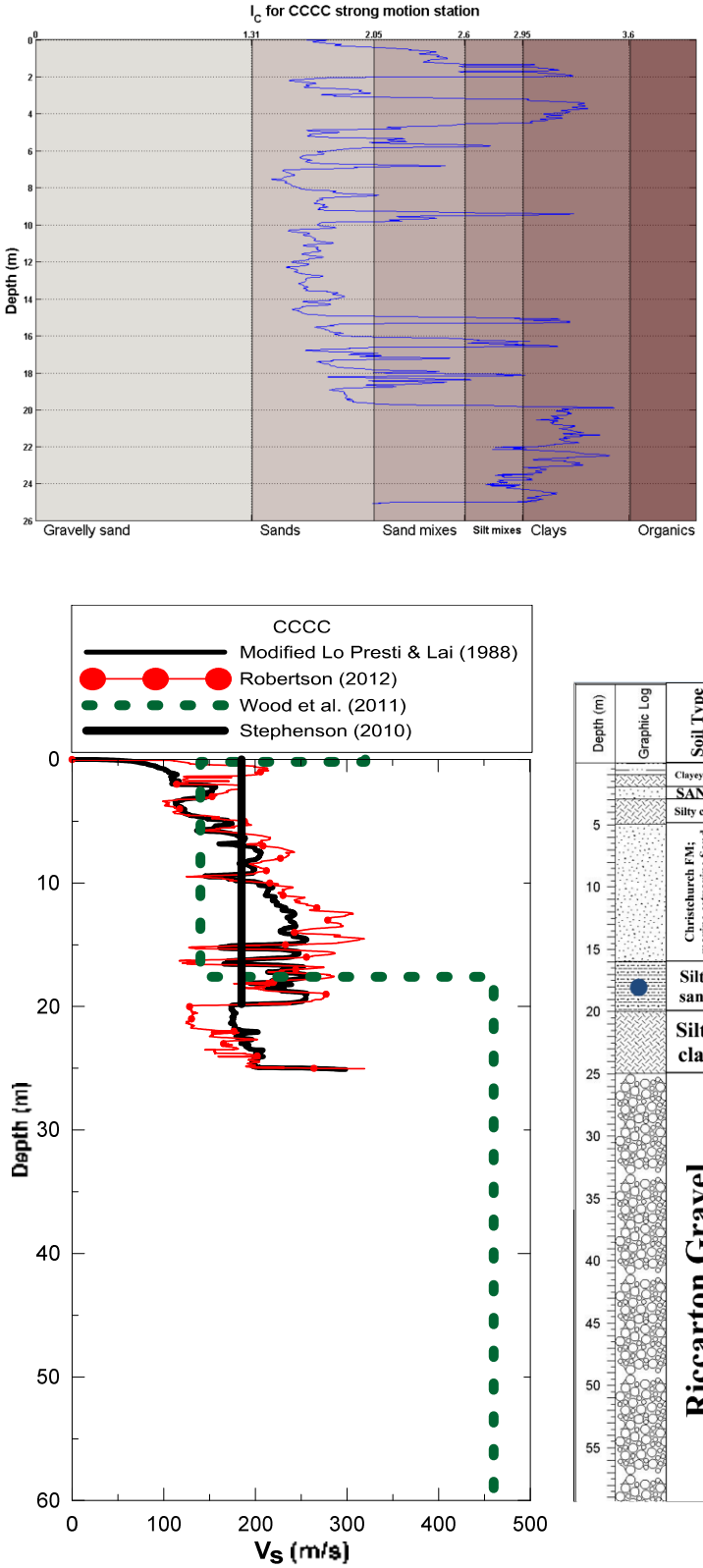

Figure A.8 Soil type index (top), shear wave velocity (left) and stratigraphy (right) profile (modified after Wood et al., 2011, CERA, 2013, Stephenson et al., 2010)

A.2.4 Christchurch Resthaven: REHS

The REHS strong motion station is located on swamp deposits and Riccarton Gravel underlies the site at ~20 m below ground surface. Depth to water table is reported to be ~2 m below ground level (CERA 2012). The liquefaction susceptibility is considered to be medium in this location, nevertheless no liquefaction was observed during the 4 September 2010 Darfield earthquake; minor ejected sand was observed during the 22 February 2011 Christchurch earthquake. Aerial photography interpretations infer that the site subsided about 0.4 – 0.5 m after the Canterbury earthquake sequence (CERA, 2013). Based on a CPT test conducted at ~40m away from the station the soil type index was computed and is illustrated in Figure A.9. The top layers of the site appear to be mainly silty sand interbedded with low-plasticity clayey silt and peat layers (Toshinawa et al., 1997). The sensors are three-component accelerometer at surface and the model is Kinemetrics FBA-23-DECK 1675.

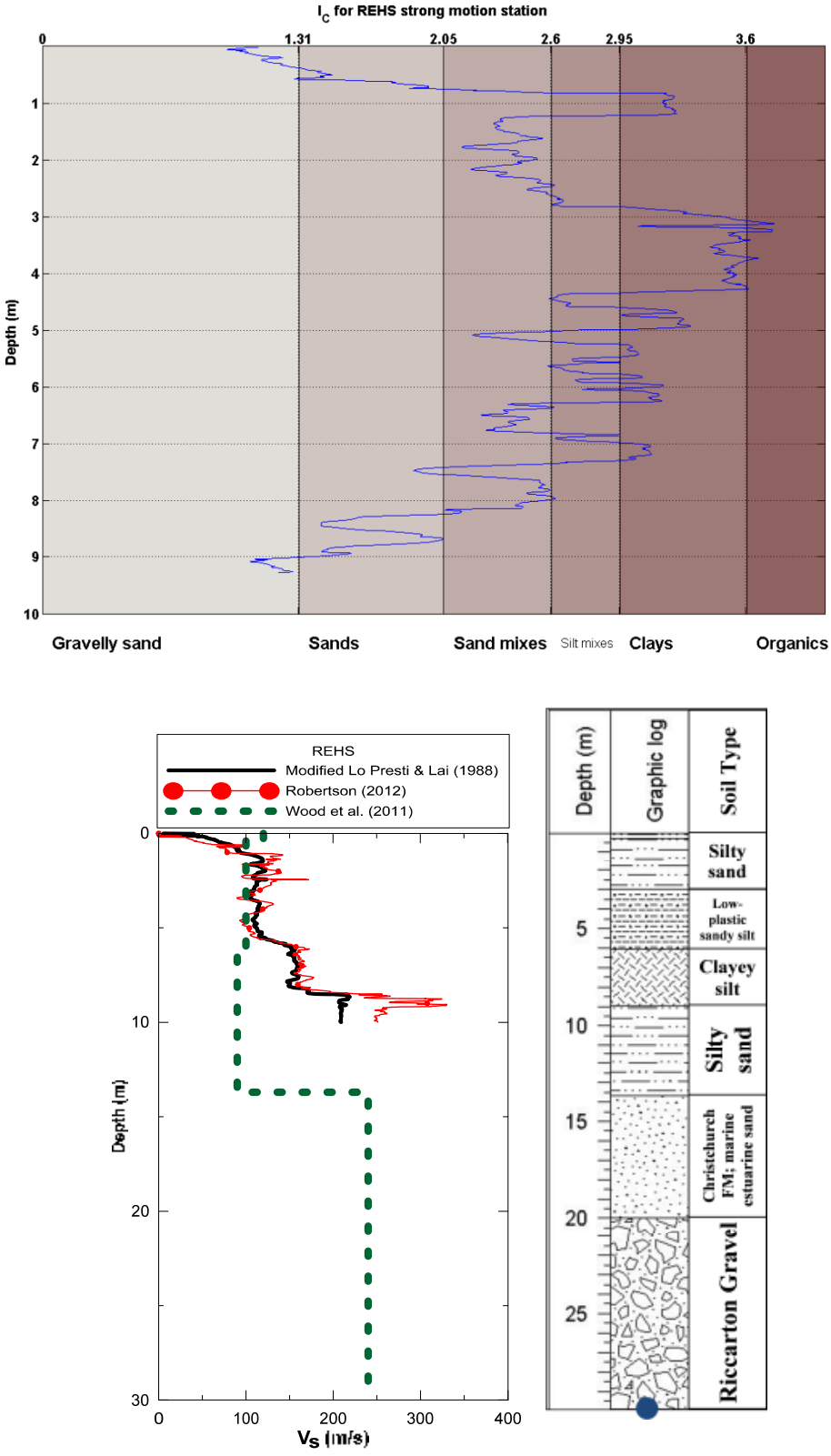

Figure A.9 Soil type index (top), shear wave velocity (left) and stratigraphy (right) profile at the REHS station (modified after Wood et al., 2011, CERA, 2013)

Appendix B: Programming codes for the proposed stress-strain model

B.1 C++ interface

```
#ifndef DampMas_h
#define DampMas_h

// Following code may not be included more than once such as the DampMas class definition
#include <UniaxialMaterial.h>

// Defining a new data type; The following data members are accessible
class DampMas : public UniaxialMaterial
{
  public:
    DampMas(int tag, double G0, double Gamar, double Alpha,
                 double M0, double M1, double M2);
    DampMas();

    // The following destroys an object when it is no longer required
    ~DampMas();

    // Function headers
       int setTrialStrain(double strain, double strainRate = 0.0);

       // void means has no input parameters
    double getStrain(void);
    double getStress(void);
    double getTangent(void);

       // returns the G0
    double getInitialTangent(void) {return G0;};

    int commitState(void);
    int revertToLastCommit(void);
    int revertToStart(void);

    UniaxialMaterial *getCopy(void);

    int sendSelf(int commitTag, Channel &theChannel);
    int recvSelf(int commitTag, Channel &theChannel,
              FEM_ObjectBroker &theBroker);

    void Print(OPS_Stream &s, int flag =0);

  protected:

  private:
         // Material properties
       double G0;           // Maximum shear modulus
       double Gamar;        // reference shear strain
       double Alpha;        // the curvature coefficient
       double M0;           // The n-gama coefficients
       double M1;
       double M2;
```

```
        // Current (trial) step
        double epsmax;              // Maximum previous strain eps
        double maxeps;              // Maximum previous strain eps for 3rd rule
        double epsr;                // eps at last inversion point
        double sigr;                // sig at last inversion point
        int    kon;                 // Index for unloading/reloading
        double n;                   // Masing coefficient of the current loop
        double phi;                 // Curvature of the current loop
        double eps;                 // trial strain
        double sig;                 // current trial stress
        double e;                   // current trial tangent

        // Previous converged step
        double epsmaxP;             // Maximum previous strain eps
        double maxepsP;             // Maximum previous strain eps for 3rd rule
        double epsrP;               // eps at last inversion point
        double sigrP;               // sig at last inversion point
        int    konP;                // Index for unloading/reloading
        double nP;                  // Masing coefficient of the current loop
        double phiP;                // Curvature of the current loop
        double epsP;                // Strain at previous converged step
        double sigP;                // Stress at previous converged step
        double eP;                  // Stiffness at previous converged step

        int    iflag;
        int iflagP;

        double* loopA;
        double* loopB;
        double* loopC;
        double* loopD;
        int*   loopa;

        double* loopE;
        double* loopF;
        double* loopG;
        double* loopH;
        int*   loopb;

        int           numClosedLoop1;
        int           numClosedLoop;
};
#endif
```

B.2 C++ implementation

```
#include <elementAPI.h>

// Looks for the header in the current directory
#include "DampMas.h"
#include <Vector.h>
#include <Channel.h>
#include <math.h>
#include <float.h>

#ifdef _USRDLL
// C is globally defined elsewhere
#define OPS_Export extern "C" _declspec(dllexport)
#elif _MACOSX
#define OPS_Export extern "C" __attribute__((visibility("default")))
#else
#define OPS_Export extern "C"
#endif

// Variable defined and accessible locally but continues to exist after exiting
the block
static int numDampMas = 0;

OPS_Export void *
OPS_DampMas()
{
  // Print out some KUDO's
  if (numDampMas == 0) {
    opserr << "Uniaxial material - Written by Jawad Arefi University of
Canterbury (c) 2012\n";
    numDampMas =1;
  }

  // Pointer to a uniaxial material that will be returned
  UniaxialMaterial *theMaterial = 0;

  // Parse the input line for the material parameters

  int    iData[1];
  double dData[6];
  int numData;
  numData = 1;
  if (OPS_GetIntInput(&numData, iData) != 0) {
    opserr << "WARNING invalid uniaxialMaterial DampMas tag" << endln;
    return 0;
  }

  numData = 6;
  if (OPS_GetDoubleInput(&numData, dData) != 0) {
    opserr << "WARNING invalid G0 & gamar\n";
    return 0;
  }

   // Create a new material

  theMaterial = new DampMas(iData[0], dData[0], dData[1], dData[2], dData[3],
dData[4], dData[5]);

  if (theMaterial == 0) {
```

```
    opserr << "WARNING could not create uniaxialMaterial of type DampMas\n";
    return 0;
  }

  // Return the material
  return theMaterial;
}

DampMas::DampMas(int tag, double g0, double gamar, double alpha, double m0,
double m1, double m2)
:UniaxialMaterial(tag, 0),
 G0(g0), Gamar(gamar), Alpha(alpha), M0(m0), M1(m1), M2(m2)
{
       loopA = 0;    loopB = 0;    loopC = 0;    loopD = 0;    loopa = 0;
       loopE = 0;    loopF = 0;    loopG = 0;    loopH = 0;    loopb = 0;
       numClosedLoop1 = 0;  numClosedLoop = 0;

       konP = 0;     kon = 0;
       eP = G0;      e = G0;
       epsP = 0.0; eps = 0.0;
       sigP = 0.0; sig = 0.0;

    epsmaxP = 0.0000001;
       maxepsP = 0.0000001;
       epsrP = 0.0; sigrP = 0.0;
       epsr = 0.0;  sigr = 0.0;
       n = 1.0;     phi = 1.0;
       nP = 1.0;    phiP = 1.0;
       iflag = 1;   iflagP = 1;
}

DampMas::DampMas()
:UniaxialMaterial(0, 0),
 G0(0.0), Gamar(0), Alpha(0), M0(0), M1(0), M2(0)
{
       loopA = 0;    loopB = 0;    loopC = 0;    loopD = 0;    loopa = 0;
       loopE = 0;    loopF = 0;    loopG = 0;    loopH = 0;    loopb = 0;
       numClosedLoop1 = 0;  numClosedLoop = 0;

       konP = 0;     kon = 0;
       eP = G0;      e = G0;
       epsP = 0.0; eps = 0.0;
       sigP = 0.0;   sig = 0.0;

    epsmaxP = 0.0000001;
       maxepsP = 0.0000001;
       epsrP = 0.0;  sigrP = 0.0;
       epsr = 0.0;   sigr = 0.0;
       n = 1.0;        phi = 1.0;
       nP = 1.0;     phiP = 1.0;
       iflag = 1;    iflagP = 1;
}

DampMas::~DampMas()
{
  // Does nothing
}

int
DampMas::setTrialStrain(double strain, double strainRate)
{
```

```
	if(fabs(eps - strain) < DBL_EPSILON)
		return 0;

	eps = strain;
	double deps = eps - epsP;

	if (kon == 0)
	{
		if (deps >= 0.0)
		{
				kon = 1;
				iflag = 1;
		}
		else
		{
				kon = 2;
				iflag = 1;
		}
	}

	if (kon==1 && deps < 0.0) {

		kon = 2;
		iflag = 2;

		epsr = epsP;
		sigr = sigP;

		if (iflagP == 1){

			epsmax = fabs(epsr);
			if (fabs(epsr) > maxeps)
			maxeps = fabs(epsr);
		}
		else {

			epsmax = fabs(epsr - epsrP)/2.0;
		}

		n = M0 * pow(epsmax * 100.0, M1);
		if (n > 2.0) {
			n = 2.0;
		}
		else if ( n < 0.1 ) {
			n = 0.1;
		}

		if (iflagP ==1) {

			phi = log(1.0 + pow(fabs(epsmax/Gamar),Alpha))/log(1.0 +
pow(fabs(epsmax*2.0/Gamar/n),Alpha));
		}
		else {
	 phi = log(G0 * fabs((epsr - epsrP)/ (sigr - sigrP)))/log(1.0 +
pow(fabs((epsr - epsrP)/Gamar/n),Alpha));
		}

	} else if (kon == 2 && deps > 0.0)
	{

		kon = 1;
```

```
              iflag = 2;

              epsr = epsP;
              sigr = sigP;

              if (iflagP == 1){

                     epsmax = fabs(epsr);
                     if (fabs(epsr) > maxeps)
                     maxeps = fabs(epsr);
              }
              else {

                     epsmax = fabs(epsr - epsrP)/2.0;
              }

              n = M0 * pow(epsmax * 100.0, M1);
              if (n >2.0) {
                     n = 2.0;
              }
              else if ( n < 0.1 ) {
                     n = 0.1;
              }

              if (iflagP ==1) {

                     phi = log(1.0 + pow(fabs(epsmax/Gamar),Alpha))/log(1.0 +
pow(fabs(epsmax*2.0/Gamar/n),Alpha));
              }
              else {
        phi = log(G0 * fabs((epsr - epsrP)/ (sigr - sigrP)))/log(1.0 +
pow(fabs((epsr - epsrP)/Gamar/n),Alpha));
              }
       }

       if (fabs(eps) >= maxeps && iflag ==2) {
           iflag = 1;
              epsr = 0.0;
              sigr = 0.0;
              n       = 1.0;
              phi     = 1.0;
              numClosedLoop = 0;
              numClosedLoop1 = 0;

              loopA = 0;
              loopB = 0;
              loopC = 0;
              loopD = 0;
              loopa = 0;

              loopE = 0;
              loopF = 0;
              loopG = 0;
              loopH = 0;
              loopb = 0;
       }
    else if (kon ==2 && iflag == 2 && numClosedLoop > 0 && (loopE != 0) && eps
<= loopE[numClosedLoop - 1]) {

              epsr = loopA[numClosedLoop1 - 2];
              sigr = loopB[numClosedLoop1 - 2];
```

```
                n       = loopC[numClosedLoop1 - 2];
                phi  = loopD[numClosedLoop1 - 2];
                numClosedLoop = numClosedLoop - 1;
                numClosedLoop1 = numClosedLoop1 - 1;
        }
        else if (kon ==1 && iflag == 2 && numClosedLoop1 > 0 && (loopA != 0) &&
eps >= loopA[numClosedLoop1 - 1]) {

                epsr = loopE[numClosedLoop - 2];
                sigr = loopF[numClosedLoop - 2];
                n       = loopG[numClosedLoop - 2];
                phi  = loopH[numClosedLoop - 2];
                numClosedLoop1 = numClosedLoop1 - 1;
                numClosedLoop = numClosedLoop - 1;
        }

        double sigtrial;
        if (iflag == 1)
        {
                sigtrial = G0 * eps / (1.0 + pow(fabs(eps/Gamar),Alpha));
        }
        else {
                        sigtrial = G0 * ( eps - epsr ) / pow(1.0 + pow(fabs(( eps
- epsr )/Gamar/ n),Alpha), phi) + sigr;
        }

        sig = sigtrial;
        if (kon == 1) {
                // The derivate of the above equation
e = (G0 * pow(n * Gamar, Alpha * phi) * pow(pow(n * Gamar, Alpha)+
    pow(eps - epsr,Alpha),phi));
e = e - G0 * (eps - epsr) * pow(n*Gamar, Alpha * phi) * Alpha * phi *
    pow(pow(n*Gamar,Alpha)+pow(eps-epsr,Alpha),phi-1)*pow(eps - epsr, Alpha-1);
e = e / pow(pow(n*Gamar,Alpha)+pow(eps - epsr,Alpha),2.0*phi);

        } else if (kon == 2){
                // The derivative of the stress equation
e =    (G0*pow(n * Gamar ,Alpha * phi) * pow(pow(n * Gamar, Alpha)+
        pow(epsr-eps,Alpha),phi));
e = e - G0 * (eps-epsr) * pow(n * Gamar, Alpha * phi) * Alpha * phi *
    pow(pow(n*Gamar,Alpha) + pow(epsr-eps,Alpha),phi-1)*pow(epsr-eps,Alpha-1);
e = e / pow(pow(n*Gamar,Alpha)+pow(epsr - eps,Alpha),2.0*phi);
                                }
        return 0;
}

double
DampMas::getStrain(void)
{
  return eps;
}

double
DampMas::getStress(void)
{
  return sig;
}

double
DampMas::getTangent(void)
{
```

```
  return e;
}

int
DampMas::commitState(void)
{
	double deps = eps - epsP;

	if (konP == 1 && deps < 0.0)
	{
		double *newA = new double[numClosedLoop1 + 1];
		double *newB = new double[numClosedLoop1 + 1];
		double *newC = new double[numClosedLoop1 + 1];
		double *newD = new double[numClosedLoop1 + 1];
		int	*newa = new int[numClosedLoop1 + 1];

		for (int i=0; i<numClosedLoop1; i++)
		{
		newA[i] = loopA[i];
		newB[i] = loopB[i];
		newC[i] = loopC[i];
		newD[i] = loopD[i];
		newa[i] = loopa[i];
		}

		newA[numClosedLoop1] = epsr;
		newB[numClosedLoop1] = sigr;
		newC[numClosedLoop1] = n;
		newD[numClosedLoop1] = phi;
		newa[numClosedLoop1] = iflagP;

		if (loopA != 0) delete [] loopA;
		if (loopB != 0) delete [] loopB;
		if (loopC != 0) delete [] loopC;
		if (loopD != 0) delete [] loopD;
		if (loopa != 0) delete [] loopa;

		loopA = newA;
		loopB = newB;
		loopC = newC;
		loopD = newD;
		loopa = newa;

		numClosedLoop1 += 1;
	}

		if (konP == 2 && deps > 0.0)
	{
		double *newE = new double[numClosedLoop+1];
		double *newF = new double[numClosedLoop+1];
		double *newG = new double[numClosedLoop+1];
		double *newH = new double[numClosedLoop+1];
		int	*newb = new int[numClosedLoop+1];

		for (int i=0; i<numClosedLoop; i++)
		{
		newE[i] = loopE[i];
		newF[i] = loopF[i];
		newG[i] = loopG[i];
		newH[i] = loopH[i];
		newb[i] = loopb[i];
```

```
                }
                newE[numClosedLoop] = epsr;
                newF[numClosedLoop] = sigr;
                newG[numClosedLoop] = n;
                newH[numClosedLoop] = phi;
                newb[numClosedLoop] = iflagP;

                if (loopE != 0) delete [] loopE;
                if (loopF != 0) delete [] loopF;
                if (loopG != 0) delete [] loopG;
                if (loopH != 0) delete [] loopH;
                if (loopb != 0) delete [] loopb;

                loopE = newE;
                loopF = newF;
                loopG = newG;
                loopH = newH;
                loopb = newb;

                numClosedLoop += 1;
        }

        eP = e;
    epsmaxP = epsmax;
        maxepsP = maxeps;
        epsrP = epsr;
        sigrP = sigr;
        epsP = eps;
        sigP = sig;
        phiP = phi;
        nP = n;
        konP = kon;
        iflagP = iflag;

        return 0;
}


int
DampMas::revertToLastCommit(void)
{
        e = eP;
    epsmax = epsmaxP;
        maxeps = maxepsP;
        epsr = epsrP;
        sigr = sigrP;
        eps = epsP;
        sig = sigP;
        phi = phiP;
        n = nP;
        kon = konP;
        iflag = iflagP;
        return 0;
}

int
DampMas::revertToStart(void)
{
  eP = G0;
  epsP = 0.0;
  sigP = 0.0;
```

```
  e = G0;
  eps = 0.0;
  sig = 0.0;
  epsmaxP = 0.0000001;
  maxepsP = 0.0000001;

  konP = 0;
  iflagP = 0;
  epsrP = 0.0;
  sigrP = 0.0;
  n = 2.0;
  phi = 1.0;

  return 0;
}


UniaxialMaterial *
DampMas::getCopy(void)
{
  DampMas *theCopy =
    new DampMas(this->getTag(),G0,Gamar,Alpha,M0,M1,M2);
  theCopy->eps = this->eps;
  theCopy->sig = this->sig;
  theCopy->e = this->e;

  return theCopy;
}

int
DampMas::sendSelf(int cTag, Channel &theChannel)
{
  int res = 0;
  static Vector data(13);
  data(0) = this->getTag();
  data(1) = G0;
  data(2) = Gamar;
  data(3) = Alpha;
  data(4) = epsrP;
  data(5) = sigrP;
  data(6) = epsP;
  data(7) = sigP;
  data(8) = eP;
  data(9) = phiP;
  data(10) = nP;
  data(11) = konP;
  data(12) = iflagP;

  res = theChannel.sendVector(this->getDbTag(), cTag, data);
  if (res < 0)
    opserr << "DampMas::sendSelf() - failed to send data\n";

  return res;
}
int
DampMas::recvSelf(int cTag, Channel &theChannel,
                              FEM_ObjectBroker &theBroker)
{
  int res = 0;
  static Vector data(13);
  res = theChannel.recvVector(this->getDbTag(), cTag, data);
```

```
  if (res < 0)
    opserr << "DampMas::recvSelf() - failed to recv data\n";
  else {
    this->setTag(data(0));
    G0    = data(1);
    Gamar = data(2);
    Alpha = data(3);
    epsrP   = data(4);
    sigrP   = data(5);
    epsP = data(6);
    sigP = data(7);
    eP = data(8);
    phiP = data(9);
    nP = data(10);
    e = eP;
    sig = sigP;
    eps = epsP;
    konP = data(11);
    iflagP = data(12);
  }
  return res;
}
void
DampMas::Print(OPS_Stream &s, int flag)
{
  s << "DampMas tag: " << this->getTag() << endln;
  s << "  G0: " << G0 << endln;
  s << "  Gamar: " << Gamar << endln;
  s << "  Alpha: " << Alpha << endln;
  s << "  stress: " << sig << " strain: " << eps << "  tangent: " << e <<
endln;
}
```

Appendix C: 1D OpenSees model of a layered soil column

This appendix describes the OpenSees simulation of a soil deposit located above a visco-elastic half-space using total stress analysis. This analysis should be conducted in conjunction with the .dll file of the C++ code presented in Appendix B.

For simplicity, this appendix explains only how to model a single soil layer and therefore it is intended to outline the basic modelling approach. Note that as a viscous damper is used to simulate the finite rigidity of the half-space, velocity time history of the selected ground motion should be employed instead of acceleration (e.g. Joyner and Chen, 1975, McGann and Arduino, 2012). To run this example, the user must save the .dll file in the same directory as OpenSees .exe file. Once this has been done, the user can then run the analysis. The soil is modelled in one dimension with single degree-of-freedom using truss elements. A general schematic picture of the model is shown in Figure C.1. The soil node and element numbering schemes begin at the bottom of the soil column.

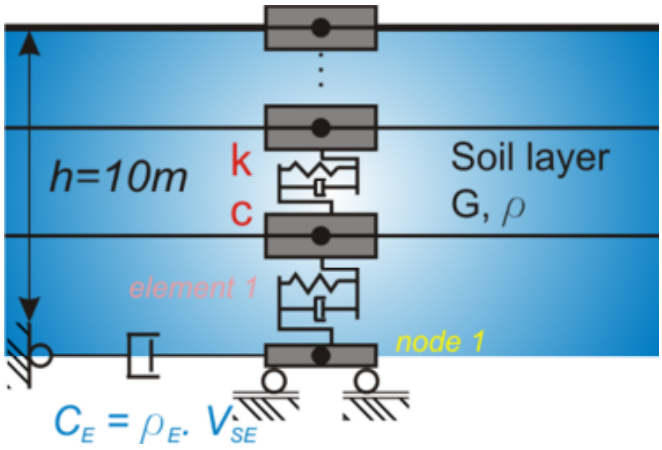

Figure C.1 Schematic representation of the site response model (after McGann and Arduino, 2012)

To account for the finite rigidity of the underlying half-space, a dashpot (e.g. Joyner and Chen, 1975) is incorporated at the base of the soil column using a zeroLength element and the viscous uniaxial material. The dashpot is assigned a dashpot coefficient equal to the product of the mass density and shear wave velocity of the underlying layer. The soil column is excited at the base by a horizontal force time history which is proportional to the known velocity time history of the ground motion.

The horizontal force time history is applied as a Path TimeSeries object using the velocity time history file. The force history is obtained by multiplying the known velocity time history by a constant factor set as the product of the mass density and shear wave velocity of the underlying layer. A series of material properties are required to define the constitutive behaviour of the soil and the underlying elastic half-space. The main soil properties are the mass density, the shear wave velocity, the reference strain and modified Masing coefficient function (n-γ relationship). Truss elements are used to model the soil using the spring-type behaviour. The soil elements in each layer are assigned the material tag of the material object corresponding to that layer. The transient analysis is conducted with the Newmark integrator using the γ and β coefficients. These values are set at 0.5 and 0.25, respectively. Since the model considers nonlinear soil behaviour, there is inherent hysteretic damping which occurs, however, a small amount of stiffness proportional Rayleigh damping is used so there is still some damping at low strain values. The level of Rayleigh damping is controlled by the damping ratio and the circular frequency of the natural mode of vibration.

```
# This file models a single layer 1D soil column
wipe
set g 9.81
set gama 18.0;                      # Unit weight, kN/m3
set Vs 150.;                        # Layer shear wave velocity, m/s2
set numLayers   10
set layerThick  1.0
set G [expr $gama/$g * $Vs * $Vs];  # Maximum shear modulus
set motionDT 0.02

# bedrock shear wave velocity (m/s)
set rockVS  500
# bedrock mass density (Mg/m3)
set rockDen 2.0

# Rayleigh Damping Parameters---------------------------
set pi  3.141592654
set xi 0.005;                       # Damping ratio

set f1  0.0
for {set k 1} {$k <= $numLayers} {incr k 1} {
    set f1 [expr $f1 + $layerThick/$Vs]
    }
set f1 [expr 1.0 /(4.0 * $f1)];
set omega1 [expr 2.0*$pi*$f1]
set omega2 0.0
set a0 0.0
set a1  [expr 2.0*$xi/($omega1 + $omega2)]

# Analysis Parameters----------------------------------
#   newmark parameters
set gamma   0.5
set beta    0.25

#   ------------------------------------------------------------
#   Define Nodes for Soil Elements
#   ------------------------------------------------------------

#   soil nodes are created in 1 dimension, with 1 dof (translational)
model BasicBuilder -ndm 1 -ndf 1
set xCoord  0.0
    node 1 $xCoord;
#   loop over layers
for {set k 1} {$k <= $numLayers} {incr k 1} {
    set xCoord [expr {$xCoord + $layerThick}]
    node    [expr $k+1] $xCoord
}
    node 200 0.0
    node 201 0.0
# Calculated parameters ----------------------------------------
set MassL 0.0
set MassU [expr $gama /$g * $layerThick/2.]
mass 1 [expr $MassL + $MassU]

for {set k 2} {$k <= $numLayers} {incr k 1} {

    # Set nodal mass
    set MassL $MassU
    set MassU [expr $gama /$g * $layerThick/2.]
```

```
    # Assign nodal mass
    mass $k [expr $MassL + $MassU]
#puts "[expr $MassL + $MassU]"
}
    mass [expr $numLayers + 1] $MassU

#   ------------------------------------------------------------
#   Define Boundary Conditions and Equal DOF
#   ------------------------------------------------------------

# define fixity of base node
fix 1 0;

# define fixity of dashpot nodes
fix  200  1
fix  201  0

# define equal DOF for dashpot and base soil node
equalDOF 1 201 1

# loop over layers to define materials
for {set k 1} {$k <= $numLayers} {incr k 1} {
uniaxialMaterial DampMas $k $G 0.0008 0.90 0.2 -0.20 0.0
}

#   ------------------------------------------------------------
#   Define Soil Elements
#   ------------------------------------------------------------

# loop over layers
for {set k 1} {$k <= $numLayers} {incr k 1} {
    set iNode [expr $k]
    set jNode [expr $k + 1]
    element truss $k $iNode $jNode 1.0 $k -doRayleigh 1
}

#   ------------------------------------------------------------
#   Define Material and Element for Viscous Damper
#   ------------------------------------------------------------

# dashpot coefficient
set mC  [expr $rockDen*$rockVS]
# material
uniaxialMaterial Viscous 4000   $mC 1

# element
element zeroLength 5000 200 201 -mat 4000 -dir 1

#   ------------------------------------------------------------
#   Load Pattern
#   ------------------------------------------------------------
# define constant facfor for applied velocity
set cFactor [expr $rockDen*$rockVS]
# define velocity time history file
set velocityFile 1@460.out
# timeseries object for force history
timeSeries Path 1 -dt $motionDT -filePath $velocityFile -factor
$cFactor
# loading object
pattern Plain 10 1 {
```

```
load 1 1.0
}
#   ------------------------------------------------------------
#   Recorders
#   ------------------------------------------------------------

# record nodal acceleration
recorder Node -file a_Node.out -time -dT 0.02 -node [expr $numLayers
+ 1] -dof 1 accel
# record deformation
recorder Element -file d_Element.out -dT 0.02 -eleRange 1 $numLayers
deformations;

#   ------------------------------------------------------------
#   Analysis objects
#   ------------------------------------------------------------

constraints Transformation
test NormDispIncr 1.0e-4 20
algorithm Newton
numberer RCM
system BandGeneral
integrator Newmark $gamma $beta
rayleigh $a0 $a1 0. 0. ;
analysis Transient
analyze 88000 0.0005
wipe
```

Appendix D: Cyclic stress-strain curves of FB sand

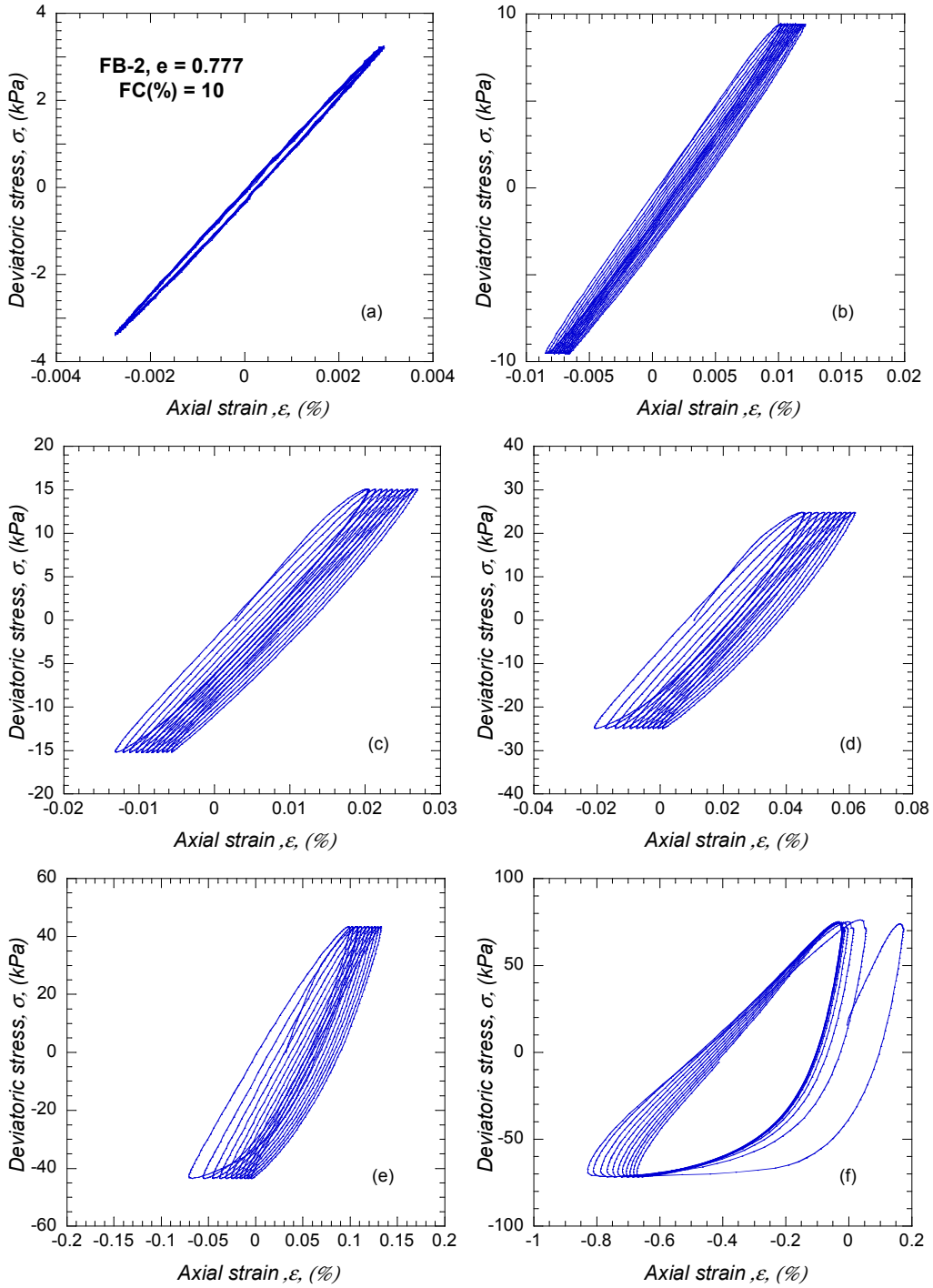

Figure D.1 Stress-strain curves of FB-2 specimen with e = 0.777

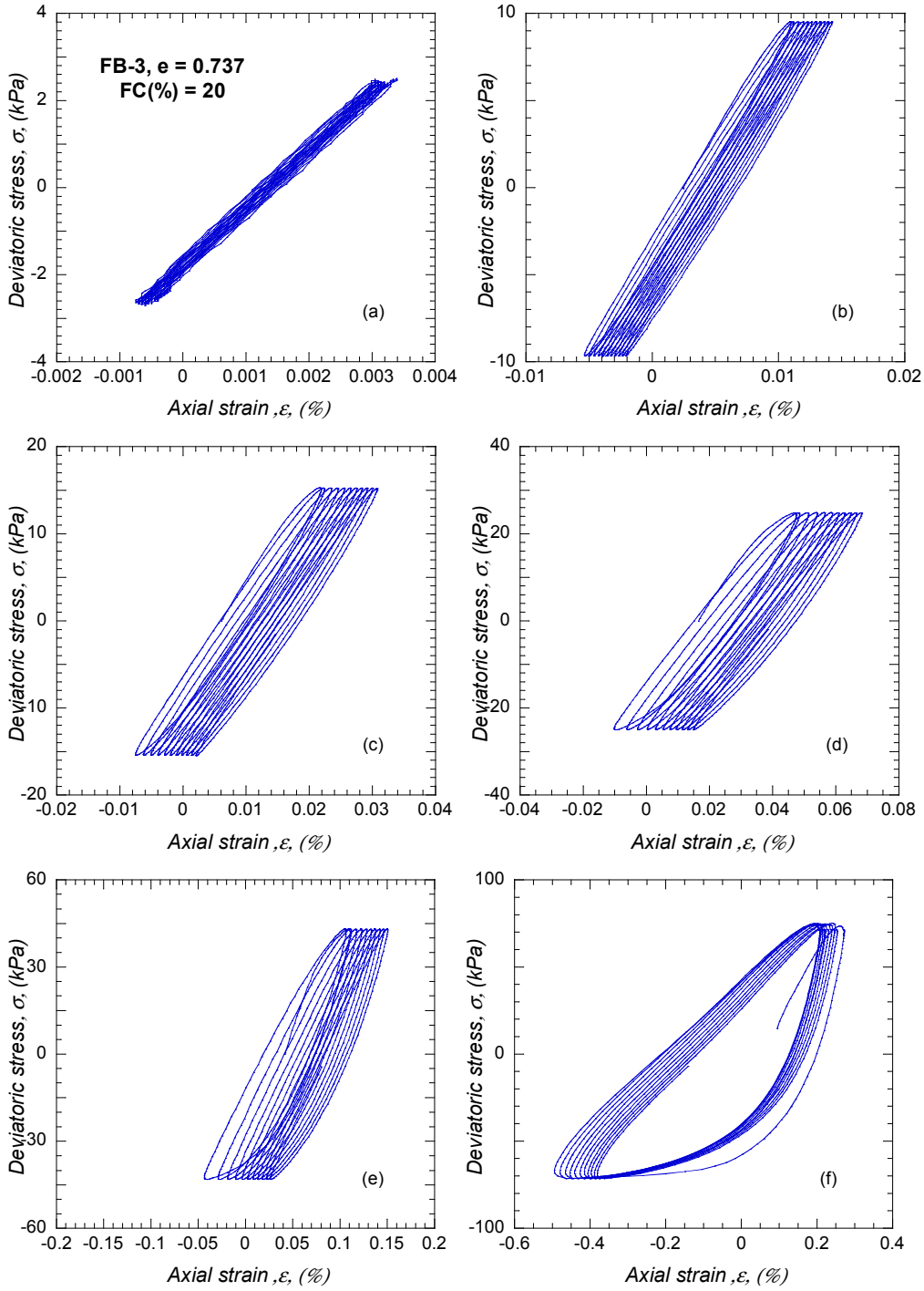

Figure D.2 Stress-strain curves of FB-3 specimen with e = 0.737

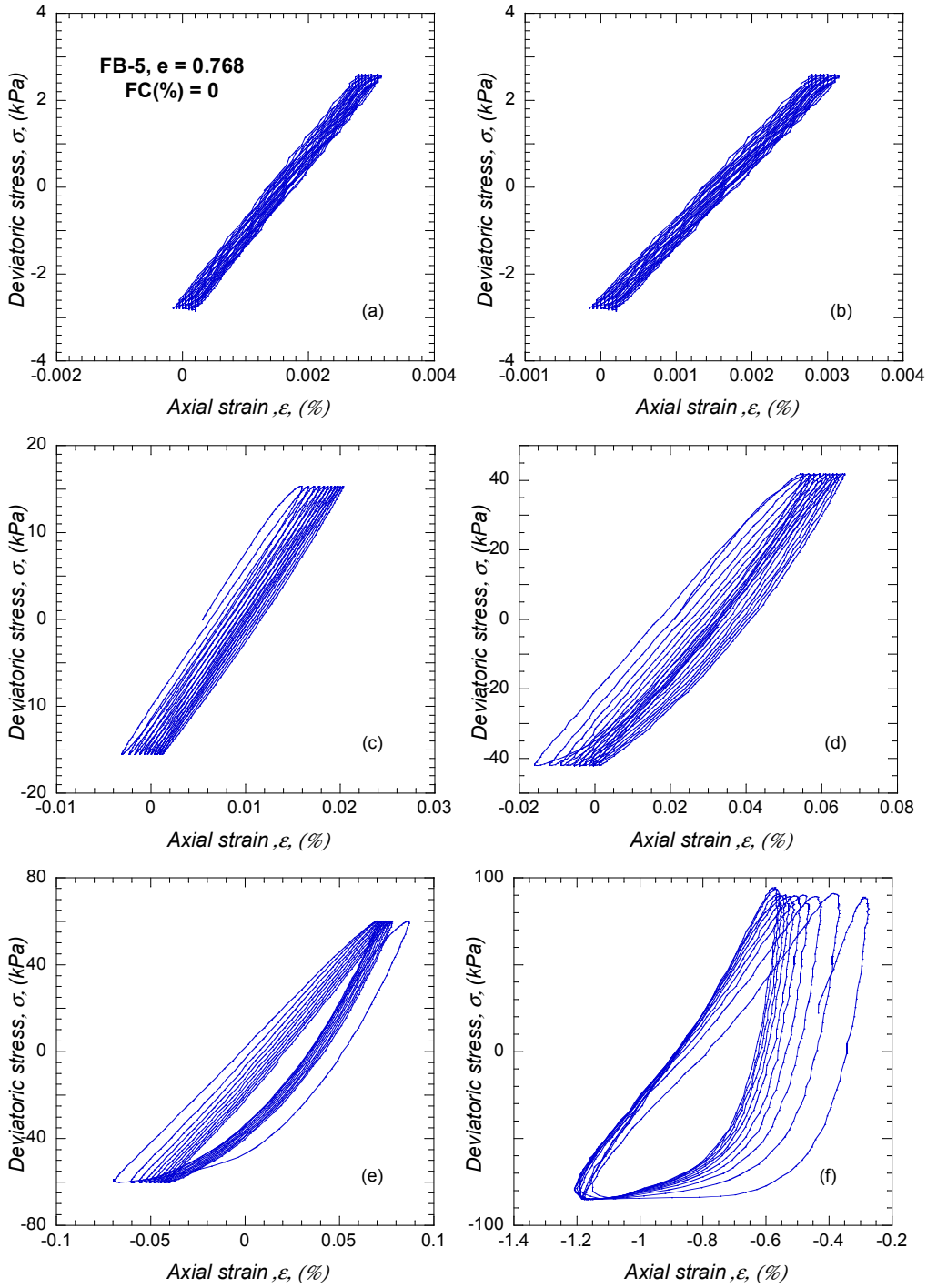

Figure D.3 Stress-strain curves of FB-5 specimen with e = 0.768

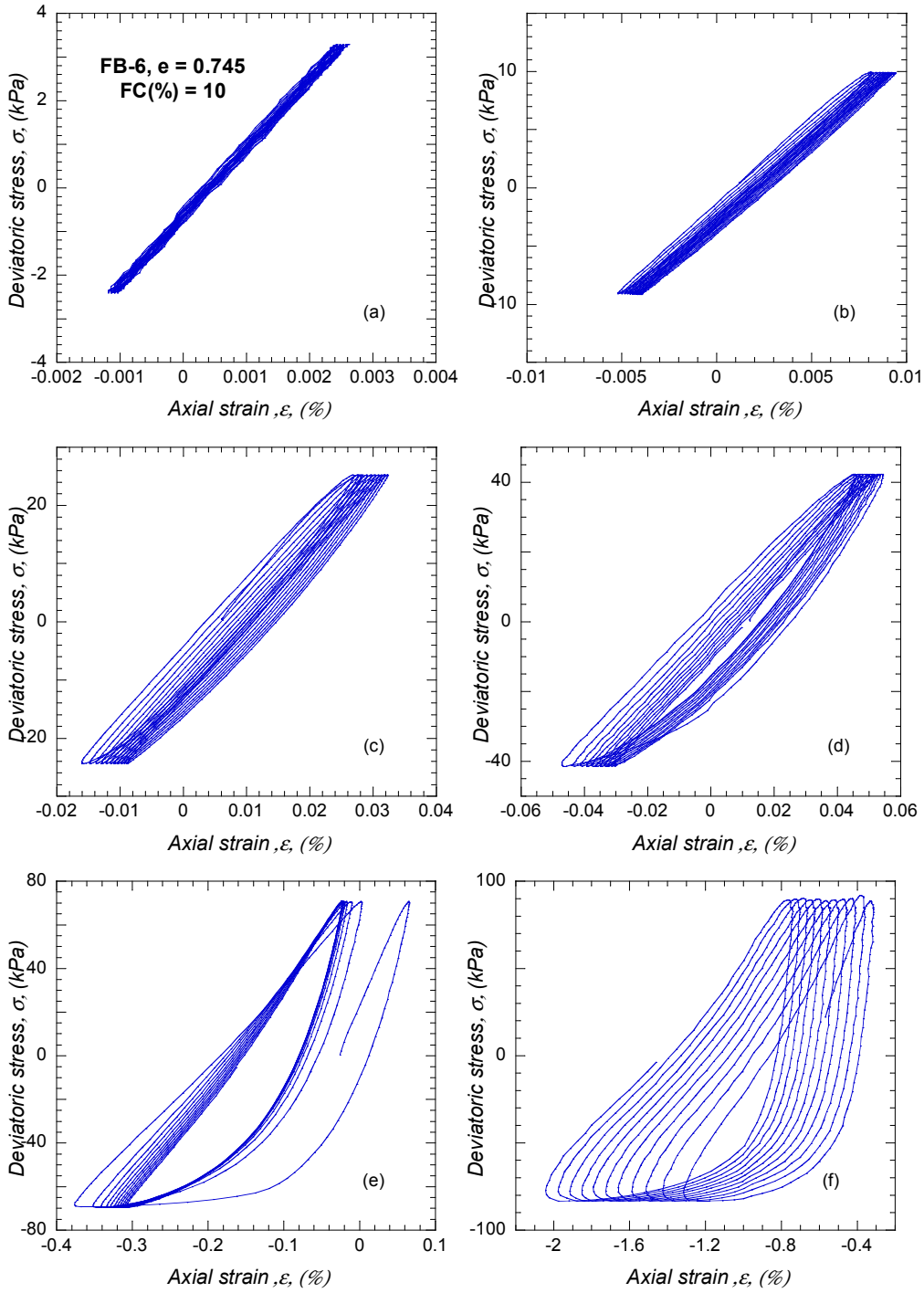

Figure D.4 Stress-strain curves of FB-6 specimen with e = 0.745

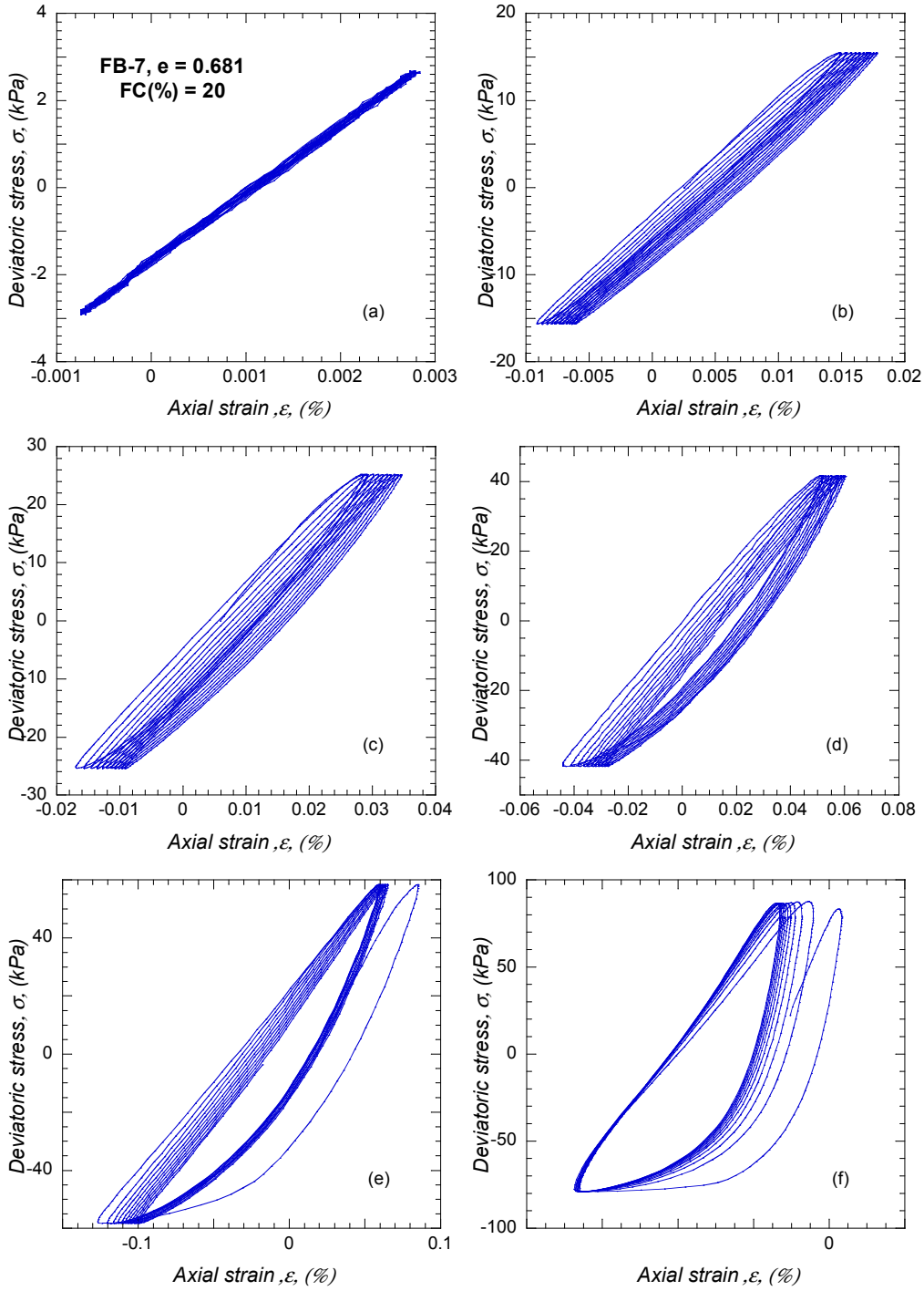

Figure D.5 Stress-strain curves of FB-7 specimen with e = 0.681

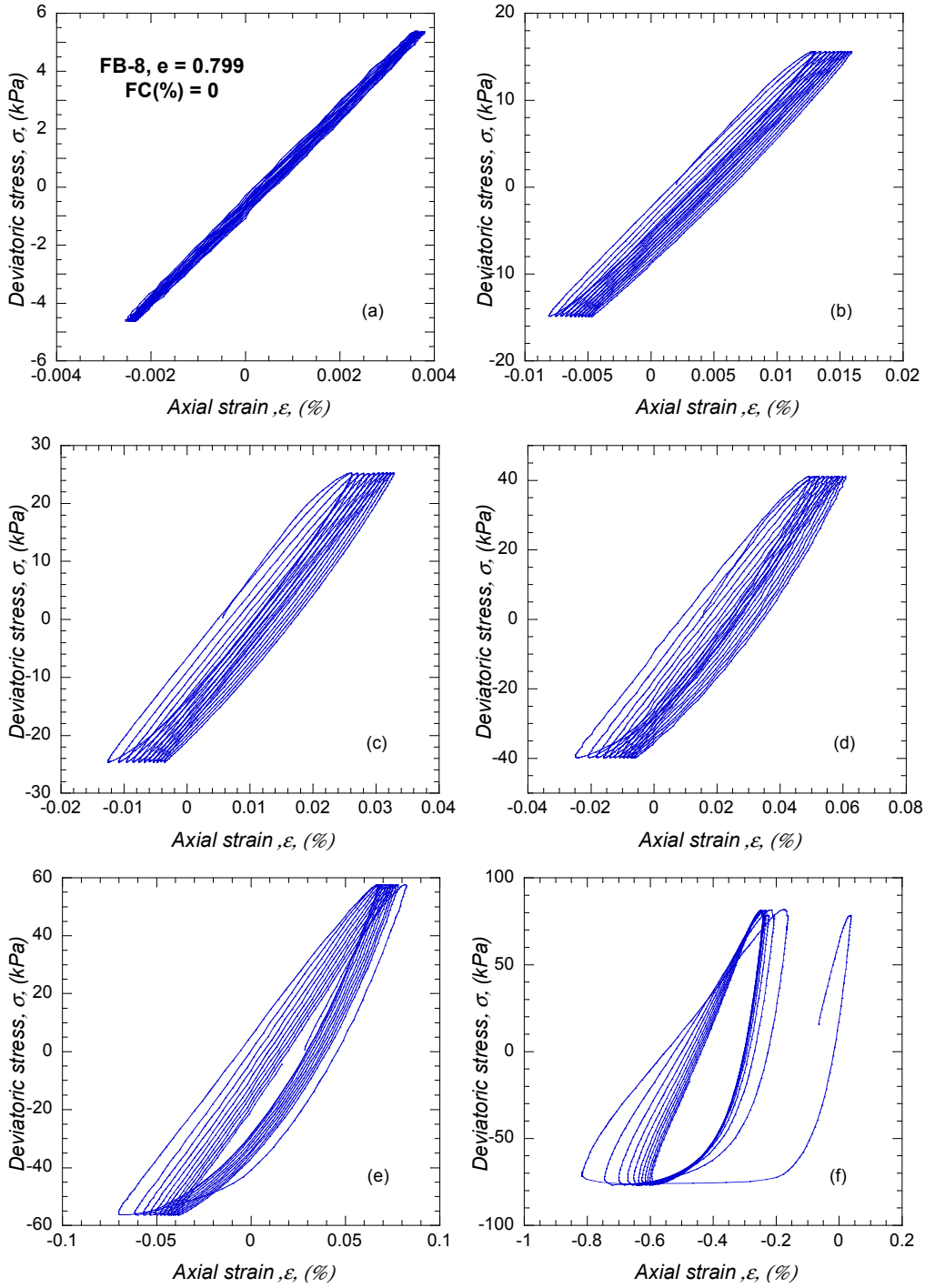

Figure D.6 Stress-strain curves of FB-8 specimen with e = 0.799

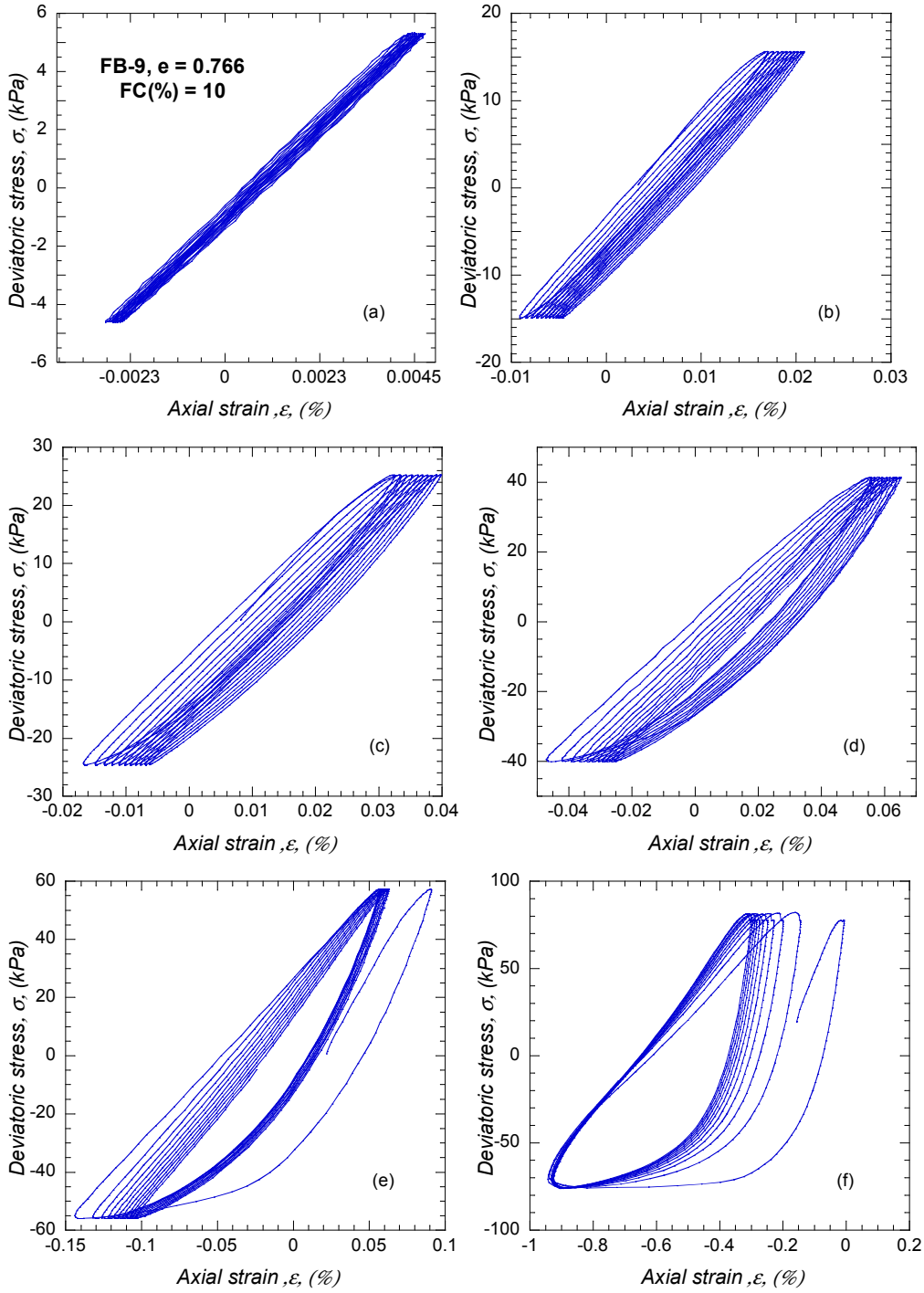

Figure D.7 Stress-strain curves of FB-9 specimen with e = 0.766

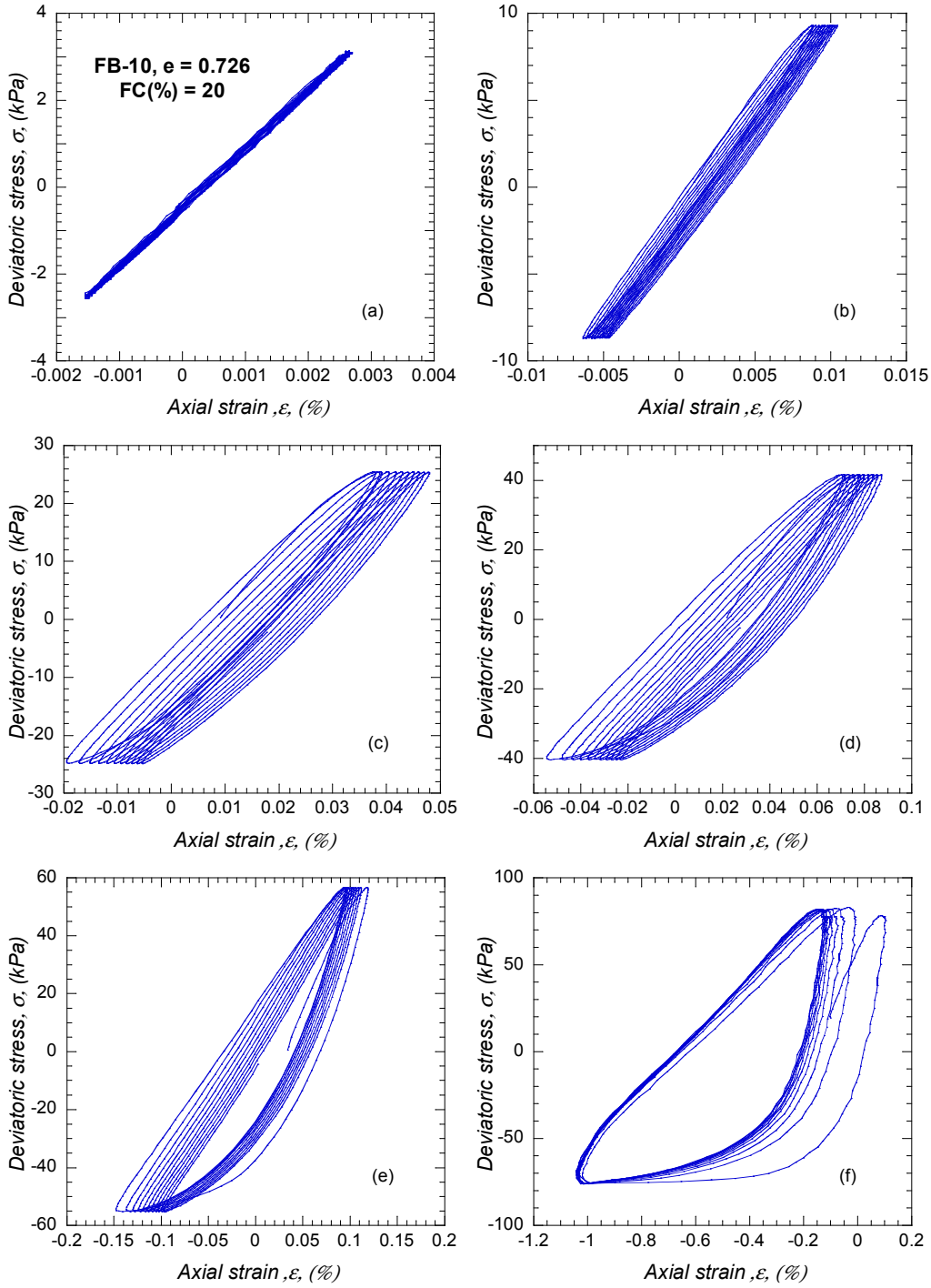

Figure D.8 Stress-strain curves of FB-10 specimen with e = 0.726

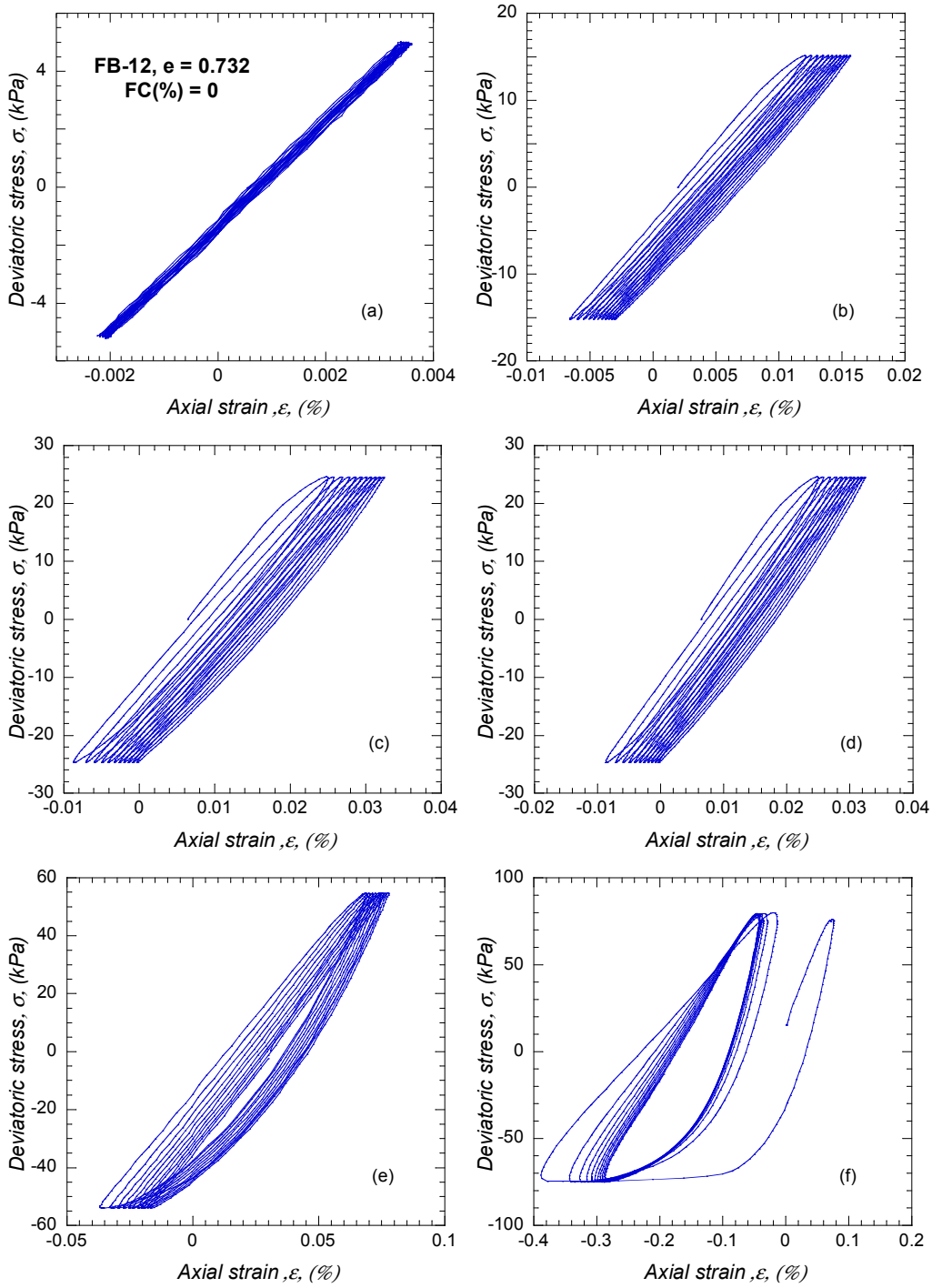

Figure D.9 Stress-strain curves of FB-12 specimen with e = 0.732

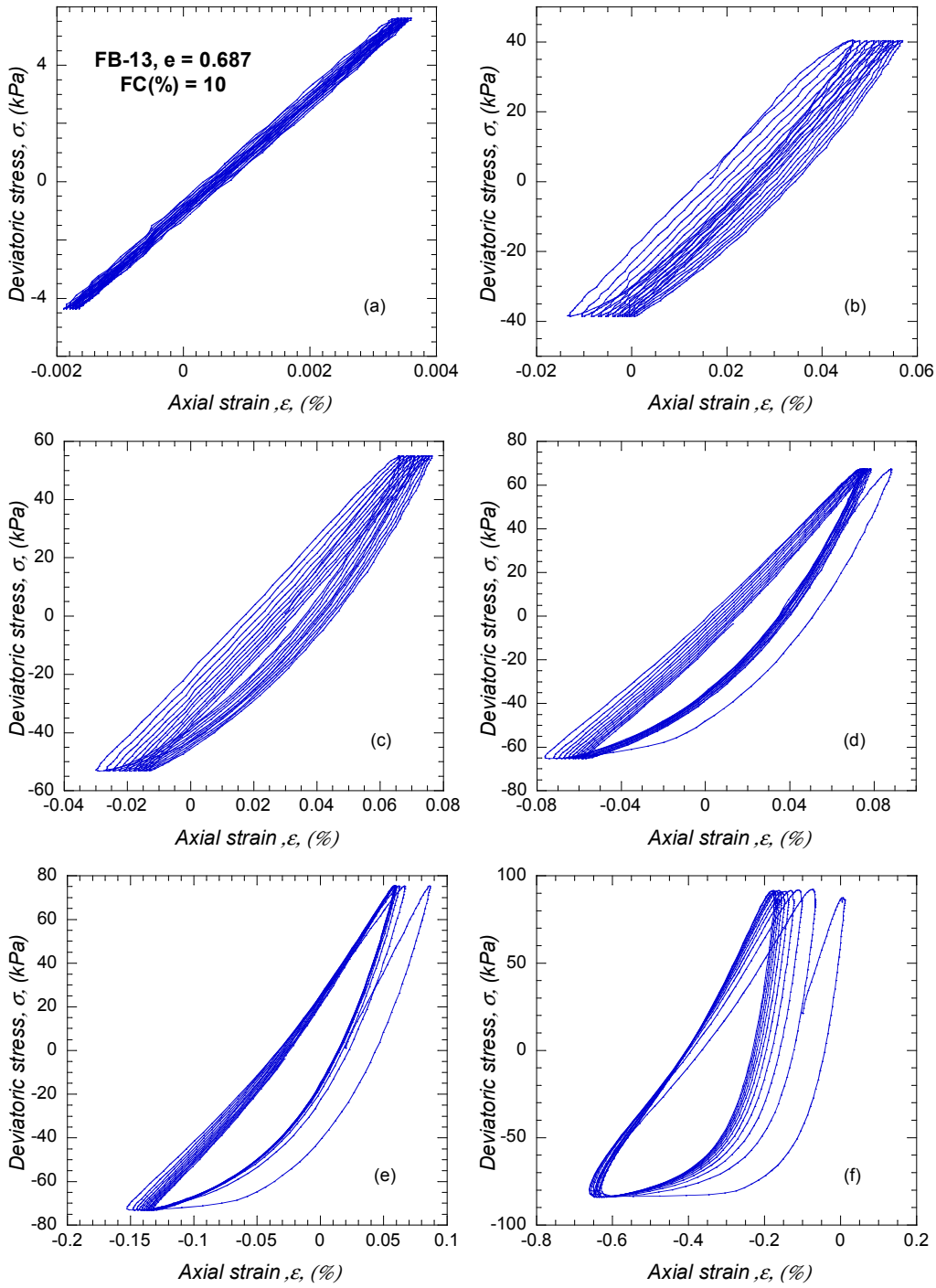

Figure D.10 Stress-strain curves of FB-13 specimen with e = 0.687

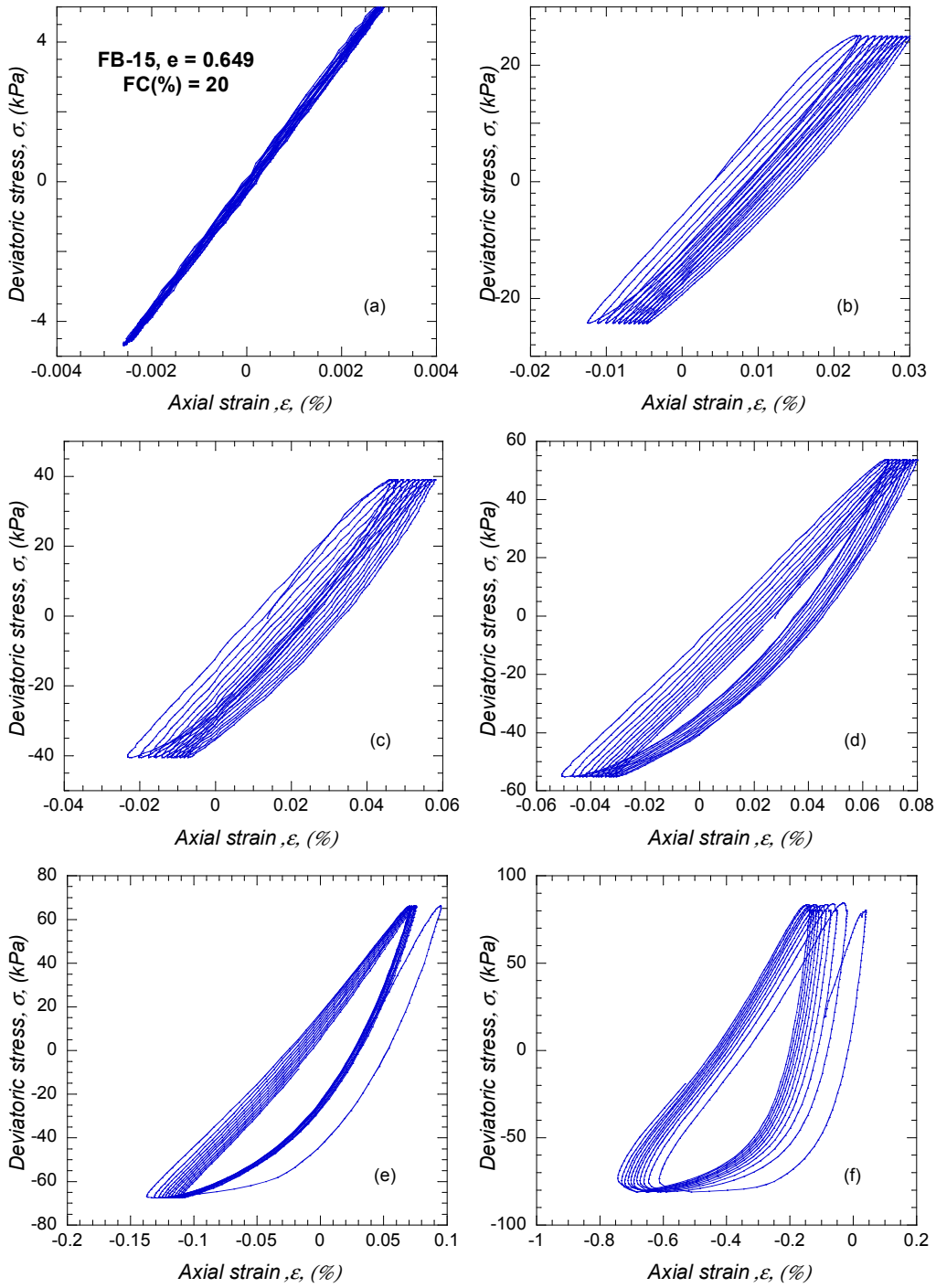

Figure D.11 Stress-strain curves of FB-15 specimen with e = 0.649

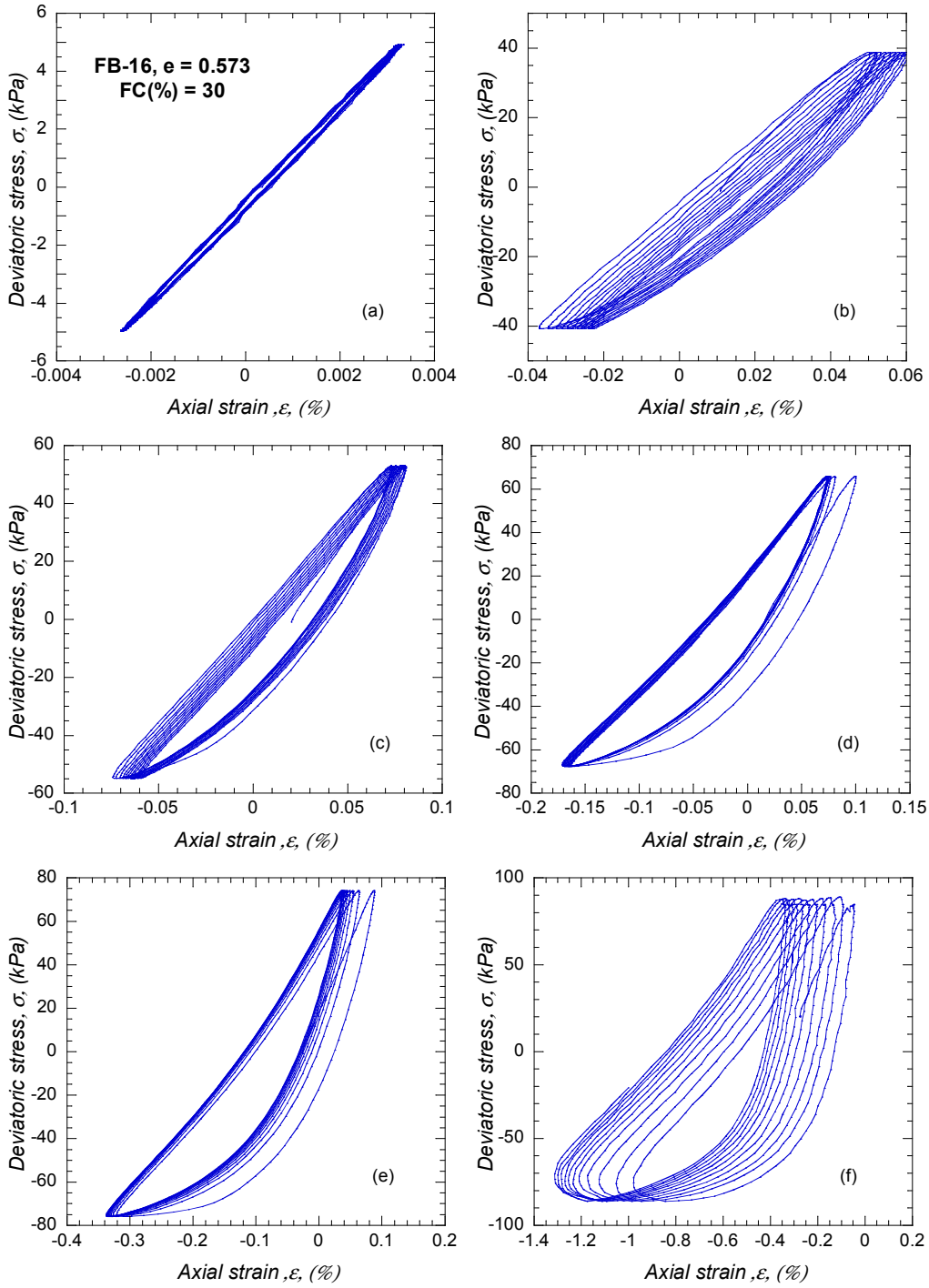

Figure D.12 Stress-strain curves of FB-16 specimen with e = 0.573

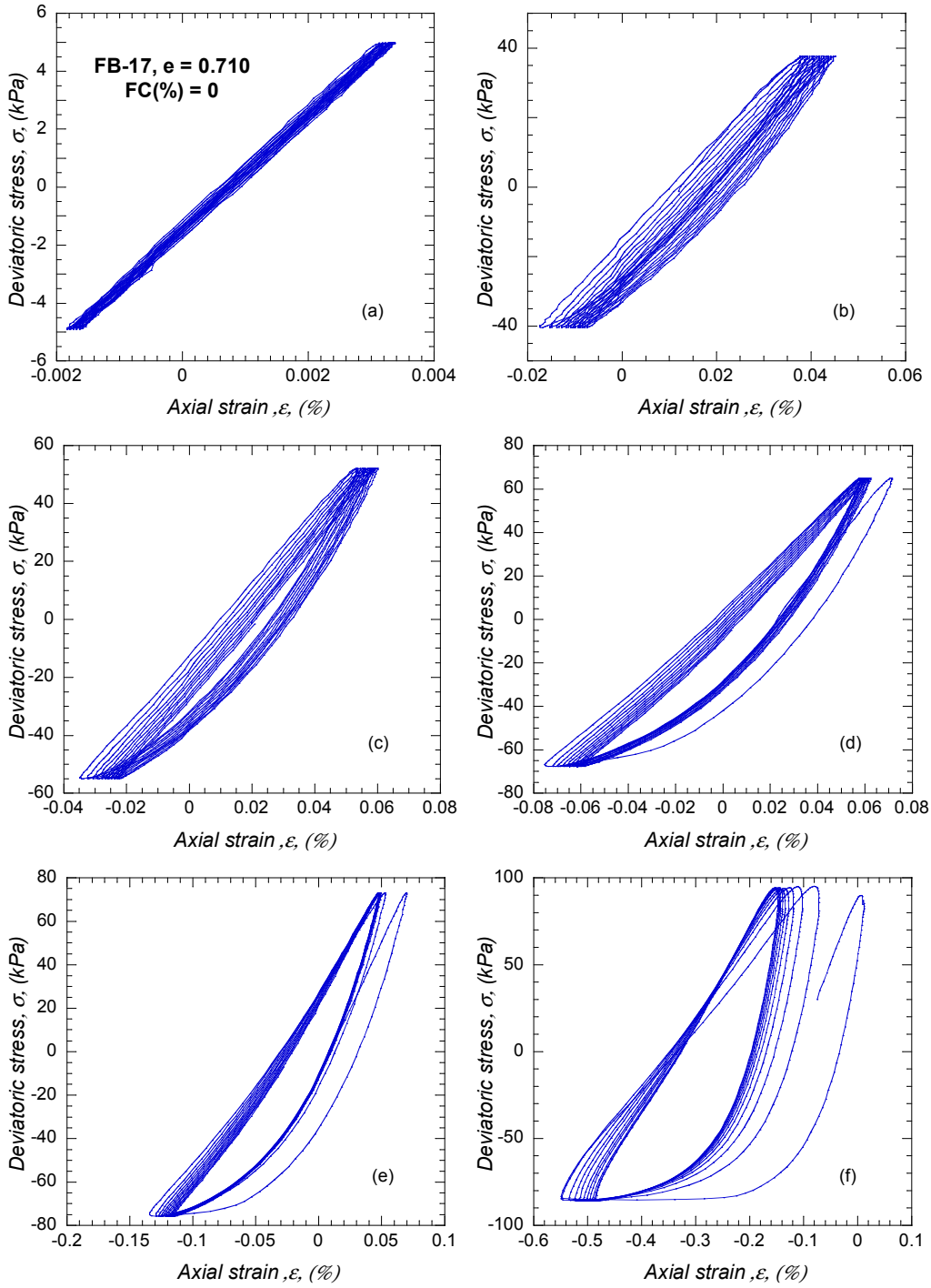

Figure D.13 Stress-strain curves of FB-17 specimen with e = 0.710

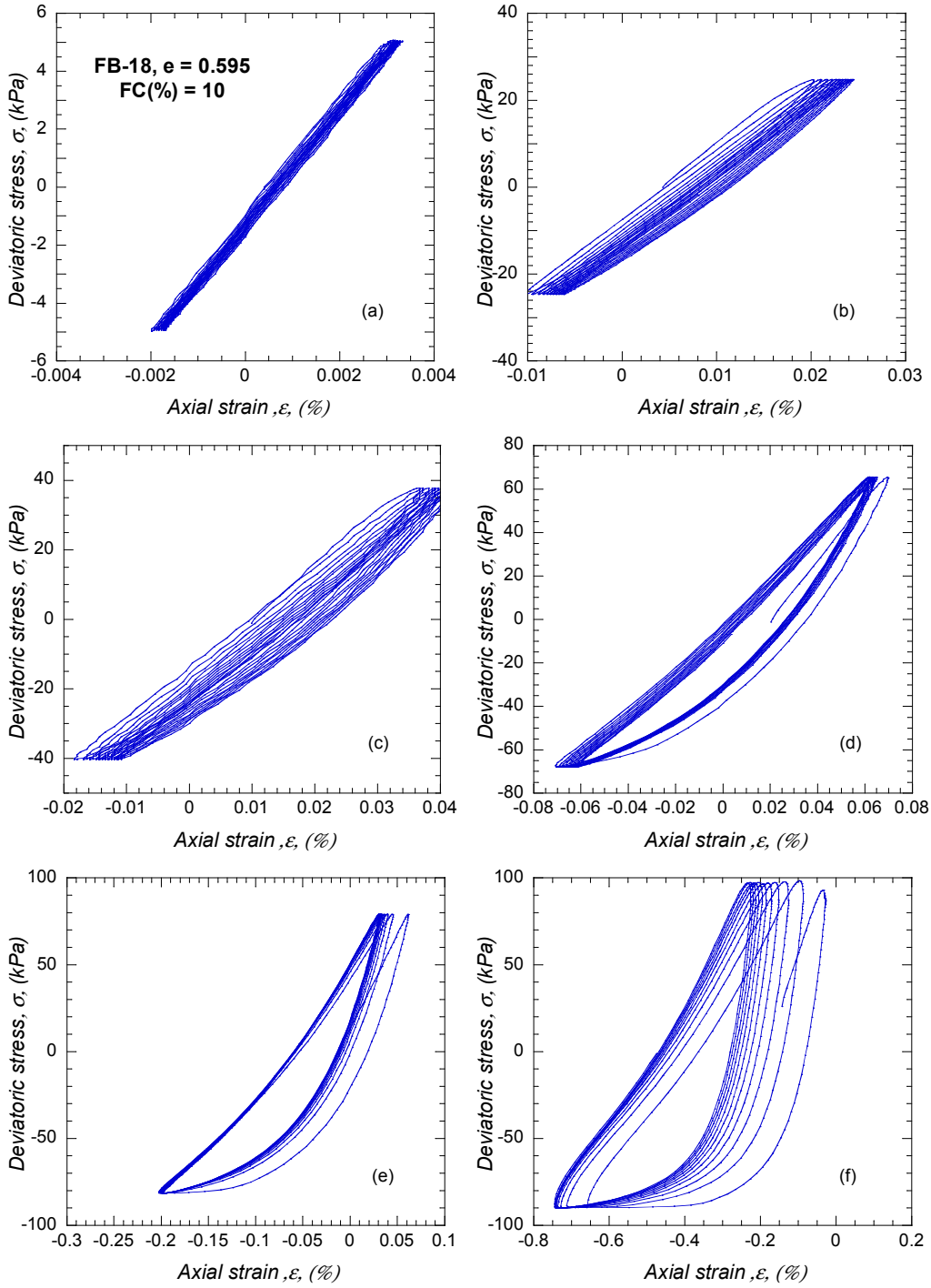

Figure D.14 Stress-strain curves of FB-18 specimen with e = 0.595

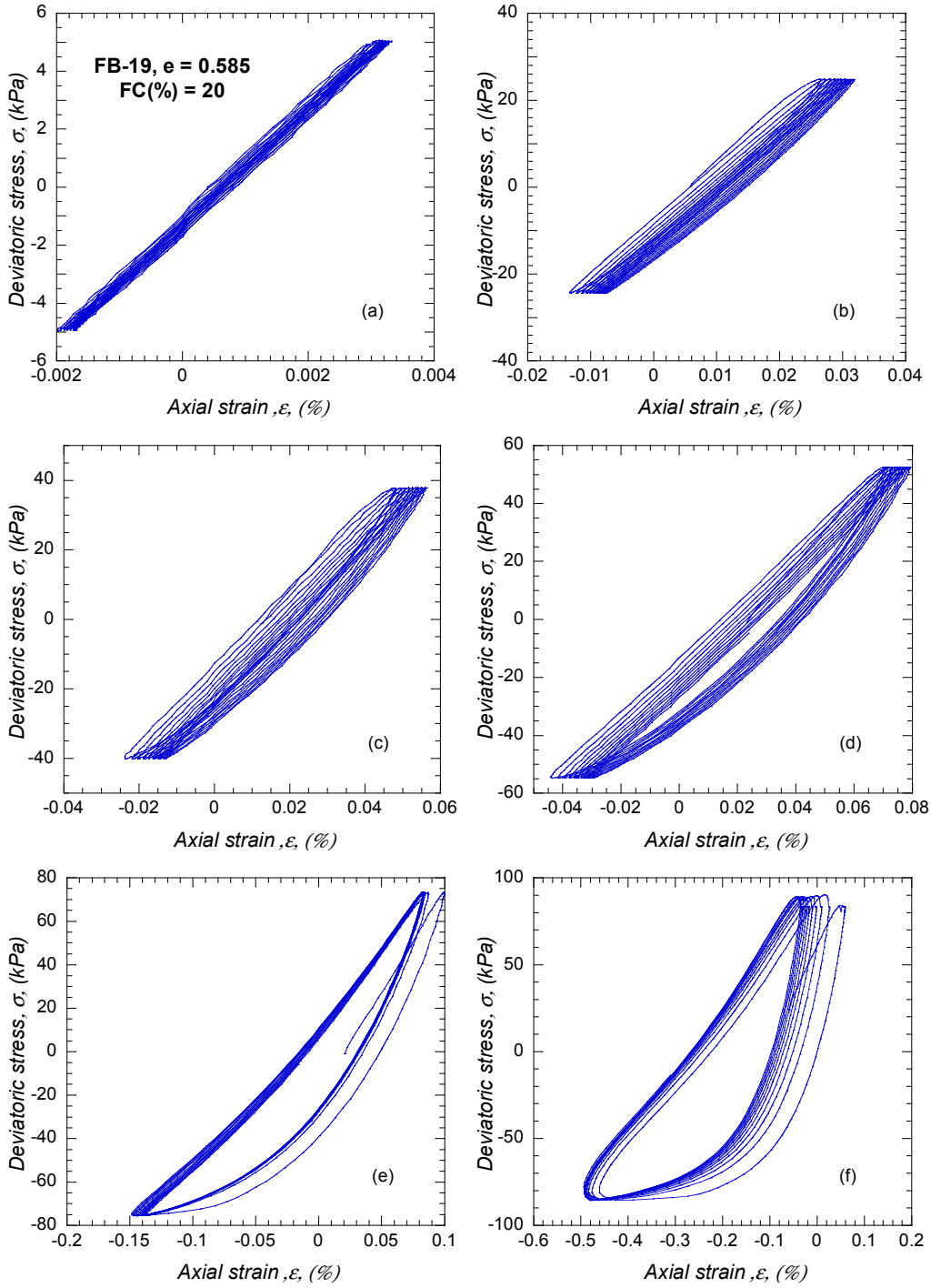

Figure D.15 Stress-strain curves of FB-19 specimen with e = 0.585

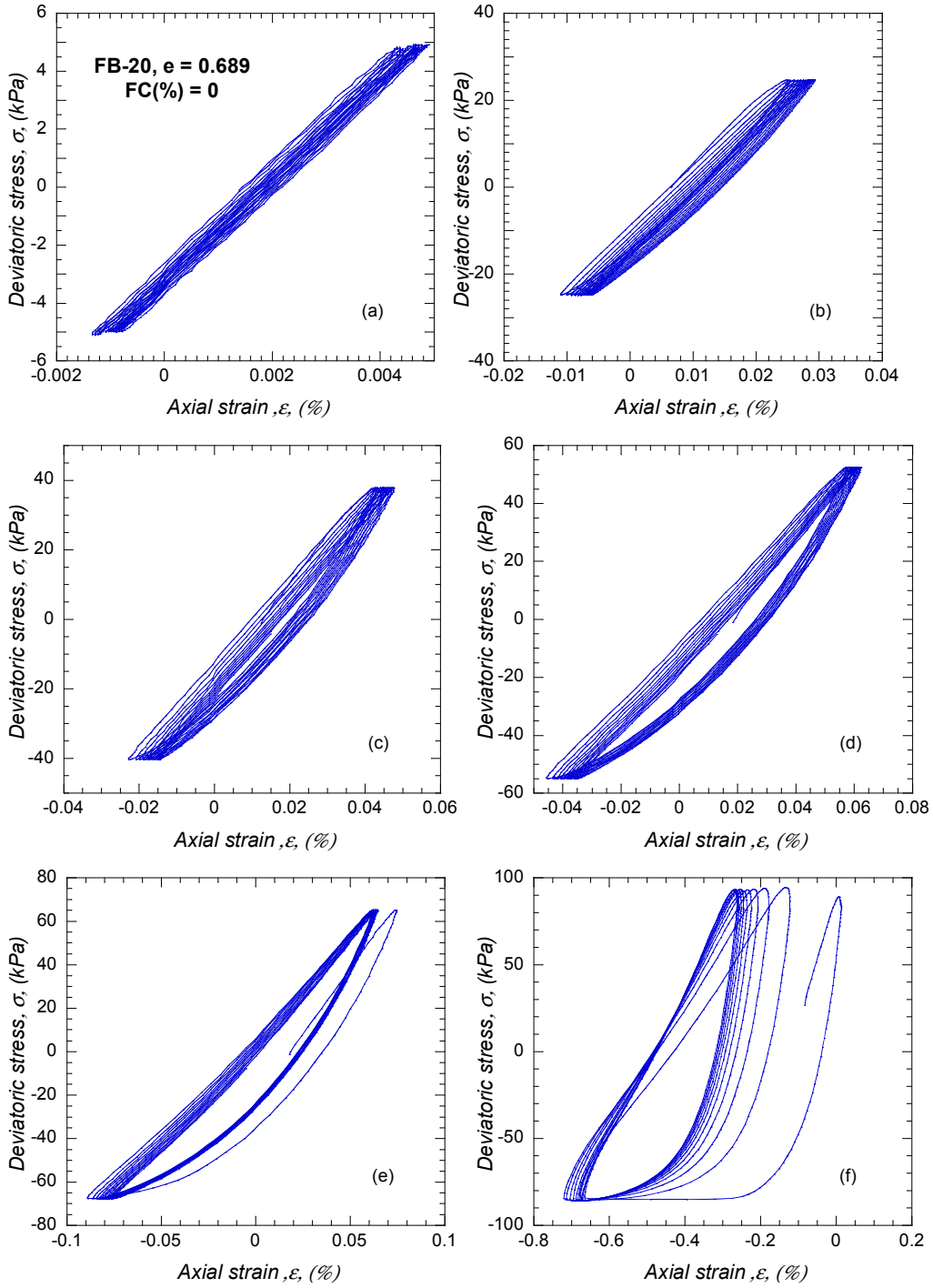

Figure D.16 Stress-strain curves of FB-20 specimen with e = 0.689

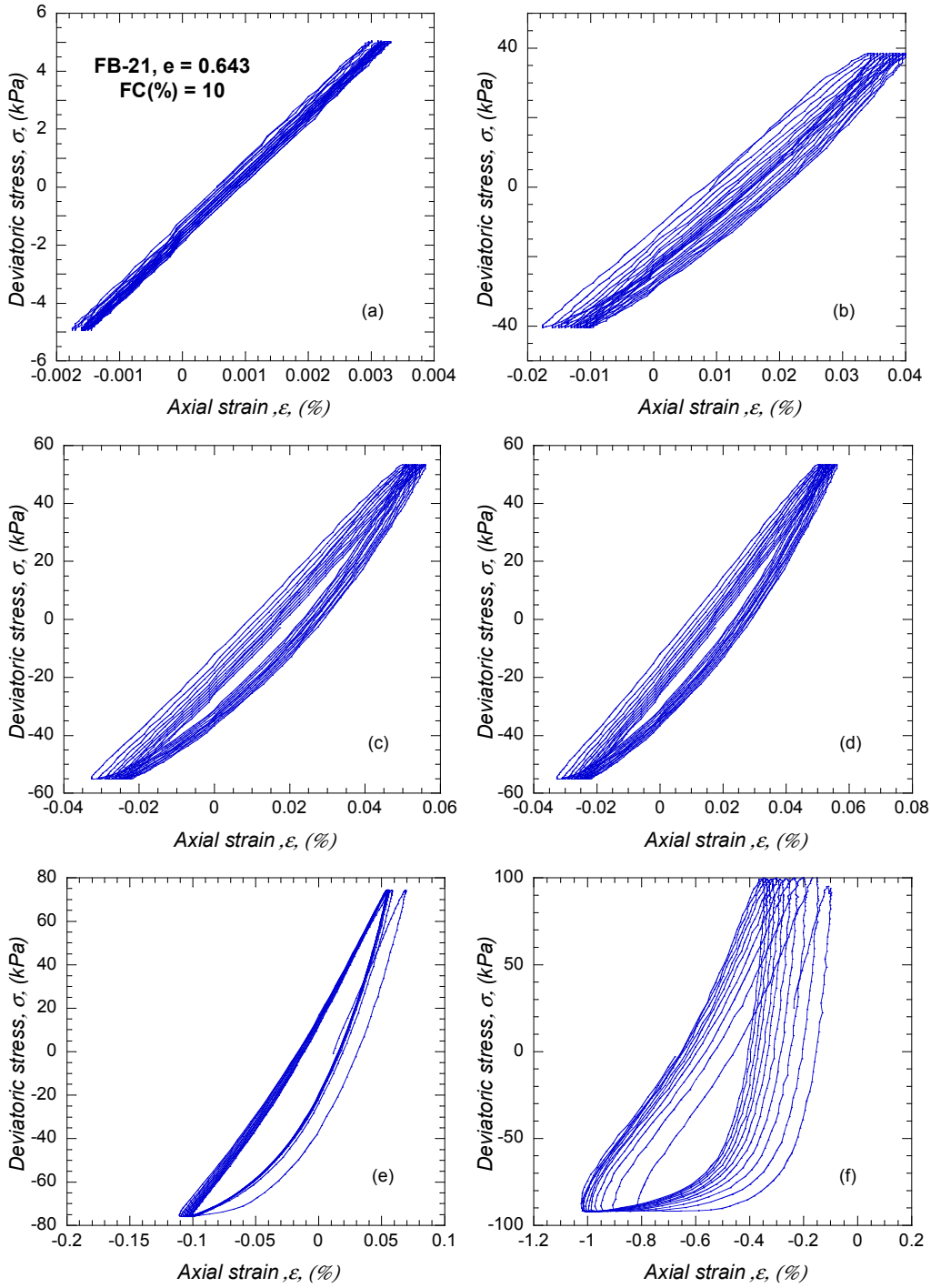

Figure D.17 Stress-strain curves of FB-21 specimen with e = 0.643

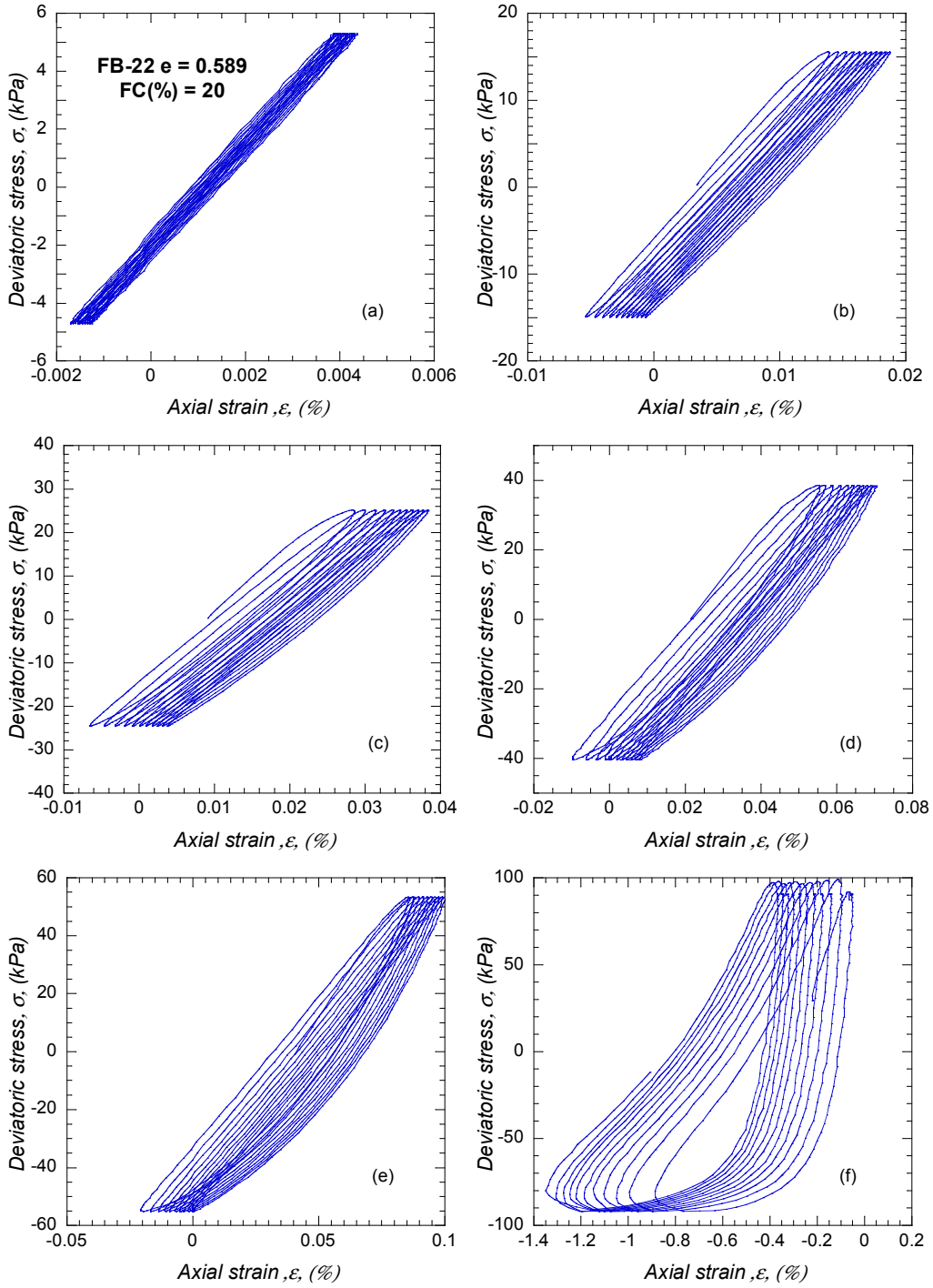

Figure D.18 Stress-strain curves of FB-22 specimen with e = 0.589

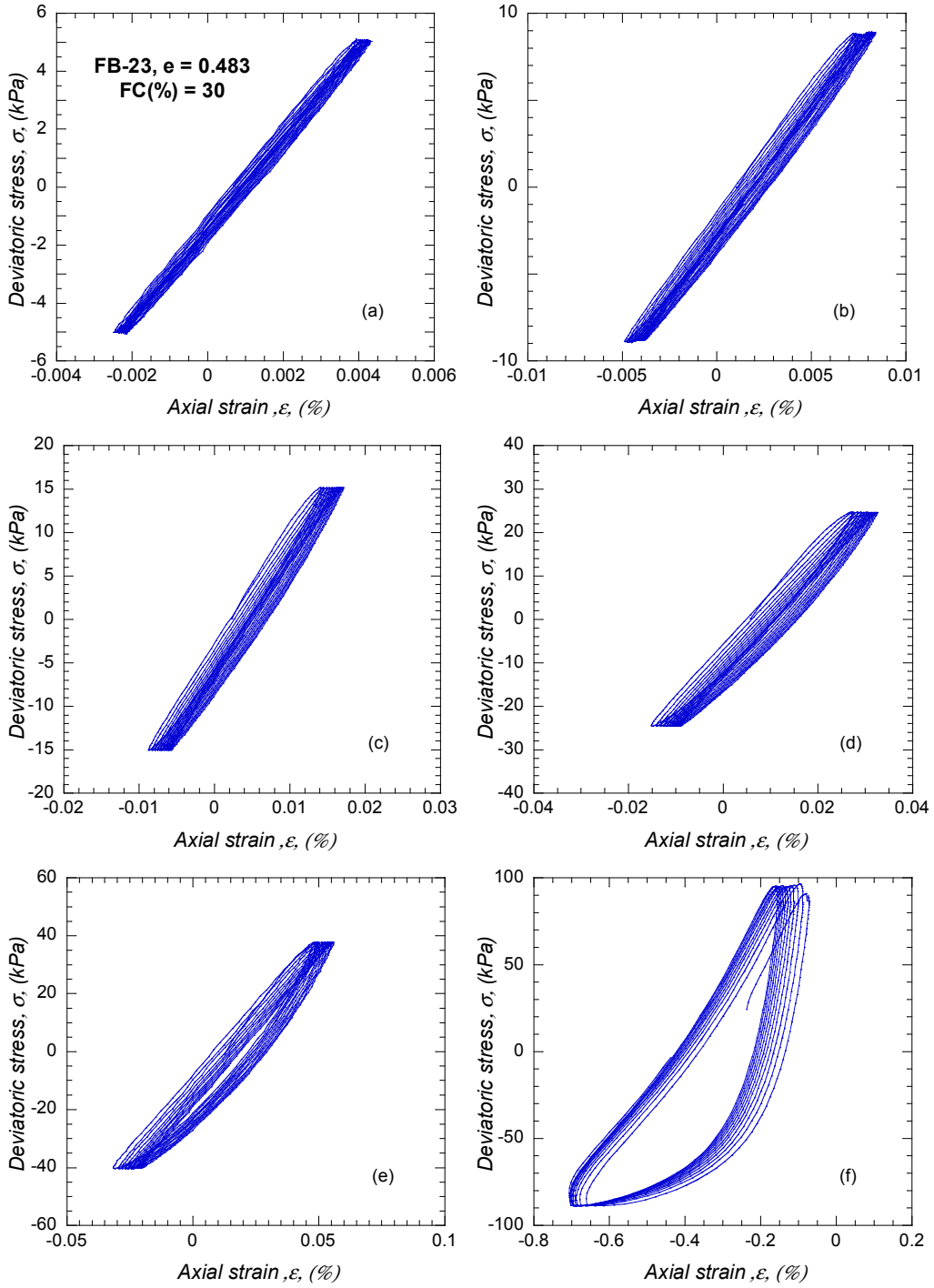

Figure D.19 Stress-strain curves of FB-23 specimen with e = 0.483

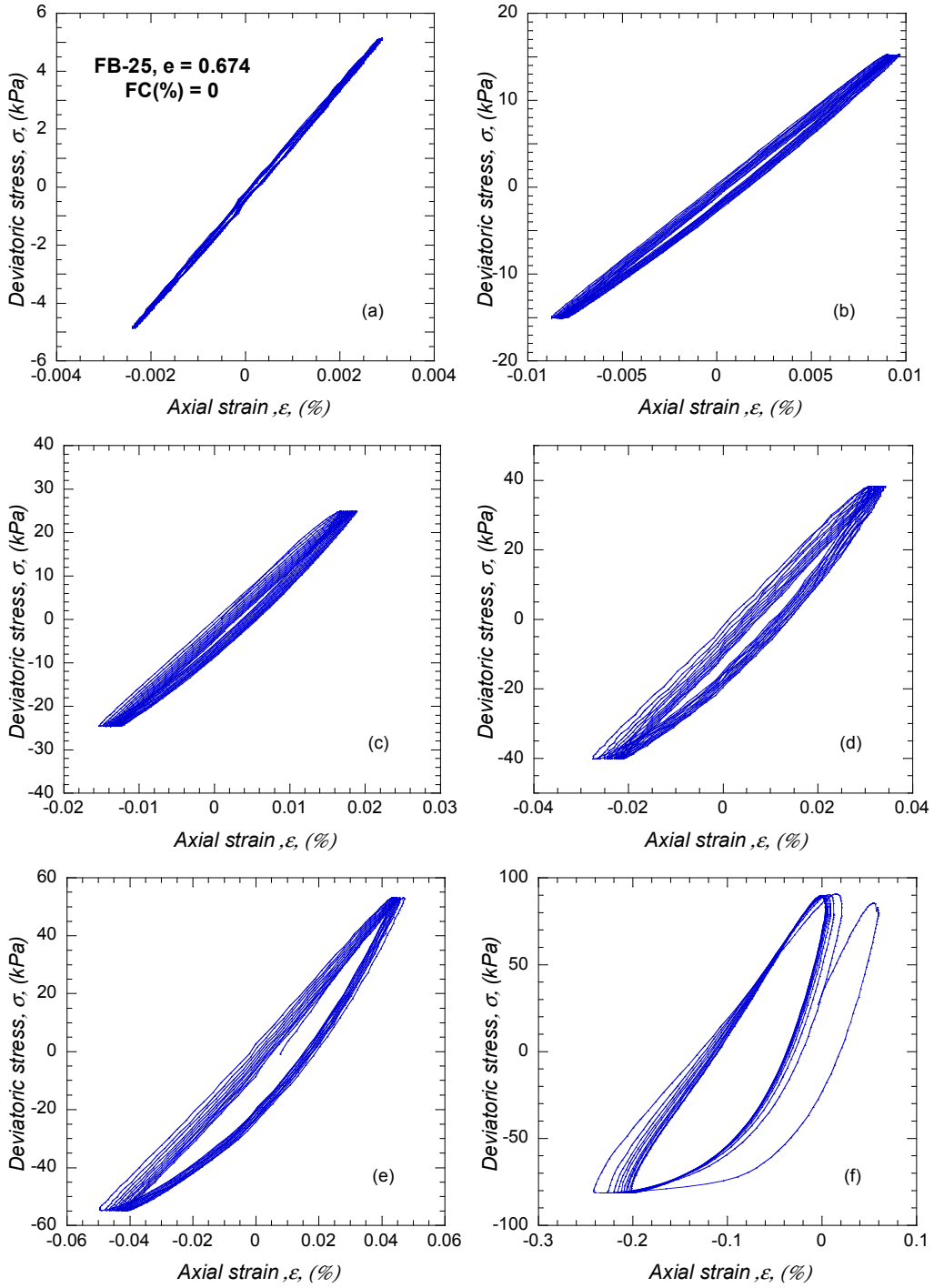

Figure D.20 Stress-strain curves of FB-25 specimen with e = 0.674

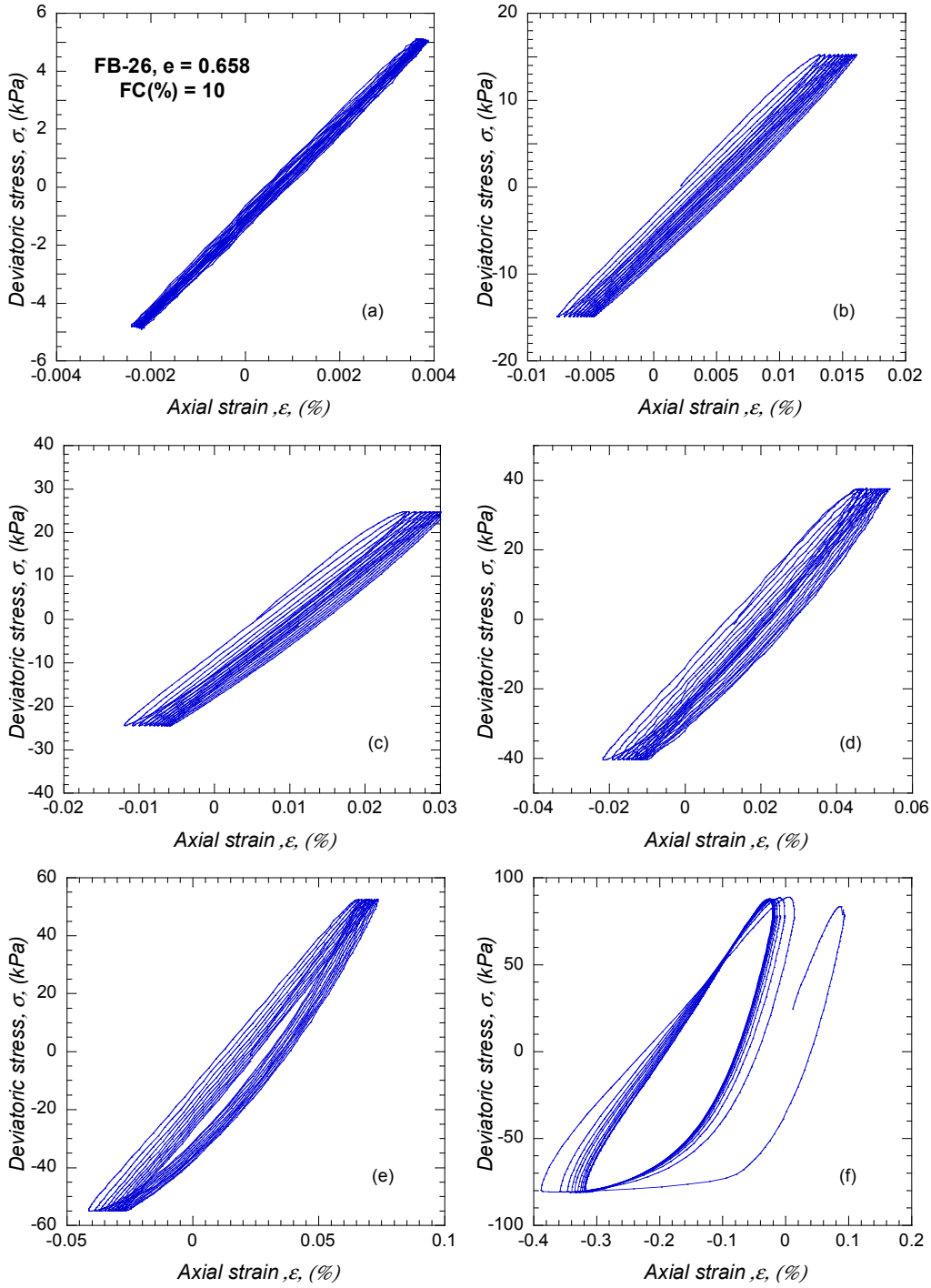

Figure D.21 Stress-strain curves of FB-26 specimen with e = 0.658

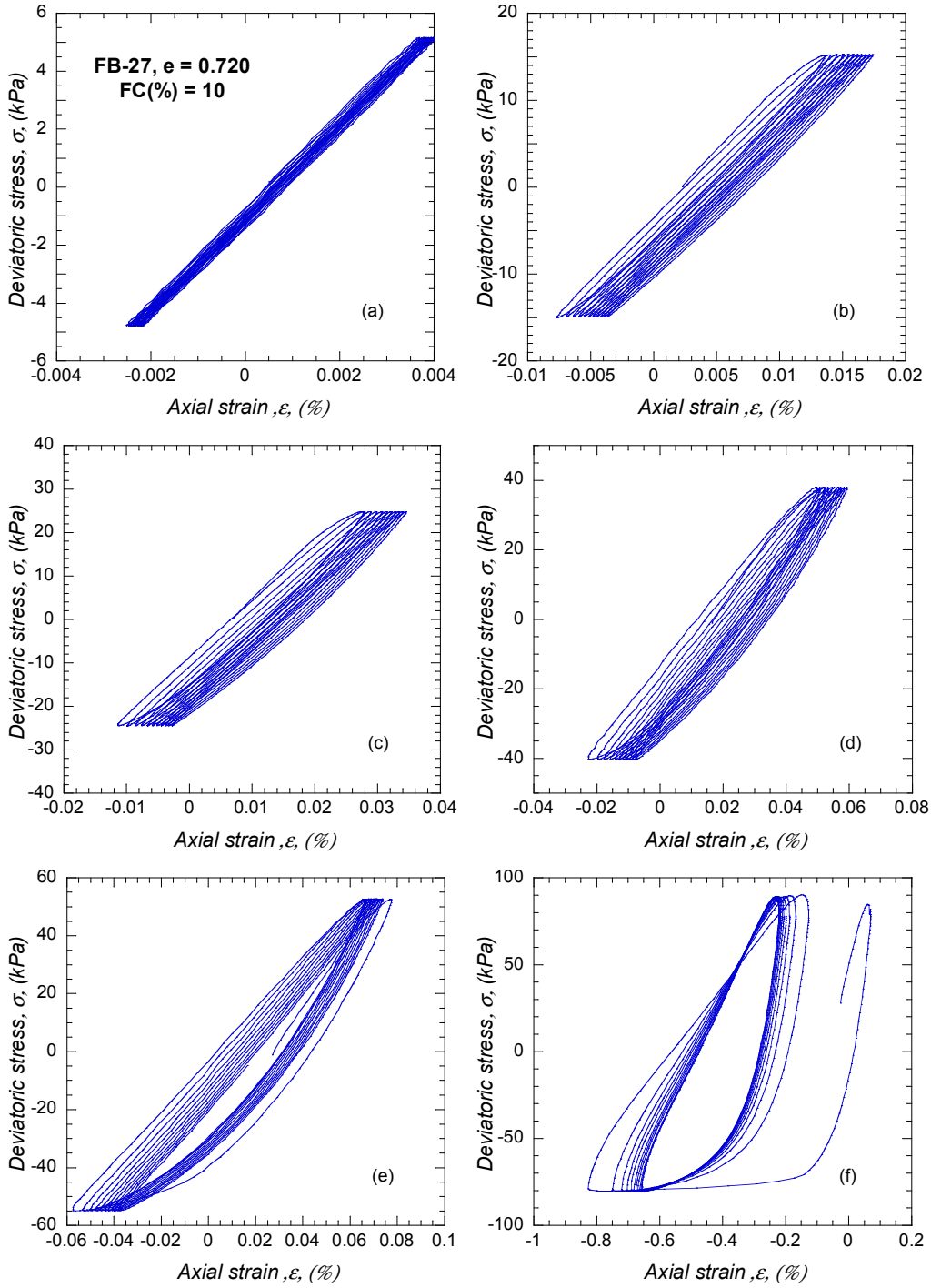

Figure D.22 Stress-strain curves of FB-27 specimen with e = 0.720

References

BALDI, G., BELLOTTI, R., GHIONNA, V. N., JAMIOLKOWSKI, M. & LO PRESTI, D. C. F. Modulus of sand from CPT's and DMT's. *In:* ICSMFE, P. C. O. X., ed. Twelfth international conference on soil mechanics and foundation engineering, 13-18 August 1989 Rio de Janeiro. Rotterdam, Netherlands: A. A. Balkema, 165-170.

BALDI, G., BRUZZI, D., SUPERBO, S., BATTAGLIO, M. & JAMIOLKOWSKI, M. 1988. Seismic cone in Po river sand. *In:* DE RUITER, J., ed. First international symposium on penetration testing - ISOPT-1, 20-24 March 1988 Orlando. Rotterdam: A. A. Balkema, 643-650.

BERRIL, J. B., DAVIS, R. O. & MCCAHON, I. F. 1993. Christchurh seismic hazard pilot study. *Bulletin of the New Zealand national Society for earthquake engineering,* 26**,** 14-27.

BERRYMAN, J. G. 1980. Confirmation of Biot's theory. *Applied Physics Letters,* 37**,** 382-384.

BLEWETT, J., BLEWETT, I. J. & WOODWARD, P. K. 1999. Measurement of shear-wave velocity using phase-sensitive detection techniques. *Canadian Geotechnical Journal,* 36**,** 934-939.

BRADLEY, B. 2012b. Ground motions observed in the Darfield and Christchurch earthquakes and the importance of local site response effects. *New Zealand Journal of Geology and Geophysics,* 55**,** 279-286.

BRADLEY, B. 2012c. Observed ground motions in the 4 September 2010 Darfield and 22 February 2011 Christchurch earthquakes. *Annual technical conference of New Zealand society for earthquake engineering: Implementing lessons learnt,* . Christchurch, New Zealand.

BRIGNOLI, E. G. M., GOTTI, M. & STOKOE, K. H. 1996. Measurement of shear waves in laboratory specimens by means of piezoelectric transducers. *Geotechnical testing Journal,* 19**,** 384-397.

BRITISH STANDARD INSTITUTION 1990. Methods of tests for soils for civil engineering. *Part 4: Compaction-related tests.*

BROWN, L. J. & WEEBER, J. H. 1992. *Geology of the Christchurch urban area,* Lower Hutt, New Zealand, Institute of geological & nuclear sciences Ltd.

CAMACHO-TAUTA, J., REYES-ORTIZ, O. J. & SANTOS, J. A. 2012. Evaluation of the frequency effects on the shear wave velocity of saturated sands. *15th World conference on earthquake engineering*. Lisbon, Portugal.

CASSARO, M. A. & ROMERO, E. M. 1986. Proceedings of the conference, The Mexico earthquakes - 1985: factors invovled and lessons learned. September 19-21 1986 Mexico city, Mexico. New York: American society of civil engineers.

CERA 2013. Canterbury Earthquake Recovery Authority: https://canterburygeotechnicaldatabase.projectorbit.com/Registration/Login.aspx.

COUSINS, J. 2013. *RE: Personal communication.*

CUBRINOVSKI, M. 1993. *A constitutive model for sandy soils based on a stress-dependent density parameter.* Doctor of Engineering, University of Tokyo.

CUBRINOVSKI, M., BRADLEY, B., WOTHERSPOON, L. M., GREEN, R. A., BRAY, J. D., WOOD, C. M., PENDER, M., ALLEN, J., BRADSHAW, A., RIX, G., TAYLOR, M., MA, K., WINKLEY, A., ZUPAN, J., O'ROURKE, T., DEPASCALE, G. & WELLS, D. 2011. Geotechnical aspects of the 22 February 2011 Christchurch earthquake. *Bulletin of the New Zealand Soceity for Earthquake Engineering,* 44**,** 205-226.

CUBRINOVSKI, M. & ISHIHARA, K. 1998. Modelling of sand behaviour based on state concept. *Soils and Foundations,* 38**,** 115-127.

CUBRINOVSKI, M. & ISHIHARA, K. 2002. Maximum and minimum void ratio characteristics of sands. *Soils and Foundations,* 42**,** 65-78.

CUBRINOVSKI, M. & REES, S. 2008. Effects of fines on undrained behaviour of sands. *Geotechnical earthquake engineering and soil dynamics IV*.

CUBRINOVSKI, M., REES, S. & BOWMAN, E. 2010. Effects of Non-plastic Fines on Liquefaction Resistance of Sandy Soils. *In:* GAREVSKI, M. & ANSAL, A. (eds.) *Earthquake Engineering in Europe.* Springer Netherlands.

DAFALIAS, Y. F. 1986. Bounding surface plasticity. I: Mathematical foundation and hypoplasticity. *Journal of Engineering Mechanics,* 112**,** 22.

DARENDELI, M. B. 2001. *Development of a new family of normalized modulus reduction and material damping.* Ph.D., The University of Texas at Austin.

DAVIS, R. O. & SELVADURAI, A. P. S. 1996. *Elasticity and geomechanics*, Cambridge university press.

DOBRY, R. & VUCETIC, M. 1987. Dynamic properties and seismic response of soft clay deposits. *In:* MENDOZA, M. J. & MONTANEZ, L. (eds.) *State-of-the art reports in the proceedings of the internaional symposium on geotechnical engineering of soft soils.* Mexico City: Sociedad Mexicana de Mecanica de Seulos.

ELDER, D. M., MCCAHON, I. F. & YETTON, M. D. 1991. The earthquake hazard in Christchurch: a detailed evaluation. Soils & foundations Ltd.

GAJO, A., FEDEL, A. & MONGIOVI, L. 1997. Experimental analysis of the effects of fluid-solid coupling on the velocity of elastic waves in saturated porous media. *Geotechnique,* 47**,** 993-1008.

GARINI, E., PANAGOULIAS, S., TASIOPOULOU, P. & GAZETAS, G. 2013. Canterbury earthquakes: the Resthaven records and soil amplification response. *ICEGE, from case history to practice; In honour of Prof. Kenji Ishihara.* Istanbul.

GEONET 2012. http://www.geonet.org.nz/index.html.

GUHA, S., BRAY, J. D. & DRNEVICH, V. P. 1993. Characteristics of the deep old bay clay deposits in the east San Francisco bay area.

HARDIN, B. O. 1978. The nature of stress-strain behavior for soils. *ASCE Geotech Eng Div Spec Conf, Earthquake Eng and Soil Dyn.* Pasadena, Calif: ASCE, New York, NY.

HARDIN, B. O. & DRNEVICH, V. P. 1972a. Shear modulus and damping in soils: Design equations and curves. *Journal of Soil Mechanics and Foundation Division,* 98**,** 667-692.

HARDIN, B. O. & DRNEVICH, V. P. 1972b. Shear modulus and damping in soils: Measurement and parameter effects. *Journal of Soil Mechanics and Foundation Division,* 98**,** 603-624.

HASHASH, Y. M. A. & PARK, D. 2001. Non-linear one-dimensional seismic ground motion propagation in the Mississippi embayment. *Engineering Geology,* 62**,** 185-206.

HASHASH, Y. M. A., PHILLIPS, C. & GROHOLSKI, D. R. 2010. Recent advances in non-linear site response analysis. *In:* PRAKASH, S. (ed.) *Fifth International Conference on Recenet Advances in Geotechnical Earthquake Engineering and Soil Dynamics.* San Diego.

HODDER, S. B. 1983. Computer processing of New Zealand strong-motion accelerograms. *Bulletin of the New Zealand national Society for earthquake engineering,* 16**,** 234-246.

IDRISS, I. M. & SUN, J. I. 1991. SHAKE91: a computer program for conducting equivalent linear seismic response anlalyses of horizontally layered soil deposits. 91 ed. Davis: Center for geotechnical modeling.

ISHIHARA, K. 1996. *Soil behaviour in earthquake geotechnics,* Oxford, Oxford science publications.

ISO 2005. International organization for standardization 23649:2005(E) : Bases for design of structures - Seismic actions for designing geotechnical works. Switzerland.

IWAN, W. D. 1967. On a Class of Models for the Yielding Behavior of Continuous and Composite Systems. *Journal of Applied Mechanics,* 34**,** 612-617.

IWASAKI, T. & TATSUOKA, F. 1977. Effects of grain size and grading on dynamic shear moduli of sands. *Soils and Foundations,* 17**,** 17.

IWASAKI, T., TATSUOKA, F. & TAKAGI, Y. 1978. Shear moduli of sands under cyclic torsional shear loading. *Soils and Foundations,* 18**,** 18.

JAMIOLKOWSKI, M., LEROUEIL, S. & LO PRESTI, D. C. F. 1991. Design parameters from theory to practice. *International Conference on Geotechnical Engineering for Coastal Development, GEO-COAST.* Yokohama: Japan coastal development institute of technology.

JAPANESE GEOTECHNICAL SOCIETY 2000. Standards of Japanese geotechnical society for laboratory shear test. *Method for cyclic triaxial test to determine deformation properties of geomaterials.* Japan: Japanese geotechnical society.

JOVICIC, V., COOP, M. R. & SIMIC, M. 1996. Objective criteria for determining G_{max} from bender element tests. *Geotechnique,* 46**,** 357-362.

JOYNER, W. B. & CHEN, A. T. F. 1975. Calculation of nonlinear ground response in earthquakes. *Bulletin of the Seismological Society of America,* 65**,** 1315-1336.

KABILAMANY, K. & ISHIHARA, K. 1990. Stress dilatancy and hardning laws for rigid granular model of sand. *Soil Dynamics and Earthquake Engineering,* 9**,** 66-77.

KIM, T. C. & NOVAK, M. 1981. Dynamic properties of some cohesive soils of Ontario. *Canadian Geotechnical Journal,* 18**,** 371-389.

KOKUSHO, T. 1980. Cyclic triaxial test of dynamic soil properties for wide strain range. *Soils and Foundations,* 20**,** 45-60.

KOKUSHO, T., YOSHIDA, Y. & ESASHI, Y. 1982. Dynamic properties of soft clay for wide strain range. *Soils and Foundations,* 22**,** 1-18.

KONDNER, R. L. & ZELASKO, J. S. 1963. A hyperbolic stress-strain formulaiton of sands. *2nd Pan. Am. Conf. on Soil Mechanics and Foundation Engineering.* Sao Paulo, Brazil.

KOTTKE, A. & RATHJE, E. M. 2010. Strata, http://nees.org/resources/692.

KRAMER, S. L. 1996. *Geotechnical earthquake engineering,* Upper Saddle Rive, N.J., Prentice Hall.

KUMAR, J. & MADHUSUDHAN, B. N. 2010. A note on the measurement of travel times using bender and extender elements. *Soil Dynamics and Earthquake Engineering,* 30**,** 630-634.

KURIBAYASHI, E., IWASAKI, T. & TATSUOKA, F. 1974. Effects of stress conditions on dynamic properties of sands. *Bulletin of the international institute of seismology and earthquake engineering,* 12**,** 14.

LADE, P. V., LIGGIO, C. D. & YAMAMURO, J. A. 1998. Effects of non-plastic fines on minimum and maximum void ratios of sand. *Geotechnical testing Journal,* 21.

LADE, P. V. & NELSON, R. B. 1987. Modelling the elastic behaviour of granular materials. *International Journal for numerical and analytical methods in geomechanics,* 11**,** 521-542.

LEE, J.-S. & SANTAMARINA, J. C. 2005. Bender Elements: Performance and Signal Interpretation. *Journal of Geotechnical and Geoenvironmental Engineering,* 131**,** 1063-1070.

LEONG, E. C., YEO, S. H. & RAHARDJO, H. 2005. Measuring shear wave velocity using bender elements. *Geotechnical testing Journal,* 28.

LO PRESTI, D. C. F., JAMIOLKOWSKI, M., PALLARA, O., CAVALLARO, A. & PEDRONI, S. 1997. Shear modulus and damping of soils. *Geotechnique,* 47**,** 603-617.

LO PRESTI, D. C. F., LAI, C. G. & IGNAZIO, P. 2006. ONDA: Computer code for nonlinear seismic response analyses of soil deposits. *Journal of Geotechnical and Geoenvironmental Engineering,* 132.

MATASOVIC, N. & VUCETIC, M. 1993. Cyclic characterization of liquefiable sands. *Journal of Geotechnical Engineering,* 119**,** 1805-1822.

MCGANN, C. & ARDUINO, P. 2012. *Site response analysis of a layered soil column* [Online]. Available: http://opensees.berkeley.edu/wiki/index.php/Site_Response_Analysis_of_a_Layered_Soil_Column_%28Total_Stress_Analysis%29 [Accessed September 2012].

MCKENNA, F. & FENVES, G. L. 2001. Open System for Earthquake Engineering Simulation, OpenSees. v2.3.2 ed.: Pacific earthquake engineering research center, Univeristy of California, Berkeley.

MOMEN, H. & GHABOUSSI, J. Stress dilatancy and normalized work for sands. IUTAM conference on deformation and failure of granular materials, 31 Aug.-3 Sep. 1982 Delft. 10.

MROZ, Z. 1967. On the description of anisotropic workhardening. *Journal of the Mechanics and Physics of Solids,* 15**,** 163-175.

MURAVSKII, G. & FRYDMAN, S. 1998. Site response analysis using a non-linear hysteretic model. *Soil Dynamics and Earthquake Engineering,* 17**,** 227-238.

NEW ZEALAND STANDARD 1986. NZS 4402: 1986, Methods of testing soils for civil engineering purposes. New Zealand.

NI, Q., TAN, T. S., DASARI, G. R. & W., H. D. 2004. Contribution of fines to the compressive strength of mixed soils. *Geotechnique,* 54**,** 561-569.

NZS 1170.5 2004. Structural design actions. *Part 5: earthquake actions - New Zealand.* Wellington, New Zealand: Standards New Zealand.

OSINOV, V. A. 2003. Cyclic shearing and liquefaction of soil under irregular loading: an incremental model for the dynamic earthquake-induced deformation. *Soil Dynamics and Earthquake Engineering,* 23**,** 535-548.

PARK, D. & HASHASH, Y. M. A. 2004. Soil damping formulation in nonlinear time domain site response analysis. *Journal of earthquake engineering,* 8**,** 249-274.

PEER. 2013. *http://peer.berkeley.edu/peer_ground_motion_database* [Online].

PENNINGTON, D. S. 1999. *The anisotropic small strain stiffness of Cambridge Gault clay.* Doctor of Philosophy, University of Bristol.

PHILLIPS, C. & HASHASH, Y. M. A. 2009. Damping formulation for nonlinear 1D site response analyses. *Soil Dynamics and Earthquake Engineering,* 29**,** 1143-1158.

PREVOST, J. H. 1989. DYNA1D - A computer program for nonlinear seismic site response analysis technical documentation. *NCEER*. Buffalo: National center for earthquake engineering research.

PYKE, R. 1979. Nonlinear soil models for irregular cyclic loadings. *Journal of Geotechnical Engineering Division,* 105**,** 715-726.

QIU, T. & FOX, P. J. 2008. Effective soil density for propagation of small strain shear waves in saturated soil. *Journal of Geotechnical and Geoenvironmental Engineering,* 134**,** 1815-1819.

RAHMAN, M. M. 2009. *Modelling the influence of fines on liquefaction behaviour.* Phd, The University of New South Wales.

RAHMAN, M. M., CUBRINOVSKI, M. & LO, S. R. 2011. Initial shear modulus of sandy soils and equivalent granular void ratio. *Geomechanics and Geoengineering***,** 11.

RAHMAN, M. M., LO, S. R. & GNANENDRAN, C. T. 2008. On equivalent granular void ratio and steady state behaviour of loose sand with fines. *Canadian Geotechnical Journal,* 45**,** 1439-1456.

RAMBERG, W. & OSGOOD, W. R. 1943. Description of stress - strain curves by three parameters. Washington: National advisory committee for Aeronautics.

REES, S. 2009. *Effects of fines on the undrained behaviour of Christchurch sandy soils.* Ph.D., University of Canterbury.

RIX, G. & STOKOE, K. H. 1991. Correlation of initial tangent modulus and cone penetration resistance. *In:* HUANG, A.-B., ed. First internatioanl symposium on calibration chamber testing/ ISOCCT1, June 1991 Postday, New York. New York: Elservier, 351-362.

ROBERTSON, P. K. 1990. Soil classification using the cone penetration test. *Canadian Geotechnical Journal,* 27**,** 151-158.

ROBERTSON, P. K. 2009. Interpretation of cone penetration tests - a unified approach. *Canadian Geotechnical Journal,* 46**,** 1137-1355.

ROBERTSON, P. K. 2012. Interpretation of in-situ tests - some insights. *4th International Conference on Geotechnical and Geophysical Site Characterization, ISC'4.* Brazil.

ROBERTSON, P. K. & CAMPANELLA, R. G. 1983. Interpretation of cone penetration tests- Part I: Sands. *Canadian Geotechnical Journal,* 20**,** 718-733.

RODRIGUEZ-MAREK, A., BRAY, J. D. & ABRAHAMSON, N. A. 2001. An Empirical Geotechnical Seismic Site Response Procedure. *Earthquake Spectra,* 17**,** 65-87.

ROESSET, J. M. 1977. Soil amplification of earthquakes. *In:* DESAI, C. S. & CHRISTIAN, J. T. (eds.) *Numerical methods in geotechnical engineering.* McGraw-Hill.

SCHNABEL, P. B., LYSMER, J. & SEED, H. B. 1972. SHAKE: a computer program for earthquake response analysis of horizontally layered sites. *EERC.* Berkeley: University of California.

SEED, H. B. & IDRISS, I. M. 1970. Soil moduli and damping factors for dynamic response analyses. Berkeley: Earthquake engineering research center.

SEED, H. B., ROMO, M. P., SUN, J. I., JAIME, A. & LYSMER, J. 1987. Relationships between soil conditions and earthquake ground motions in Mexico City in the earthquake of Sept. 19, 1985. *Earthquake engineering research center.* Berkeley, California: College of engineering, University of California, Berkeley.

SEED, H. B., WONG, R. T., IDRISS, I. M. & TOKIMATSU, K. 1984. Moduli and damping factors for dynamic analyses of cohesionless soils. *Earthquake engineering research center.* Berkeley: University of California.

SHIBUYA, S., TATSUOKA, F., TEACHAVORASINSKUN, S., KONG, X. J., ABE, F., KIM, Y.-S. & PARK, C.-S. 1992. Elastic deformation properties of geomaterials. *Soils and Foundations,* 32**,** 26-46.

SHIRLEY, D. J. 1978. An improved shear wave transducer. *Journal of Acoustical society of America,* 63**,** 1643-1645.

SILVA, W. J., DARRAGH, R., GREGOR, N., MARTIN, G., ABRAHAMSON, N. A. & KIRCHER, C. 2000. Reassessment of site coefficient and near-fault factors for building code provisions. Pacific engineering and analysis.

SILVA, W. J., TURCOTTE, T. & MORIWAKI, Y. 1988. Soil response to earthquake ground motion. Walnut Creek, California: Woodward-Clyde consultants.

SILVER, M. L. & SEED, H. B. 1969. The behavior of sands under seismic loading. Berkeley: Earthquake engineering research center.

SMYROU, E., TASIOPOULOU, P., BAL, I. E. & GAZETAS, G. 2011. Ground motions versus geotechnical and structural damage in the February 2011 Christchurch earthquake. *Seismological research letters,* 82**,** 882-892.

STEPHENSON, W. R., BRUCE, Z., BARKER, P. R. & BEETHAM, R. D. 2010. Immediate report on the use of microtremors (SPAC measurements) for assessing liquefaction potential in the Christchurch area. *GNS science report, 2011/25*. Lower Hutt: GNS science.

STEWART, J. P., KWOK, A. O.-L., HASHASH, Y. M. A., MATASOVIC, N., PYKE, R., WANG, Z.-L. & YANG, Z. 2008. Benchmarking of nonlinear geotechnical ground response analysis procedures. Berkeley: Pacific earthquake engineering research center.

STOKOE, K. H., DARENDELI, M. B., ANDRUS, R. D. & BROWN, L. T. 1999. Dyanmic soil properties: Laboratory, field and correlation studies. Second international conference on earthquake geotechnical engineering, June 21-25 1999 Lisboa, Portugal. Rotterdam ; Brookfield, VT, USA : A.A. Balkema: A.A. Balkema, 811-845.

STOKOE, K. H. & SANTAMARINA, J. C. 2000. Seismic - wave - based testing in geotechnical engineering. *International Conference on Geotechnical and Geological Engineering, GeoEng 2000.* Melbourne, Australia.

SUN, J. I., GOLESORKHI, R. & SEED, H. B. 1988. Dynamic moduli and damping ratios for cohesive soils. Berkeley: University of California.

TATSUOKA, F. & SHIBUYA, S. 1991. Deformation characteristics of soils and rocks from field and laboratory tests. *The 9th Asian regional conference on soil mechanics and foundation engineering.* Bangkok.

THEVANAYAGAM, S. 2007. Intergrain contact density indices for granular mixes--I: Framework. *Earthquake engineering and engineering vibration,* 6**,** 123-134.

THEVANAYAGAM, S. & LIANG, J. 2001. Shear wave velocity relations for silty and gravely soils. *In:* PRAKASH, S. (ed.) *Fourth international conference on recent advances in geotechnical earthquake engineering and soil dynamics.* San Diego, California.

THEVANAYAGAM, S. & MOHAN, S. 2000. Intergranular state variables and stress-strain behaviour of silty sands. *Geotechnique,* 50**,** 1-23.

THEVANAYAGAM, S., SHENTHAN, T., MOHAN, S. & LIANG, J. 2002. Undrained fragility of clean sands, silty sands, and sandy silts. *Journal of Geotechnical and Geoenvironmental Engineering,* 128**,** 849-859.

TOSHINAWA, T., TABER, J. J. & BERRILL, J. B. 1997. Distribution of ground-motion intensity inferred from questionnaire survey, earthquake recordings, and microtremor measurements—A case study in Christchurch, New Zealand, during the 1994 arthurs pass earthquake. *Bulletin of the Seismological Society of America,* 87**,** 356-369.

TOWHATA, I. 2008. *Geotechnical earthquake engineering,* Berlin, Springer.

TRONCOSO, J. H. & VERDUGO, R. 1985. Silt content and dynamic behavior of tailing sands. *11th International Conference on Soil mechanics and foundation engineering*.

VERDUGO, R. 1992. *Characterization of sandy soil behavior under large deformation.* D. Engineering, University of Tokyo.

VIGGIANI, G. & ATKINSON, J. H. 1995. Interpretation of bender element tests. *Geotechnique,* 45**,** 149-154.

VUCETIC, M. 1990. Normalized behavior of clay under irregular cyclic loading *Canadian Geotechnical Journal,* 27**,** 29-46.

VUCETIC, M. & DOBRY, R. 1991. Effect of Soil Plasticity on Cyclic Response. *Journal of Geotechnical Engineering,* 117**,** 89-107.

VUCETIC, M., LANZO, G. & DOROUDIAN, M. 1998. Damping at Small Strains in Cyclic Simple Shear Test. *Journal of Geotechnical and Geoenvironmental Engineering,* 124**,** 585-594.

WAIR, B. R., DEJONG, J. T. & SHANTZ, T. 2012. Guidelines for estimation of shear wave velocity profiles. *PEER2012-08.* Pacific earthquake engineering research center.

WICHTMANN, T. & TRIANTAFYLLIDIS, T. 2010. On the influence of the grain size distribution curve on dynamic properties of Quartz sand. *In:* PRAKASH, S. (ed.) *Fifth International conference on recent advances in geotechnical earthquake engineering and soil dynamcis2010.* San Diego, California.

WOOD, C. M., COX, B. R., WOTHERSPOON, L. M. & GREEN, R. A. 2011. Dynamic site characterization of Christchurch strong motion stations. *Bulletin of the New Zealand Soceity for Earthquake Engineering,* 44**,** 195-204.

WOTHERSPOON, L. M. 2013. *RE: Personal communication.*

YAMAMURO, J. A. & LADE, P. V. 1997. Static liquefaction of very loose sands. *Canadian Geotechnical Journal,* 34**,** 905-917.

YOUN, J.-U., CHOO, Y.-W. & KIM, D.-S. 2008. Measurement of small-strain shear modulus G_{max} of dry and saturated sands by bender element, resonant column, and torsional shear tests. *Canadian Geotechnical Journal,* 45**,** 1426-1438.

ZEGHAL, M., ELGAMAL, A.-W. & TANG, H. T. 1995. Lotung downhole array: evaluation of soil nonlinear properties. *Journal of Geotechnical Engineering,* 4**,** 363-378.